



Dipartimento di Scienze

Dottorato in Scienza della Materia, Nanotecnologie e
Sistemi Complessi

XXXII Ciclo

Coordinatore Dottorato

Prof. Fabio Bruni

**“Characterization of molecules of biological interest and
their application in biosensors”**

Ph.D. student:
Jacopo Chiarinelli

Supervisors:
Prof. Alessandro Ruocco
Dr.ssa Paola Bolognesi

a.a. 2018/19

Alla mia Famiglia

Abstract

Biomolecules and molecules of biological interest, thanks to their diversified chemical physical properties and their unlimited list of functions in chemical reactions and biological processes, are more and more used in several fields, from fundamental science to technological applications in medicine, agrifood monitoring and detection of environmental pollutant.

These perspectives call for new strategies and techniques to investigate the intrinsic properties (electronic structure, conformation, mechanical properties, etc.) of these macromolecules, to handle and to embed them in devices as well as to study their functioning in different environments, from their natural biological settings to the ones relevant for the diverse applications.

The study of the intrinsic chemical physical properties can be performed with a high level of accuracy, by a combination of sophisticated experimental and theoretical approaches, on model systems. However, the size of the model systems is often reduced to small building blocks of the large biomolecules and the employed methodologies cannot be directly scaled up to more complex and realistic systems.

The motivation of this thesis is to introduce methodologies to study biomolecules and their applications which contribute to fill the gap between small and complex biomolecular systems.

The electronic structure and photofragmentation mechanisms of a group of molecules belonging to the oxygen mimetic class of radiosensitisers, which are used in radiotherapy to increase the efficacy and selectivity of the medical treatment, are investigated by several spectroscopic techniques (valence band photoemission, photoelectron-photoion coincidence and appearance energy measurements) and advanced quantum mechanical calculations. Molecules of increasing complexity are characterized in a bottom up approach from model systems (imidazole and nitroimidazole isomers) to real drugs (misonidazole and metronidazole) in order to unravel the correlation between intrinsic properties and their functions in medical applications.

To move the investigation towards more complex and realistic systems that can be handled experimentally, the electrospray ionization, ESI, a novel technique for production of beams of multicharged complex molecules has been adopted. A vacuum apparatus equipped with a non-commercial ESI source and electron optics devices has been designed and characterized comparing computer simulations, performed by SIMION software, and experimental measurements to achieve a realistic and detailed understanding and control of the ion beam. The main purpose of this characterization is to optimise the performances of the instrument, reaching a sufficiently intense ion flux either to perform spectroscopic measurements or to deposit the molecules for making biosensors.

The ESI technique at ambient pressure condition has been also used for enzyme immobilisation and biosensors application. Laccase, a well known enzyme, has been used to validate the technique and promising results have been obtained. Indeed it has been demonstrated that at least 75% of enzymatic activity is preserved after ESI deposition, with the additional benefit of well controlled deposition parameters. The activity has reached the stage to produce a working biosensor on commercial screen printed electrodes, whose response is comparable with laccase based biosensor currently available.

The results of this thesis have opened up many possibilities for both fundamental and applied future work.

Contents

Abstract	i
Contents	ii
1 Introduction	1
1.1 Biomolecules and their functions	1
1.2 Radiation damage, radiotherapy and radiosensitisers	3
1.3 Biomolecules and Biosensors	5
2 Experimental techniques and theoretical methods	9
2.1 Production, handling and characterization of isolated biomolecules in gas phase	9
2.1.1 Different vacuum regimes for gas phase experiments	9
2.1.2 Production of biomolecules in gas phase	12
2.1.2.1 Thermal evaporation and the laser Induced thermal desorption (LITD)	13
2.1.2.2 Soft ionization techniques: ESI and MALDI	15
2.1.3 Characterization of biomolecules by photofragmentation	20
2.1.3.1 Radiation sources: rare gas discharge lamp and synchrotron radiation	21
2.1.3.2 Mass spectroscopies: TOF-MS, PEPICO spectroscopy and AE measurements	24
2.1.4 The ESI apparatus	34
2.1.4.1 Technical description of the ESI source	34
2.1.4.2 The experimental measurement of ion current	36
2.1.4.3 Radiofrequency devices: the octupole	38
2.1.4.4 Simulations with SIMION software	40
2.2 The apparatus for ESI deposition at ambient pressure	44
2.3 Theoretical Methods	46
2.3.1 Calculation of energy of a molecule	46
2.3.2 Valence orbitals IP and photofragmentation	48
2.3.3 Potential energy surface, fragmentation path, AE and fragmentation rate	49
3 Photofragmentation of nitroimidazole based radiosensitisers	53
3.1 model systems: imidazole and nitroimidazole isomers	53

3.1.1 TOF mass spectra	54
3.1.2 Relative branching ratios from PEPICO measurements	56
3.1.3 Appearance energy measurements	58
3.1.4 Discussion of the experimental and theoretical data	60
3.1.5 Metastable processes in nitroimidazole photo-fragmentation and their Simulations	67
3.2 From model systems to real drugs: misonidazole and metronidazole	79
3.2.1 TOF mass spectra	79
3.2.2 Relative branching ratios from PEPICO measurements	81
3.2.3 Appearance energy measurements	82
3.2.4 Discussion of main fragmentation paths	82
3.3 Conclusions	86
4 Enzymes deposition by ESI for biosensor application	87
4.1 The laccase enzyme and its activity	87
4.2 Deposition of laccase by ESI, experimental procedure and activity measurement	89
4.3 Characterization of the electrospray deposition technique	92
4.3.1 Deposition area	92
4.3.2 Deposition rate	92
4.4 Characterization of the deposited enzyme: chemical-physical investigation by XPS	95
4.5 The laccase biosensor on screen printed electrodes	102
4.6 conclusions	104
5 Construction and characterization of in vacuum ESI apparatus	105
5.1 strategy of the simulation to study the apparatus	105
5.2 Apparatus transmission vs scanning voltages: a qualitative overview	106
5.2.1 Capillary voltage scan	108
5.2.2 Tube lens voltage scan	108
5.2.3 Octupole voltage scan	109
5.2.4 Lens L11 voltage scan	111
5.3 Choice of initial conditions for the simulations	112
5.4 Estimate of the ion beam kinetic energy	117

5.4.1 The role of fluid dynamics	117
5.4.2 Differences and analogies between experiments and simulations	120
5.4.3 Experimental vs simulated: explanation	123
5.4.4 The energy barrier controlled by lens L11	124
5.4.5 Determination of the ions kinetic energy distribution	126
5.4.6 Can the ion's kinetic energy be controlled?	128
5.5 Tests with different molecules (adenine and laccase)	133
5.6 Summary	135
5.6 Conclusions and future work	137
Appendix of chapter 5	138
A.5.1 I_{ch} modulation due to channeltron detector efficiency	138
A.5.2 The retarding field analyser	140
6 Conclusions	143
Bibliography	145
List of publications	159
Acknowledgements (Ringraziamenti)	161

1 Introduction

The aim of this thesis is the characterization of the chemical-physics properties of molecules of biological interest of increasing complexity and the exploitation of their possible applications. While detailed experimental and theoretical techniques, derived from molecular physics, can be directly applied to model systems (amino acids or DNA bases), these same methods are unsuitable for larger molecules (proteins or DNA strands). Thus, after having applied the available molecular physics approaches to a class of model systems, the nitroimidazole molecules, the activity moved on to the study, development and characterization of a novel technique for production of beams of multicharged complex molecules based on the electrospray ionization, ESI, technique. This ESI source has a dual purpose; on one hand spectrometric and spectroscopic techniques can be applied to these complex molecules once they are produced in sufficiently intense beams under vacuum conditions, while on the other hand these same ion beams of enzymes, proteins or DNA strands can be deposited on proper substrates to produce devices like biosensors. This thesis is focussed on the application of the electrospray for the immobilisation of enzymes. Having proved the validity of the ESI technique for laccase enzyme deposition at ambient conditions, an instrument for deposition in vacuum has been built and characterized.

The choice of the molecular targets to be studied in the different activities of the thesis has been driven by their biological functions. The class of the nitroimidazole molecules has been chosen because of their role as radiosensitisers in radiotherapy, while the laccase enzyme in the application of the ESI technique because of its wide use in biosensors. Therefore, in the following three sections, biomolecules and their functions (1.1), radiation damage/radiotherapy and radiosensitisers (1.2) and finally biomolecules and biosensors (1.3) have been included to briefly introduce the three main pillars of this work.

1.1 Biomolecules and their functions

Biomolecules are a wide class of molecules, present in living organisms and essential for biological processes [1]. Macromolecules like proteins, nucleic acids (DNA and RNA), polysaccharides etc. belong to this class together with their building blocks amino acids, nucleotides and monosaccharides, respectively. The main components of biomolecules are oxygen, nitrogen, carbon and hydrogen although heavier elements like sulphur, copper, zinc, iron etc., present in low percentage, can play a key role in certain biological processes. A well known example is represented by the iron atoms in the haemoglobin of red cells used to bond oxygen molecules and transport them throughout all the body.

An even larger class is represented then by the “molecules of biological interest”, which include small molecules like water (H_2O), oxygen (O_2), carbon di oxide (CO_2), abundant also outside the living organisms, as well as synthetic molecules based on biomolecules or designed on purpose to interact with them, not spontaneously found in nature.

In a biological process each biomolecule has specific functions (enzymes catalyse specific chemical reactions like redox, synthesis or fragmentation of molecules; chlorophylls and some pigments absorb energy from the solar radiation and use it in the photosynthesis, haemoglobin binds and transports oxygen in the human body, DNA stores genetic information just to mention a few examples). This variety of properties and functionalities

have triggered a broad interest on biomolecules and encouraged their application in science and technology.

In medicine, the focus has been on a more and more detailed understanding of the biological functions as well as on innovative applications, spanning across the most diverse fields. For example, polysaccharides from the shells of shrimp and other crustaceans have been proposed for tissue engineering and regenerative medicine applications [2,3], while surface modification of inorganic prosthesis with biomolecules are proposed to improve the adhesion between soft tissues and prosthesis [4,5].

In nanotechnology, devices have been designed to exploit the same properties of biomolecules at work in biological processes, as for example biosensors based on enzymes and solar cells based on reaction centres of photosynthesis [6]. Also other characteristics, not directly used in living organisms, have been exploited in devices, like for example the DNA used as charge transfer element in solar cells [7,8] or in new nanostructured material for its mechanical properties or in “nanomachine”, to measure and control forces in the piconewton scale [9].

From this brief description of applications of biomolecules in science and technology, it is evident how information on both the intrinsic chemical physics characteristics of biomolecules and their behaviour and functioning in complex systems, where they interact with other elements, is indispensable to identify and optimise their use.

The study of the intrinsic chemical physics properties (conformation in space, electronic structure, fragmentation channels) can be performed on model systems, either in single molecule in a low density beam or deposited on the ideal surface of a single crystal. In both cases the interaction between the biomolecule and the environment is excluded or limited and well controlled. The size of model systems is often reduced to a single DNA base, amino acid or small peptides, that are the building blocks of large biomolecules. Techniques like mass spectrometry, photoionization, scanning tunnel microscopy (STM), etc., can provide accurate information on these systems and their size makes them accessible by theoretical simulations based on quantum mechanical calculations.

However, these very accurate methods cannot be scaled up to more complex systems like large macromolecules, especially in working conditions during a biological process or in operating device. Therefore real systems are generally studied by the analysis of their macroscopic characteristics, neglecting properties of single molecules, whose behaviour is inferred by the similarity with other complex systems. Very often, the properties of interest are optimized by a trial and error approach.

Some effort has been devoted to fill the gap between model systems and real/realistic systems (i.e. systems used in practical applications), for instance with photoemission experiments at near ambient pressure [10,11] or in liquid jet [12,13], with the application of atomic force microscopy (AFM) to biomolecules in solution [14] or with diffraction studies on crystallised protein [15] and electron cryotomography of biological systems [16].

The motivation of this thesis is to contribute to the filling of this gap as shown in chapter 3, where mass spectrometry and photoionization are applied to a series of molecules going from the model system to a real drug used in therapy, and in chapters 4 and 5 where the description of a set-up to produce a beam of multicharged molecular ions of complex biomolecules is described.

1.2 Radiation damage, radiotherapy and radiosensitisers

A medical application where the use and investigation of synthetic drugs is of great importance is radiotherapy, where the use of drugs called radiosensitisers tested to selectively increases the efficacy of radiotherapy on tumour cells during the medical treatment.

The interaction of energetic ionizing radiation with living cells is known to produce a damage which is sometimes permanent. However this potentially lethal effect of radiation, can also be exploited in radiotherapy to irradiate specific regions of the human body, where a tumour is located, in order to kill unhealthy cells. The source of radiation can be located directly inside the body, close to the tumour (brachytherapy), but more commonly it is provided by an external device (external beam radiotherapy) [17]. The radiation beam is composed either by charged particles (electrons or ions) or photons. Electron beams usually have energy in the range 4-20 MeV and are used to treat surface tumours (skin, limbs etc.) because the maximum radiation dose is deposited within few centimeters (1-5 cm) from the exposed surface [17] (Figure 1.1, left panel). More recently, also heavy particles like protons or bare atomic nuclei are used for cancer treatment therapy (hadron therapy) with the advantage of a deeper penetration in the body and a higher spatial localisation of the energy release. This is due to the nature of the collisional process involving heavy particles and the existence of the Bragg peak (Figure 1.1, left panel) [17,18]. This is a very promising therapeutic approach, which requires a deep understanding and characterisation of radiation-matter interaction at the nanoscale of the molecular level. Photon beam radiotherapy is the most widespread approach; it can be used in many oncological situations because the penetration depth is generally higher with respect to electrons and 'tunable' with photon energy. The energy range of a therapeutic photon beam spans from the X - to Gamma-rays (200 keV to 25 MeV) depending on the depth required for the treatment (Figure 1.1 left panel) [17].

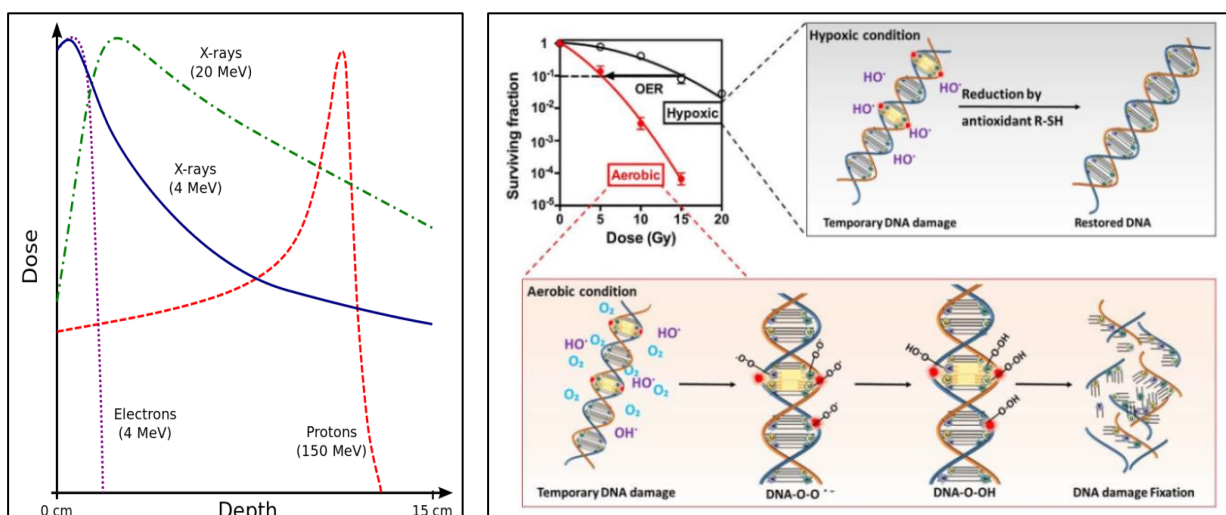


Figure 1.1. left: Radiation dose versus penetration depth for various radiotherapy methods [19]. **Right:** The oxygen fixation hypothesis. Under aerobic conditions, radiation induced DNA radicals are able to react with oxygen, resulting in permanent DNA damage and strand breaks [21].

The radiation damage eventually manifested at the macroscopic level of organs and tissues is initiated at the microscopic level, where the interaction of radiation with the elementary constituents of the biological system takes place, from cells down to DNA chain and its

constituent molecules. It is commonly recognised that the damage can be generated both by direct interaction of photons with the DNA and by secondary effects, where the energy is released by the radiation to the environment surrounding the DNA and produces a chain of secondary events as formation of radical species ($\cdot\text{OH}$, $\cdot\text{O}_2^-$, etc.), ions and a large number of secondary electrons in a wide energy range, from several keV to thermal energy. These secondary products, in particular electrons of energy as low as few eV [20], can efficiently lead to molecular dissociation, break-up chemical bonds in DNA and inhibit biological functions and cellular duplication [17,21].

Radical species, like the hydroxyl radical ($\cdot\text{OH}$) produced by the interaction between water and primary radiation or secondary electrons [21], effectively attach neighbouring DNA molecules. The damage is due to the abstraction of a H-atom or to the formation of OH-DNA bases adducts [22,23,24]. All of these species are created by the radiation interaction with the elementary molecular systems within microseconds from the irradiation and extinguish their direct effects within milliseconds. However, the processes they trigger will persist long after radiation exposure and are at the very heart of the radiotherapy effect.

One of the main problems in radiotherapy is the lack of selectivity in the energy release, as cancer cells are equally damaged as healthy tissues all along the track of the radiation beam. Several technical strategies are being developed to limit this drawback, in particular acting on the delivered intensity (intensity modulated radiation therapy) and changing the position of radiation source (stereotactic body radiation therapy) in a crossed beam approach that decreases the amount of dose released in healthy tissues and spreads the energy surplus in a wider region, thus lowering the toxicity. Computerized systems to plan the radiotherapy treatment and imaging techniques are among the most innovative progresses in this direction [17,25,27].

Another strategy to increase the effectiveness of radiotherapy is based on the use of radiosensitising drugs. These drugs used in conjunction with the radiotherapy treatment, selectively enhance the damage on the DNA of cancer rather than healthy cells. This in turn allows reducing the overall dose delivered to the patient, containing the 'side effects' and toxicity of radiotherapy.

There are several categories of radiosensitisers based on different chemical or biological mechanisms [21,26]. Among them in this work, we have focussed the attention on the so called "oxygen mimetic" class of radiosensitisers.

Molecular oxygen, O_2 , being one of the molecules with the highest electron-affinity in the human body reacts with damaged DNA by mean of radical species inhibiting natural molecular repair mechanisms (Figure 1.1, right panel) [21,27]. Indeed, one of the most important causes for radiotherapy failure is hypoxia, a condition of low concentration of oxygen, in the area of the cancer cells. In tumours, it may result from the unbalanced oxygen availability and consumption (chronic hypoxia) and/or from the temporary closing of blood vessels due to the malformed vascularisation of the tumour (acute hypoxia) [21,27]. As a result, hypoxic tumours are particularly difficult to treat as they are more resistant to radiotherapy.

Oxygen mimetic radiosensitisers have been observed to be particularly effective on hypoxic tumours. They are highly reactive species that, like oxygen, are able to produce permanent damage in the DNA structure. However, differently with respect to oxygen, they are not metabolized in cells and can be accumulated in hypoxic tumour tissues; this is a crucial point because they need to be present during radiotherapy in order to be effective sensitisers [27,28]. Nitric oxide (NO) and nitroimidazole based molecules (metronidazole, misonidazole,

etanidazole, pimonidazole, nimorazole etc.) [21,26,28] belong to this class of radiosensitisers and some of them have reached the stage of clinical trials.

Unfortunately some of them have little efficacy in improving the clinical response and have been discarded because of the neurotoxicity side effect [27,28,29]. It has been observed that drugs based on 2-NI, for example misonidazole, pimonidazole, etanidazole etc.[26,30], show better results [30,31] even though not as much as initially expected.

Recently, relevant improvements in hypoxia imaging and monitoring have been obtained and important changes in radiation dosage during radiotherapy has been proposed. Tests with these new therapeutic methodologies have shown higher efficiency of oxygen mimetic radiosensitizers with respect to earlier studies [27].

The study of possible mechanisms of functioning of this class of radiosensitizers has been the object of one of the activities of this thesis. In chapter 3 the photofragmentation of a series of nitroimidazole molecules of increasing complexity in the VUV range is studied. VUV radiation has been chosen, because the secondary processes subsequent to radiation absorption in the radiotherapy, i.e. the processes that are at the core of radiotherapy efficacy, occur on the energy scale of a few tens of eV involving the ionization of valence and inner valence region of the molecule, i.e. the same states accessed in the VUV photon energy range.

1.3 Biomolecules and Biosensors

Biosensors are analytical devices used to detect and quantify the abundance of a specific chemical substance [32,33,34]. The name is due to the presence of a sensitive biological element (bioreceptor) that interacts with the substance to be detected (analyte). The response of the interaction is converted, for example by a chemical physical transduction mechanism, in an electric signal which is amplified and analysed (Figure 1.2). Several classes of bioactive materials as enzymes, antibodies, nucleic acid, cells or microorganisms can be used as bioreceptors [32,33,34,35], because they have characteristic and selective chemical interactions (Figure 1.2). For example, the enzymes are a special class of proteins that catalyse a specific or a restricted type of chemical reactions transforming a chemical specie in a new one, while antibodies have a binding site that fits a specific antigen and nucleic acids have a strong base pair affinity.

Biosensors can be classified according to their physical or chemical response, resulting from the interaction between the analyte and the bioreceptor, and the subsequent transduction mechanism. Five classes of biosensors (see Table 1.1) are generally recognized: electrochemical, electric, optical, piezoelectric and thermometric [33,34,36,42].

The class of interest in the present work is the one of the electrochemical biosensors based on enzymes as bioreceptor. These devices, thanks to the large variety of natural and specifically designed synthetic enzymes and the many functions they can perform, have been proposed for applications in different fields from clinical diagnosis to food control and environmental screening [33,34]. The most successful example is the electrochemical biosensor based on the immobilisation of glucose oxidase enzyme to monitor glucose level in blood [37].

Electrochemical biosensors are generally small devices composed of an electrochemical cell with three electrodes (Figure 1.3.A) [33,38,39]: the enzyme is immobilised on the working electrode (WE), where the redox reaction takes place; the reference electrode (RE) made of standardised materials, like silver chloride, is used as reference to measure the potential on

the working electrode; the counter electrode (CE) is used to close the circuit and to balance the electric current that flows across the working electrode. The three electrodes, normally isolated to each other, are placed in electric contact during the measurement through the solution containing low concentrations of the analyte to be detected; the electric current generated by the interaction between analyte and bioreceptor is then measured between WE and CE by a potentiostat that controls the three electrodes. The three electrode cells systems for biosensors application are commercial devices (Figure 1.3.B) [40] although methods to obtain more efficient and environmental friendly device are currently under investigation [36,39,41].

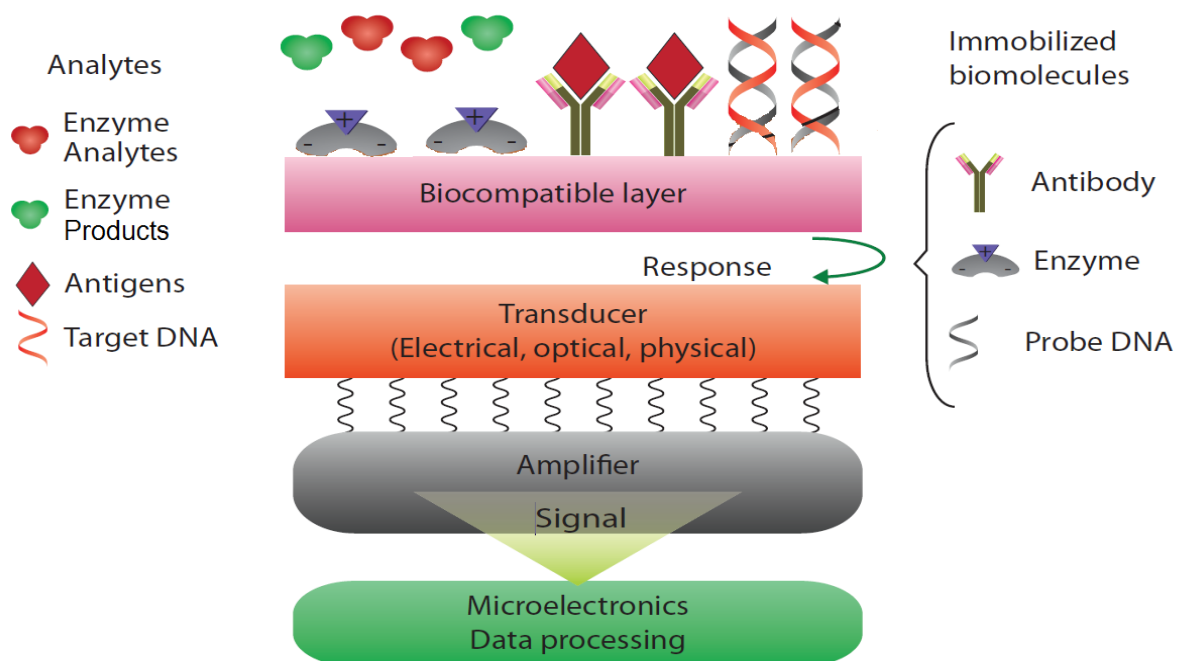


Figure 1.2. Schematic structure and operating principles of a biosensor with examples of analytes (left) and active bioreceptors (right) [42]; the mechanism of transduction for generation of a physical chemical signal is also indicated.

Class of biosensor	Operating mechanism
Electrochemical	<ul style="list-style-type: none"> - measurement of the electric current due to redox reactions, directly induced by the active biological element or due to new species produced by the interaction between enzyme and analyte, on an electrode; - measurement of the variation of electric potential across an ion selective membrane separating two solutions.
Electric	<ul style="list-style-type: none"> - production of ions or electrons that modify conductivity or resistivity of a solution.
Optical	<ul style="list-style-type: none"> - detection of fluorescence; - monitoring of variations in the response of the active region when illuminated by an external source of light.
Piezoelectric	<ul style="list-style-type: none"> - variation of mass, and therefore in the resonance frequency of piezoelectric devices like quartz crystal, typically in the range of ng to μg.
Thermometric	<ul style="list-style-type: none"> - production of heat monitored by a temperature measurement.

Table 1.1. Examples of operating mechanism for each class of biosensors [33].

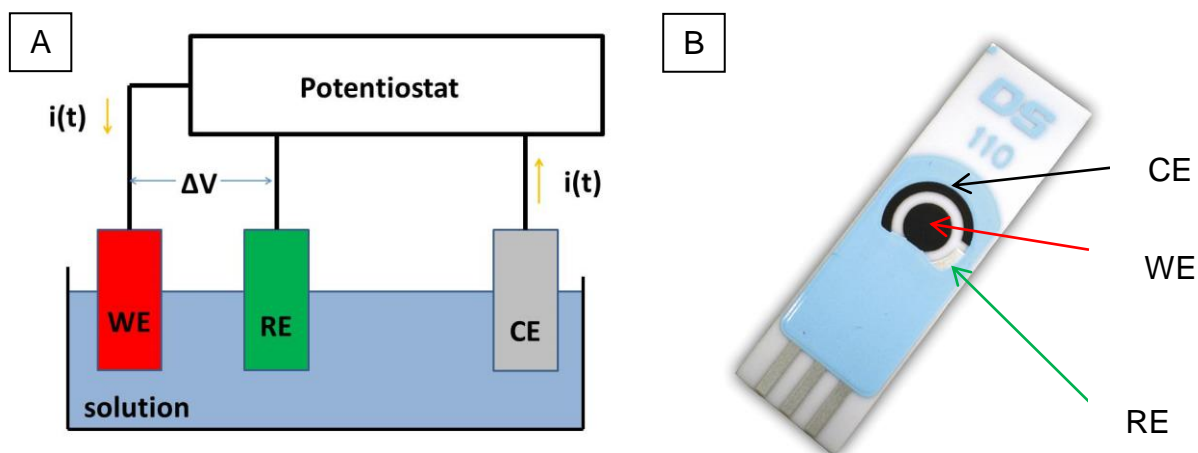


Figure 1.3. A) Schematic description of a three electrodes electrochemical cell. B) Commercial DropSense screen printed electrode (SPE) [40] with the three electrodes indicated by arrows.

Among the parameters that characterise a biosensor (Table 1.2), some, like selectivity, depend exclusively on the bioreceptor, but the majority, like detection range, reproducibility, stability, etc. is influenced by the technique and method used to produce the device and to immobilise the bioreceptor [43].

The technique used to deposit the enzyme on the working electrode and the adhesion mechanism (immobilization) are crucial elements for the performance of the biosensor. The enzyme can be directly in contact with the electrode. In this case the immobilization is due either to the formation via long range interactions of Van der Waals or hydrogen bonds (physisorption) [44], or to the formation of covalent bonds (chemisorption) [33,42]. The enzyme can be also linked to the working electrode by other molecules (linkers), embedded in a porous matrix [32,33,42], or deposited on nanostructured electrodes for enhanced performances [32,45,46].

Biosensor characteristic	Description
Selectivity	Ability to discriminate between different analytes
Reproducibility intra-electrode and inter-electrodes	Ability of the same (intra-electrode) or different (inter-electrode) sensors to produce the same response when exposed several times to the same amount of analyte.
Working stability	Degree of susceptibility to ambient disturbances in and around the biosensing system.
Storage stability	Reproducibility of response after a storage period under controlled conditions.
Sensitivity or Limit of detection	The minimum amount of analyte that can be detected by a biosensor, sometimes referred to as limit of detection (LOD).
Linearity or Detection range	Range of analyte concentration that produces a response for a set of measurements with different concentrations of analyte to a straight line of signal versus concentration.
Response time	Time necessary to obtain a measurable and stable response.

Table 1.2. The main characteristics of a biosensor.

Standard techniques for the immobilisation of the enzymes are drop casting or spin coating. More sophisticated techniques like MAPLE, electrospinning and printing methods have been proposed and are nowadays tested [32,36,41,47]. Each of these techniques has advantages and disadvantages. The most critical parameter to determine the choice of a technique is certainly the biocompatibility, i.e. the capability to preserve the enzymatic activity, which is at the very base of the performance of the biosensor.

The ESI technique, with its ability to produce beams of intact biomolecules of every size and weight, is an attracting tool to be used for deposition of biomolecules and for manufacturing biosensors.

As it will be demonstrated in chapter 4, ambient pressure electrospray deposition, (ESD) provides the possibility to preserve the activity of an enzyme and to control deposition parameters like size, amount or uniformity of deposited material. Thus it will be proposed as a suitable strategy to overcome some of the shortcomings of less sophisticated technique like drop casting.

As a further step towards in-vacuum deposition, where a cleaner sample with controlled conformation of the biomolecules is possible, a new set-up has been designed and is being built to the purpose. This set-up will be composed of 3 stages: the first to produce and to transfer in vacuum the beam of molecular ions, the second equipped with a quadrupolar mass filter to select the ions according their m/z ratio and the third where an electrostatic deflector guides the ion beam either towards an UHV deposition chamber or a branch line for gas phase spectrometry/spectroscopy. The construction and characterization via a combination of measurements and ion-optics simulation of the first stage of the set-up is the object of chapter 5.

2 Experimental techniques and theoretical methods

In the introduction, the importance of biomolecules in science and technology has been outlined. This wide use of biomolecules calls for information about their intrinsic physical-chemical properties, their functions and behaviour in the complex and heterogeneous environments where they are at work. To obtain this information different approaches and methods are required. This chapter describes the most relevant techniques I have used during my PhD project and includes a more general overview about the source used for the production of complex biomolecules as isolated species in the gas phase.

Section 2.1 introduces the studies of isolated biomolecules, discussing the meaning of the term “isolated” biomolecules and the methods to produce them, the experiments that can be performed and the instrumentation used to obtain the results described in chapters 3. This section includes a description of the basic principles of the electrospray ionisation (ESI) mechanism and an introduction of the in-vacuum ESI apparatus that will be characterised in chapter 5. In section 2.2 is reported, a detailed description of the ESI setup used for the deposition of enzymes at ambient pressure presented in chapter 4.

In section 2.3 then a brief description of the theoretical methods used to interpret the experimental results of chapter 3 is reported.

2.1 Production, handling and characterization of isolated biomolecules in gas phase

The definition of “isolated” molecule refers not only to molecules which are not incorporated in a solid or deposited on a surface, but are not even interacting in the gas phase with other nearby molecules. This is obtained using low density molecular beams in vacuum condition.

Results presented in this work were obtained by experiments performed in different pressure regimes. Gas phase mass spectroscopy results presented in chapter 3 require High Vacuum (HV) or Ultra High vacuum (UHV), while deposition with an electrospray ionization (ESI) source can be done at ambient pressure (chapter 4) or in vacuum (chapter 5). In particular, in the ESI apparatus described in section 2.1.4 several vacuum regimes are experimented by the ions flying from the source, operated at ambient pressure, to the final stages in HV/UHV for the characterization or deposition. This has a relevant impact on the performance of the apparatus. For this reason, in the following section the different vacuum regimes will be described.

2.1.1 Different vacuum regimes for gas phase experiments

The term “vacuum” refers to a region with a pressure lower than atmospheric condition (10^3 mbar) and the different vacuum regimes are generally subdivided in:

- *Rough vacuum* (RV): $1 \times 10^3 - 1$ mbar
- *Medium vacuum* (MV): $1 - 1 \times 10^{-3}$ mbar
- *High vacuum*, (HV): $1 \times 10^{-3} - 1 \times 10^{-7}$ mbar
- *Ultra high vacuum* (UHV): $1 \times 10^{-7} - 1 \times 10^{-11}$ mbar
- *Extremely high vacuum* (EHV): $< 1 \times 10^{-11}$ mbar

A useful parameter to quantify the vacuum regime experienced by a molecule is the mean free path, λ , defined as the distance travelled by a molecule between two successive collisions with surrounding molecules:

$$\lambda = \frac{1}{\sqrt{2} n \sigma} \quad (2.1)$$

where σ is the geometrical cross section and n is the number of molecules per unit of volume.

The mean free path is linked to pressure (Table 2.1) by the law of the ideal gas

$$n = \frac{P}{kT} \quad (2.2)$$

where P is pressure, k the Boltzmann constant and T the temperature.

Another relevant parameter to understand physical conditions of a molecule in a gas is the collision rate (c_r) defined as the ratio between molecular velocity, v , and mean free path λ

$$c_r = \frac{v}{\lambda} = \frac{\sqrt{\frac{3kT}{m}}}{\lambda} \quad (2.3)$$

In Table 2.1 the values of n , λ and c_r for several ranges of pressures for a molecule with mass 100 Da at 300 K are reported.

Pressure (mbar)	n (molecules/m ³)	λ (m) $\sigma = 10^{-18} \text{ m}^2$	c_r (collision/s) $T = 300 \text{ K}, m = 100 \text{ Da}$
10^3	10^{25}	10^{-8}	10^4
1	10^{22}	10^{-5}	10
10^{-3}	10^{19}	10^{-2}	10^{-2}
10^{-6}	10^{16}	10^1	10^{-5}
10^{-9}	10^{13}	10^4	10^{-8}

Table 2.1 . Order of magnitude of molecular density, mean free path λ and collision rate c_r , calculated for several ranges of pressure, P , in the approximation of the ideal gas.

To describe the fluid dynamics of a gas two theoretical models, related to two completely different regimes mainly determined by the gas pressure (Figure 2.1), are considered:

- **Continuous or viscous flow (high pressure)** models are based on the hypothesis that the gas flow can be described as a fluid in a continuum, neglecting the molecular structure of the constituents gas [48,49]. In this approximation, all physical properties as temperature, pressure, velocity, density etc. are defined in each point and vary with continuity. The Navier-Stokes equations describe the fluid statics or dynamics, depending on further conditions, like compressibility or viscosity [50].
- **Molecular flow (low pressure)** models [50], in which intermolecular collisions have a low or negligible influence because c_r is very low. The boundary layers of the flow are characterized by the interaction between free molecules and the surface of the container [48,49,51]. The momentum and energy of this rarefied gas are assumed to have a Maxwellian distribution and can be calculated entirely from the kinetic theory of gases. Collisions between molecules can be treated by simple classical mechanics in the hard sphere approximation, considering momentum and energy conservation;

in a successive step the internal molecular degrees of freedom calculated by quantum mechanics theories can be introduced.

The Knudsen number (K_n), defined as the ratio between λ and a representative physical length scale of the system, L , generally the diameter of an aperture, tube or chamber through which the sample passes [52],

$$K_n = \frac{\lambda}{L} \quad (2.4)$$

is a useful quantity to discriminate between the continuum, molecular and transition (or Knudsen) regimes. According to the value of the Knudsen number we can identify (Figure 2.1):

- Continuous or viscous regime, $K_n < 0.01$
- Transition or Knudsen regime, $0.01 < K_n < 0.5$
- Molecular regime, $K_n > 0.5$

The continuous and molecular regimes are generally well described by their respective theoretical and numerical approaches used in the simulations of the experiments, providing very accurate results [48,49]. The transition regime is the most difficult to treat and simulate because i) the approximations adopted in other regimes do not hold and ii) the numerical approaches are generally either not accurate or too expensive from the computational point of view [48,53].

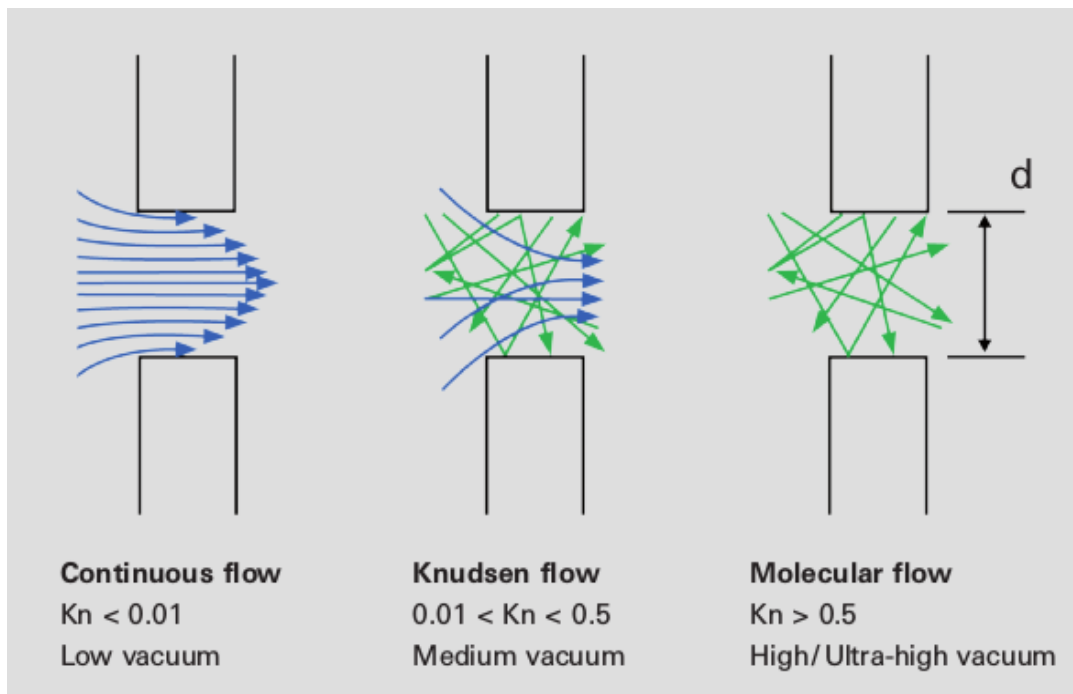


Figure 2.1. Schematic description of the gas flow in different vacuum regimes. The arrows indicate molecular trajectories and show how the flow is continuous or random at low or high K_n number, respectively [54].

2.1.2 Production of biomolecules in gas phase

As described in the introduction, the term “biomolecules” indicates a broad class of molecules with different chemical-physical properties which are used in a variety of technical and scientific applications. For this reason, a large number of techniques to produce biomolecules in gas phase, to study their intrinsic properties and to obtain molecular deposits on proper substrates have been proposed [52,63,71]. Each technique presents advantages and disadvantages and is generally used for a specific application with a restricted class of biomolecules.

The molecular stability, determined by the strength of the chemical bonds in the molecule, is one of the most relevant parameters that guides the choice of the technique to be used. Biomolecules are generally more fragile than inorganic matter (metals, semiconductors, etc.) due to the presence of weak bonds (hydrogen bonds and Van der Waals interactions) which determine the three-dimensional structure. The size and the mass of a biomolecule have a double effect on the stability, because on the one hand the structural relevance of the weak bonds is generally higher in large biomolecules as proteins where the tertiary structure is mainly due to hydrogen bonds but, on other hand, large molecules have more possibility to dissipate the acquired energy therefore reducing possible structural damage [55]. The relative importance of these two aspects depends on the specific molecular structure and on the way the energy is transferred to the molecule (collision, photon absorption, etc.). Evaporation techniques can be classified as “soft” when, independently on the molecular mass, the energy transferred to the biomolecule is low and the structure of the molecule is preserved during desorption; generally, these techniques use intermediate processes to indirectly transfer energy to the molecule. In general, bigger biomolecules are considered more fragile and for this reason a technique can be considered “soft” or not depending on the largest mass of intact biomolecules that can bring to the gas phase.

Thermal evaporation is a commonly used technique because it is simple, cheap and generally allows to obtain high evaporation rate useful both for spectroscopy and in vacuum deposition [56]. Also, laser induced thermal desorption, LITD, allows to reach good results in terms of evaporation rate to be used for mass spectrometry; however, none of these techniques can be applied with fragile biomolecules that would suffer decomposition even before desorption [63]. For the same reason, techniques like ions sputtering or fast atom bombardment [57] are not recommended, because high energetic (keV) ions or atom beams would decompose the biomolecules.

The only way to bring large and fragile biomolecules like enzymes, proteins or DNA strands as intact units in gas phase is to use specific “soft” evaporation techniques; the most common are electrospray ionization (ESI) [58,76,78,] and matrix assisted laser desorption ionization (MALDI) [59, 66]. These methods present the inconvenience i) to have a low rate production of gas phase biomolecules and ii) to require more complex and/or expensive experimental setups with respect to thermal desorption techniques.

The following section describes some of the most common techniques used to produce biomolecular beams in gas phase. More attention will be given to the techniques used in the PhD project.

2.1.2.1 Thermal evaporation and the laser induced thermal desorption (LITD)

Thermal evaporation

Thermal evaporation consists in heating up a pure sample of the biomolecule of interest in a crucible in the vacuum chamber to produce an effusive molecular beam. Thermal evaporation is possible only for sufficiently “robust” molecules (generally small biomolecules of less than 1 kDa [71]), which can acquire enough thermal energy to desorb from the condensed phase without suffering decomposition.

Although thermal evaporation seems to be a simple technique, several parameters and characteristics of the oven must be considered to obtain a good effusive molecular beam and to avoid perturbations in the subsequent analysis of the biomolecules [60].

- **Heating method:** several approaches can be used to heat the crucible depending on the required temperature and the material of the crucible; to evaporate biomolecule in vacuum condition generally low temperature is required (from few tens to few hundreds of °C) and a resistive heating systems based on the Joule effect is used. The temperature of the oven, and consequently the evaporation rate of the sample, can be varied acting on current intensity of the resistive heater [52,60]. A non-inductive wiring, where two closely spaced and parallel windings cancel out the magnetic field produced by the circulating electric current, warranties a field free region in the area surrounding the oven. This is an essential feature in gas phase experiments, where charged particles are generated near the oven and the spurious magnetic field could affect the measurement. This can be achieved by proper construction or by convenient commercial heating elements [61].

Higher temperatures (thousands of °C) would require different approaches, like electron bombardment, for example. However these are certainly not suitable for biomolecules evaporation.

- **Crucible material:** the material is chosen to be vacuum compatible, able to stand the required temperature and as chemically inert as possible, in order not to interact with the sample. Inert metals, like stainless steel, molybdenum or aluminium, as well as ceramic or quartz are generally used. The choice of the material is sometimes dictated also by practical reasons: the handling of fragile quartz, for example, can present difficulties [62].

- **Crucible size and shape:** the crucible is generally a container with an internal volume of about 1 cm³, where the sample is heated and transported towards the target zone (ionisation region, substrate for deposition etc.) via a nozzle. The internal volume of the crucible influences the evaporation rate of the sample and the shape of the nozzle defines the pressure inside the oven and the geometrical characteristics of the effusive beam [52]. The nozzle is generally a capillary used to collimate the molecular beam and therefore increase molecular density in the target zone [52,60] improving the signal-to-background ratio and to decrease the contamination from residual gases in the vacuum chamber.

Both mass spectrometers used in the experiments described in chapter 3 are equipped with a thermal evaporation system composed by a stainless steel crucible and a resistive heating element. In Figure 2.2 the heating system and crucible used in the mass spectrometer installed at CNR-ISM in Rome are shown as example. The resistive element (Figure 2.2.A) is a twin core Thermocoax [61], and the winding is more dense in the region approaching the

exit of the crucible (away from the flange) in order to reach higher temperature in that region. This part is further extended in a smaller hollow tube in order to accompany and preserve the temperature of the capillary of the crucible that will be hosted here, and prevent clogging. The temperature is monitored by two K-type thermocouples located at the tip and in the middle of the system. In the routine operation of the system, the crucible (Figure 2.2.B) is mounted on a stainless steel rod sliding down the oven until its final position is reached. The long and thin capillary is needed in order to enter in the extraction region of the time of flight spectrometer without perturbing the extracting field. This system could also be used with a gas line or high vapour pressure liquids hosted outside the vacuum chamber. A similar system is adopted also for the synchrotron radiation experiments performed at Elettra. In Table 2.2 the sizes of both crucibles used in Rome or in Trieste are reported.



Figure 2.2. Pictures of A) heating system and B) crucible used in time of flight mass spectrometer installed at the CNR-ISM laboratory in Rome.

Experimental apparatus location	Crucible			Capillary		
	Inner diameter (mm)	Outer diameter (mm)	Length (mm)	Inner diameter (mm)	Outer diameter (mm)	Length (mm)
CNR-ISM, Rome	5	8	60	0.5	1.1	70
Elettra, Trieste	7	10	35	1	1.5	30

Table 2.2. Geometry of crucibles used at CNR-ISM (Rome) and Elettra (Trieste).

Laser induced thermal desorption, LITD

Another technique commonly used to obtain biomolecules in gas phase is the laser induced thermal desorption (LITD). In this technique the sample is pre-deposited on a substrate, generally after evaporation of a solution containing the analyte, and the thermal energy is provided by a pulsed laser beam in the UV wavelength range [63]. The energy is mainly absorbed by the substrate and transferred to the analyte molecules by thermal processes [63,64,65]. Short laser pulses (ns duration) increase the surface temperature up to 1000 – 5000 K for the time duration of the pulse. This technique is commonly used with biomolecules of mass up to 1-2 kDa [66] and produces intact molecules, positive and negative ions as well as fragments. Ions are produced both by electron transfer from the surface to molecules and by protonation of the analyte depending on the type of molecules and morphology/composition of the surface [63,65] (i.e. peptides are preferentially protonated). Intact molecules are generally produced with high internal energy (some eV) and this may induce successive fragmentation [65].

In order to bring even larger molecules in the gas phase, nanostructured or porous surfaces (in particular silicon based surfaces) can be used to i) decrease thermal conductivity ii) increase temperature reached and iii) favour non-thermal processes [63,65,67]. In this way molecules with relatively high mass up to 6 kDa [67] can be desorbed. The use of an IR laser has been also reported as a useful tool to obtain the desorption of large proteins (mass up to 19 kDa) [68], even though the fraction of intact molecules is very small.

2.1.2.2 Soft ionization techniques: MALDI and ESI

To extend the mass range of molecules than can be brought to the gas phase, softer techniques have been developed. The most common and widely spread techniques are the matrix assisted laser desorption ionisation (MALDI) and the electrospray ionization (ESI), often coupled to laboratory analytical tools.

Matrix assisted laser desorption (MALDI)

MALDI is an evolution of the LITD technique and the main difference is the sample preparation. While LITD uses an approximately pure deposit of the biomolecule of interest, in MALDI the analyte is embedded in a matrix of small molecules that protect the analyte during the exposition to the laser beam and the subsequent desorption. The disintegration of the matrix following photon absorption brings isolated analyte molecules in vacuum without transferring high amounts of energy and preventing fragmentation [66]. To fulfil this protective effect, the matrix has to absorb efficiently the photons produced by the laser. Therefore, the best performances are obtained when the laser wavelength is near the maximum of the matrix photon absorption [69] and the matrix is in excess with respect to the analyte [70]. In this way the matrix provides an effective “radiation absorbing” medium reducing the internal energy delivered to the analyte and preventing its aggregation.

The analyte is not completely free of interactions with the matrix. These interaction, during desorption as well as in the ion plume, may lead to the formation of negative or protonated species [66,71]. However, the majority of molecules are produced as neutrals and the ratio between neutrals and ions has been estimated to be in the order of 10^3 - 10^5 [66,70]. Optimal performances have been obtained with a wide range of combinations analyte/matrix and molar concentration that can vary from 10^{-9} to 10^{-2} molar (M) depending on the analyte [66]. Pulsed lasers in the UV or IR ranges can be used to excite, respectively, electronic or vibrational states of molecules in the matrix. It has been found that a laser in the UV range may increase photochemical reactions, which may be a limitation or an advantage depending on specific purposes [66,72]. The most important parameters for the energy transfer are the laser power and the pulse duration that determine the amount of energy transfer and how fast it is provided; these information can be summarized in the laser fluence, i.e. the amount of energy deposited in the sample per unit of surface by a single pulse (measured in J/m^2). By increasing the fluence, the number of molecules and ions produced by a single laser shot increases until the threshold at which degradation of the analyte becomes the main process. A shorter pulse is required to prevent an excessive analyte thermal excitation before matrix disintegration [66]. Common values of fluence are about 10-100 J/m^2 and pulse duration about 1-10 ns [66,73,74]. These values produce an increase of the temperature from one to several thousand Kelvin [75].

Electrospray ionization (ESI)

The electrospray ionization is the most widely used technique to produce large and fragile biomolecules in the gas phase, especially for analytical purposes [71,76,77,78].

The general structure of an ESI source like the one used in the present work is shown in Figure 2.3. A diluted solution with an analyte concentration of about $10^{-3} - 10^{-6}$ M is mechanically pushed through a microfluidic line in a metallic needle (inner diameter $\sim 0.1 - 0.2$ mm) by a syringe pump with a flow rate of few $\mu\text{l}/\text{min}$; between the needle and the grounded counter electrode located 10-30 mm away (the entrance to the mass spectrometer or the target holder for in-air deposition) a high voltage of 2-6 kV is applied [58,78].

The spray formation takes place in the region at atmospheric pressure between needle and counter electrode (Figure 2.4). Due to the presence of the strong electric field, the formed droplets become smaller and smaller while travelling towards the counter electrode until bare protonated/deprotonated species are obtained.

In spectroscopic applications the counter electrode is a capillary that works as entrance to a vacuum chamber for further transport, selection, analysis and characterization of the analyte.

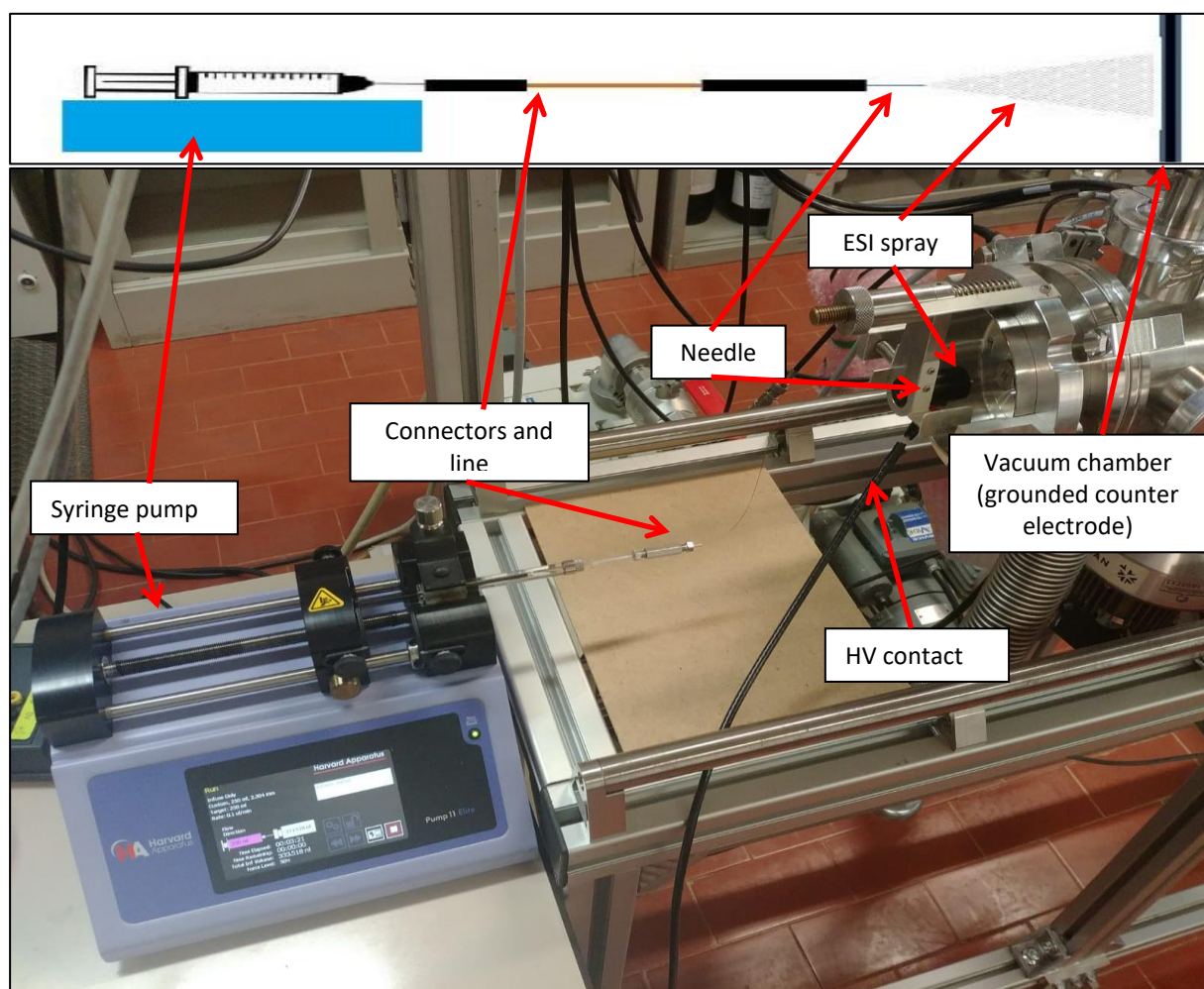


Figure 2.3. Scheme (top) and a picture (bottom) of the ESI source installed in our lab at CNR-ISM in Rome. The main elements are indicated: syringe and syringe pump, connectors and micro-fluidic line, needle manipulator and chamber.

The most fundamental process in this technique is related to proton addition or subtraction to the analyte, which then results in charged or multiply charged species that can be furtherly guided and mass over charge, m/z , selected for a large variety of applications, from analytical studies in the gas phase to the deposition for fundamental studies or biosensor applications. For this reason, the best results in terms of efficiency of the ESI process are obtained with analytes having several basic/acid polar functional groups as proteins, amino-acid chains etc. [79,81].

The production of an ion in the ESI source occurs in three steps: i) formation of charged droplets of analyte/solution, ii) droplet evolution by solvent evaporation and coulombic explosion and iii) production of isolated analyte molecules.

i) Formation of charged droplets

The solution containing the analyte is generally a mix of several solvents (water, ethanol, methanol, acetonitrile etc.), to which protonating agents (acetic acid, formic acid, etc.) are often added in small amounts. The contact of the solution with the polarized needle generates several electrochemical reactions. If a positive voltage is set to the needle it tends to acquire electrons, solvents are oxidised and positive ions (generally H^+) are produced. Viceversa, for negative voltages the needle tends to lose electrons, solvents are reduced and negative ions are dispersed in the solution (OH^- , H_2O^- , etc.). These ions produced at the solution/metal interface are repelled towards the needle's axis by the high voltage applied to the needle. At the needle outlet, the accumulated charge is subject to high electric field that, competing with the liquid surface tension, deforms the liquid meniscus to produce the Taylor cone [78] (Figure 2.4). At the tip of the Taylor cone the high field causes the ejection of a jet of liquid that eventually breaks into small droplets with a diameter of 1-10 μm . These highly charged droplets repel each other and produce a spray driven by the electric field.

ii) Charge droplets evolution

In each droplet, the ions are distributed on the surface [78,81]. The competition between the Coulomb repulsion and the surface tension determines the fate of the droplet (Figure 2.4). Flying towards the counter electrode, a droplet loses neutral solvent molecules by evaporation and reduces its size until the minimum stable radius, R , for a droplet of charge z as defined by the Rayleigh equation (2.5) is reached:

$$z e = 8 \pi \sqrt{\epsilon_0 \gamma R^3} \quad (2.5)$$

where e is the elementary charge, ϵ_0 the permittivity of the surrounding medium and γ the surface tension of the solvent.

At that point the Coulomb repulsion overtakes the surface tension, a Coulomb explosion occurs and the droplet breaks up into smaller ones. This process occurs several times until a "gas" of nano-droplets containing just one analyte molecule is formed. The time needed for the full evolution of the process depends on several parameters, like temperature, chemical composition, presence of neutral gas counter-flow etc. The typical life time of a droplet is in the order of ms.

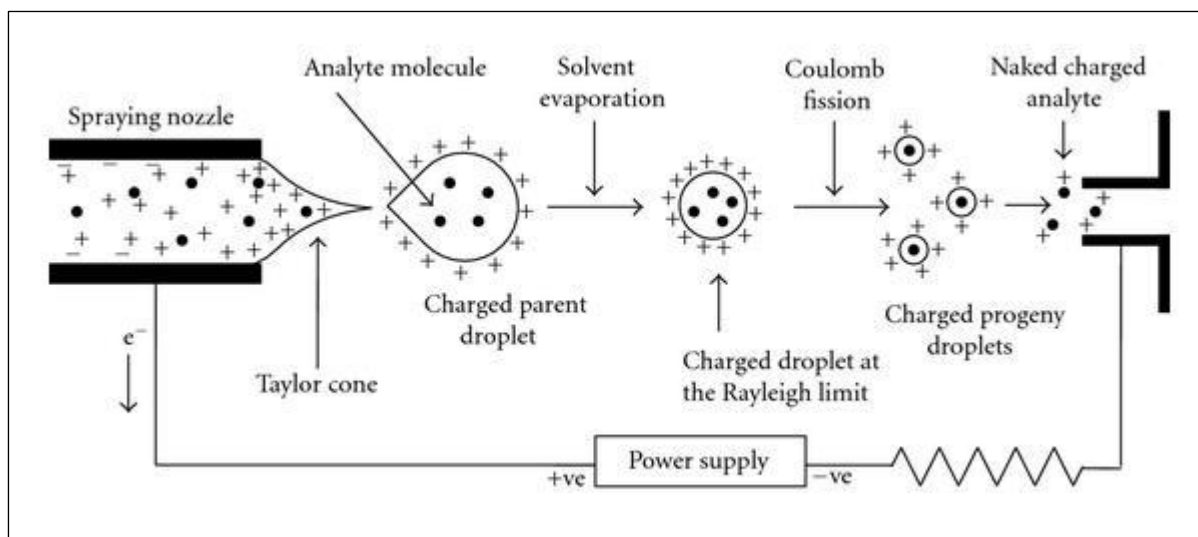


Figure 2.4. Schematic representation of the formation of the spray as evolution of the droplets by solvent evaporation and Coulomb explosion [78].

iii) Production of isolated analyte molecules

Two different models have been proposed to describe the final stage of droplet evolution and the formation of isolated ions in the ESI process: the Charge Residual Model (CRM) [81,78] and the Ion Evaporation Model (IEM) [58, 78].

Charge Residual Model. The CRM model (Figure 2.5) [78,81] assumes that the evaporation of the solvent molecules from a droplet causes charge deposition on the analyte, leading to small but highly charged droplets (same size as the analyte) containing just one, multiply charged, analyte molecule that then produces the bare ion in gas phase.

Following this model and using the Rayleigh equation (2.5), the relation between mass and charge of the ion in gas phase is [78]:

$$z = 4 \left(\frac{\pi \gamma \epsilon m}{\rho e^2 N_a} \right)^{1/2} = 0.078 m^{1/2} \quad (2.6)$$

where N_a is the Avogadro's number and ρ the density of the solvent.

This equation reproduces quite well several experimental data for analytes in a globular structure (Figure 2.6) [83]. Relevant deviations from this trend, however, can be observed especially for unfolded proteins, where a very large surface is exposed to the solvent and higher charge state can be obtained for the same mass.

Ion Evaporation Model. In this model (Figure 2.5) [81], bare ions may be produced from droplets bigger than the ones taken into account in the CRM model, containing also several analyte molecules. According to the IEM model, the interaction between the analyte and the strong electric field at the droplet surface may promote the expulsion of the analyte. A similar scenario was proposed also by J.B. Fenn [80], suggesting that the neutral molecules in the core of the droplet can reach the surface of the droplet by Brownian diffusion. At the

surface they interact with the charges at the acid or basic sites (depending on the polarity of the charges at the surface). Thermal motion and charge repulsion may provide enough energy to produce the expulsion of the charged analyte.

Both these models may explain the production of ions with several charges (ions with different m/z) observed in the experiments: CRM predicts better the process for big and globular molecules, like folded proteins, while IEM works better for small or branched analytes, like unfolded proteins.

The distribution of charge states is influenced by several parameters, like solution composition, solution pH and analyte conformation. All of these parameters influence the number of exposed sites for analyte protonation/deprotonation and therefore the concentration of charged species in the solution.

One of the major advantages of the ESI technique, which is well taken into account by both models, is the very little internal energy transferred to the analyte that generally avoids fragmentation and preserves very weak non covalent bonds in gas phase. This is very important for biological samples like proteins, because their tertiary structure, mainly due to hydrogen bonds, is preserved. The tertiary structure determines the biological activity, thus also the biological activity is preserved in the ESI technique [76].

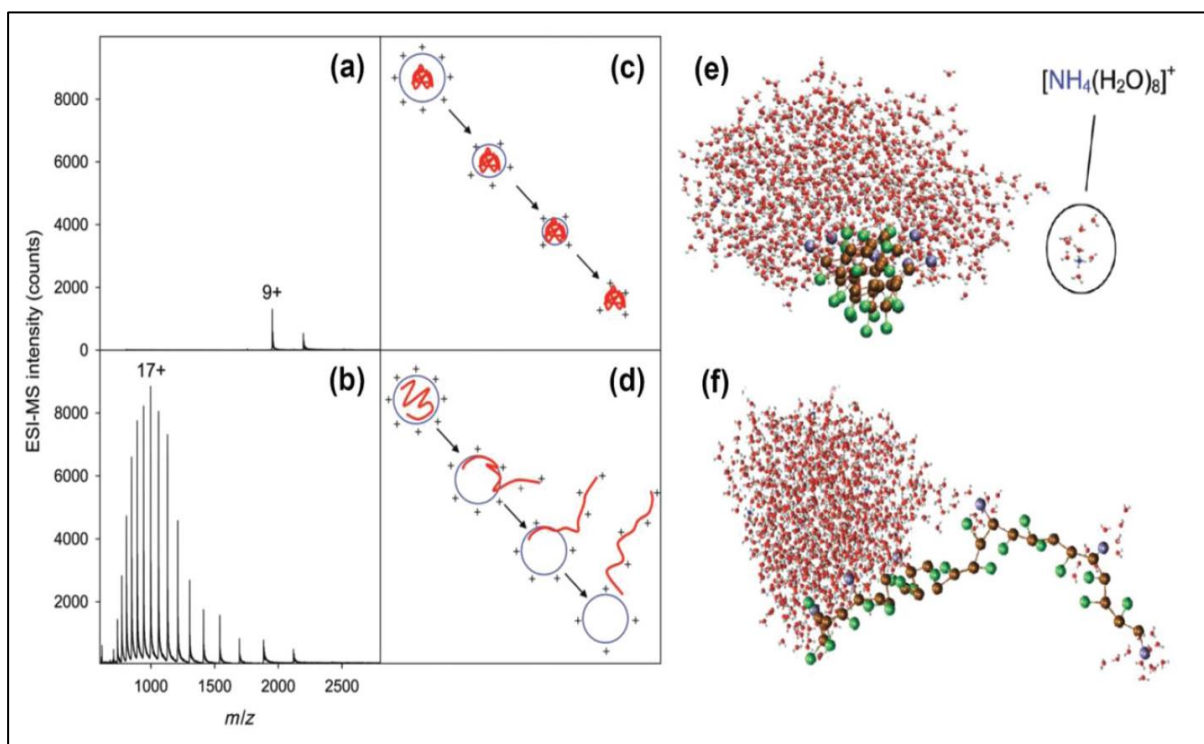


Figure 2.5. Description of the final stages of the evolution of the ESI droplets according to CRM (a,c,e) and IEM (b,d,f) models. (a,b) ESI mass spectra of folded (pH 7) and unfolded (pH 2) myoglobin protein, respectively. (c,d) Cartoons illustrating the CRM and IEM mechanisms, respectively. (e,f) Molecular dynamics simulation for a folded and unfolded polymer, respectively, in 1000 water molecules and excess NH_4^+ ions as charge carriers [81,82].

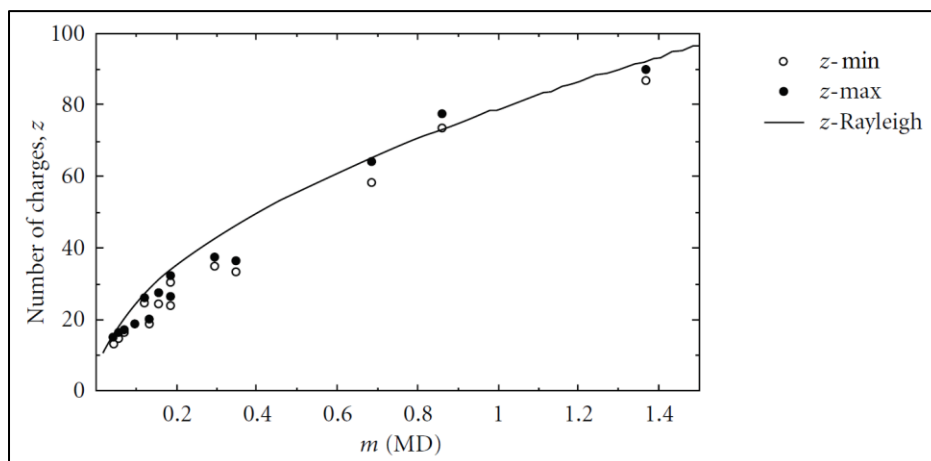


Figure 2.6. Plot of highest (black dots) and lowest (white dots) charge states against molar mass for various proteins that follow the CRM (values on x-axis are in 10^6 Da units). The solid curve corresponds to the charge state predicted by equation (2.5) [78,83].

ESI and MALDI are the two main soft techniques to produce biomolecules in gas phase. A common characteristic between the two techniques is the complex, and unfortunately expensive, experimental apparatus they require, with a large number of parameters to be controlled. They are mainly the composition of the solution and the formation of the spray for ESI and the intensity and duration of the laser pulse and matrix preparation for MALDI. In both techniques, these parameters have to be tuned for each specific biomolecule. As for the differences, ESI produces generally multiply charged ions, while MALDI produces both neutral species and singly charged ions, with the latter in a very low concentration. This represents the strength of the ESI technique, because the analysis of ions with a very large m/z is technically hard [71], while multiply charged ions with m/z in the range of 10^2 - 10^3 , which can be considered a relatively small value for molecules with a mass up to 10^5 Da, can be analysed and handled by standard instrument of mass spectroscopy [71,76]. In the ESI technique unwanted neutral molecules can be easily removed by the several differential pumping stages required to reach high vacuum conditions and finally a specific charge state can be selected. A further limitation of MALDI is due to the possible contamination of the gas phase sample due to the species in the matrix and therefore to a poor signal to noise ratio in the low mass range [63,71]. Considering all of these observations, it has been chosen to build an ESI source for the goal of this PhD project.

2.1.3 Characterization of biomolecules by photofragmentation

After the production in the gas phase, the next step involves the investigation of the intrinsic physical-chemical properties of the isolated biomolecule via proper spectroscopic techniques. The same experimental techniques can be applied to charged or neutral biomolecules. Ion beams, at variance with effusive beams of neutral species, can be directly handled, transported, purified and characterized using devices based on electric and magnetic fields as octupoles, quadrupoles and deflectors before reaching the interaction region, where they can finally interact with an external excitation/ionisation source. Among the many available techniques, here only the photofragmentation and photoionization experimental methods (section 2.1.3.1) and the main devices used to handle and to characterize a beam of ionic species (section 2.1.3.2) used in this project, will be described.

To investigate the structure and physical chemical properties of a molecule the strategy is to use the radiation as a probe, providing an energy that brings the target molecule to an excited state. By collecting electrons and ions released by the ionisation and fragmentation and analysing the outcome of the reaction, it is possible to study the molecular structure and the dynamics of the interaction with the radiation. The energy transfer can be provided by photon absorption [85] as well as collision with particles, like electrons, neutral molecules (generally rare gases) [84] or charged species, from protons to highly charge heavy ions. Clearly, each one of these processes has its own peculiarities, both in the energy delivery (quantised in photon interaction and continuous in particle scattering) and in the physical laws that govern the radiation-matter interaction. In the present work, only photon absorption will be considered.

The most relevant process for the experiments that will be discussed in chapter 3 is the single photon absorption. During this process, the molecule absorbs a photon of frequency ν increasing its internal energy by the quantity $\Delta E = h\nu$, where h is the Plank constant. Depending on the photon energy, different processes may occur and three energy ranges, described in Table 2.3, can be roughly identified:

Photon energy (eV)	Physical process	Experimental techniques (some examples)
$10^{-3} - 1$	Roto-vibrational excitation	UV, IR, RAMAN
1 – 50	Valence shell electronic excitation/ionisation Double ionisation	PES electron-electron and electron-ion coincidence
50 – 10000	Multiple ionisation Core electron excitation/ionisation	XPS, NEXAFS Auger spectroscopy Resonant Auger

Table 2.3. Physical processes and related experimental techniques in the different energy ranges.

If enough energy is provided, i.e. $h\nu > IE$ where IE is the first molecular ionisation energy, the photon absorption produces emission of an electron from a bound state to the continuum, ionizing the molecule which it then left in an ionic state (photoionization process); in section 2.3 a more detailed description of this process is reported.

2.1.3.1 Radiation sources: rare gas discharge lamp and synchrotron radiation

The experiments described in chapter 3 are devoted to study the photofragmentation of nitroimidazole based radiosensitisers with photon energies in the range 8 – 60 eV. In the following subsections the two photon sources (rare gas discharge lamp and synchrotron) used in those experiments are briefly described.

Rare gas discharge lamp

The physical principle used in this kind of photon source is the spontaneous de-excitation of atomic species by photon emission. The spectrum of the emitted radiation is composed by specific lines corresponding to the allowed atomic transitions. Several technical solutions can be adopted to excite the gas (microwave cavity, high current arc discharge electrodes, etc.)

[85]. The experimental setup installed in Rome is equipped with a discharge lamp where a high voltage, HV ~ 0.5 kV, is applied between two electrodes in a discharge region dynamically filled (and pumped) with a rare gas, at a typical gas pressure of $10^{-1} - 10^{-2}$ mbar depending on the specific gas. The HV discharge triggers and then maintains an electron current (about 5 mA) that continuously excites atoms by collisions. The subsequent de-excitation spectrum consists of discrete lines at specific energies related to the gas used in the source. The emission lines are well separated in energy and the spectrum can be defined as almost monochromatic because in most of the rare gases one of the emission lines dominates the spectrum as shown in Table 2.4, where the most intense lines of each gas used in the experiments of chapter 3 are reported.

The emitted radiation is transported by a quartz capillary (1mm bore) terminated with a set of two coaxial apertures (0.5 mm diameter) 30 mm apart used to collimate the photon beam down to a spot of less than 1mm in diameter in the interaction region of the apparatus, which is located at a distance of about 40 mm from the exit of the collimator [86].

Photoemission lines of rare gas								
Gas	Line name	Energy (eV)	Relative intensity	Gas	Line name	Energy (eV)	Relative intensity	
He	He I α	21.22	100	Ar	Ar I	11.62	100	
	He I β	23.08	2		Ar I	11.83	50	
	He I γ	23.74	0.5		Ar II	13.30	30	
	He II α	40.8	<1		Ar II	13.48	15	
Ne	Ne I α	16.67	15	Kr		10		
	Ne I α	16.85	100		Xe		8.43	
	Ne I β	19.69	<1					
	Ne I β	19.78	<1					

Table 2.4. Main photoemission spectral lines of rare gases [85]. The nomenclature is determined by the charge state of the emitting atom (I : neutral atom, II : singly ionized atom) and electronic states involved (α : from $n=2$ to $n=1$, β : from $n=3$ to $n=1$, etc). Relative intensities can be affected by operational conditions like pressure and current in the discharge region.

Synchrotron radiation

Synchrotron radiation is the electromagnetic radiation emitted by a relativistic particle when is accelerated/decelerated.

A typical synchrotron radiation machine (Figure 2.7.A) consists of a booster ring and/or LINAC that pre-accelerate and inject bunches of electrons in the storage ring, where the electrons are guided in a roughly “circular” path in UHV condition, maintained at constant energy in the GeV range. The “almost circular” path is in fact a sequence of straight and bent sections, containing many different electromagnetic devices meant to deviate (bending magnets), to restore the energy loss by the beam (radiofrequency devices), to focus and collimate (quadrupole/sextupole devices) the electron bunches, forcing them to wiggle through “insertion devices” (wigglers and undulators) (Figure 2.7.D) where intense radiation emission takes place [87]. Indeed, the relativistic velocity of the electrons produces the emission of radiation over a wide spectrum of frequencies into a narrow cone in the forward direction (Figure 2.7.B and C). The emitted radiation is directed towards the beamline, where it is monochromatised, focussed and finally transported towards the experimental end station by diffraction gratings and mirrors.

Even though bending magnets are still in use, the insertion devices are the primary radiation source in modern, third generation synchrotron radiation sources (Figure 2.7.D). In wigglers and undulators the electrons trajectories are deflected by a periodic magnetic structure and driven in an oscillatory path, which modulates the characteristics of the emitted radiation as brightness, polarization and photon intensity [87, 88]. The intensity of the emitted radiation from an undulator source (like the one used on the GasPhase beamline of Elettra, for example) is proportional to the square of the number N of periods in the undulator.

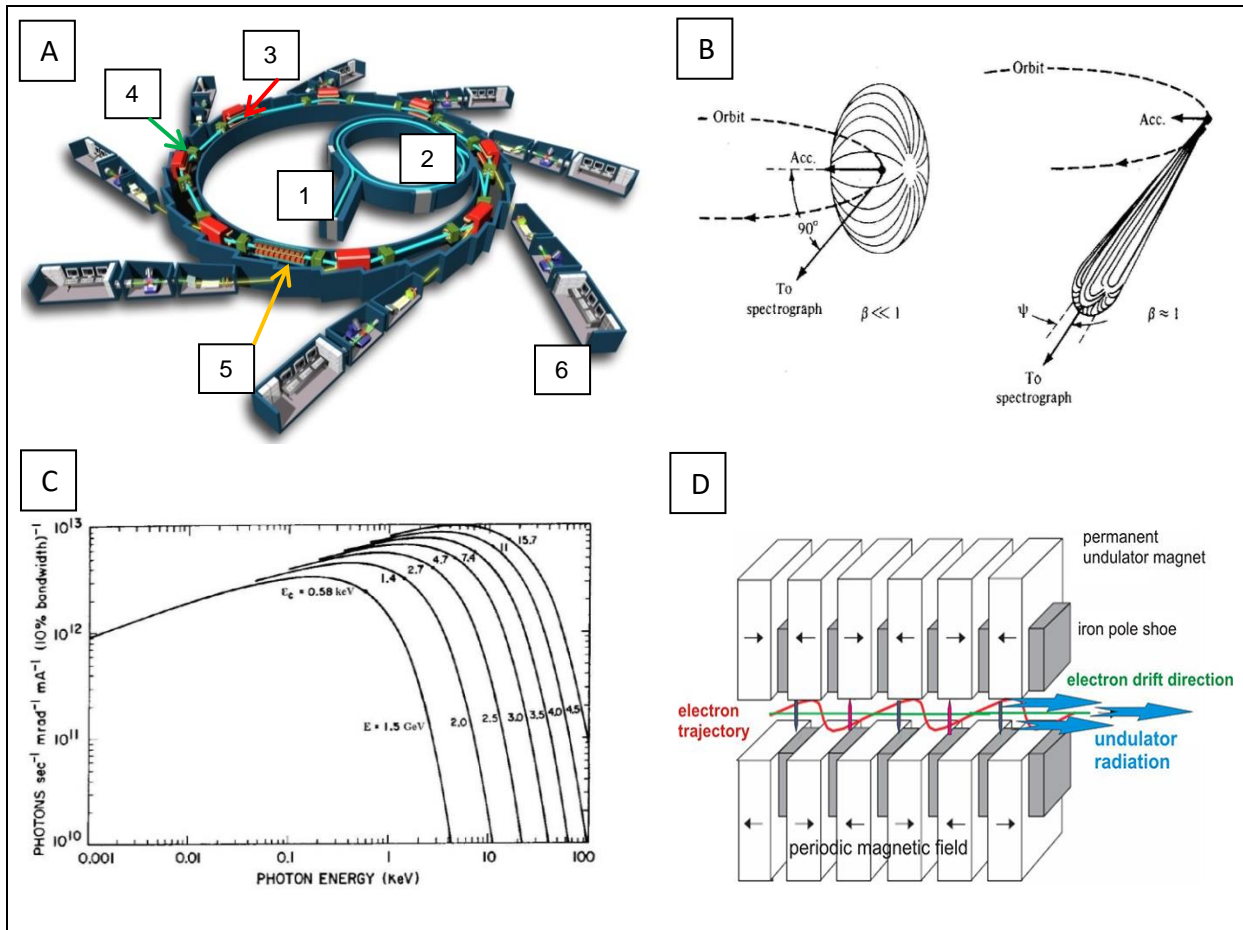


Figure 2.7. **A)** Schematic description of a synchrotron facility with LINAC (1) and booster (2) accelerators, bending magnets (3), radiofrequency cavities (4), insertion devices (5) and beamlines (6)[89]. **B)** Angular distribution of the radiation emitted by the electrons in a circular trajectory: moving from slow ($\beta=v/c \ll 1$) to relativistic ($\beta \sim 1$) velocity the emission evolves from a dipole (left) to the so-called “torch-like” shape (right)[87]. **C)** Spectral distribution of synchrotron radiation as a function of the electron energy in the storage ring [87]. The typical operation mode at Elettra is 2 or 2.4 GeV. **D)** Structure of an undulator with indicated the electron trajectory, periodic magnetic field and direction of the emitted radiation [90].

Beamline	Energy range (eV)	Resolving power ($\Delta E/E$)	Insertion device	Light polarization	Monochromators	Intensity of radiation (Photons/sec)
GasPhase (GAPH)	13-1000	10000	Undulator period 12.5 cm 4.5 m long	Linear	SGM (spherical grating monochromator)	$6.3 \cdot 10^{10}$ @45 eV ($\Delta E/E > 25000$)
Circular Polarization (CiPo)	5 - 900	5000	Electromagnetic wiggler	Linear or circular	SGM and NIM (normal incident monochromators)	$4 \cdot 10^{10}$ @16.7 eV ($\Delta E/E = 1000$)

Table 2.5. Some general characteristics of GasPhase and CiPo beamlines of Elettra.

Some of the experiments discussed in chapter 3 are performed at GasPhase [91] and CiPo [92] beamlines of Elettra synchrotron (Trieste, Italy); in Table 2.5 the most relevant characteristics of GasPhase and CiPo beamlines are summarized.

2.1.3.2 Mass spectroscopy techniques: TOF-MS, PEPICO spectroscopy and AE measurements

The previous section described the photon sources used to induce ionisation/fragmentation of the molecular species studied in the present work. This section introduces the experimental techniques and related experimental setups used to collect and analyse the resulting charged particles (electron and ions).

Time of flight mass spectroscopy (TOF-MS)

Mass spectrometry consists in the analysis of the charged fragments produced by the dissociation of a parent compound after its ionisation. Fragments analysis is performed by measuring the mass spectrum i.e. the ion yield versus the mass to charge (m/z) ratio [93,94]. One of the most common techniques is time of flight mass spectrometry (TOF-MS) [93,94,95]; in this technique ions with different m/z are discriminated by their flight time from the ionisation source to the detector. To understand the principles of this technique a general description of a TOF mass spectrometer (Figure 2.8) is used.

The general principle of operation of a TOF-MS is based on the use of static and homogeneous electric fields over three regions (Figure 2.8 and Figure 2.9):

- **Ionization and extraction region:** the ionisation region is defined by the intersection of the gas jet and the ionising beam, i.e. where the ions are generated, and it is located inside the extraction region confined between repeller and extractor electrodes. It should be as small as possible to increase the spectrometer resolution. The ionisation event is the “time zero” of the experiment, while the measurement of the time of flight of the ion to the detector begins at the time t_0 , when the ion is extracted and accelerated towards the TOF spectrometer. When the ions are extracted with a negligible delay with respect to the ionisation event, then $t_0 \sim 0$. Assuming that the component of the velocity in the direction parallel to the axis of the spectrometer is $v_{\parallel} \sim 0$, then it can be easily calculated that the ions will leave the extraction region after a time t_e with a velocity v_e

$$v_e = \sqrt{\frac{2E_e Z s_e}{m}} \quad (2.7)$$

$$t_e = \frac{v_e}{E_e z/m} = \frac{\sqrt{2 E_e s_e m/z}}{E_e} \quad (2.8)$$

where E_e is the electric field applied in the extraction region and $2s_e$ is the length of the extraction region. It is worth mentioning that $v_{\parallel} \sim 0$ is a good assumption in all experiments of single ionization of chapter 3, where the fragments do not gain additional speed by coulombic repulsion and only a limited amount of kinetic energy release is involved in the fragmentation. The velocity due to thermal motion is orders of magnitude lower than the velocity acquired in the acceleration region.

- **Acceleration region:** from the extraction region, the ions are “injected” in the next region at the time t_e and with velocity v_e . Here they are further accelerated by the electric field (E_a) and eventually leave this region at the time t_a with velocity v_a

$$v_a = \sqrt{\frac{2(E_a s_a z)}{m} + v_e^2} = \sqrt{\frac{z}{m}} \sqrt{2(E_a S_a + E_e S_e)} \quad (2.9)$$

$$t_a = \frac{v_a - v_e}{E_a z/m} = \sqrt{\frac{m}{z}} \frac{\sqrt{2(E_a S_a + E_e S_e)} - \sqrt{2E_e S_e}}{E_a} \quad (2.10)$$

where s_a is the length of the acceleration region.

- **Drift tube:** this is a field free region and ions, which have entered this region at the time ($t_e + t_a$), continue travelling with the same velocity v_a , acquired in the acceleration region, up to the ion detector located at the end of drift tube. The time spent in the drift tube is t_d

$$v_d = v_a \quad (2.11)$$

$$t_d = \frac{D}{v_a} = \frac{D}{\sqrt{2(E_a S_a + E_e S_e)}} \sqrt{m/z} \quad (2.12)$$

where D is the length of the drift tube.

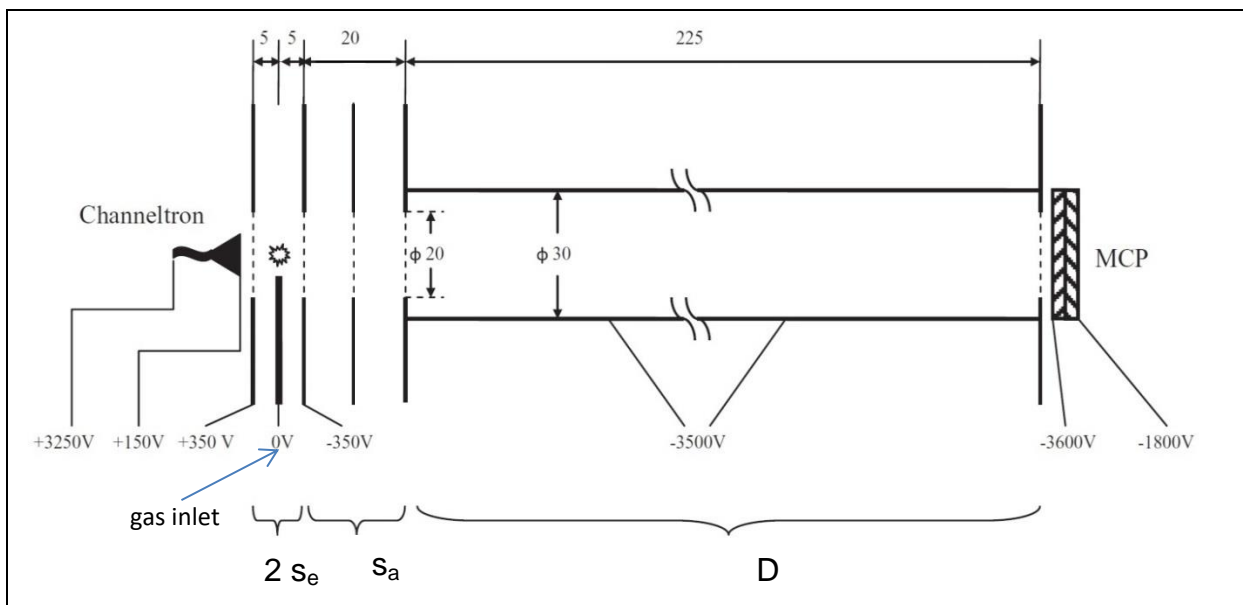


Figure 2.8. Schematic of the TOF setup installed in the apparatus at CNR-ISM, Rome, where $2s_e$, s_a and D represent the extraction, acceleration and free-flight drift tube regions, respectively. The typical voltages applied to the electrodes as well as the geometrical size of the different elements (in mm) are indicated. The dashed lines represent high transparency (90 %) gold meshes that warranty electric field uniformity [86]. In this system, the detection of a kinetic energy unresolved photoelectron with a channeltron mounted opposite to the TOF spectrometer provides the “time zero” for the measurement of the time of flight.

The total time of flight is $t_{\text{tot}} = t_e + t_a + t_d$, and is proportional to $\sqrt{m/z}$.

A good understanding of the flight times in the different regions of the TOF is essential for the analysis of the metastable decay that will be discussed in section 3.3.5.

Ions with different m/z experience different accelerations in the extraction and acceleration regions, but the discrimination in t_{tot} is dominated by the length of the drift tube, which explains why D is generally longer with respect to s_a and s_e (D 10-100 cm, s_a and s_e 1- 5 cm). However, a compromise must be found, as a longer drift tube requires a bigger vacuum chamber and a larger detector, because the ions that have a non-zero component of the velocity vector in the direction perpendicular to the spectrometer axis will move away from the axis over a longer travel.

The mass resolution defined as $M/\Delta M$ can change in different ranges of mass and a way to quantify the overall resolution of the spectrometer is to consider the largest mass for which two adjacent peaks ($\Delta M = 1$) are completely separated.

One of the main limitations in the mass resolution is due to the spread in the initial position of the parent molecule; this spread can be limited by reducing the size of the ionization region (gas jet and ionising radiation) as much as possible. However, these will still have a finite size.

In order to address this issue, the most widespread design for TOF spectrometers follows the Wiley-McLaren strategy [97] for refocusing the ions of equal m/z generated in different positions of the interaction region. The s_e value in eq.s (2.7)-(2.12) can be replaced by the variable s_0 defined in the range $s_e - \Delta s_e < s_0 < s_e + \Delta s_e$ where $2\Delta s_e$ is the size of the overlap between incident radiation and gas jet. The basic idea is based on the observation that ions generated more distant from the drift tube have to travel over a longer distance, but spend more time in the extraction/acceleration regions and therefore acquire a higher velocity with respect to ions generated closer the drift tube. Therefore, the space-focusing condition is obtained imposing that

$$\left. \frac{dt_{\text{tot}}}{ds_0} \right|_{s_e} = 0 \quad (2.13) \rightarrow D = 2s_e k_0 \sqrt{k_0} \left(1 - \frac{s_a}{(k_0 + \sqrt{k_0})s_e} \right) \quad (2.14)$$

where k_0 is

$$k_0 = s_e E_e + \frac{s_a E_a}{s_e E_e} \quad (2.15)$$

Eq.s (2.13)-(2.15) sets constraints between the applied electric fields (E_e and E_a) and the geometry of the device (s_e , s_a and D) [95,96,97].

To perform the experiments reported in section 3 two different TOF-MS have been used, one installed at CNR-ISM in Rome (Figure 2.9)[86] and another one installed in the VG-TOF end-station at the GasPhase beam line of Elettra (Figure 2.10)[91,98]. Both spectrometers have been built according to the Wiley-McLaren scheme. The sample is injected by a stainless steel capillary located about 2 mm away from the photon beam; the use of a long capillary allows to obtain a collimated molecular beam even though it may introduce some perturbation to the homogeneity in the extraction field.

The TOF-MS installed in Rome is equipped with a rare gas discharge lamp (Figure 2.9) and the size of ionization region is estimated to be around 1.2 mm by the collimator set in front of the discharge lamp [86].

For the spectrometer installed at the GasPhase beamline the size of the ionization region is mainly determined by the diameter of the photon beam in the experimental chamber (0.3 mm).

Other main characteristics of these two spectrometers are reported in Table 2.6

TOF-MS apparatus	Extraction field (V/cm)	Acceleration field (V/cm)	s_e (mm)	s_a (mm)	D (mm)	Extraction mode
CNR-ISM, Rome	700	1575	5	20	225	continuous
GasPhase beamline, Trieste	370	2840	7.5	5	320	pulsed

Table 2.6. Typical operating conditions of the TOF-MS installed in CNR-ISM laboratory in Rome (Figure 8 and Figure 9) and at the GasPhase beam line of Elettra.

Typical values for flight times and velocities reached in each region are reported in Table 2.7.

Region	Velocity (m/s)	Travelling Time (s)
Extraction	$v_a \sim 2.6 \cdot 10^4$	$t_a \sim 3.8 \cdot 10^{-7}$
Acceleration	$v_e \sim 8.2 \cdot 10^4$	$t_e \sim 3.7 \cdot 10^{-7}$
Free flight	$v_D \sim 8.2 \cdot 10^4$	$t_D \sim 2.7 \cdot 10^{-6}$

Table 2.7. Velocity reached at the exit of each TOF regions in the spectrometer installed in Rome using equations 2-7 – 2.10 with parameters reported in Table 2.6, for a singly charged ion with mass $m=100$ Da.

The main difference between the two TOF spectrometers used in Rome and Trieste is concerned with the determination of the t_0 value and the technical solution adopted to extract the ions.

In the spectrometer installed in Rome, t_0 is given by the detection of the kinetic energy unresolved photoelectron produced by the ionization process. In the extraction region, the electric field produced by the repeller and extractor electrodes polarised with antisymmetric voltages is continuously applied. Therefore, the electrons are pushed in the opposite direction with respect to ions and are detected by a channeltron (Figure 2.9). The flight time of the electron to the channeltron is in the order of ns or less in such a system, which is a negligible time compared to the μ s flight time of the ions; therefore, $t_0 \sim 0$ [86].

In the apparatus installed at the GasPhase beamline, instead, the electric field in the extraction region is pulsed and the ionisation event occurs in a field free region. The trigger for the fast raising of the voltages to the repeller/extraction electrodes, which is the t_0 for the measurement of the flight time of the ion, is given either by the detection of a kinetic energy resolved electron or by a random pulse generated by a pulser with a constant rate (0.1 or 1 kHz, depending on the measure). The time needed to the photoelectrons to travel from the ionization region to the detectors via the hemispherical analyser produces a delay between ionization event and the trigger t_0 . This delayed trigger, which has been estimated to be in the order of several hundreds of ns in case of PEPICO experiments [100], has very important consequences in the analysis of the results as it will be discussed in chapter 3.

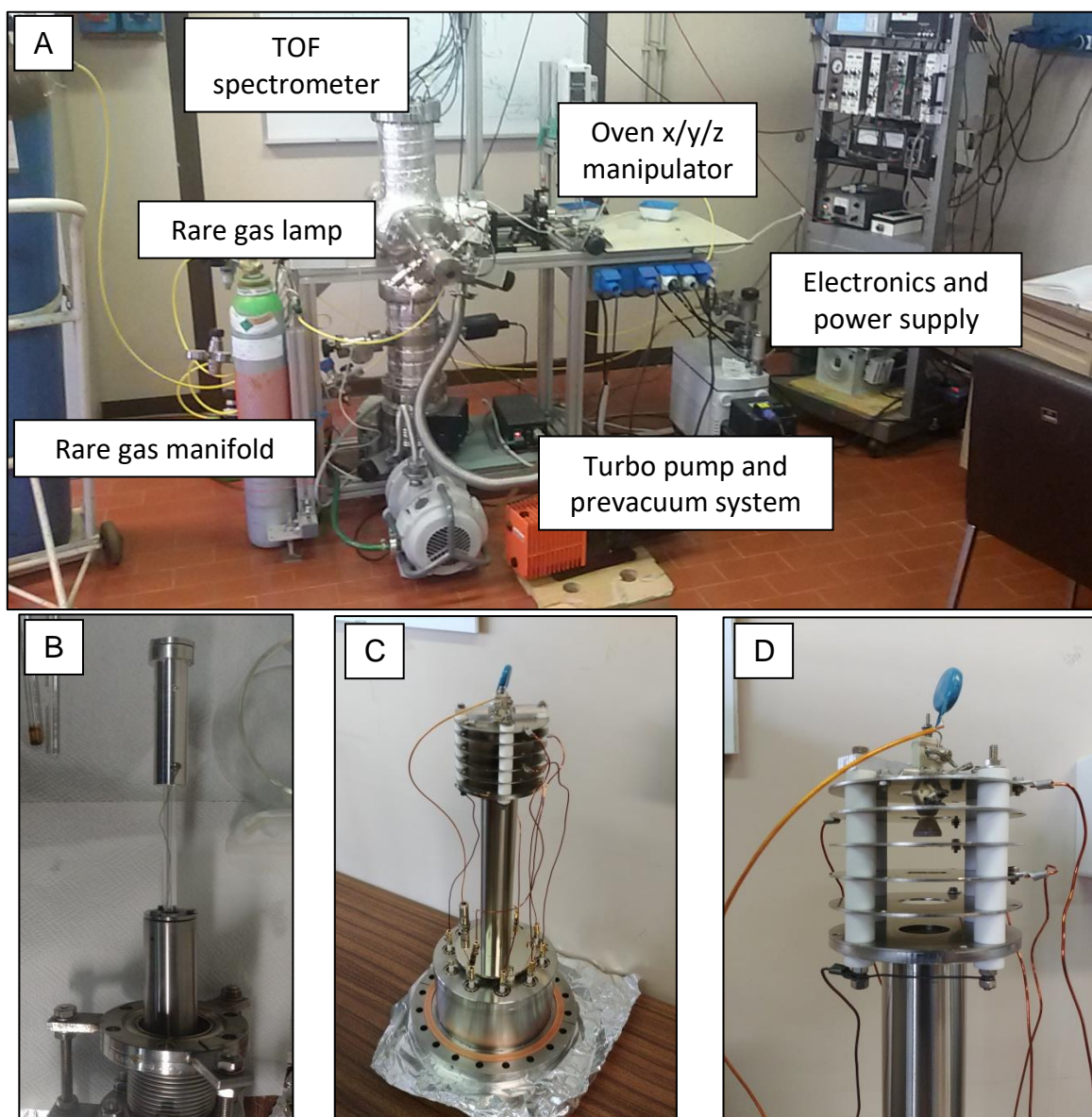


Figure 2.9. **A)** The CNR-ISM spectrometer equipped with a rare gas discharge lamp, turbomolecular pump and a stage for sample evaporation. **B)** The rare gas discharge lamp mounted on the vacuum flange for the connection to the chamber, glass capillary and collimator system. **C)** The TOF spectrometer. **D)** Detail of the extraction and acceleration regions of the TOF and the channeltron electron multiplier used to trigger the measurement of the ion's flight time.

Another important stage of the experimental setup is the electronic processing of the electron/ion signals required to obtain the mass spectra. Signals from the electron/ion detectors pass through an electronic chain made by a pre-amplifier and a constant fraction discriminator before being sent to a time-to-digital converter (TDC, model AM-GPX, ACAM Messelectronic) that registers the arrival time of STOP signals (ions) with respect to the START signal (electron). The START signal opens a time window during which the STOP signals are acquired, while all further START signals are ignored; the duration of the time window is generally set to 5-10 μs for ions of m/z 200-300 and in general depends of the flight time of the heaviest expected mass. A scheme of the system adopted in Elettra, Trieste, is given in Figure 2.10.

The photoelectron-photoions coincidences (PEPICO) technique

The PEPICO technique has been used in the present work as a powerful tool to investigate the state-selective fragmentation of the target molecules [98,99,100] following valence shell photoionisation.

The experiments have been performed at the GasPhase beamline. The setup is shown in Figure 2.10 and it consists of a TOF spectrometer and a hemispherical electron spectrometer (VG 220i) mounted opposite to each other at the magic angle ($54^\circ 44'$) with respect to the polarisation axis of the radiation [100]. This apparatus can be used to acquire independently TOF mass spectra and electron spectra, or in time coincidence mode to perform PEPICO measurements.

The PEPICO experiment can be ideally schematized as it follows:

- **Photoionization and photofragmentation:** the target molecule is ionized by a photon of energy $h\nu$. The kinetic energy, KE, of the emitted electron and the binding energy, BE, of the ionized orbital are related by the energy conservation law, $h\nu = BE + KE$. The experiment is performed at a fix photon energy (typically 60 eV), large enough to allow the ionization of the entire valence/inner valence region. If there is sufficient internal energy in the ionised orbital, this can fragment in a combination of two or more neutral and charged species.
- **Electron and ion detection:** the ejected electrons are collected by the hemispherical deflector analyser (VG 220i) over an accepted angle of $\pm 3^\circ$ with an energy resolution of about 3% of the pass energy (typical pass energies are 5 or 20 eV for high resolution PES or PEPICO mode, respectively) while the ions are extracted and m/z analysed by the TOF-MS.
The electron and ion signals are handled by preamplifiers and constant fraction discriminators to be formatted into NIM or TTL standard pulses. In the PEPICO mode, the electron signal is used to trigger the pulsed extraction field of the TOF-MS and eventually fed as START signal into the TDC - ACAM card to initialise the measurement of the ion's flight time, while the ion signal is used as STOP in the same TDC card (see Figure 2.10.B).
Being selected in kinetic energy, only electrons from a specific molecular orbital (within experimental energy resolution) are used to trigger the acquisition of the TOF-MS and therefore a *state-selected* mass spectrum is acquired.
- **Kinetic energy scan:** thanks to the multi-detection capability of the VG 220i analyser, which is equipped with 6 channeltron detectors, for a specific nominal KE value, electrons of six discrete kinetic energy values are acquired simultaneously over an energy window whose width is 3% of the pass energy. Scanning the KE value, the acquisition proceeds until the entire KE range of interest is covered. The step size is chosen in order to have overlapping windows, for normalization purposes.

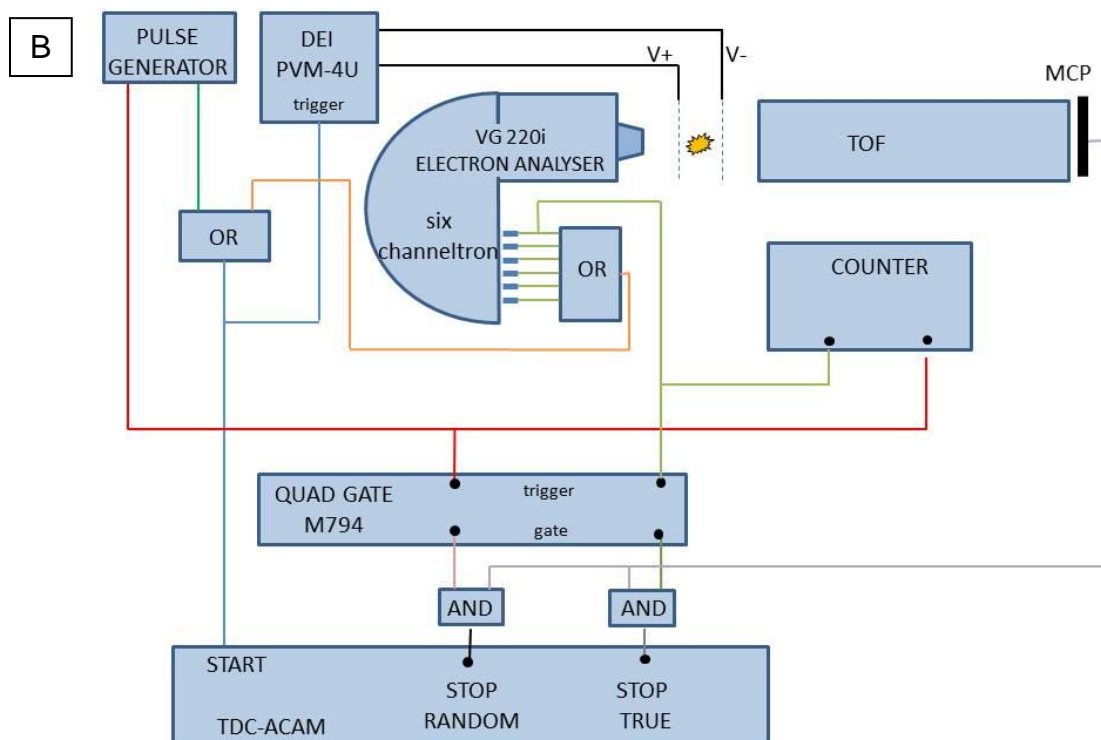
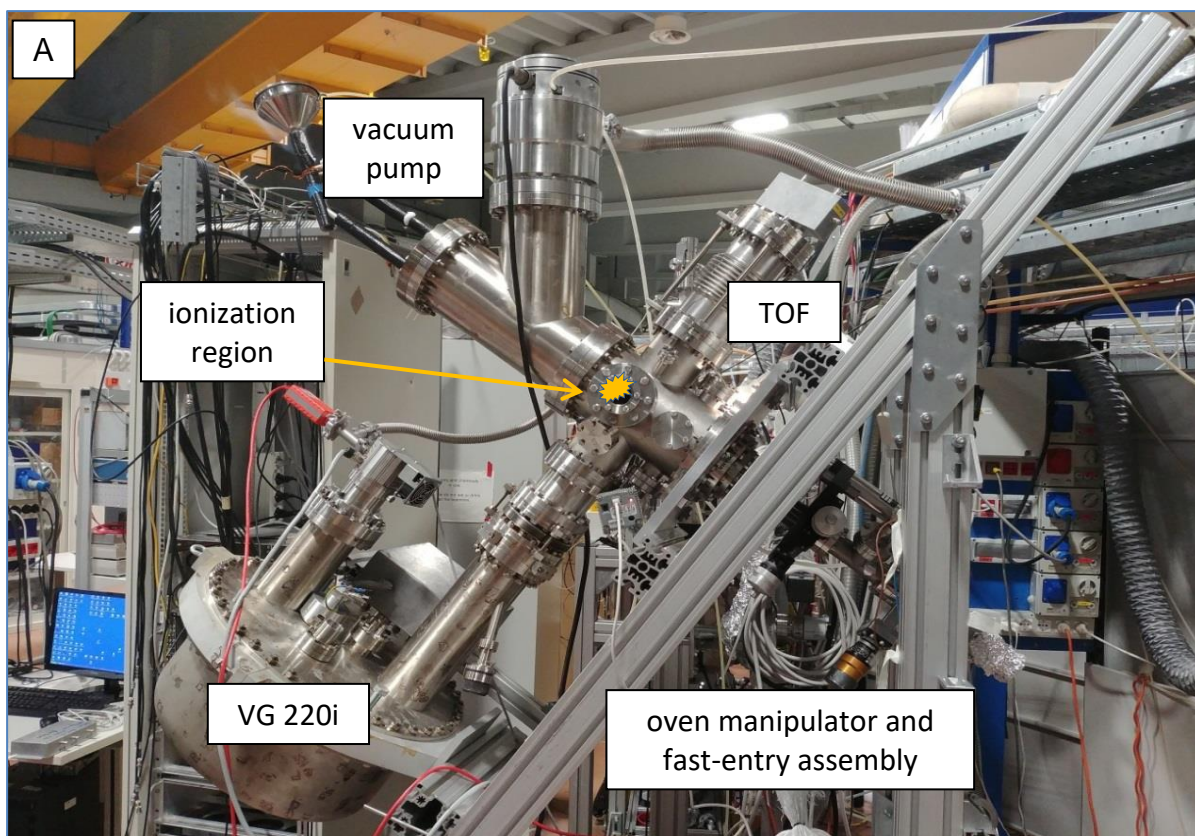


Figure 2.10. A) Picture of the VG-TOF end-station at the GasPhase beamline of Elettra. The main parts are indicated. **B)** Schematic of the electronic setup adopted for the acquisition of the PEPICO signal. For a specific setting of the analyser in terms of collection energy and pass energy, each one of the six channeltron detects an electron of different kinetic energy, and leads to the acquisition of an independent PEPICO spectrum. For simplicity only the electronic chain of one channeltron signal has been represented.

In the PEPICO mode, for each KE window, the acquired data consists of six TOF mass spectra already sorted according to the kinetic energy of the triggering electron within the acquisition window of the VG 220i analyser. Therefore each spectrum represents the fragmentation pattern of the electronic state identified by that specific electron kinetic energy.

Concerning the data analysis, a first and crucial step is the subtraction of the 'random coincidences'. Synchrotron radiation is, in first approximation, a continuous ionisation source. Thus ions produced by processes occurring before the detection of the photoelectron which triggers the extraction voltage, and that reside in the interaction region are also detected and recorded by the TDC-ACAM card. Therefore, there is a finite probability that an ion not correlated to the triggering electron hits the detector and is recorded as a coincidence event. This is a "random coincidence" event. Clearly, true and random processes are undistinguishable, and may only be treated on a statistical base. To remove the contribution of the random coincidences from a PEPICO measurement, a pure random coincidence mass spectrum, where the ion extraction is triggered by a random pulse not correlated to any specific ionisation event (electron), is also acquired. This is done by using a pulse generator with a rate of 100 Hz, i.e. a frequency comparable to the electron count rate [98,100] to trigger the coincidence acquisition using the electronic chain schematised in Figure 2.10.B. In this way, the electron-triggered and random-triggered coincidence mass spectra are normalized to the number of true (electrons) and random (pulser) triggers, respectively, and then the random spectrum is subtracted from the others. In Figure 2.11.A some examples of the random subtracted PEPICO mass spectra in the different binding energy regions (Figure 2.11.B) of the imidazole molecule are shown.

The next step in the data analysis consists in evaluating the area of the peak corresponding to each fragment in every state-selected PEPICO mass spectrum. The ratio of this area with respect to the total area of the coincidence spectrum represents the branching ratio of the fragment, i.e. probability for that fragment to be produced at that BE. By reporting the branching ratio of a fragmentation channel as a function of the BE of the molecular orbitals (Figure 2.11.C), a correlation between the fragmentation paths and the ionisation of the different molecular orbitals can be established.

The BE scale is finally calibrated against a reference compound (H_2O , N_2 , etc.) [98,99].

The TDC-ACAM card adopted in both apparatuses (Rome and Trieste) has eight independent STOP channels and multi-hit capabilities.

In the PEPICO experiments performed in Trieste the multi-channel feature is essential to match the multidetector of the VG 220i electron spectrometer. The electronic chain required for the data acquisition in the PEPICO experiments is schematized in Figure 2.10 (adapted from ref [100]). An analogic OR logic unit fed by the signals of the pulser (100 Hz) and the six channeltrons triggers the extraction voltages of the TOF-MS and provides the START signal to the TDC-ACAM card. Six of the STOP signals ($i= 1$ to 6) of the TDC-ACAM card come from an analogic AND logic unit fed by the ion signal and the i -channeltron signal. The latter signal is stretched by a gate unit to a signal with a duration equal to the TDC-ACAM acquisition window. The STOP channel 7 comes from an analogic AND unit fed by the ion and the random pulse signals. Also in this case the random pulse signal is stretched into a long pulse of width equal to the acquisition time of the TDC-ACAM card.

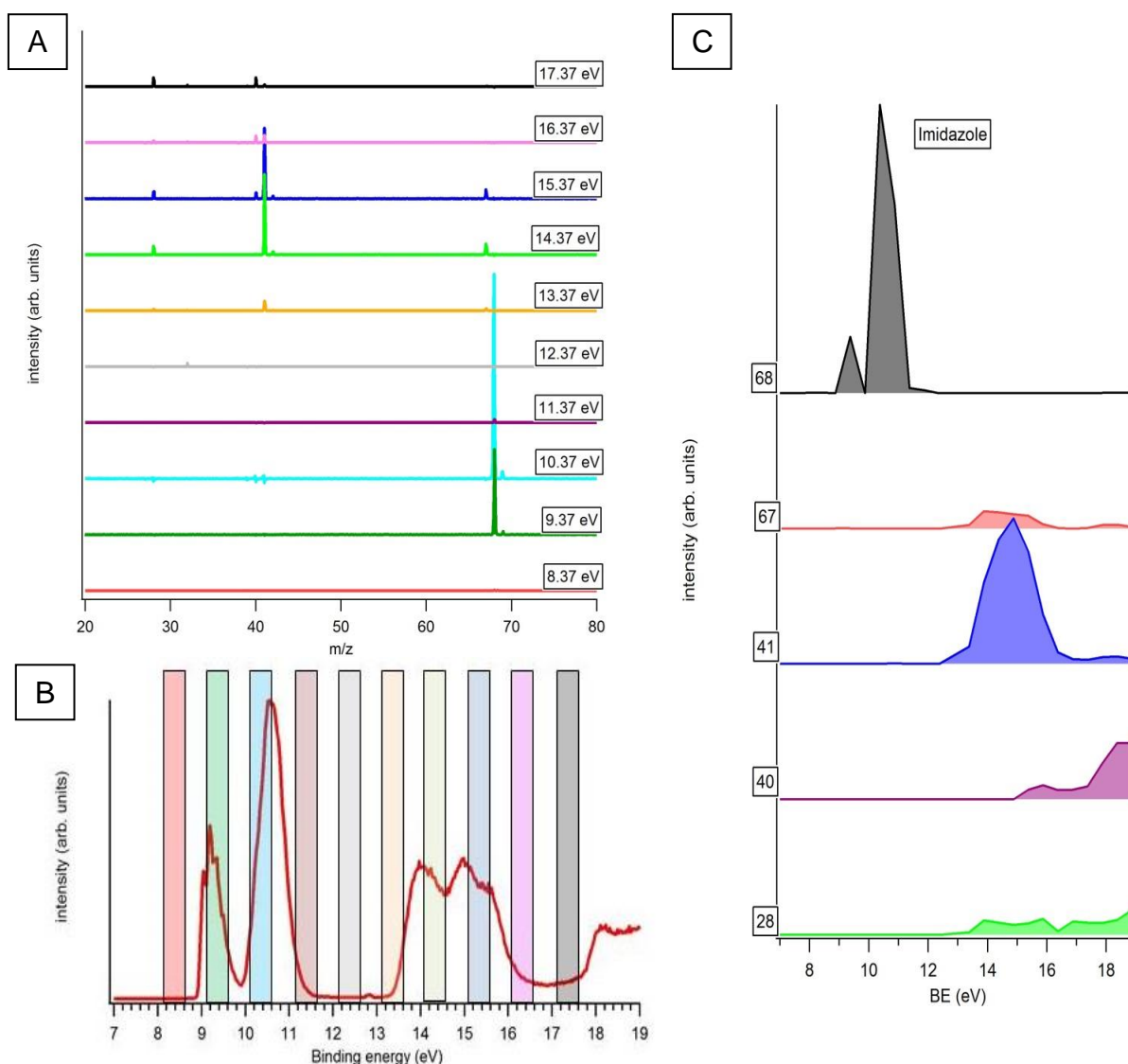


Figure 2.11. Example of PEPICO coincidence data for imidazole molecule (more detailed and complete set of data for imidazole will be presented in chapter 3). **A)** PEPICO mass spectra obtained from a selected region of valence band, indicated as coloured boxes of about 0.5 eV KE acceptance in panel B. **B)** PES spectrum and energy regions of the valence band considered for the PEPICO spectra in A. **C)** Examples of the branching ratio of the different ions vs binding energy for the main fragments observed in mass spectra.

Appearance Energy Spectroscopy

In a molecule, the appearance energy (AE) of a specific fragment is defined as the minimum energy needed to produce that fragment. For the parent ion, the AE value is commonly referred to as the ionisation energy, IE [101].

Experimentally, the measurement of the AE necessarily requires the use of a tunable ionising source, like synchrotron radiation or an electron beam, and a mass spectrometer. The experiments discussed in chapter 3 have been performed at the Circular Polarization (CiPo) beamline of Elettra synchrotron. The experimental setup (Figure 2.12.A) consists of an effusive beam of the molecules under investigation that is crossed by the monochromatic synchrotron radiation at right angle. A set of electrodes extracts the ions from the ionization region and focuses them into a commercial quadrupole mass spectrometer, QMS (10 – 4000 m/z, Extrel 150-QC 0.88 MHz) where they are m/z selected by a combination of DC voltages and a radiofrequency [101,102] before being counted with a channeltron detector. For each fragment, the channeltron signal is recorded vs the scanning photon energy (Figure 2.12.B).

To extract the appearance energy (ionization energy) value in the data analysis the ion yield vs photon energy is fitted by two straight lines, one for the background below threshold and the other one for the yield in the threshold region. The intersection of the two straight lines corresponds to the experimental determination of AE (IE). The procedure is repeated several times for different energy ranges of the two regions used for the linear fits. The mean value and the standard deviation of these fits are taken as the experimental determination of AE (IE) and its uncertainty for the studied fragments, respectively [103].

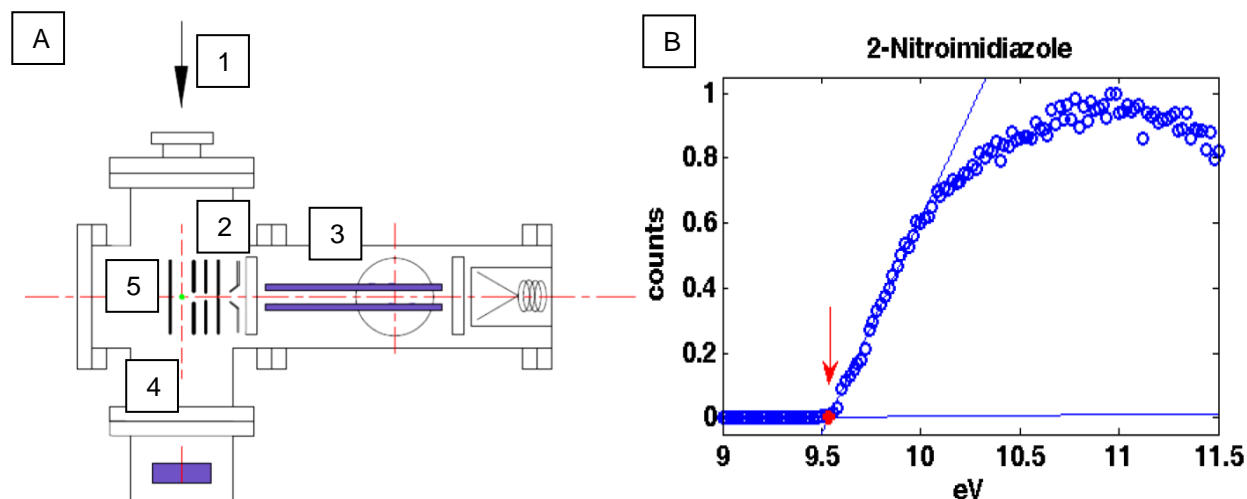


Figure 2.12. A) Schematic of the experimental apparatus used at the CiPo beamline of Elettra for the AE measurements: (1) direction of propagation of the photon beam, (2 and 5) electrostatic lens to extract the ions; (3) quadrupole mass spectrometer (QMS), (4) photodiode. The effusive gas beam is perpendicular to the plane of the drawing and crosses the synchrotron beam at the centre of the extraction region. B) example of ion yield vs photon energy measured to obtain ionisation energy of 2-nitroimidazole parent ion. The two lines used to fit data and obtain IE value (red dot) are represented.

2.1.4 The ESI apparatus

The electrospray ionisation (ESI) setup recently installed at the CNR-ISM laboratory in Rome (Figure 2.13.A) consists of several vacuum chambers containing: i) a heated capillary acting as counter electrode to transport the charged species in vacuum, ii) a skimmer that defines the access to a first differential pumping stage equipped with an octupole ion guide, iii) a polarizable gate valve with several optical elements to guide the beam from the octupole through the valve and into the high vacuum chamber; iv) a quadrupole mass filter with pre- and post-focusing as well as entrance and exit lenses to select in m/z the ion beam and v) a quadrupolar deflector to direct it towards either the diagnostic or the deposition stage. All in all, the transport line under vacuum consists of almost 20 optical elements, including beam deflectors (Figure 2.13.B). Each device produces a reduction of the ion flux and the optimized voltages for these electrodes cannot be determined from first principles. Also, semi-empirical methods cannot be adopted, because they can hardly converge to the best solution due to the large number of combinations of the parameters.

On the other hand, a detailed control of the process (efficient transmission of the particles through the apparatus, m/z filtering, elimination of neutral particles as well as kinetic energy control) is needed in order to

- identify the best operating conditions for maximum transmission;
- understand the most critical elements of the setup;
- propose further improvements in the design.

Therefore, a detailed modelling and a start- to-end computer simulation of the apparatus has been undertaken to study the role and the effect of each electrostatic component on the ion beam parameters and transmission.

The newly developed apparatus is currently under commissioning, running in parallel experimental tests and ion optics computer simulations by SIMION software [104].

The comparison of the simulated results with the experimental ones measured at different check-points in the apparatus provides the essential feedback to validate the simulations, which in turn allow for deep insights on the behaviour of the setup providing access to parameters which are not directly measurable.

In this section a detailed technical description of the first vacuum stage composed by the capillary and octupole chambers will be presented (section 2.1.4.1), introducing the strategy used to monitor experimentally the molecular beam (section 2.1.4.2), describing the radiofrequency (RF) devices used in the ESI source (section 2.1.4.3) and the SIMION software used to perform simulations.

In chapter 5 the comparison between the simulated and experimentally measured performances of the first stage of the apparatus, from the heated capillary up to the octupole exit lenses will be presented.

2.1.4.1 Technical description of the ESI source

The first stage of the ESI source (Figure 2.14) is composed of two vacuum chambers containing the heated capillary and the octupole ion guide.

A syringe (Hamilton 250 μ l Gastight 1725) acts as a reservoir for the solution containing the analyte. The solution is continuously pumped by a syringe pump (Harvard Apparatus pump 11 elite) in a microfluidic line composed by a metallic connector (1/16"-1/16"), a silica tube (250 μ m internal diameter), a second metallic adaptor (1/16"-1/32") and a thin stainless steel needle.

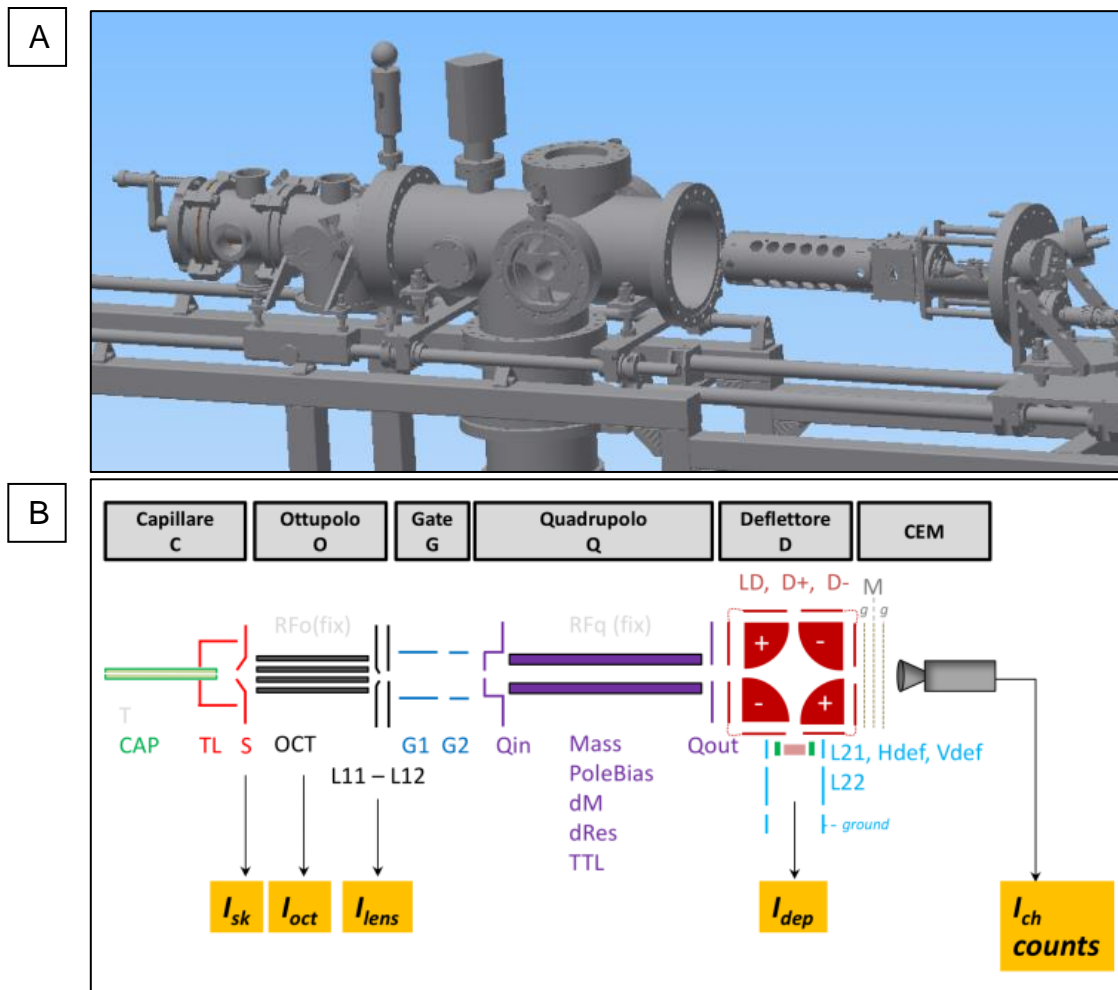


Figure 2.13. A) Mechanical scheme of the entire ESI setup installed at CNR-ISM, Rome, composed of three vacuum chambers, for the transport of the beam under vacuum and the m/z selection stages. **B)** Scheme of the ion optics. Available “check-points” for current readings are indicated by the yellow boxes.

This line is used to gradually reduce the internal diameter down to the 100 μm internal diameter of the needle set at a high voltage (3-4 kV) that acts like spraying nozzle of the ESI system. In front of the needle the heated capillary (125 mm long and 300 μm inner diameter stainless steel tube), that acts as counter electrode and transfers the ion beam in vacuum, is placed. The capillary can be heated by a Thermocoax system up to 300 $^{\circ}\text{C}$ (a value of 100-150 $^{\circ}\text{C}$ is generally used in operating condition) and can be polarized to a defined voltage. The in-vacuum end of the capillary pushes the molecular beam toward the skimmer (1mm internal diameter); the capillary and the skimmer are intentionally displaced by 1 mm out of axis to reduce the amount of neutral molecules transported in the octupole chamber, the charge particles are instead focused by an electrostatic electrode tube lens.

The octupole ion guide is composed by eight metallic roads 13.3 cm long and 2 mm in diameter, the distance between the edges of two opposite roads is 5.5 mm. At the end of the octupole the ion beam is guided by two electrodes (lens L11 and L12, 6 mm and 8.4 mm in internal diameter, respectively) towards the following stage. Presently, for the characterisation of the first stages of the setup, a diagnostic chamber with a particle detector has been installed (the six-way cross in Figure 2.14). However, in the next stage the chamber with the polarisable gate valve and the quadrupole mass selector will be connected at this stage to complete the ESI transport line.

All electrodes of this stage (except for the octupole ion guide that will be described in section 2.1.4.3) are polarized by computer controlled power supply (± 200 V).

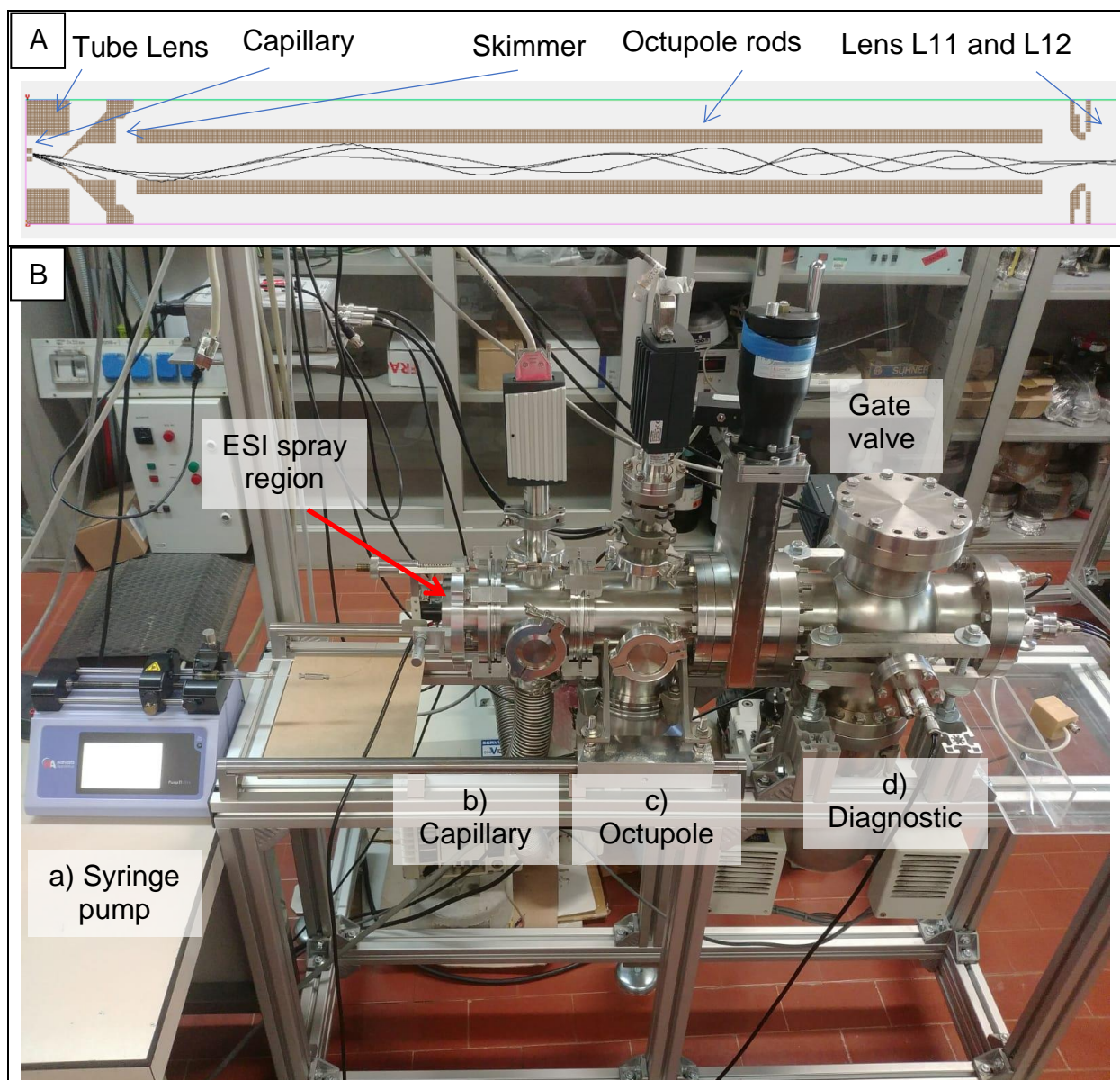


Figure 2.14. **A)** Section of the first stage of the apparatus (capillary, tube lens, skimmer, octupole and exit lenses) as drawn in the SIMION simulation code: the oscillating ion trajectories in the octupole are due to the radiofrequency field that pulls ions to different radial directions during their flight. **B)** The first stages of the ESI source installed at the CNR-ISM in Rome and assembled for the commissioning (six way cross for ion current diagnostic). This first part of the apparatus is composed of: a) the syringe pump connected to a $100\ \mu\text{m}$ spraying nozzle; b) the capillary chamber containing a heated capillary to transfer the ion beam in vacuum and a skimmer; c) the octupole ion guide with entrance and exit lenses; d) the 6-way cross chamber after a gate valve hosting the detector for the diagnostic of the ion beam.

2.1.4.2 The experimental measurement of the ion current

In order to compare the simulated results and the experimental performances of the apparatus, the ion current, representative of the setup transmission, is monitored at different stages of the apparatus via two picoammeters, (Keithley 617 and 485) connected to different optical elements along the ion path (see Figure 2.13.B).

A first check-point for the ion current is the skimmer. This point has the advantage to be characterized by a significant current (about $100\ \text{pA}$) which can be read without interfering

with the normal operation of the apparatus, because this element is normally at ground potential.

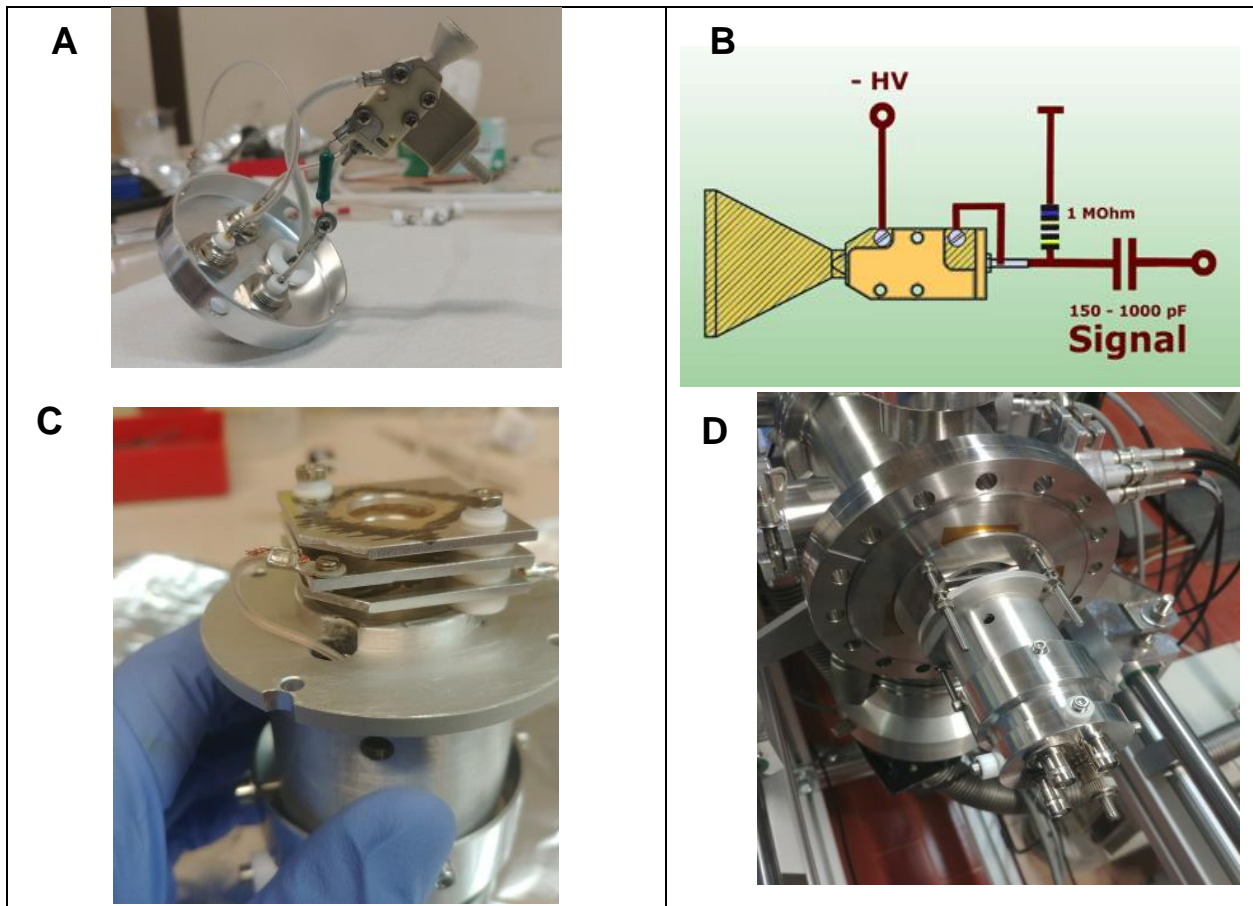


Figure 2.15. Components of the retarding field analyser used to monitor the ion beam: picture (A) and scheme (B) of the channeltron detector wired in “current mode” reading (model Dr. Sjuts XBL10RS); the three-mesh system of the KE filter (C) and its mounting (D) in the apparatus after the exit lens, L12, of the octupole. The retarding field analyser is housed in a 6-way cross chamber connected to the octupole chamber.

A second check-point is located at the exit of the octupole, after the L12 lens (see Figure 2.13.B). Considering that the ion current read on L12 is of the order of few pA, and its measurement heavily interferes with the normal operation of the apparatus (L12 is normally polarised in the range -50 to -100 V), we installed a channeltron electron multiplier (CEM) to amplify the low current produced by the ion beam. We tested the use of either a bare CEM placed in a shielding box with open view, ≈ 6 cm away from L12 or a *retarding field analyser* with three independently polarizable meshes [105] in front of it (Figure 2.15.C and D). After several preliminary tests (see appendix A.5.2 of chapter 5) the use of the retarding field analyser was discarded due to unquantifiable field penetration of the high voltage of the CEM through the meshes, and the detector configuration with only the CEM was adopted.

2.1.4.3 Radiofrequency devices: the octupole

Charged particles can be handled by electric and/or magnetic fields and a wide class of instruments based on radiofrequency (RF) electric field (megahertz) has been developed [106] to several purposes, such as to transport (multipole guide, ion funnel etc.) [107,108,114], to confine (multipole trap, Paul trap etc.) [109] or to select (quadrupole mass filter) [110,115] ions.

The analytical description of such devices is possible with some approximations and allows to understand the role of the most relevant parameters to operate these instruments.

The force F acting on a particle with mass m and charge q in an oscillating electric field $E = E_0 \cos(\omega t)$ is:

$$F = m a = q E_0 \cos(\omega t) \quad (2.16)$$

The trajectory of the particle is described by:

$$r(t) = r(0) - \frac{q E_0}{m \omega^2} \cos(\omega t) \quad (2.17)$$

where $r(0)$ and $r(t)$ are the initial position and the position at time t .

If the electric field is not homogeneous ($E = E_0(r) \cos(\omega t)$) an analytical solution of trajectories is generally not possible and the motion of the ions is the combination of fast oscillations, due to the radiofrequency, and a slow drift toward regions of weaker field due to the not homogeneity of the field [106]. If the oscillations have a small amplitude and are faster than the drift motion (quantitative parameter will be given later) the two components can be considered separately and the fast oscillations are neglected (Adiabatic Approximation) [106,111].

In this approximation, the ion trajectory can be derived by the time-independent mechanical pseudo-potential [106,112]:

$$V^*(r) = \frac{q^2 E_0^2(r)}{4 m \omega^2} + q U_0 \quad (2.18)$$

where U_0 is the static component of the electrical potential.

The applicability of the adiabatic approximation can be monitored by the adiabatic parameter $\eta(r)$

$$\eta(r) = \frac{2q}{m \omega^2} |\nabla E_0(r)| \quad (2.19)$$

Observations based on experiments and simulations show that good operating conditions should maintain [106,111]:

$$\eta(r) < 0.3 \quad (2.20)$$

This constrain can be achieved by using a sufficiently high radiofrequency, ω .

A class of radiofrequency devices used for several applications, i.e. ion guide, filter and trap, are the multipoles, composed of long rods assembled in parallel on the vertexes of a regular polygon; the number of used rods ($2n$) defines the specific name of the multipole: $2n=4$ quadrupole, $2n=6$ hexapole, $2n=8$ octupole and so on (Figure 2.16).

The ion position in the multipole can be described by a system of cylindrical coordinates R , φ and Z where R is the distance from the central symmetry axis of the multipole, φ is the

angle between R and a reference axis on a plane perpendicular to symmetry axis and Z the position measured along the symmetry axis (Figure 2.16); the ideal potential on a plane perpendicular to the main axis is defined by [106,111]:

$$V(R, \varphi) = (U_0 - V_0 \cos(\omega t)) \cos(n\varphi) \left(\frac{R}{R_0}\right)^n \quad (2.21)$$

where R_0 is the internal radius of the multipole (Figure 2.16). This potential is derived in the approximation of rods with a hyperbolic profile, but for technical reasons simple cylindrical rods are generally used.

Except specific cases, i.e. quadrupolar mass filter, U_0 is equal to zero and from equation (2.21) the amplitude of the electric field, E , the pseudopotential, V^* , and the adiabatic parameter η can be obtained [106,111,108]:

$$|E_0| = \frac{V_0}{R_0} n \left(\frac{R}{R_0}\right)^{n-1} \quad (2.22)$$

$$V^*(R, \varphi) = \frac{2n^2}{8} \frac{(qV_0)^2}{m\omega^2 R_0^2} \left(\frac{R}{R_0}\right)^{2n-2} + qU_0 \cos(n\varphi) \left(\frac{R}{R_0}\right)^n \quad (2.23)$$

$$\eta(R) = \frac{2(n-1)nqV_0}{m\omega^2 R_0^2} \left(\frac{R}{R_0}\right)^{n-2} \quad (2.24)$$

Generally high order ($n > 3$) multipoles are preferred as ion guides because in this case the adiabatic parameter goes to zero near the axis and the constrain described in equation (2.20) is more easily fulfilled. Moreover, considering how the effective potential becomes steeper increasing n (see equation 2.23), ions are more effectively confined in the multipole [106,111].

The use of a radiofrequency multipole as ion guide has advantages when operated at high pressure (10^{-1} - 10^{-2} mbar) because ions loose kinetic energy by collisions with buffer gas and are focussed along the multipole axis [115,111].

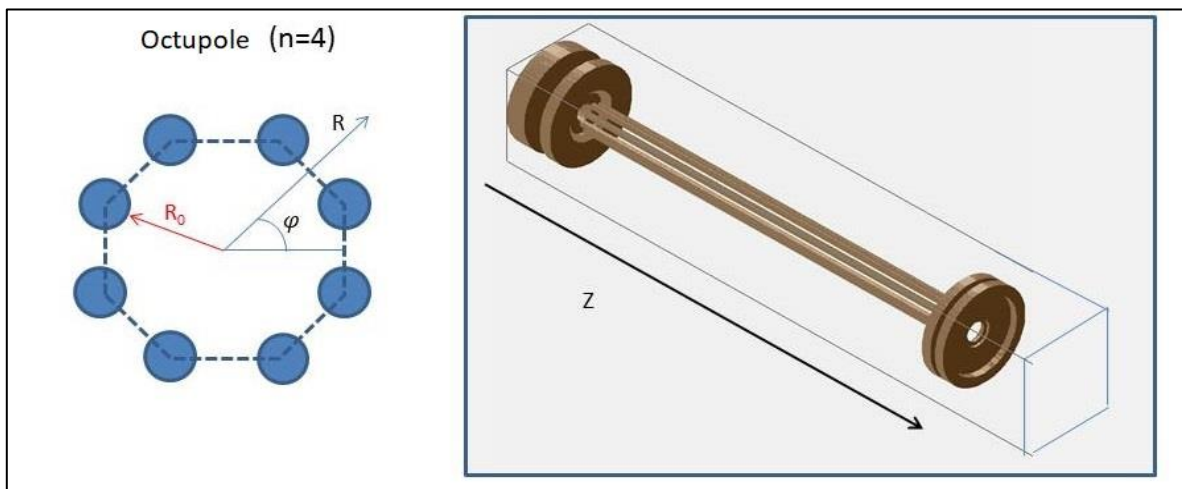


Figure 2.16. Schematic description of octupole with indicated the reference system used in the text for the analytical description. On the left, the SIMION geometry of the octupole guide used in the present apparatus is shown.

Equations (2.23) and (2.24) for an octupole (n=4) became:

$$V^*(R, \varphi) = \frac{4}{1} \frac{(qV_0)^2}{m\omega^2 R_0^2} \left(\frac{R}{R_0}\right)^6 + qU_0 \cos(6\varphi) \left(\frac{R}{R_0}\right)^4 \quad (2.25)$$

$$\eta(R) = \frac{24qV_0}{m\omega^2 R_0^2} \left(\frac{R}{R_0}\right)^2 \quad (2.26)$$

Considering the specific parameters of the octupole installed in the setup described in section 2.1.4.1, Figure 2.14 and summarised in Table 2.8, the adiabatic parameter becomes:

$$\eta = 3400 \frac{z}{m'} \left(\frac{R}{R_0}\right)^2 \quad (2.27)$$

where z is the number of unitary charges of the ion and m' is the mass in Da.

The constrain in eq.(2.20) is satisfied for ions with a m'/z > 100 in region with R < 0.1 R₀.

R ₀ (mm)	V ₀ (V)	ω (MHz)
2.75	80-120	2.5 – 3

Table 2.8. Summary of the relevant parameters for the octupole installed in setup described in section 2.1.4.1. The V₀ and ω parameters can be adjusted by dedicated power supplies.

The main problem in the characterization of a radiofrequency device is that all relevant parameters like transmission, angular divergence and beam waist of the outgoing ion beam are strictly related to the features of the incoming ion beam, i.e. kinetic energy, spatial distribution, and angular divergence [108,114,115]. Obtaining these parameters for a specific experimental setup can be very difficult, especially when the radiofrequency device is coupled to other elements in a more complex ion optics system. In this case computer simulations become the most powerful tool to achieve a realistic description of the setup.

2.1.4.4 Simulations with SIMION software

The goal of the computer simulations is to perform a “virtual” experiment that could be considered a realistic representation of a real one. This provides a detailed understanding and description of the ion beam trajectories in the apparatus, supports the choice of optimised operating conditions and allows to maximize the setup transmission and final ion flux. Additional relevant information that can also be obtained from the simulations are the beam size and the angular divergence as well as the distribution of the kinetic energy of the ions along the path from the source to the detector.

Several of the ion optic devices installed in the vacuum chambers, like octupole, quadrupole, quadrupolar deflector and some of the lenses, can be described by first principles of electrostatics and there are equations to represent ion trajectories inside these devices and their transmission, angular acceptance, resolution etc. For isolated devices in ideal condition this is a very useful support. However, it is really hard to obtain from first principles [113,114,115] a description of these properties for a beam of finite size passing through two or more devices coupled together. Moreover, additional features make the system clearly unsolvable from a purely theoretical approach based on first principles: a) several non-standard objects, whose behaviour cannot be analytically calculated, are included along the

path; b) in some stages of the apparatus, especially near the first chambers, the background pressure is not negligible and collisions defocus the beam from its “ideal” path imposed by the electrostatic fields; c) the ESI process itself, that generates the ions, is a very complex, statistical process, therefore the initial conditions (mass, charge, kinetic energy, degree of solvation, angles of emission...) of the ions injected are unknown; d) the first stages devoted to the transfer of the ion beam into vacuum can be described exactly only with the inclusion of fluid dynamics effects, due to the fast moving background gas.

Many (but not all) of these effects can be accounted for by using ion optics simulation packages, like SIMION chosen for the present work [104]. The comparison between simulated and experimental results allows to determine unknown parameters, finally providing detailed information about the ion beam and the most suited conditions for its efficient transport.

The software used to perform ion optic simulations is SIMION 8.0 [104]. The input data are the geometrical descriptions of all the optical elements in the apparatus that has to be simulated, stored in the .GEM file.

Complex devices made-up of several different electrodes with different (planar, spherical, cylindrical) and custom shapes can be easily represented using the .GEM files. In the so called “refine procedure”, SIMION solves the Laplace equation and calculates the electrostatic potential and the electric field generated in the area specified in the .GEM file by the overlapping effects of all the elements included in the simulation.

The field is calculated in the three dimensional grid; the size of each cube of this grid is called ‘grid unit’ (GU) and the conversion factor mm/GU defines the spatial resolution in the field calculation [116], see Figure 2.17. A careful choice of the resolution has to be made, balancing the need of a proper description of the optical elements (rounded elements, for example, like octupole or quadrupole rods) and the corresponding computing resources needed for the chosen accuracy. Indeed, during the refine procedure SIMION creates a file for each electrode (named .PAn file, where n is the number that identifies the electrode) with the calculated electric field generated at each grid unit point of the whole simulated volume; for example, to reproduce a volume of 1 dm^3 with a resolution of 0.1 mm/GU (1000 GU for each edge of the cube) the dimension of each .PA file is about 8 Gb; if in the volume there are 3 independent electrodes, SIMION will create 3 files of 8 Gb each. During the simulation, all of these files are loaded in the computer RAM. For this reason, the mm/GU conversion factor must be a compromise between computer RAM required to run the simulation and accuracy in the field description.

Once the geometries of the electrodes are defined in the .GEM file, the other initial parameters for the simulation are the voltages applied to the electrodes and the kinetic energy, KE, mass, m , charge, z , of the ions, the size of source region in (x,y,z) coordinates and polar/azimuthal angles of emission. Starting with these initial conditions, the simulation is performed by calculating ion parameters under the effect of the field at each grid point and then “moving” the ion according to the equations of motion to the next grid point. Finally, the trajectory for each ion through the entire apparatus is produced.

The simulation provides at each grid point information like value of the electrostatic potential, the kinetic energy or time of flight of the ion.

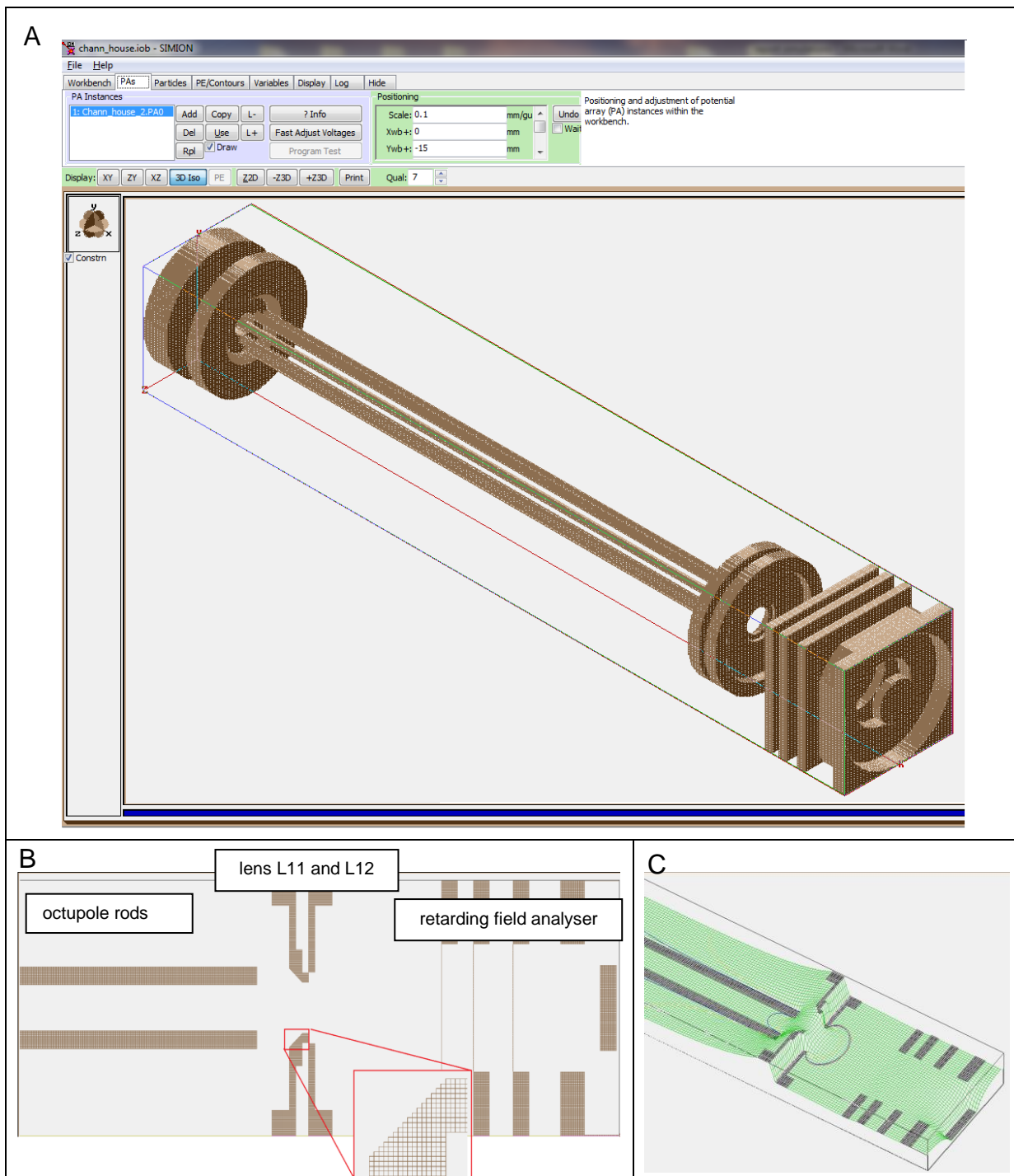


Figure 2.17. An example of the SIMION simulation of the ESI source up to the exit lens of the octupole. **A)** Image of SIMION interface with the 3D geometry of the skimmer, octupole, exit lens and retarding field analyser; the top panel is used in SIMION to define several parameters among which the mm/GU scale factor (0.1 mm/GU in this case). **B)** View of a section of the final part of the geometry shown in A. In the zoomed red box, squares related to GU are shown to indicate the spatial resolution of the simulation. **C)** The representation of the electrostatic potential in the final part of the setup calculated with the refine procedure of the software.

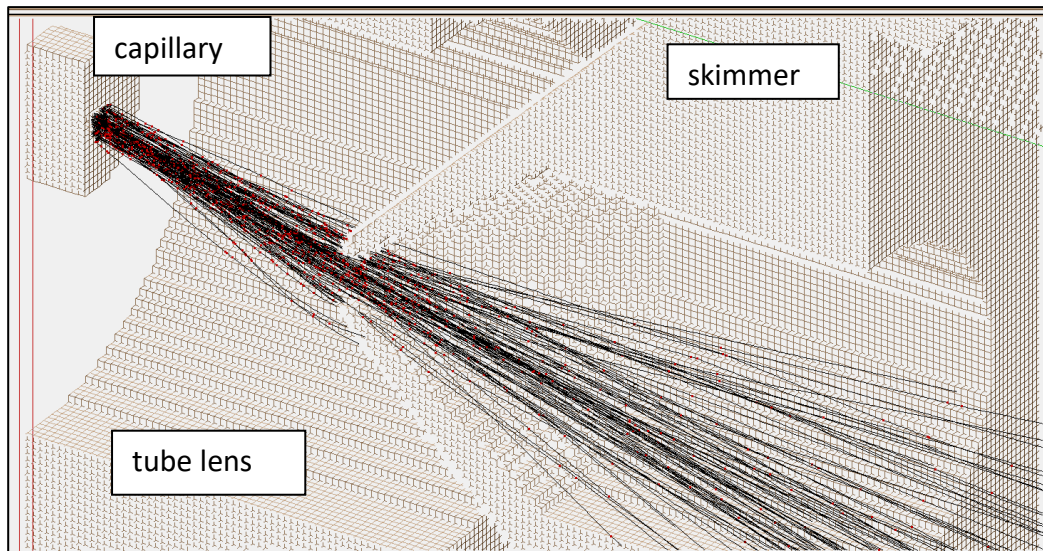


Figure 2.18 Expanded view of the skimmer region (see Figure 2.12.A): red dots mark collisions with the buffer gas when a residual gas is included in the simulation. The different density of red dots (collisions) before and after the skimmer is due to the different pressure conditions in these two regions.

The flexibility of SIMION is enormously extended by the possibility to work dynamically on simulation parameters during the simulation itself by codes written in the LUA programming language. In this way voltages applied at electrodes, ion direction, speed and other parameters can be changed during the simulation, allowing to simulate devices as octupoles and quadrupoles, where the radiofrequency applied voltage rapidly changes in time (2.5 MHz and 440 MHz, respectively, for the octupole and quadrupole in the setup). Using LUA scripts it is also possible to simulate the presence of a background gas at different pressure values in each section of the apparatus. The latter is done by simulating collisions with the buffer gas, changing ion velocity and direction according to the principles of kinetic theory of gases [117,118], as shown in Figure 2.18. The power and limits of this implementation will be discussed in the chapter 5.

2.2 The apparatus for the ESI deposition at ambient pressure

In this section the prototype setup used to perform ambient pressure ESI deposition for application in biosensors is described. In Figure 2.19 pictures and the scheme of the apparatus are reported, while elements of the setup are listed in Table 2.9.

The microfluidic line (1-4) is the same as described in section 2.1.4.1, even though the high voltage can be different due to the different geometry of the system. The position of the needle can be adjusted by acting on a x/y/z translator (5). The spray is illuminated by a led (6) and can be monitored during deposition by a camera (7). In front of the needle, on a x/y translator (8), is placed the target (9) acting as grounded counter electrode. The spray can be focused by a cone electrode (10) polarized at a voltage intermediate between ground and the HV of the needle.

The apparatus is placed inside a plexiglass box mounted on Bosch bars, designed and built in order to keep the deposition environment as clean as possible and not subject to instabilities due to air drafts.

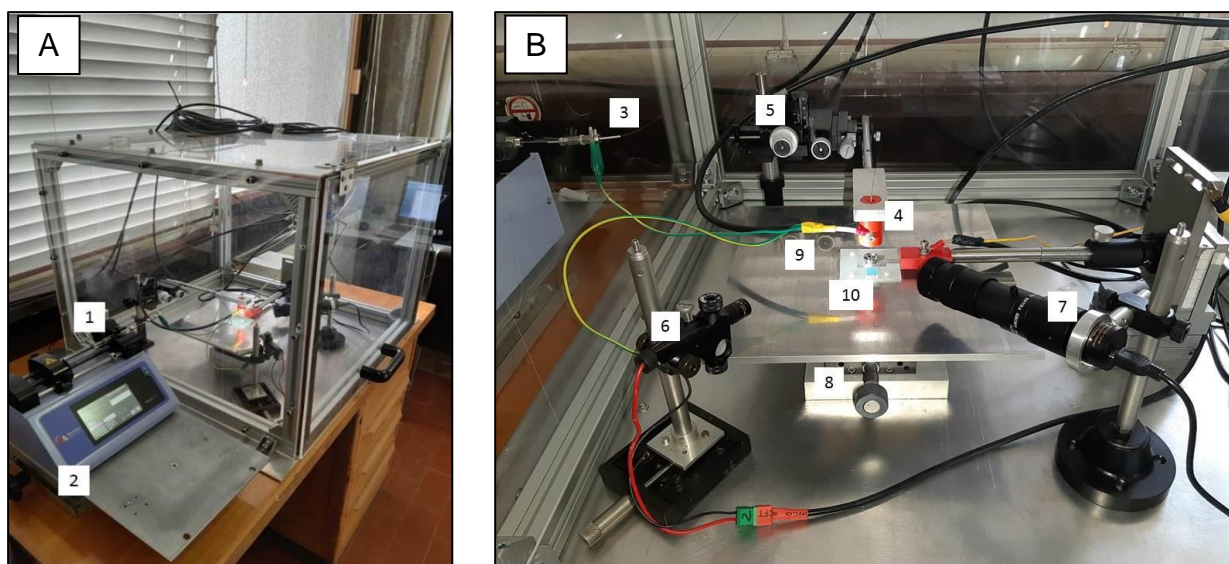


Figure 2.19. **A)** The setup for ESI deposition at ambient pressure: Harvard Apparatus Pump 11 elite and the syringe are located outside the protection box. **B)** Components of the setup inside the protection box. The numbers indicate the components listed in Table 2.9.

Components of the ESI setup for depositions at ambient pressure	
1	Hamilton 250 μ l Gastight 1725 syringe
2	Harvard Apparatus Pump 11 elite
3	silica capillary 50 cm long and 250 μ m inner diameter (Agilent Technologies)
4	flat-tipped steel needle: 2 cm long and 100 μ m inner diameter (Vita Needles company)
5	x/y/z translator for the alignment of the needle (Thorlabs)
6	LED light source to improve the image contrast for the camera
7	M-0616-E camera monocular 6x16/10° and associated software program, for real-time control of the spray stability (SPECWELL)
8	x/y translator for the alignment of the sample holder (Thorlabs)
9	target
10	steel focusing cone

Table 2.9. List of the components of the set-up shown in Figure 2.19.

The alignment between spraying capillary, focusing cone electrode and target is a crucial parameter for the deposition (see chapter 4), moreover the distance between these three elements can be influenced by the composition of sprayed solution. For these reasons the three elements can be moved by independent micrometric translators for fine alignment. The deposition region is shown in Figure 2.20 where a picture (panel A) and a schematic description (panel B) with typical values of distances and applied voltages are shown. In Figure 2.20.C a picture of the Taylor cone and spray in stable condition is reported.

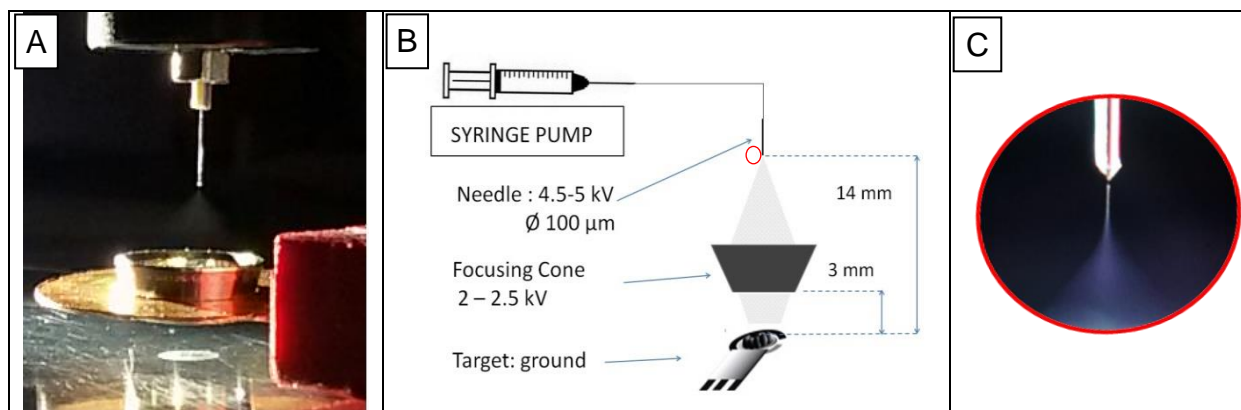


Figure 2.20. **A)** Picture of deposition region where the ESI spray, the focusing electrode and the obtained deposit are visible. **B)** Schematic of the setup configuration: geometry and applied voltages. Location of the Taylor cone is indicated by a red circle. **C)** Image recorded by the SPECWELL camera during the deposition of the spray formation region highlighted by a red circle in B where Taylor cone is visible.

In this study four kinds of targets, for different and specific purposes, have been used:

- aluminium plates (Figure 2.20.A). These targets are plates, several cm large, obtained out of standard aluminium foil; they are used for preliminary tests to optimize deposition conditions because they offer a large deposition area, the deposit is clearly visible and, after cleaning procedure, are easily reusable.
- conductive glass (see section 4.4). These targets are obtained cutting small pieces (1-2 cm in lateral size) from commercial glass plates (10 cm x 10 cm) with a conductive side realised with a layer of fluorine doped tin oxide (FTO, Sigma Aldrich); these targets are used because they offer a large and relatively flat conductive deposition area.
- quartz crystal microbalance (QCM) (see section 4.3.2): these targets are quartz crystal disks with two gold contacts; they are used to “weight” the amount of deposited enzyme.
- screen printed electrodes (SPE). These devices are composed of three conductive traces (electrodes) on an insulating material: the working electrode, the counter electrode and reference electrode (see section 1.3). Each one of these electrodes has a specific function; the biologic material is deposited on the working electrode. SPE have been used to realise biosensors and perform electrochemical tests on the enzymatic activity.

2.3 Theoretical Methods

In this section a brief description of the theoretical methods used to interpret experimental data presented in chapter 3 about photofragmentation of nitroimidazole compounds is reported.

First of all, the theoretical framework to calculate molecular energy is introduced, then photoionisation and photofragmentation are quickly described. Finally the procedures to explore fragmentation paths and kinetics of fragmentation are presented. All calculations are performed by the theoretical group (A. Casavola, M. Satta and A. Cartoni) using the Gaussian09 software [119].

2.3.1 Calculation of energy of a molecule

A molecule is a system of several atoms composed by nuclei and electrons all interacting with each other; one of the main focuses of computational chemistry is to identify an accurate quantum mechanics description of this kind of system. The starting point for a theoretical investigation is the time independent Schrodinger equation:

$$\hat{H} |\Psi_i(\vec{r}, \vec{R}, \vec{s})\rangle = E_i |\Psi_i(\vec{r}, \vec{R}, \vec{s})\rangle \quad (2.28)$$

where, using the Dirac notation, \hat{H} is the Hamiltonian operator, $|\Psi_i(\vec{r}, \vec{R}, \vec{s})\rangle$ and E_i the wave function and energy of i^{th} state of the system. The wave functions depend on \vec{r} , coordinates of electrons, \vec{R} , coordinated of nuclei, and \vec{s} , the electronic spin. In the following discussion electronic spin is neglected for simplicity but in the calculation it is considered.

For a molecule the Hamiltonian can be written as [120].

$$\hat{H} = \hat{T}_e + \hat{T}_N + \hat{V}_{ee} + \hat{V}_{NN} + \hat{V}_{eN} \quad (2.29)$$

The first two terms \hat{T}_e and \hat{T}_N describe the kinetic energy of electrons and nuclei, respectively, \hat{V}_{ee} the electrostatic repulsion between electrons and \hat{V}_{NN} the electrostatic repulsion between nuclei, the last term \hat{V}_{eN} is the attractive potential energy between electrons and nuclei.

Solving the Schrodinger equation with the complete Hamiltonian just described is too complicated and several approximations are generally applied; one of the main difficulties is due to the presence of the term V_{eN} , which depends on both nuclear and electronic coordinates. Nuclei and electrons can be considered separately because the mass of the nuclei is several orders of magnitude larger than the mass of an electron and the interacting forces have the same magnitude, therefore nuclei are much slower than electrons and can be considered stationary in fixed positions meanwhile electron dynamics takes place. This observation is the core of Born-Oppenheimer approximation [120] in which nuclear and electronic motion are considered separately, the wave function can be separated between nuclear, $|\Psi_N(\vec{R})\rangle$, and electronic, $|\Psi_e(\vec{r}|\vec{R})\rangle$, wave function where nuclear coordinates are parameters and not variables. The Schrodinger equation can be modified in:

$$\hat{H}|\Psi_i(\vec{r}, \vec{R}, \vec{s})\rangle = (\hat{H}_N + \hat{H}_e) |\Psi_e(\vec{r}|\vec{R})\rangle |\Psi_N(\vec{R})\rangle = (E_N + E_e) |\Psi_e(\vec{r}|\vec{R})\rangle |\Psi_N(\vec{R})\rangle \quad (2.30)$$

where \hat{H}_e and $|\Psi_e(\vec{r}|\vec{R})\rangle$ can be expressed as

$$\hat{H}_e |\Psi_e(\vec{r}|\vec{R})\rangle = (\hat{T}_e + \hat{V}_{ee} + \hat{V}_{eN}) |\Psi_e(\vec{r}|\vec{R})\rangle = E_e |\Psi_e(\vec{r}|\vec{R})\rangle \quad (2.31)$$

The strategy is first to solve the electronic Schrodinger equation (equation 2.31) and then the complete Hamiltonian (equation 2.30). To calculate explicitly the electronic wave function different methods can be used, like the Hartree–Fock [120] or Density Functional Theory (DFT) [121] methods. DFT is the level of theory adopted to perform calculations in chapter 3 and will be introduced later in this section.

A quantity of primary interest is the ground state energy E_0 ; the variational theorem states that E_0 , and the respective ground state wave function $\Psi_{e0}(\vec{r}|\vec{R})$, can be obtained by the following minimization

$$E_0 = \min_{\Psi} \langle \Psi_{e0} | \hat{H}_e | \Psi_{e0} \rangle \quad (2.32)$$

Ψ_{e0} is written in an explicit analytical form depending on a series of parameters used to minimize E_0 and to find an approximate but appropriate electronic wave function; obviously the quality of the results depends on the initial analytical form of Ψ_{e0} . This is generally an expensive calculation and the required computational time increases exponentially with the size of the system and with the accuracy required; DFT theory allows to simplify this problem proposing a versatile approach applicable on a wide class of systems.

In DFT methods the target of computational research is moved from the wave function to the spatial electron density function $n_e(\vec{x})$, which is the real interesting quantity, because it describes the spatial distribution of the electron cloud (equation 2.33):

$$n_e(\vec{x}) = N_e \int \dots \int |\Psi(x, r_2, \dots, r_{N_e})|^2 dr_2 \dots dr_{N_e} \quad (2.33)$$

where the integration is performed on all electronics coordinates except one used as spatial coordinate, \vec{x} .

The DFT is based on Hohenberg-Kohn theorem [122] that establishes two fundamental points:

- Given $n_e(x)$ for the electronic ground state, this determines univocally, up to an arbitrary additive constant, the external potential V_{eN} and consequently the electronic Hamiltonian \hat{H}_e that describes the many body system, the wave function becomes a functional $|\Psi_e[n_e(x)]\rangle$ which depends on the electronic density $n_e(x)$.
- The variational theorem [120,122] can be applied to the electronic energy functional $E[n]$

$$E[n] = \langle \Psi_e[n_e(x)] | \hat{T}_e + \hat{V}_{ee} + \hat{V}_{eN} | \Psi_e[n_e(x)] \rangle = F[n] + \int V_{eN} n_e(x) dx \quad (2.34)$$

where

$$F[n] = \langle \Psi_e[n_e(x)] | \hat{T}_e + \hat{V}_{ee} | \Psi_e[n_e(x)] \rangle \quad (2.35)$$

and the ground state energy E_0 is obtained by

$$E_0 = \min_{n_e} (F[n] + \int V_{eN} n_e(x) dx) \quad (2.36)$$

Even if there are more accurate theoretical methods than DFT to describe molecular energy levels (Coupled Cluster CCSD functional [123], Moller-Plesset MP2 functional [124,125], etc.), the main advantage of DFT is the possibility to describe a wide class of systems, with many atoms, still obtaining good results in terms of the required computational time.

Obviously, also in DFT good results are obtained only if a properly analytical representation of $n_e(x)$ is adopted. Becke, 3-parameter, Lee–Yang–Parr (B3LYP) functional [126] is widely used and fairly reliable, for this reason it has been adopted in all the calculations proposed in chapter 3.

In the previous discussion electronic spin has been neglected but wave functions, and consequently $n_e(x)$, contain information about the spin configurations and related energy levels; generally in all calculations described in chapter 3 only the ground state multiplicity with the lowest energy is considered except when, for a more accurate comparison with experimental results, also fragmentation of states of different multiplicity is considered.

2.3.2 Valence orbitals IP and photofragmentation

In this section a quick description of photodissociation and ionisation energy is reported.

A neutral molecule, assumed in the electronic ground state, can be promoted in an excited electronic state by photon absorption. There are several excited electronic states and, if enough energy is provided, the electron can be removed from the molecule to form the molecular ion [85]. Ionization Energy IE is the minimum energy required to promote one electron from a bound state to a free electron state. Energetic levels of a neutral molecule can be identified by a quantum number for electronic state (ϵ) and one for vibrational states (ν); similarly, for the molecular ion where states are indicated by ϵ' and ν' .

To calculate IE two different approaches can be used:

- Adiabatic IE : is the energy difference between the neutral and the ionic state of the molecule, both assumed in the electronic and vibrational ground state.
- Vertical IE : is the energy difference between the neutral molecule, assumed in the electronic and vibrational ground state, and the lowest vibrational state of the electronic ground state of the ion which allows to maintain the same nuclear coordinates.

Theory can calculate both the vertical and adiabatic IE, even though only the second one will be directly compared to the experimental measurement.

Increasing the photon energy, $h\nu$, above the ionisation threshold molecular dissociation can occur producing neutral and charged fragments; considering electronic states evolution, three possible paths can produce molecular fragmentation [85] (Figure 2.21):

- The molecule is excited in a dissociative state; there is no energy minimum and atoms continue to move apart until fragmentation happens (Figure 2.21.A)

- The excited state has some vibrational bounded states but the photon energy is higher than the fragmentation limit (red line in Figure 2.21) and the molecule fragments (Figure 2.21.B)
- The molecule is excited in a bound vibrational level that has an intersection with another dissociative electronic state: the molecules can change electronic state at the same energy and undergoes fragmentation (Figure 2.21.C).

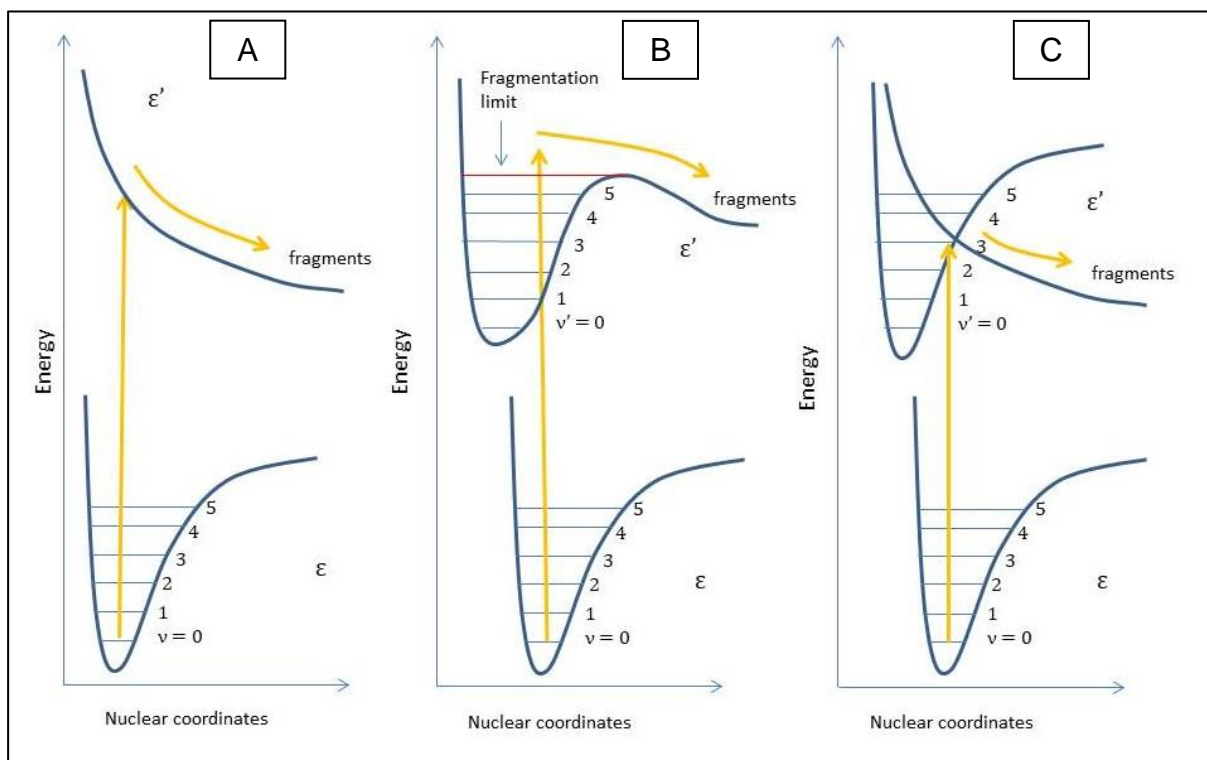


Figure 2.21. Schematic description of energy level evolution leading to molecular ion fragmentation; the three cases differ for the intrinsic characteristics of the electronic states of the ion.

As specified in the following, during the calculations of the molecular fragmentation both parent molecule and fragments are assumed to be in the electronic ground state; this assumption is based on the observation that de-excitation to the electronic ground state is generally faster with respect to fragmentation [85,120].

2.3.3 Potential energy surface, fragmentation path, AE and fragmentation rate

In the previous section theoretical methods to compute the energy of the molecule in a specific structure/conformation have been introduced; here the focus is to describe the molecular fragmentation [127].

Molecular fragmentation is a transition between two stable configurations, i.e. reactants and products, in the potential energy landscape. Each point of this multi-dimensional space is determined by a specific molecular configuration and the energy is calculated considering the system in the electronic ground state. The number of variables required to univocally describe a configuration of the system depends on the specific molecular structure and number of atoms; these variables are generally associated to physical parameters of the

molecular structure, like bond length or angle between two bonds, and are generally called reaction coordinates.

Reactants and products can be directly connected by a fragmentation path (Figure 2.22.A) and energy difference of the two stable configurations (ΔE_0) is equal to the energy barrier to be overcome to obtain the reaction. This energy value in photofragmentation studies has the name of appearance energy (AE).

It happens that the energy barrier (AE) to move from one stable configuration to the other is different from the energy difference of the two minima ΔE_0 (Figure 2.22.B). This situation is related to the presence of a transition state that is a saddle of the potential energy surface and determines the minimal energy required to obtain a specific reaction.

Only saddle points which are minimum in just one direction and maximum in all others are real transition states and connect two minima. Gaussian09 software has specific inbuilt methods to find real transition states. However, to prove that a transition state is really the one that connects the two minima of interest is more complex and a specific procedure is required. This procedure is called Intrinsic Reaction Coordinate (IRC) calculation (Figure 2.22.C) and consists in following the path in both directions (reactant and products) from the transition state towards the two minima, optimizing the geometry and calculating the electronic ground state of the molecular system in each point along the path. In this way the calculation unequivocally connects the two minima by a path which passes through the transition state between them. The calculation takes also in account the charge distribution and gives information about ions that will be produced in the fragmented state (Figure 2.22.C).

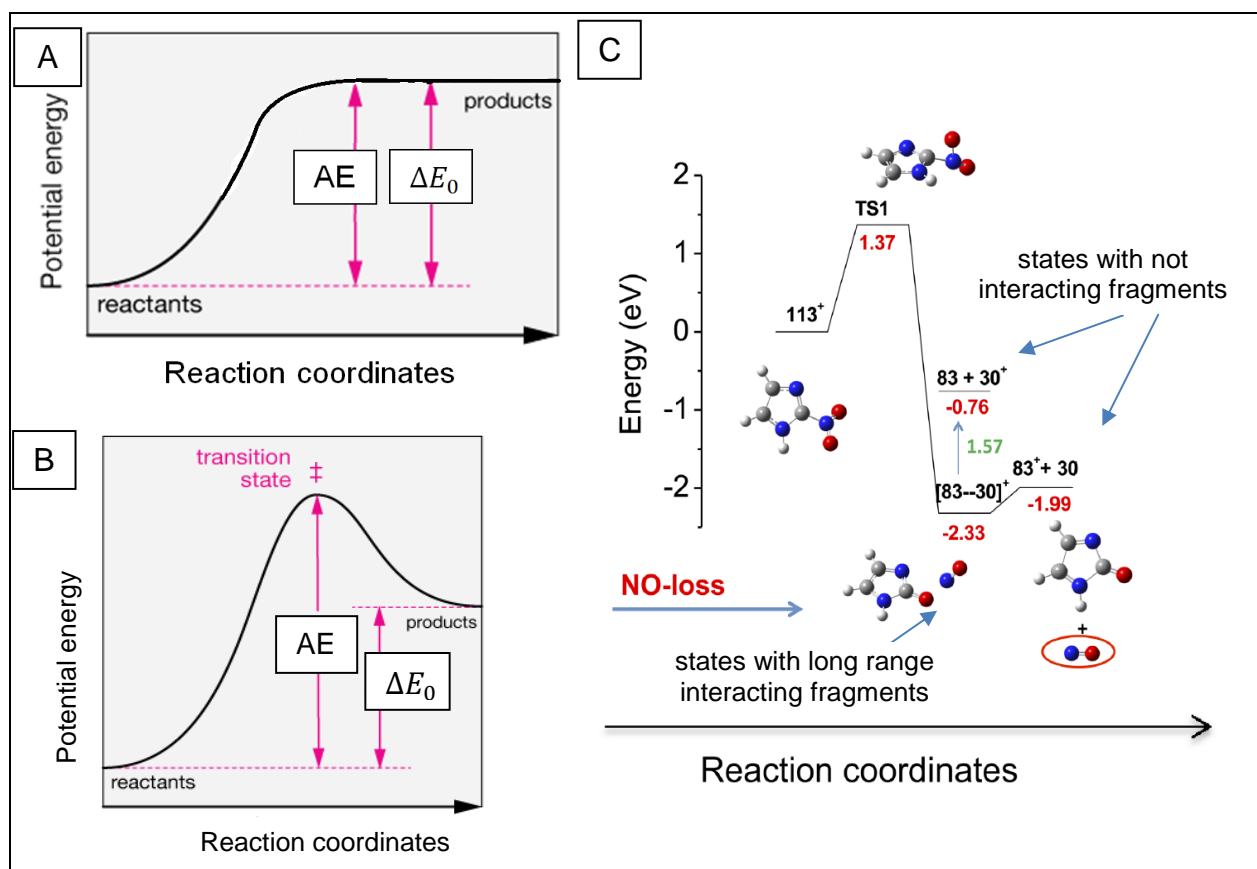


Figure 2.22. Schematic description of potential energy vs reaction coordinates when the energy difference of the two minima (ΔE_0) and the appearance energy (AE) are equal (A) or different (B). In C is reported an example of fragmentation path obtained by IRC calculation for 2-nitroimidazole molecule (a detailed description of 2-nitroimidazole fragmentation is described in chapter 3).

Once information about the energy and structure of initial, final and transition states is obtained, another interesting aspect to investigate is the fragmentation rate, k . This fragmentation parameter can be obtained by the following formula:

$$k(T) = \frac{k_B T}{h} \frac{q_{TS}(T)}{q_R(T)} \exp\left(\frac{-\Delta E_{TS}}{k_B T}\right) \quad (2.37)$$

where k_B is the Boltzmann constant, h the Planck constant, T the temperature, ΔE_{TS} the energy difference between reactant and transition state (TS), $q_{TS}(T)$ and $q_R(T)$ are the partition functions for transition state and reactant, respectively, and are function of the temperature. To convert temperature in internal energy, E_{int} , the Bose-Einstein statistic is used; the total energy of the reactant, i.e. the parent ion, is obtained by adding up the energy in each vibrational state (equation 2.38)

$$E_{int} = \sum_{i=1}^n \frac{h \nu_i}{\exp\left(\frac{h \nu_i}{k_B T}\right) - 1} \quad (2.38)$$

where n is number of vibrational degrees of freedom and ν_i the frequency of each vibrational mode. Number of vibrational degrees of freedom is $3N-5$ for linear molecules and $3N-6$ for non linear molecules, where N is the number of atoms in the molecules.

Considering vibrational modes of the reactant, i.e. the parent ion, and equation (2.38), the fragmentation rate for several E_{int} values can be obtained. These data are finally analyzed by a fitting procedure by the modified Arrhenius equation [128,129]:

$$k(E_{int}) = \alpha \left(\frac{E_{int}}{\chi}\right)^\beta \exp\left(-\frac{\gamma}{E_{int}}\right) \quad (2.39)$$

where α , β , χ and γ are the fitting parameters. By this procedure, the relation between fragmentation rate and parent ion internal energy is obtained.

In equation (2.37) reactant, products and transition state are assumed to be in thermal equilibrium, because the two partition functions are calculated at the same temperature. This hypothesis allows energy exchanges with the external environment, that make the reaction possible even if the E_{int} of the reactant is lower than the energy barrier ΔE_{TS} . In the experiments performed in vacuum condition the hypothesis of thermal equilibrium is not applicable and the fragmentation rate $k(E_{int})$ obtained by equation (2.37) has to be considered as an upper limit.

3 Photofragmentation of nitroimidazole based radiosensitisers

This first chapter of the results is devoted to the presentation and discussion of the photoionisation and photofragmentation study of nitroimidazole compounds, molecules representative of the nitroimidazole “oxygen mimetic” class of radiosensitisers [21,26,30]. The strategy in the selection of the compounds to be studied consists in the choice of molecules of increasing complexity, from the imidazole, the building block of the class, to nitroimidazole isomers (2-nitroimidazole (2-NI), 4-nitroimidazole (4-NI) and 5-nitroimidazole (5-NI)) and the more complex metronidazole (METRO) and misonidazole (MISO) molecules, which are used in therapy and built on 5-NI and 2-NI, respectively.

This represents an example of a “bottom-up” approach. The goal is to identify correlations between intrinsic physical and chemical properties, extracted from the knowledge acquired on the model system, and the functions performed by the radiosensitiser. For example different efficiencies has been observed the 2-NI and 4(5)-NI based drugs [30,130], thus the understanding of the specific physical chemical mechanisms at the base of the radiosensitising effect, may in the future guide the development of new and targeted radiosensitisers, which nowadays are mainly developed via “trial and error” approaches.

The chemical structure and relevant information on the studied molecules are collected in Table 3.1.

Section 3.1 presents and discusses the experimental results on imidazole and nitroimidazole isomers [98,103], considered as model systems for this class of radiosensitisers, and section 3.2 is devoted to the investigation of the real drugs, metronidazole and misonidazole [131] molecules.

3.1 Model systems: imidazole and nitroimidazole isomers

The target molecules have been purchased from Sigma Aldrich with purity between 97 and 98 %. They are all in the form of white powders at standard ambient pressure and temperature conditions. The gas phase effusive beam of the sample of interest is produced by sublimation of the powder kept in the crucible under vacuum, at room temperature for imidazole or heated up at about 80°C for 2-NI and 4-NI. Interestingly, it has been observed by previous XPS measurements [132] that the 4-NI and 5-NI regioisomers are both present in the gas phase, even though the sublimated sample was initially a pure 4-NI sample. These two compounds differ by the position of the nitro group on C4 or C5, respectively, but their structure can ‘switch’ from one to the other by the migration of the hydrogen atom from N1 to N3. It has been proposed that, being the most stable structure in water and in condensed phase, 4-NI would be the ‘natural’ structure at ambient conditions. However, being these two molecules almost degenerate in energy, the heating up of 4-NI during sublimation may induce isomerisation in the condensed (most likely) or gas phase, so that the two isomers coexist in the gas phase [132].

Therefore, all experimental results reported in this section refer to a mixture of 4(5)-NI. The estimated relative population of the 4-NI:5-NI isomers was 0.7 in the work of ref. [132] at a similar temperature, but it cannot be excluded that a temperature dependent effect may influence this proportion.

Name	Chemical formula	Mass (Da)	Description	Structure
Imidazole	C ₃ N ₂ H ₄	68	Aromatic heterocycle composed by 3 carbon and 2 not adjacent nitrogen atoms. It is the ring structure in the nitroimidazole compounds.	
2-Nitroimidazole 4-Nitroimidazole 5-Nitroimidazole	C ₃ H ₃ N ₃ O ₂	113	Isomers that differ by the position of the nitro group (NO ₂) to the imidazole ring, i.e. C2, C4 or C5 atoms. They are the model molecules for nitroimidazole radiosensitisers.	
Metronidazole	C ₆ H ₉ N ₃ O ₃	171	Organic compound built on the 5-NI core structure. It is used in medicine as antibiotic and has been tested as radiosensitiser in medical trials.	
Misonidazole	C ₇ H ₁₁ N ₃ O ₄	201	Organic compound built on the 2-NI core structure. It is used in medicine as radiosensitiser or in the hypoxia imaging. It has been reported [30] to have a better efficiency, but higher toxicity than metronidazole.	

Table 3.1. Structure and relevant information on imidazole and nitroimidazole compounds considered in this work.

3.1.1 TOF mass spectra

The TOF mass spectra of imidazole, 2-NI and 4(5)-NI obtained at the GasPhase beamline of the Elettra synchrotron with a photon energy of 60 eV are reported in Figure 3.1. In Table 3.2 the proposed assignments for the main peaks in the mass spectra according to previous literature ([138] for imidazole and [98,103,147] for NI isomers) are listed.

The parent ions (M⁺) are clearly detected in all compounds. In the imidazole case it has the largest branching ratio, suggesting that this molecule is more stable against fragmentation with respect to the nitroimidazole isomers; further proofs of this statement will be shown later by the PEPICO measurements.

The mass spectrum of imidazole produced by photon absorption (hν = 21 eV) [138] and electron impact [133] has been reported in literature. There is an overall good agreement between the present and the previous results as for the observed fragments and their relative intensities, apart for the relative intensity of the parent ion (m/z 68⁺). This difference may be ascribed to the different photon energies used or to the different cross section for electron/photon ionisation, although an experimental artefact due to the efficiency of the ion detector at large masses cannot be excluded.

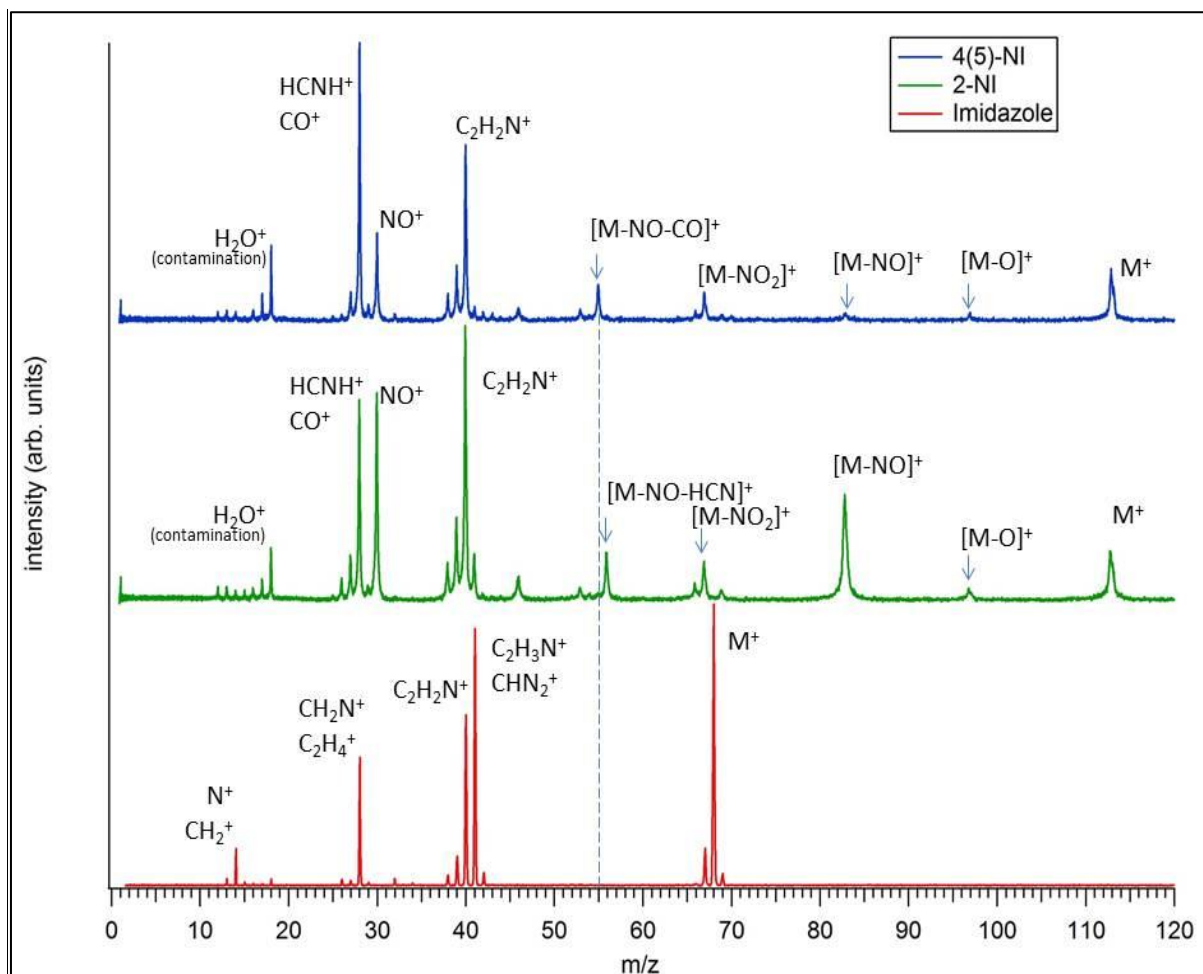


Figure 3.1. Mass spectra of imidazole (bottom), 2-NI (central) and 4(5)-NI (top) measured at 60 eV photon energy. The assignment of the relevant fragments is indicated and “M⁺” is the parent ion in each case. The dashed line marks m/z 55⁺ and is meant to highlight the difference between peaks at m/z 55⁺ (4(5)-NI) and 56⁺ (2-NI) that will be discussed in the text.

The NI compounds are characterized by the peaks at m/z 97⁺ and 83⁺ assigned to the O- and NO-losses, respectively. The latter has completely different intensities in the two spectra. The ion at m/z 67⁺ is assigned to the aromatic/imidazole ring after NO₂-loss in the NI isomers and H-loss in imidazole. The fragments at m/z 56⁺ and 55⁺ are the heaviest fragments produced in the fragmentation of the ring. They are not observed in imidazole. While the fragment at m/z 56⁺ is typical of 2-NI, the other one is observed only in 4(5)-NI. The region m/z 38⁺ - 42⁺ displays a series of peaks that, although with different intensity, are very intense in all of three mass spectra. These ions are likely produced in the fragmentation of the imidazole ring. The fragment m/z 30⁺, assigned unequivocally to NO⁺, is observed in both the NI isomers, but with a different relative intensity. The peak at m/z 28⁺, observed in all the three spectra, has different assignment in NI isomers and imidazole. Finally, the region m/z 0-20⁺ is dominated by H₂O⁺ and its fragments, present as contaminant likely because the NI samples are highly hygroscopic, while only the ion at m/z 14⁺ assigned to N⁺ or CH₂⁺ is clearly observable in the mass spectrum of imidazole.

In summary, interesting differences have been observed in the mass spectra of the NI isomers: namely (i) peaks at m/z 83⁺ and 30⁺, which are more intense in 2-NI than in 4(5)-NI and (ii) the peaks at m/z 56⁺ and 55⁺ which are observed only in 2-NI or 4(5)-NI, respectively.

m/z	Imidazole	2-NI	4(5)-NI
113		M ⁺	M ⁺
97		[M-O] ⁺	[M-O] ⁺
83		[M-NO] ⁺	[M-NO] ⁺
68	M ⁺		
67	[M-H] ⁺	[M-NO ₂] ⁺	[M-NO ₂] ⁺
56		[M-NO-HCN] ⁺	
55			[M-NO-CO] ⁺
46		NO ₂ ⁺	NO ₂ ⁺
41	NC ₂ H ₃ ⁺ , N ₂ CH ⁺	HCN ₂ ⁺	HCN ₂ ⁺
40	NC ₂ H ₂ ⁺ , N ₂ C ⁺	C ₂ H ₂ N ⁺	C ₂ H ₂ N ⁺
39	NC ₂ H ⁺		
38	NC ₂ ⁺		
30		NO ⁺	NO ⁺
28	NCH ₂ ⁺ , C ₂ H ₄ ⁺	HCNH ⁺ , CO ⁺	HCNH ⁺ , CO ⁺
27		HCN ⁺	HCN ⁺
26		CN ⁺	CN ⁺
14	N ⁺ , CH ₂ ⁺		

Table 3.2 . Assignment of the main peaks observed in the TOF mass spectra of imidazole, 2-NI and 4(5)-NI reported in Figure 3.1 according the literature ([138] for imidazole and [98,103,147] for NI)

3.1.2 Relative branching ratios from PEPICO measurements

In Figure 3.2 and Figure 3.3 the branching ratio of selected fragments obtained by PEPICO for imidazole, 2-NI and 4(5)-NI together with the photoelectron spectra (PES) of the valence band are reported. Experiments have been performed at the GasPhase beamline of Elettra synchrotron (Trieste) at the photon energy of 60 eV, with an overall energy resolution of about 0.5 eV and 30 meV for the PEPICO and PES measurements, respectively.

The PES spectra of imidazole [134,135] and nitroimidazole isomers [132] are already reported in the literature and are in good agreement with the present results. The binding energy of the highest occupied molecular orbitals (HOMO) shown in Figure 3.2 and Figure 3.3 have been calculated by OVGF/6-311++G** method for NI isomers and obtained from literature for imidazole [134]. The values of the binding energies are reported in Table 3.3; only the lowest orbitals are reported because at higher binding energies the electronic correlation leading to 2-hole-1-particle final states, not considered in the calculation, may drastically influence the results. The PES spectra of all these molecules have a similar structure and are composed of a first well recognizable band due to the HOMO state, a second band attributed to two or more states and, at BE > 13 eV, a series of overlapping bands. Despite the similar structure, some differences exist among the three samples: the ionization energy of imidazole is significantly lower with respect to 2-NI and 4(5)-NI (more accurate values can be obtained from AE measurements) and the first PES band of imidazole displays several components, due to vibrational structures [135] not observable in the other samples.

As already observed in many other molecules [99,136], Figure 3.3 shows that a clear state-selectivity in the fragmentation pattern exists and this depends on the (specific) molecular orbital (MO) ionised. Even though, consistently with the AE data, there is a threshold energy

for the release of each fragment, not all the energetically open channels are actually populated. Indeed, as the BE increases new and smaller fragments, which result from the break-up of the larger ones, can be formed while the larger fragments disappear from the spectrum. Finally the parent ion of all the species is only observed in the region of the lower molecular orbitals and always below 12 eV.

Figure 3.2 shows that the imidazole parent ion is very stable, being the only ion observed over the broad energy range of the two lower photoelectron bands, from ionization threshold up to more than 3.5 eV above (i.e. at BE 13-13.5 eV). In the nitroimidazoles, instead, several fragments are observed already in correspondence of the second PES band, at BE 10.5-11 eV, Figure 3.3.

Other examples of the state-selective formation of specific ions are at m/z 83⁺ in 2-NI and in 4(5)-NI and m/z 55⁺ in 4(5)-NI. Other ions, like m/z 28⁺ in both 2 and 4(5)-NI for example, are instead produced by the ionization of several valence bands, indicating that they can be produced via different fragmentation paths, probably in multistep processes.

In several cases, like m/z 83⁺ or 28⁺, the comparison of the branching ratio of the same fragment in 2-NI and 4(5)-NI shows that, even though the shape of the ratio versus the BE is similar, its relative contribution compared to other channels can be very different.

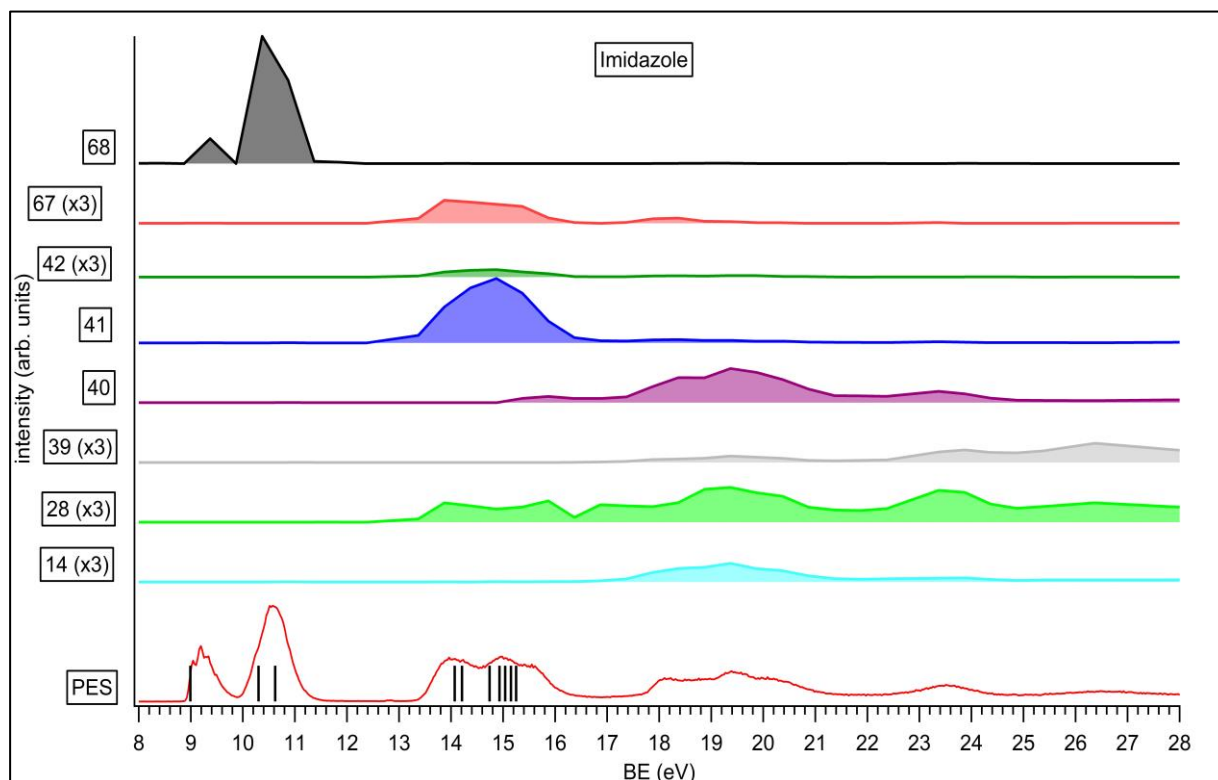


Figure 3.2. The PES spectrum and the PEPICO branching ratio of the main fragment ions observed in the mass spectrum of imidazole. The branching ratios of ions with m/z 14⁺, 28⁺, 39⁺, 42⁺, and 67⁺ have been multiplied by 3. In the PES spectrum also the theoretical position of the six lowest molecular orbitals (black bars) obtained from literature [134] is reported.

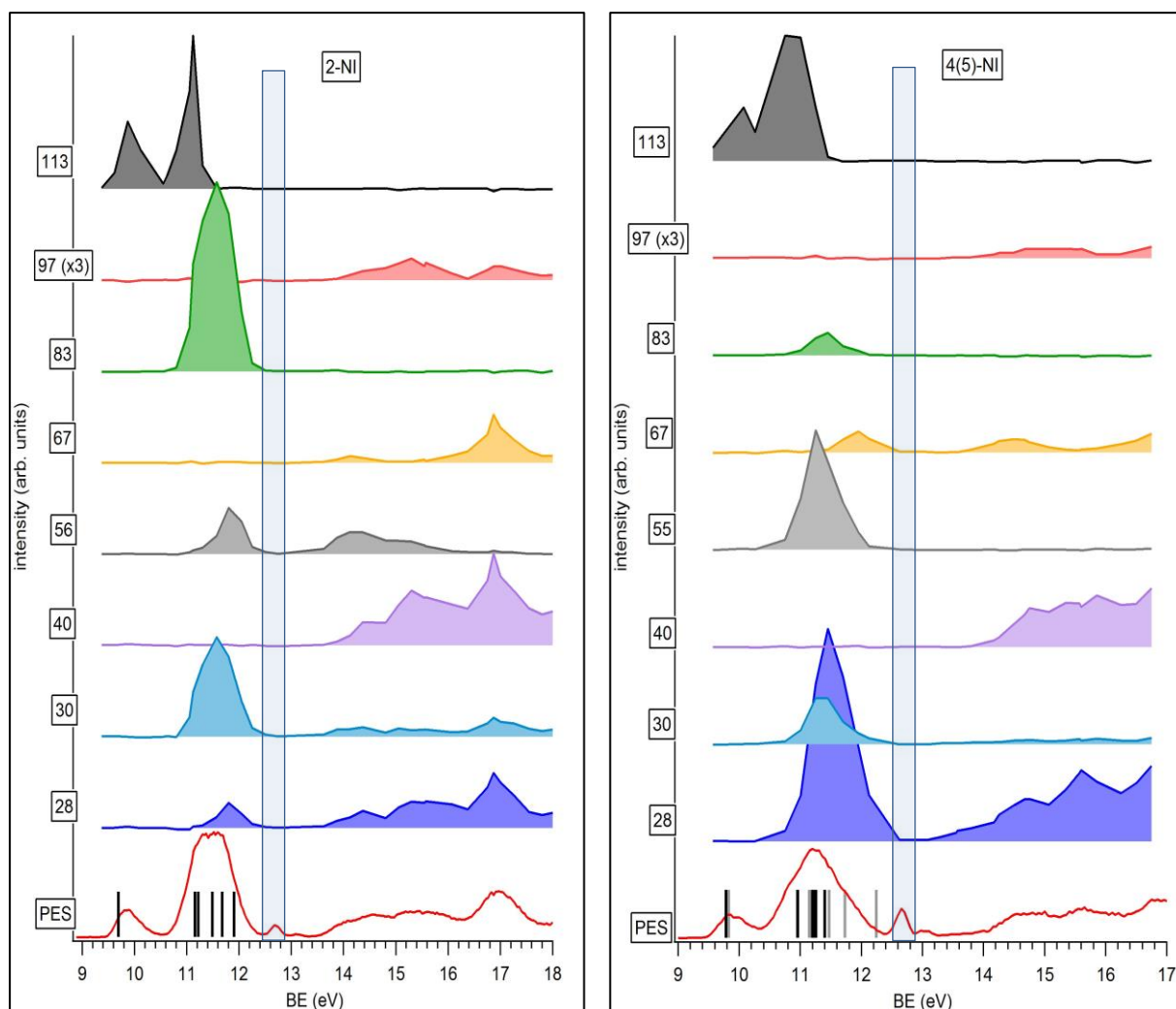


Figure 3.3. The PES spectra and the PEPICO branching ratios of the main fragment ions observed in the mass spectra of 2-NI (left panel) and 4(5)-NI (right panel); in both cases, the branching ratio of ion at m/z 97⁺ has been multiplied by 3. In the PES spectra also the theoretical position of the six lowest molecular orbitals (black bars for 2-NI and 4-NI, grey bars for 5-NI) are reported. The band at 12.6-12.8 eV in the PES spectra is due to water contamination [137], as also observed in TOF and PEPICO mass spectra.

State	Binding energy (eV)			
	Imidazole	2-NI	4-NI	5-NI
HOMO	8.99	9.694	9.781	9.829
HOMO-1	10.30	11.160	10.960	10.947
HOMO-2	10.62	11.217	11.168	11.148
HOMO-3	14.07	11.493	11.229	11.471
HOMO-4	14.21	11.679	11.258	11.733
HOMO-5	14.74	11.905	11.401	12.242

Table 3.3. Binding energy of the molecular orbitals showed in Figure 3.2 and Figure 3.3 calculated by OVGF/6-311++G** method for NI isomers and obtained from literature for imidazole [134].

3.1.3 Appearance energy measurements

The appearance energy (AE) of the main fragments of 2-NI and 4(5)-NI measured at the CiPo beamline of the Elettra synchrotron, Trieste, are reported in Table 3.4 together with the calculated values. For imidazole, the experimental AE values reported in Table 3.5 are taken from literature [138]. Although determined with a lower accuracy due to the large step size

in the coincidence experiments, also the branching ratio from the PEPICO measurements can provide a rough estimate of appearance energy. Thus, in Table 3.3 the energy range of the “first onset” of a the yield of a fragment in the PEPICO signal is reported.

A good consistency between the AE values of the NI measured at the CiPo beamline and their corresponding values estimated by the PEPICO experiments at the GasPhase beamline is found. In the case of the imidazole, most of the AE values measured in ref [138] are significantly lower than the ones determined in the PEPICO measurements. As far as the comparison between experimental and theoretical AE values in the nitroimidazoles is concerned, there is in general a good agreement, but for a few cases like for the fragment 67⁺ in 2-NI, where the AE is predicted to be lower than in the experiment.

2-NI				4(5)-NI			
m/z	AE _{th} (eV)	AE _{exp} (eV)	AE PEPICO (eV)	m/z	AE _{th} (eV)	AE _{exp} (eV)	AE PEPICO (eV)
113 ⁺	9.35-9.70	9.54 ± 0.01	9.4-9.6	113 ⁺	9.50 -9.83 (5-NI) 9.40 -9.78 (4-NI)	9.59± 0.01	9.5-9.6
83 ⁺	10.60	10.86± 0.02	10.6-11.0	83 ⁺	10.87 (5-NI)	10.88± 0.06	10.7-11
30 ⁺		10.94± 0.03	10.8-11.0	30 ⁺	10.60 (4-NI)	10.89± 0.02	10.8-11
56 ⁺	11.37	11.14± 0.06	10.8-11.1	55 ⁺		10.82± 0.06	10.26- 10.75
28 ⁺		11.16± 0.06	11-11.1	28 ⁺		10.95± 0.03	10.26- 10.75
97 ⁺	13.89	13.9± 0.2	13.9-14.1	97 ⁺	13.81 (5-NI) 13.54 (4-NI)	14.18± 0.02	13.8-14.2
40 ⁺ (t)	13.69	13.8± 0.1	13.6-13.9	40 ⁺ (t)	13.87 (5-NI) 16.00 (4-NI)	14.2 ±0.1	13.8-14.2
40 ⁺ (s)	15.16			40 ⁺ (s)	14.28 (5-NI) 14.45 (4-NI)		
67 ⁺ (t)	11.64	12.76± 0.06	12.7-13.6	67 ⁺ (t)	11.58 (5-NI) 11.46 (4-NI)	11.7± 0.14	11.0-11.5
67 ⁺ (s)	12.09			67 ⁺ (s)	12.43 (5-NI) 12.00 (4-NI)		

Table 3.4. Theoretical and experimental AE's for the main fragmentation channels of 2-NI and 4(5)-NI; for the parent ion cases the AE_{th} column reports both the adiabatic (lower value) and vertical (higher value) ionisation energy values. The (t) and (s) labels indicate the singlet and triplet spin states, respectively, which have been considered only for the fragments m/z 67⁺ and 40⁺ to explore a wider region of the potential energy surface in order to understand the discrepancy between theoretical and experimental results.

Imidazole		
m/z	AE _{exp} (eV)	AE PEPICO (eV)
68 ⁺	8.66 ± 0.003	8.8-9.3
67 ⁺	11.38 ± 0.05	12.3-13.3
41 ⁺	11.41± 0.05	12.3-13.3
40 ⁺	13.83± 0.05	14.8-15.3
39 ⁺		16.3-17.3
28 ⁺	11.34± 0.05	12.3-13.3
14 ⁺		14.3-15.3

Table 3.5. Experimental AE's obtained from literature [138] and from PEPICO spectra in Figure 3.2 for the main fragmentation channels of imidazole.

3.1.4 Discussion of the experimental and theoretical data

This section is devoted to a detailed analysis and interpretation of the photofragmentation paths of nitroimidazole isomers. The most evident and intriguing differences observed in the mass spectra of Figure 3.1 are at:

- **m/z 83⁺** assigned to (M-NO)⁺: this fragment appears with a very large intensity in the mass spectrum of 2-NI, while it gives a negligible contribution to the spectrum of 4(5)-NI. It has very similar theoretical and experimental AE values in all isomers.
- **m/z 55⁺ and 56⁺** assigned to [M-O-CO]⁺ and [M-O-HCN]⁺, respectively: each of these fragments is clearly observed in the mass spectrum of either 4(5)-NI or 2-NI, and therefore they can be considered as fingerprints for the different isomers.

In order to interpret these observations, the theoretical colleagues of the group (A. Casavola, CNR-ISM, M. Satta CNR-ISMN and A. Cartoni, Chemistry Department, Sapienza Università di Roma) have calculated the potential energy profiles of the fragmentation paths leading to the above listed fragments and also to fragments 28⁺, 67⁺ e 40⁺ (Figure 3.4).

Ion 83⁺ and the NO-loss mechanism

For all isomers, the most stable structure of the neutral molecule is almost planar, while the radical cation formation produces a transition state (TS1) where the rotation of the nitro group out of the ring plane brings one of the two oxygen atoms near the carbon atom of the C-NO₂ bond (Figure 3.4). The TS1 transient structure leads to a molecular rearrangement of the nitro group, where the swap in position between the nitrogen and oxygen atoms leaves the oxygen atom bound to the carbon favouring the NO-loss. The energy of the transient state TS1 is the energy barrier to overcome for this fragmentation to occur, and it has been calculated to be quite similar for all isomers (1.37, 1.35 and 1.52 eV for 2-NI, 4-NI and 5-NI, respectively). In the NO-loss process the charge of the molecular ion can be left on either the NO or the [M-NO] species. As it can be seen in Figure 3.4 the pair (83⁺ + 30) is energetically favoured with respect to (30⁺ + 83), even though both paths are possible. This scenario is supported by the observation that the AE for ion 83⁺ and 30⁺ are very similar in all isomers (Table 3.3), as can be expected considering that they connect to the same transition state.

In order to explain the clear difference in the intensity of fragment m/z 83⁺ in the mass spectra of 2-NI and 4(5)-NI it is necessary to take into account the evolution of its fragmentation path on the potential energy surface as shown in Figure 3.4. In 2-NI the ion 83⁺ is quite stable and its further fragmentation to produce CO (m 28), HCN (m 27) and HCNH⁺ (m/z 28⁺) requires to overcome a high energy barrier (2.75 eV). In 4-NI ion 83⁺ undergoes first a ring opening and then fragments to form CO (m 28), HCN (m 27) and HCNH⁺ (m/z 28⁺) with a total energy barrier of 0.95 eV. In 5-NI, ion 83⁺ fragments in (M-NO-CO)⁺ (m/z 55⁺) and CO (m 28) by overtaking an energy barrier of 1.14 eV. Then, ion 55⁺ in turn fragments into HCNH⁺ + HCN. So, the potential energy surfaces explain how ion 83⁺ is kinematically less stable in 4-NI and 5-NI than in 2-NI. As a consequence, even though the AE of m/z 83⁺ is similar for all of the three isomers, this ion is observed with large intensity only in the mass spectrum of 2-NI.

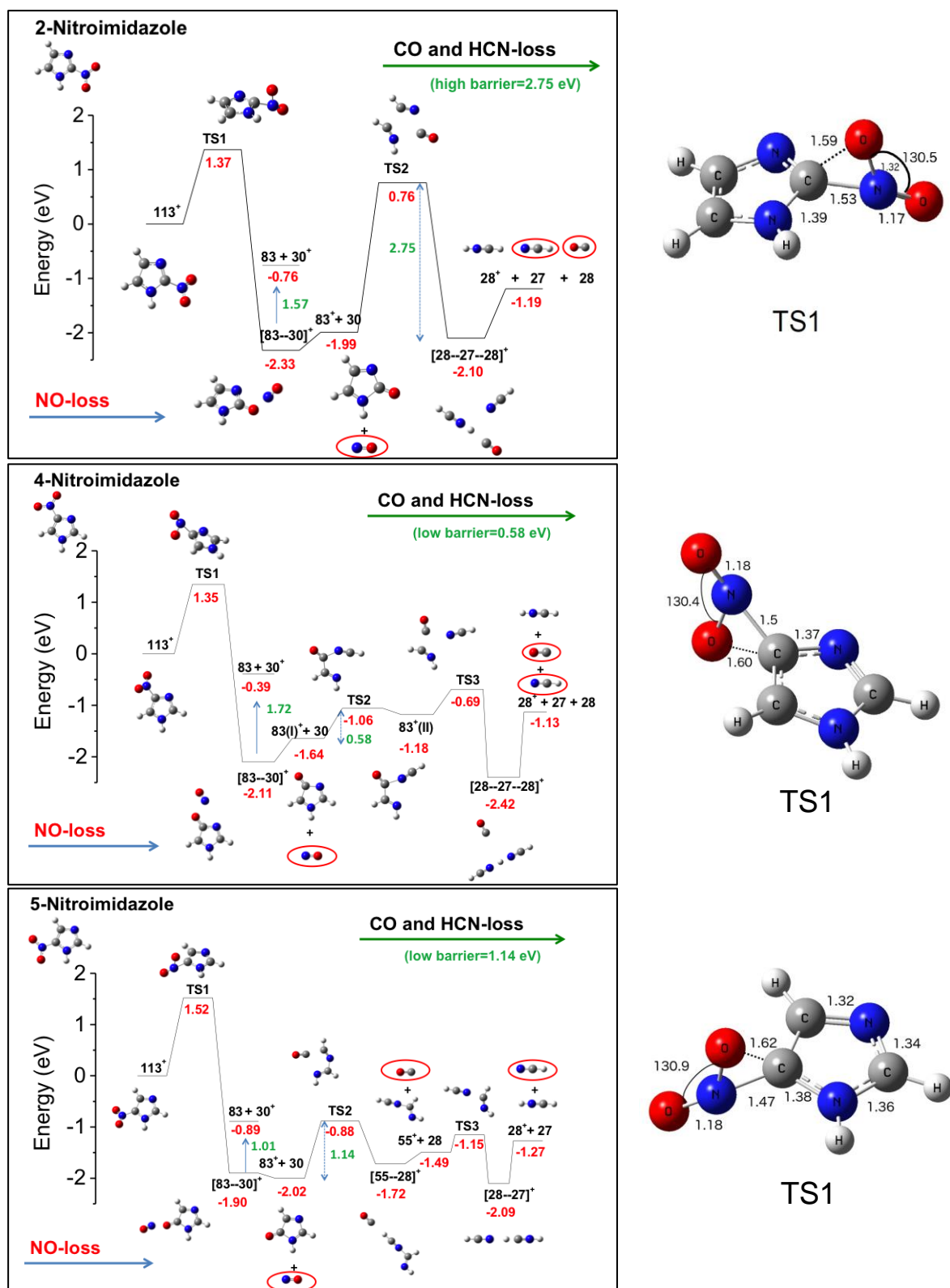


Figure 3.4. Left panels) Potential energy surfaces to produce ion 83^+ from parent ion and its subsequent fragmentations for all NI isomers. The structures of the ions before and after the fragmentation and at transition states are reported. Neutral molecules released during fragmentation and relevant for the discussion in the text (NO, CO and HCN) are highlighted by red circles. Energies of each considered structure with respect to the energy of the parent ion (m/z 113⁺) are indicated by red numbers; green numbers correspond to the energy difference indicated by the arrows while in black the fragmentation products are also reported. **Right panels)** Optimized molecular structures at the transition states TS1 for each NI isomer; it is interesting to note how, in all cases, an O atom of the nitro group moves towards the C atom of the ring where the nitro group is bound (distances in Å and angles in degree).

This explanation is supported by the measured AE's (Table 3.4) of ions 83^+ , 30^+ , 28^+ and 55^+ that in 4(5)-NI are very close to each other, almost coinciding within experimental uncertainty, and by the very similar behaviour of the branching ratio in Figure 3.3, at least in the binding energy range 9-12 eV. These experimental observations are consistent with the idea of a common origin in the formation and decomposition of 83^+ . In 2-NI the ion 28^+ has an AE about 1 eV higher than the one of ions 83^+ and 30^+ .

Ions 55^+ and 56^+

It has been already discussed in the previous section that ion 55^+ , present only in 5-NI, is formed by a sequential fragmentation mechanism originating from the decomposition of ion 83^+ . The same AE (Table 3.4) and a similar behaviour of branching ratio of these two ions (Figure 3.3), suggests that the proposed path is the only one active in the explored valence energy region (8-28 eV binding energy).

The mechanism leading to ion 56^+ , present only in 2-NI, is more complex. The potential energy surface reported in Figure 3.5, shows that several molecular rearrangements of 83^+ and an energy higher than the one needed to form 83^+ itself are required to form this ion. This explains why the AE of ion 56^+ is higher than the AE of 83^+ . Figure 3.5 shows also that ion 56^+ can furtherly fragment to form ion 28^+ , overcoming the relatively small energy barrier of the TS6 transition state.

The curves of the branching ratio (Figure 3.3) show that the fragment 56^+ can be formed also in the BE range above 13 eV, not studied in the present work.

Ion 28^+

As it is frequently the case for 'small' fragments, ion 28^+ can be produced by several fragmentation paths. Some of these can be clearly identified in the PEPICO branching ratios, interpreted with the support of theoretical calculations.

In the case of 4(5)-NI the formation of 28^+ in the region 11-12 eV is mostly related to the decomposition of 83^+ and 55^+ (see Figure 3.4); in the binding energy region above 13 eV different, and yet unexplored channels, exist.

For 2-NI we have discussed two possible fragmentation paths to obtain ion 28^+ (Figure 3.4 and Figure 3.5). Despite the path in Figure 3.5 is characterized by higher energy barriers (transition state TS4 is 2.07 eV above parent ion) than the one in Figure 3.4 (transition state TS2 is 0.76 eV above parent ion), ions 28^+ and 56^+ display similar trends of branching ratio (Figure 3.3) and similar AE values, in both cases higher with respect to the AE of ion 83^+ (Table 3.4). This observation may support the hypothesis that a direct fragmentation of ion 83^+ to form ion 28^+ is less likely to happen.

Ions 67^+ and 40^+

To complete the investigation of the photofragmentation of the NI isomers also the paths producing the other relevant fragments observed in the mass spectra have been investigated. These are ions 67^+ and 40^+ due to the NO_2 loss and residual imidazole ring, respectively.

The intense fragment at m/z 40^+ is present in the mass spectra of imidazole and all nitroimidazole isomers, qualitatively suggesting a similar assignment as part of the ring (see also Table 3.8). Indeed, the experimental and theoretical AE's indicate that a large amount of internal energy is needed to form these fragments, e.g. $\text{AE}(40^+) > 13.5\text{-}14$ eV. This suggests that the fragmentation paths involved in these cases may be different from the ones already

described, which were mostly related to ion 83^+ . For these reasons the production of ion 40^+ by further fragmentation from ion 67^+ in a ring configuration after NO_2 -loss has been studied. Of course, other paths to form ion 40^+ from 67^+ may be hypothesized as analysed in other works [138,139].

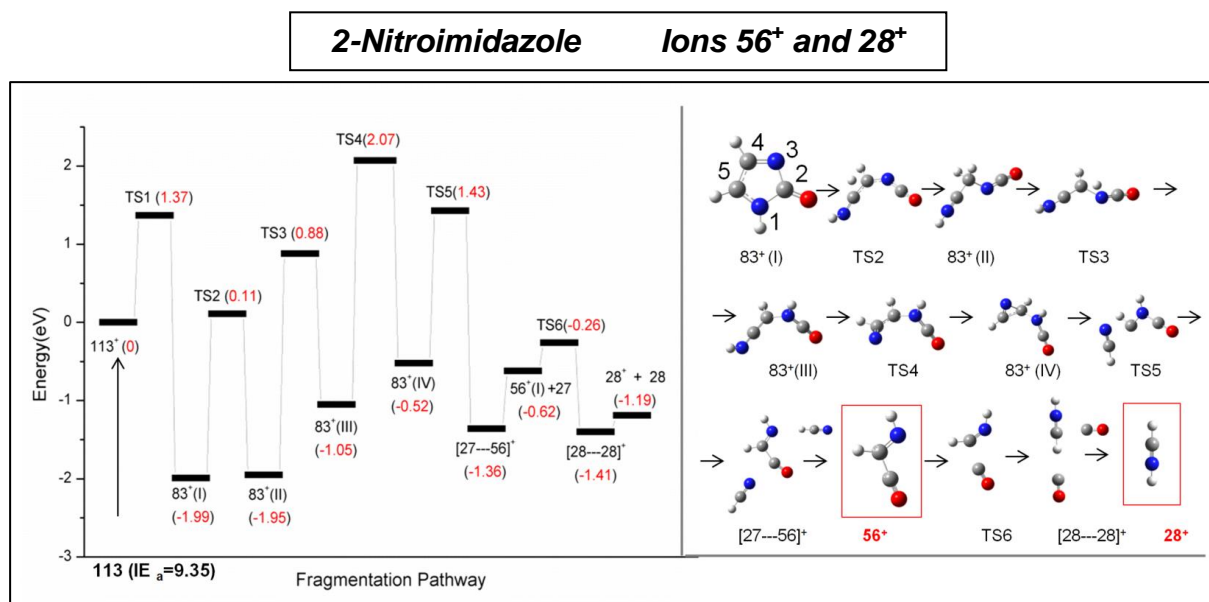


Figure 3.5. Fragmentation path to produce ions 56^+ and 28^+ from the 2-NI parent ion (m/z 113^+). **Left panel)** Potential energy surface. Ions are indicated, together with their respective energy difference with respect to the energy of the parent ion (red numbers). **Right panel)** Molecular structure for all ions, neutral fragments and transition states considered along the fragmentation path. Roman numbers are used to distinguish different structures of the same ion.

The fragmentation paths and potential energy profiles to form ion 67^+ and its possible evolution in 40^+ are reported in Figure 3.6-3.9 for 2, 4 and 5-NI, respectively. In order to investigate the relatively unsatisfactory agreement between the theoretical and experimental AE's results the modelling of fragment 67^+ has been performed considering the possibility for this ion to be formed in both singlet and triplet states. By looking at the fragmentation paths in the figures the following observations related to the main differences and similarities for each NI isomer can be done.

In 2-NI the ion 67^+ is predicted to be more stable in triplet than in singlet state, with an energy difference of 0.63 eV, see Figure 3.6. Also the formation of ion 40^+ along the path of the triplet state requires to overcome lower energy barriers than in the path of the singlet state and the predicted AE value is in good agreement with the experiment.

The predicted value of $\text{AE}(67^+)$ in both singlet and triplet state is lower than the experimental one. We do not have a clear explanation for this discrepancy, but two possibilities may be considered. The first one is that the assumption of the NO_2 -loss prior to ring opening (i.e. starting configuration of the present results) is not valid, while the second one is that higher excited electronic states, which cannot be included in the present theoretical model, may be directly involved in the fragmentation dynamics.

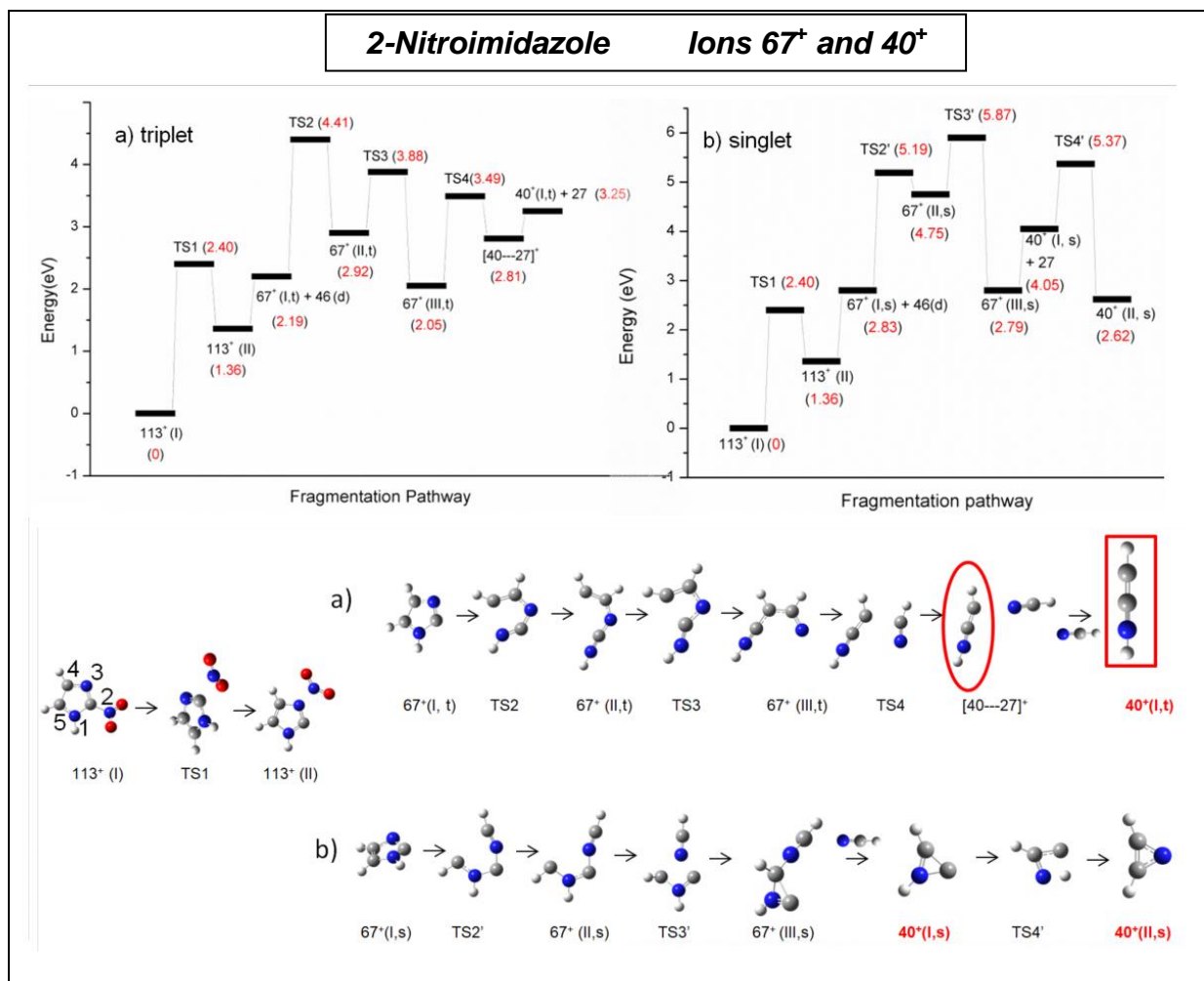


Figure 3.6. Fragmentation path to produce ion 67⁺ (in the imidazole ring conformation) from parent ion and its subsequent fragmentation leading to ion 40⁺ for 2-NI. Fragmentation paths from both singlet and triplet states of 67⁺ are considered. **Top panel)** Potential energy surface with indicated ions before and after fragmentation and at transition states with energy difference (red numbers) with respect to the energy of the parent ion. **Bottom panel)** Molecular structure for all the neutral and charged fragments and transition states considered in the fragmentation paths. Roman numbers are used to distinguish different structures of the same ion.

In 4-NI, the theoretical AE (67⁺) in triplet state is lower than the one in singlet state and very close to the experimental one. However, as for the ion 40⁺, it is the fragmentation starting from the 67⁺ singlet state that seems to produce the best agreement with the experimental results. Also in 5-NI the theoretical AE (67⁺) in triplet state is the lowest in energy and in better agreement with the experiment. Concerning the subsequent formation of ion 40⁺ from the decomposition of 67⁺, both paths from singlet and triplet states predict an AE value in reasonable agreement with the experiment (AE 13.87 and 14.28 eV for triplet a singlet state, respectively) even though the path from the singlet state produces a slightly better agreement.

Both singlet and triplet states of ion 67⁺ can contribute to the formation of ion 40⁺. However, while ion 67⁺ is produced preferentially in triplet state, ion 40⁺ seems to be produced preferentially from the fragmentation of 67⁺ in singlet state.

Considering that in the experiment 4 and 5-NI are mixed, on the basis of the dissociation paths considered in the present modelling one can state that ion 67⁺ is produced in the more energetically favoured triplet state, but then the ion 40⁺ is generated more effectively by the fragmentation of 67⁺ in singlet state. However, we cannot exclude that other paths on the

complex potential energy surface not accounted for in the present modelling can lead to different conclusions.

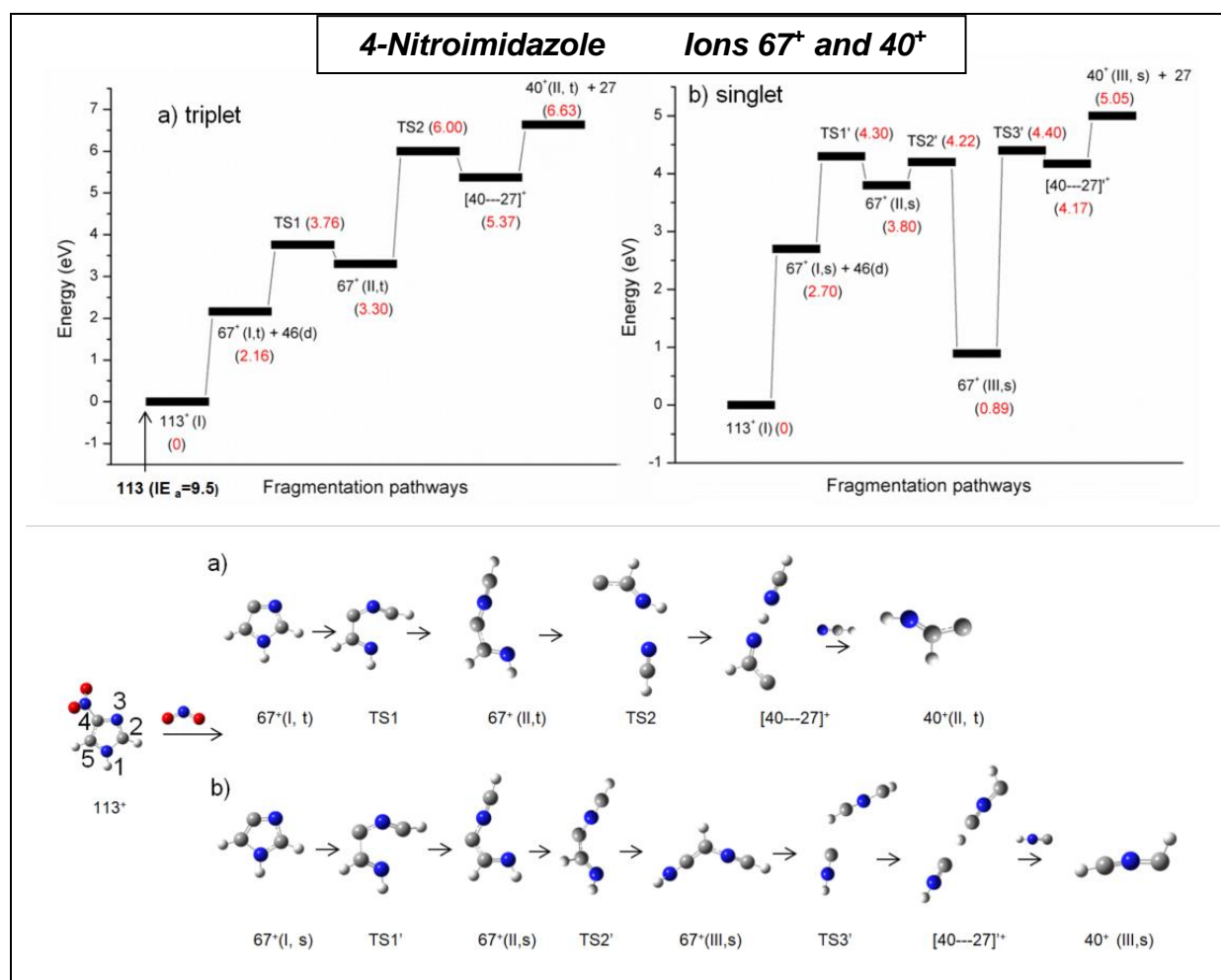


Figure 3.7. Fragmentation path to produce ions 67⁺ (in the imidazole ring conformation) from parent ion and its subsequent fragmentation to form ion 40⁺ for 4-NI. Both fragmentation paths for singlet and triplet states of ions 67⁺ are considered. **Top panel)** Potential energy surface with indicated ions before and after fragmentation and at transition states with energy difference (red numbers) with respect to the energy of the parent ion. **Bottom panel)** Molecular structure for all the neutral and charged fragments and transition states considered in the fragmentation path. Roman numbers are used to distinguish different structures of the same ion.

To summarize the results on the investigation of the model nitroimidazole compounds, a detailed description of the main fragmentation paths in the valence shell region has been proposed via a joint experimental and theoretical study. The TOF mass spectra indicate the most abundant fragments and the theoretical calculations of potential energy surfaces propose the molecular rearrangements and energy barriers (theoretical AE) to obtain these fragments. Branching ratios obtained from PEPICO, are crucial to i) guide theoretical exploration of the potential energy surface suggesting possible correlations between fragments in multistep processes and ii) identify correlations between fragmentation patterns and molecular orbitals. The reliability of energy barrier is finally proved by AE measurements.

The good agreement between theory and experiments supports the consistency of both methods and shows how a clear interpretation of the fragmentation paths relies on the combination of complementary approaches.

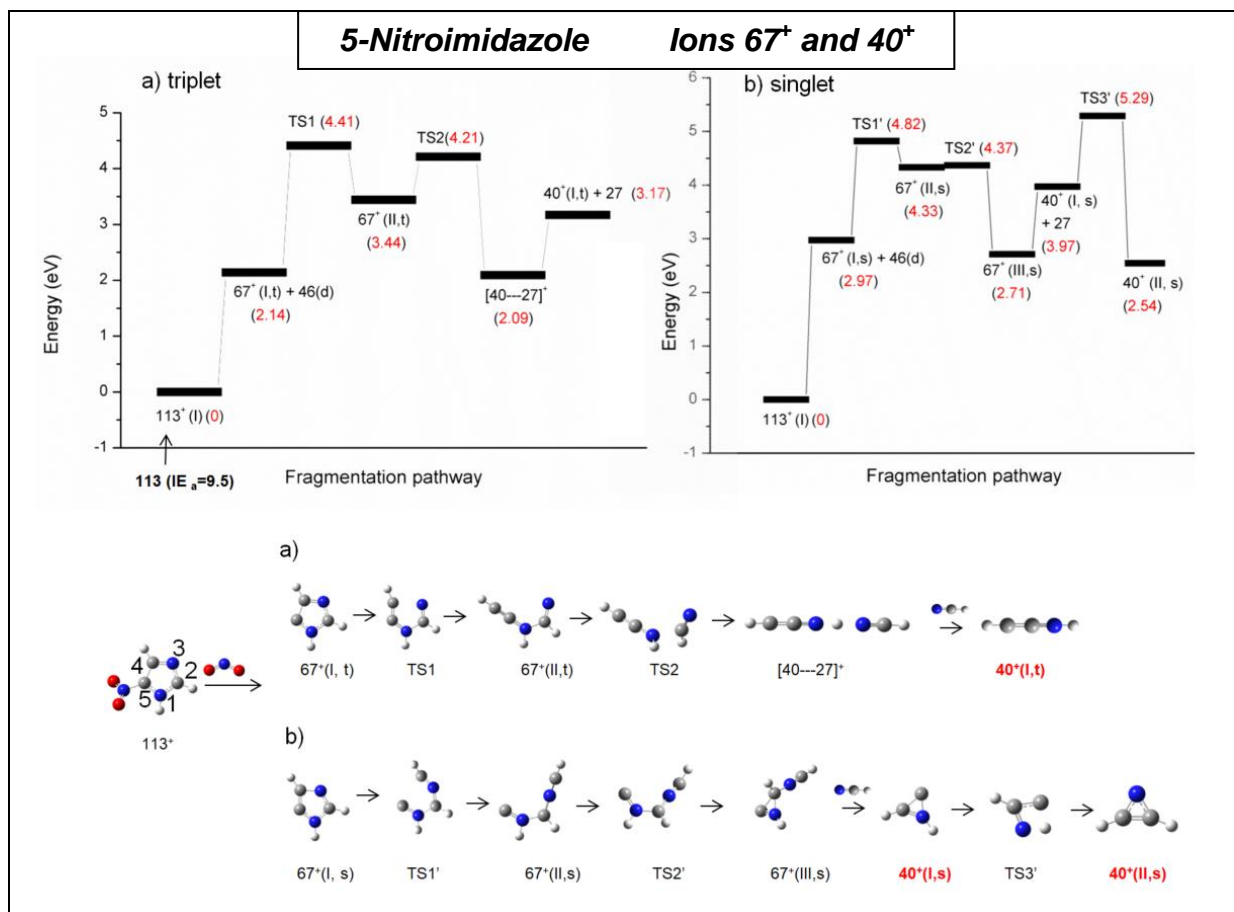


Figure 3.8. Fragmentation path to produce ions 67⁺ (in the imidazole ring conformation) from parent ion and its subsequent fragmentation to form ion 40⁺ for 5-NI. Both fragmentation paths for singlet and triplet states of ions 67⁺ are considered. **Top panel)** Potential energy surface with indicated ions before and after fragmentation and at transition states with energy difference (red numbers) with respect to the energy of the parent ion. **Bottom panel)** Molecular structure for all the neutral and charged fragments and transition states considered in the fragmentation path. Roman numbers are used to distinguish different structures of the same ion.

The results are interesting both from the fundamental, physical chemical, point of view of the characterisation of this class of compounds, as well as for the possibility to understand the connection between molecular structure and function, unravelling the mechanisms of operation of radiosensitising molecules based on their model, prototypal systems.

As far as the clinical application is concerned, the results have shown that the three NI isomers are characterised by different radiation-induced fragmentation mechanisms, which in turn may explain their different level of effectiveness as radiosensitisers. All isomers release, by direct fragmentation, the highly reactive NO radical, which can have an active role in DNA radiation damage fixation as well as in favouring the reoxygenation of the hypoxic tumour tissue, explaining their effectiveness as radiosensitisers [130]. However, due to the lower kinematic stability of the residual ion after NO loss, 4-NI and 5-NI produce a higher amount of CO and HCN. These secondary species can be toxic and produce an opposite effect [140,141] due to the high affinity of CO for haemoglobin contained in red blood cells, therefore favouring hypoxia and drastically reducing radiotherapy efficacy. Thus molecules built on 2-NI should be more effective as radiosensitisers.

3.1.5 Metastable processes in nitroimidazole photo-fragmentation and their simulations

In this section, kinetics aspects of the photofragmentation of NI isomers are investigated. Fragmentations are in general considered “prompt” processes, occurring in the ps or smaller time scales after the triggering event. It is however possible that metastable processes, which involve time scales in the range of ns to even ms, occur [142,143].

The kinetics of a specific fragmentation path is determined by the energy needed for the molecular rearrangements (energy barriers and transition states involved) and the amount of internal energy, E_{int} , available to the system. The first is an intrinsic characteristic of the system, the second depends on specific experimental or environmental conditions. The higher the internal energy with respect to the energy barrier to be overtaken, the faster will be the process. As introduced in section 2.3.3, each state is characterized by a decay rate parameter that depends on the internal energy of the system, $k(E_{\text{int}})$. The decay rate is the key parameter that describes the probability distribution for the fragmentation time of a state:

$$P(t) = \frac{1}{k} \exp(-kt) \quad (3.1)$$

In the following we refer to both the fragmentation rate, k , or its inverse, the lifetime τ .

To investigate kinetic of fragmentation dedicated techniques as threshold photoelectron - photoion coincidence (TPEPICO) can be used [143,144], but also TOF mass spectrometry is, within certain limits, a suitable tool to investigate metastable fragmentation.

The mass spectra of the NI isomers measured with the apparatus installed at the Gasphase beamline at Elettra at 60 eV (MS-1) and in the CNR-ISM laboratory in Rome with the Ar discharge lamp (MS-2) at 11.6 eV are shown in Figure 3.1 and Figure 3.9 respectively.

The most intriguing difference between the two spectra is represented by the shape of some peaks. In MS-1 all peaks are almost symmetric while in MS-2 some fragments (e.g. the one at m/z 83⁺) have an asymmetric lineshape, with tails extending towards higher masses.

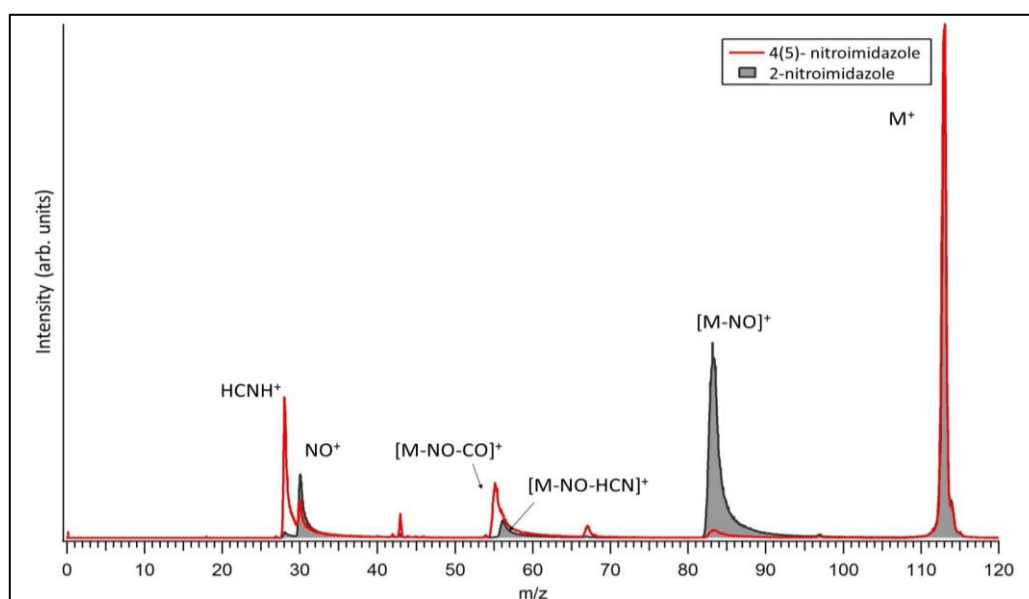


Figure 3.9. Mass spectra of 2-NI (grey) and 4(5)-NI (red) measured with the TOF mass spectrometer installed at the CNR-ISM in Rome equipped with a rare gas discharged lamp operated at 11.6 eV (Ar gas) photon energy. Peaks with an asymmetric lineshape are clearly visible.

In order to describe the physical mechanism responsible of these tails, a schematic description of a TOF spectrometer is used in Figure 3.10. If the fragmentation of $AB^+ \rightarrow A + B^+$ is prompt with respect to the formation of the parent ion AB^+ , then the time of flight of the daughter ion B^+ will depend on the fact that it has travelled the entire length of the TOF spectrometer (extraction, acceleration and drift tube regions) with the m/z of B^+ , see red arrow in Figure 3.10.

In the case of later fragmentation, i.e. when AB^+ is already in the extraction or acceleration regions of the TOF, the B^+ ion has initially travelled 'within' the parent ion AB^+ and therefore with a larger m/z (AB^+) till the time of the fragmentation. At the time of the fragmentation, the 'new born' B^+ daughter ion is still subject to the electrostatic field but with a smaller m/z (B^+). It will be instantly accelerated by the field and travel the remaining distance to the detector with higher velocity than the one of AB^+ . The time of flight of this latter ion B^+ will be longer with respect to the one of a B^+ ion produced by prompt fragmentation (green and blue arrows in Figure 3.10).

If the metastable fragmentation with formation of B^+ happens in the drift tube, which is a free flight region, then the time of flight of B^+ will be the same as in AB^+ , and this 'very late' fragmentation does not produce an effect in the mass spectrum.

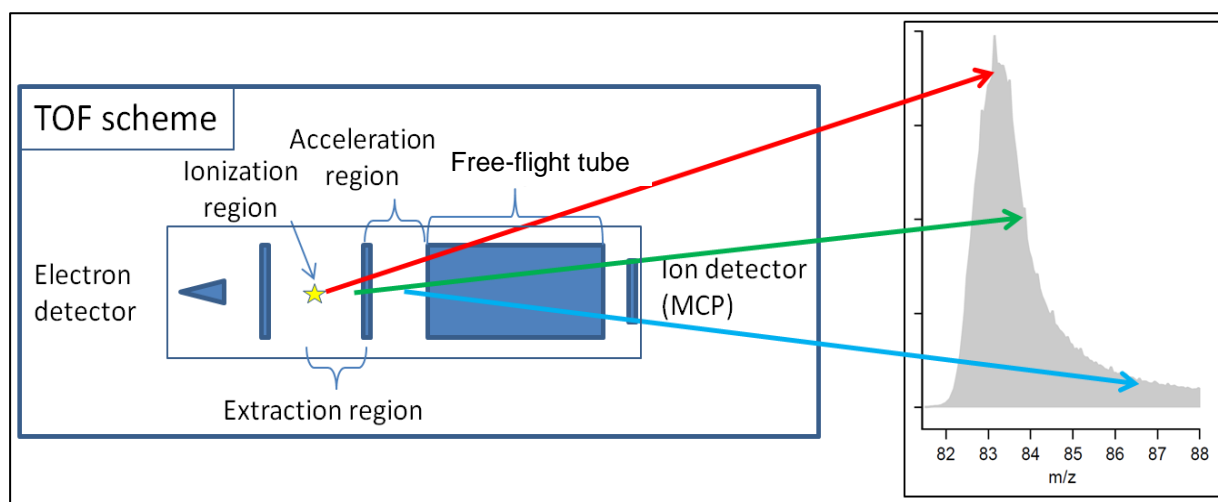


Figure 3.10. Schematic description of TOF apparatus with correlation between position of fragmentation events and relative contribution in the mass spectrum qualitatively indicated by arrows. The longer time of flight of fragments produced in metastable rather than prompt fragmentation is converted in an 'apparent' larger m/z .

The possibility to observe in the mass spectra asymmetric lineshape of fragments due to metastable processes depends on the geometry and operating conditions of the spectrometer, which determine where the parent ion is at the time of release of the daughter ion. The major difference in our experiments is in the use of a pulsed (GasPhase beamline, Figure 3.1) or continuous (CNR-ISM Rome, Figure 3.9 MS-2) extraction of the ions from the interaction region. In the GasPhase beamline apparatus the extraction voltages for the acquisition of the mass spectrum are applied by an external trigger at a rate of 1 kHz, i.e. the ions are extracted every 1 ms for a time duration of 10 μ s. This implies that during the 990 μ s in between two extraction pulses, the ions are continuously created in a free field extraction region. During this long time ('long' with respect to the time scale typical of molecular processes), different processes can happen depending on the time between ion formation and extraction. This will wash out any correlation in the measured time between ionization and fragmentation, as the time 'zero' for the measurement of the flight time is not the ionisation event (undefined) but the time when the extraction voltage is applied. In this

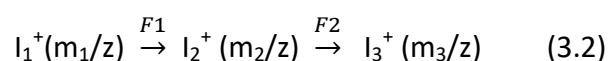
situation, only molecules ionised within ns from the extraction triggering signal produce data containing information on metastable fragmentation. These are the minority of the detected ions and in fact no evidence of metastable fragmentation can be seen in the mass spectra MS-1.

In the CNR-ISM setup in Rome, on the other hand, the extraction voltages are continuously applied, while the trigger for the measurement of the time of flight is given by the detection of an energy unselected photoelectron (see section 2.1.3.2). In this way, the parent ion is extracted immediately at the time of formation and the whole measurement is now sensitive to changes in m/z ratio during the travel in extraction and acceleration regions.

Data analysis of metastable state, setup at the CNR-ISM in Rome

The possibility to determine experimentally the fragmentation rate of the photoionised system relies on the correlation between fragmentation time and ion time of flight, which in turn depends on technical characteristics of the apparatus. For this reason, the SIMION software [104] has been used to model the electric field generated in the TOF spectrometer by the different electrodes and a procedure within the Igor platform has been developed to simulate the fragmentation process. Each 'virtual' experiment takes into account the electric fields calculated by SIMION and runs thousands of ion trajectories through the spectrometer in order to simulate the lineshape to be compared with the experimental one.

The input information for the procedure is the m/z of the involved ions, the energy released in the fragmentation and the fragmentation steps needed to get to the detected fragment. If it can be assumed that only one step is involved, the description is straightforward, while already considering two step fragmentations and therefore three ions involved (equation 3.2),



the scenario becomes unclear. Indeed the metastable fragmentation may occur on both or either one of the two steps, F1 and F2, and the discrimination among the two remains ambiguous.

Therefore, the following analysis is restricted to one-step fragmentation events.

Among the several peaks with asymmetric lineshape in the TOF mass spectra MS-2 of the NI isomers, it has been chosen to simulate the NO-loss process in 2-NI leading to fragment 83^+ in Figure 3.11.

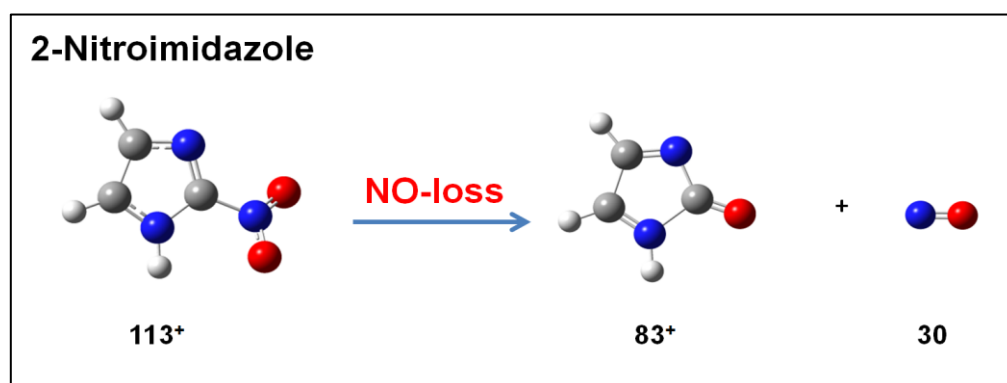


Figure 3.11. Schematic description of NO-loss process in 2-NI.

This choice is motivated by the fact that: i) as discussed in the previous section ion 83^+ in 2-NI is an important fragment, in terms of both intensity and possible medical implications; ii) it has a very prominent asymmetric profile, suggesting that the metastable process has an important contribution; iii) it presents a clear situation of one-step fragmentation, providing well defined inputs for the simulations and iv) it is the first step in several, subsequent fragmentation processes (see section 3.1.4). The analysis of ion 83^+ production in 4(5)-NI is not performed because this fragment is very low in intensity and the results would be affected by large uncertainty.

For sake of simplicity, in the simulation it is assumed that the fragmentation occurs along the axis of the spectrometer. Each one of the simulated ion trajectories for the chosen process requires specific values for several parameters:

i) starting conditions for the parent ion

- initial position: the ionization region is represented by a segment 2 mm long on the axis, centred in the extraction region. Taking into account the shape of the photon beam, at each initial position in the ionization region is attributed a probability according to a Gaussian distribution.
- initial kinetic energy: it follows the Maxwell-Boltzmann probability distribution at a given temperature of the source. The initial direction is assumed to be isotropically distributed, and only the projection along the axis is considered.

ii) time interval, t , between ionisation and fragmentation:

t is chosen according to the distribution of probability reported in equation (3.3)

$$P(t) = \tau \exp(-t/\tau) \quad (3.3)$$

where $\tau = 1/k$ is in the range 1 – 1000 ns. The ion motion in the spectrometer is simulated by an algorithm based on the midpoint method [145,146].

iii) starting condition of the daughter ion

- initial position: it is the parent ion position where the fragmentation happens.
- initial kinetic energy: is the sum of kinetic energy inherited by the daughter ion after fragmentation (according to energy and momentum conservation) and a fraction of the kinetic energy released, KER, in the fragmentation.

For a specific τ value in equation (3.3), the histogram of the time of flight of thousands of simulated ion trajectories produces the lineshape shown in Figure 3.12.

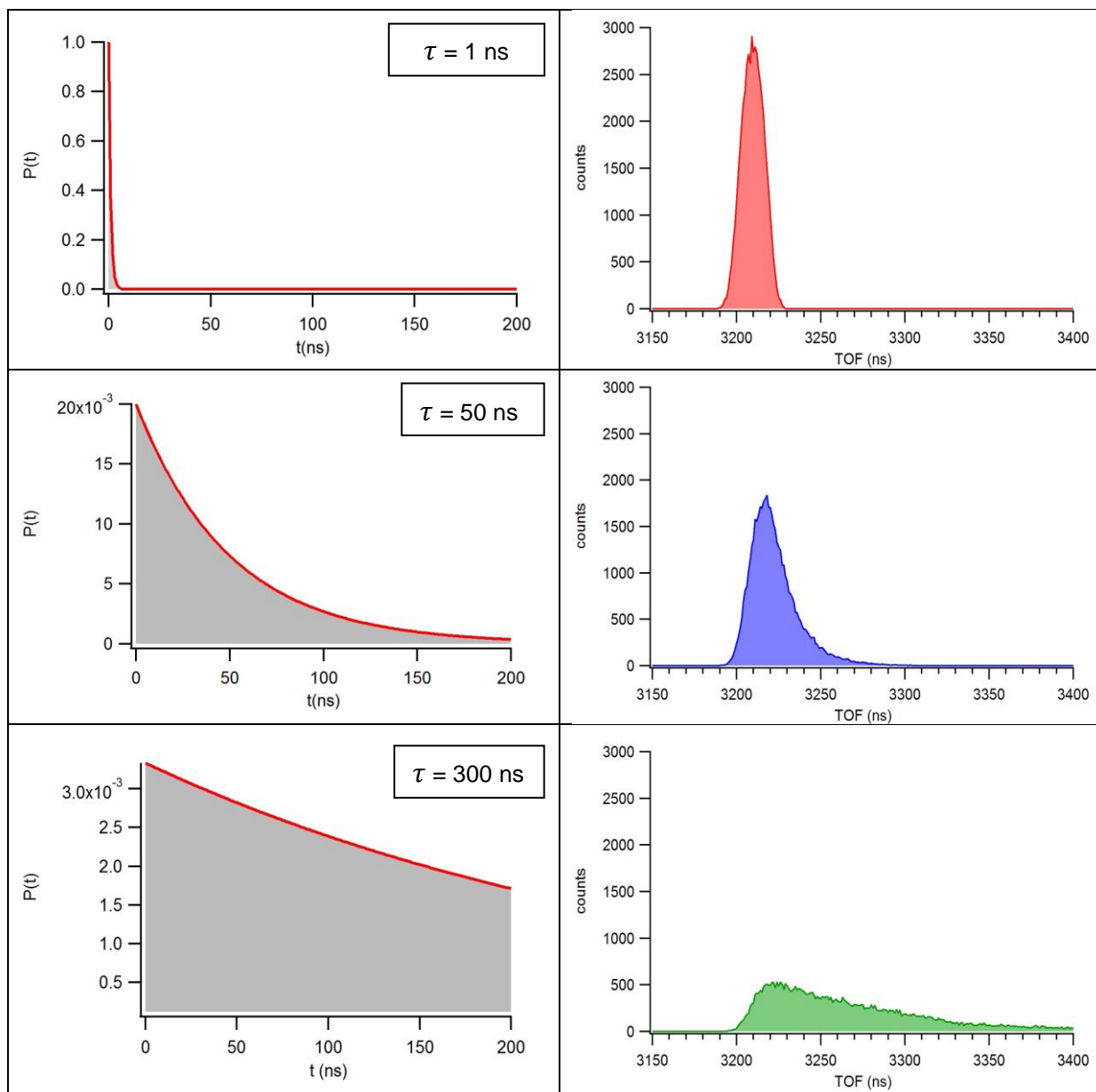


Figure 3.12. Probability distributions (left) and simulated lineshapes (right) for three different τ values: $\tau = 1$ ns (top), $\tau = 50$ ns (middle) and $\tau = 300$ ns (bottom). The results refer to the simulation of the process represented in Figure 3.11, for operating conditions of the spectrometer as illustrated in chapter 2 and a KER of 1 eV used for the simulations.

Analysis of the metastable fragmentation channel NO-loss

In Figure 3.13 the experimental mass spectra of 2-NI measured at different photon energies with the rare gas discharge lamp in the setup at the CNR-ISM in Rome have been reported as normalized to the intensity of the parent ion. It is evident that in all cases the peak at m/z 83^+ has a similar shape.

The simple approach to simulate the experimental line shape of fragment 83^+ using just one fragmentation rate does not provide a good representation. In each panel of Figure 3.14 are reported the experimental data (in grey), the simulated lineshape rescaled to the experimental data (blue spectra) and the simulated lineshape normalized and eventually shifted to overlap with the experimental data at their maximum (orange spectra) for a specific τ value: 1 ns on the left (where blue and orange spectra coincide), 50 ns in the middle and 300 ns on the right.

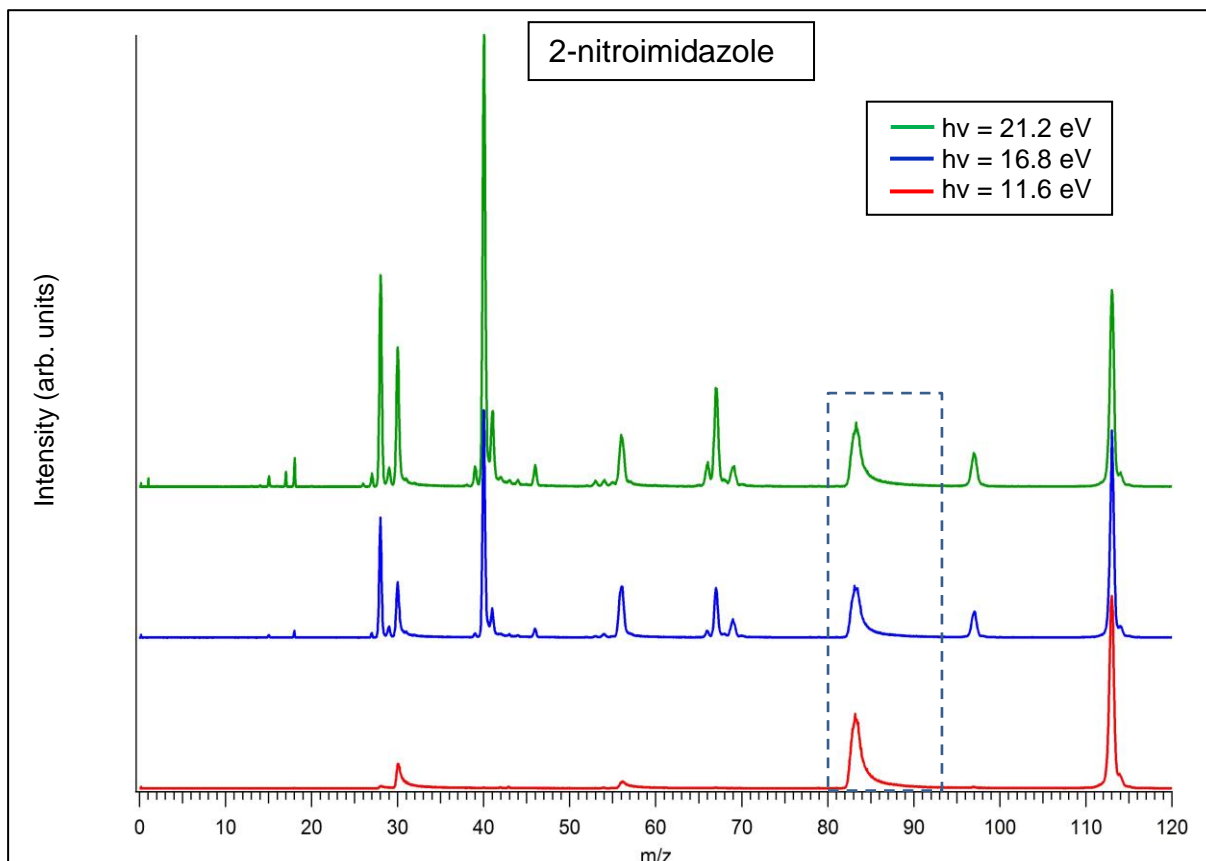


Figure 3.13. Mass spectra of 2-NI measured with the TOF mass spectrometer installed at the CNR-ISM in Rome equipped with a rare gas discharged lamp operated at 21.2 eV (He gas), 16.8 eV (Ne gas) and 11.6 eV (Ar gas) photon energy. Peaks attributed to NO-loss ($m/z 83^+$) discussed in this section are highlighted in a box.

It is clear that the short τ value cannot account for the tail at longer time of flight while increasing τ the simulation does not represent well the sharp component of the experimental lineshape.

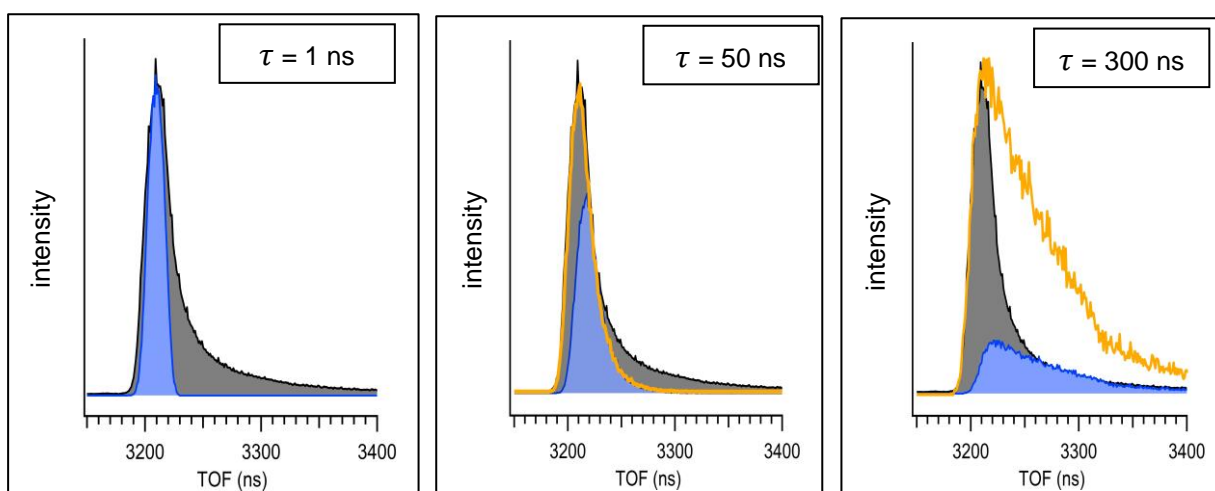


Figure 3.14. Each panel reports the experimental data of the NO-loss process in 2-NI (in grey), the simulated lineshape rescaled to the experimental data (blue spectra) and the simulated lineshape normalized and eventually shifted to overlap with the experimental data at their maximum (orange spectra). Each panel reports simulated lineshape of a specific value of τ : 1 ns on the left (where blue and orange spectra coincide), 50 ns in the middle and 300 ns on the right.

Better results are obtained when a more complex fitting procedure is used, see Figure 3.15.A. This procedure is made by three steps:

- 1) first of all, a database of lineshapes for several fragmentation rates in a wide range ($\tau \approx 1$ -1000 ns) is simulated; for each simulation the same number of ions is used in order to obtain profiles with the same area; in the simulation a kinetic energy released (KER) of 1 eV has been used, as suggested from literature [147];
- 2) a linear combination of the lineshapes from the database with randomly chosen weighting factors is calculated and normalized to the maximum of the experimental peak. The average mean square difference between experimental data and simulated profile is calculated;
- 3) point 2) is repeated several times in a fitting procedure, based on the Levenberg-Marquardt algorithm implemented in the Igor platform [148] where the weighting factors of the linear combination are the parameters and the best linear combination is selected as the one with the minimum value of mean square difference.

In Figure 3.15.B, the set of weighting factors of the lineshapes in the database of step 1 needed to achieve the best fit of the experimental profile of fragment 83^+ in 2-NI are reported. The weighting factors represent the set of τ values, i.e. the typical time ranges of the dynamics, contributing to the fragmentation process in Figure 3.11. Figure 3.15.B shows that τ in three different ranges contribute to the measured lineshape: i) $\tau = 1$ ns that in our case indicates all prompt events, ii) $\tau \approx 30$ -100 ns and iii) τ in the order of several hundreds or thousands of ns, all together providing an excellent reconstruction of the lineshape profile (Figure 3.15.A).

A clearer interpretation of these results is obtained with the support of theoretical calculations of the expected decay rate (see section 2.3.3) for this specific fragmentation channel. Equation (2.39) with parameters reported in Table 3.6 provides a good representation of the theoretical calculation of the $\tau(E_{int})$, reported in in Figure 3.16.

parameter	α	β	χ	γ
value	9.5765 s ⁻¹	4.5417	4.2269 eV	12.199 eV

Table 3.6. Values of parameters α , β , χ and γ in equation (2.39) for NO-loss in 2-NI.

Figure 3.16 shows that the time scale of the fragmentation process strongly depends on the internal energy. It spans more than 4 orders of magnitude over less than 3 eV of E_{int} . To obtain equation 3.2 the thermal equilibrium between parent ion and transition state is assumed. However, as already introduced in section 2.3.3, this hypothesis allows energy exchanges with the external environment that make the reaction possible also if the E_{int} of reactants is lower than the energy barrier ΔE_{TS} (1.37 eV). In an experiment performed in vacuum condition the hypothesis of thermal equilibrium is not verified and values of $\tau(E_{int})$ obtained by theoretical calculation have to be considered as a lower limit.

In order to link the theoretical prediction of the decay rate (Figure 3.16.A) to the experimental determination (Figure 3.15), we need to identify the internal energy range accessed by the experiment. Internal energy of the parent ion can be obtained by the following equation:

$$E_{int} = BE - IE \quad (3.5)$$

where BE is the binding energy of the ionized orbital and IE the adiabatic ionization threshold (9.35 eV for 2-Ni)

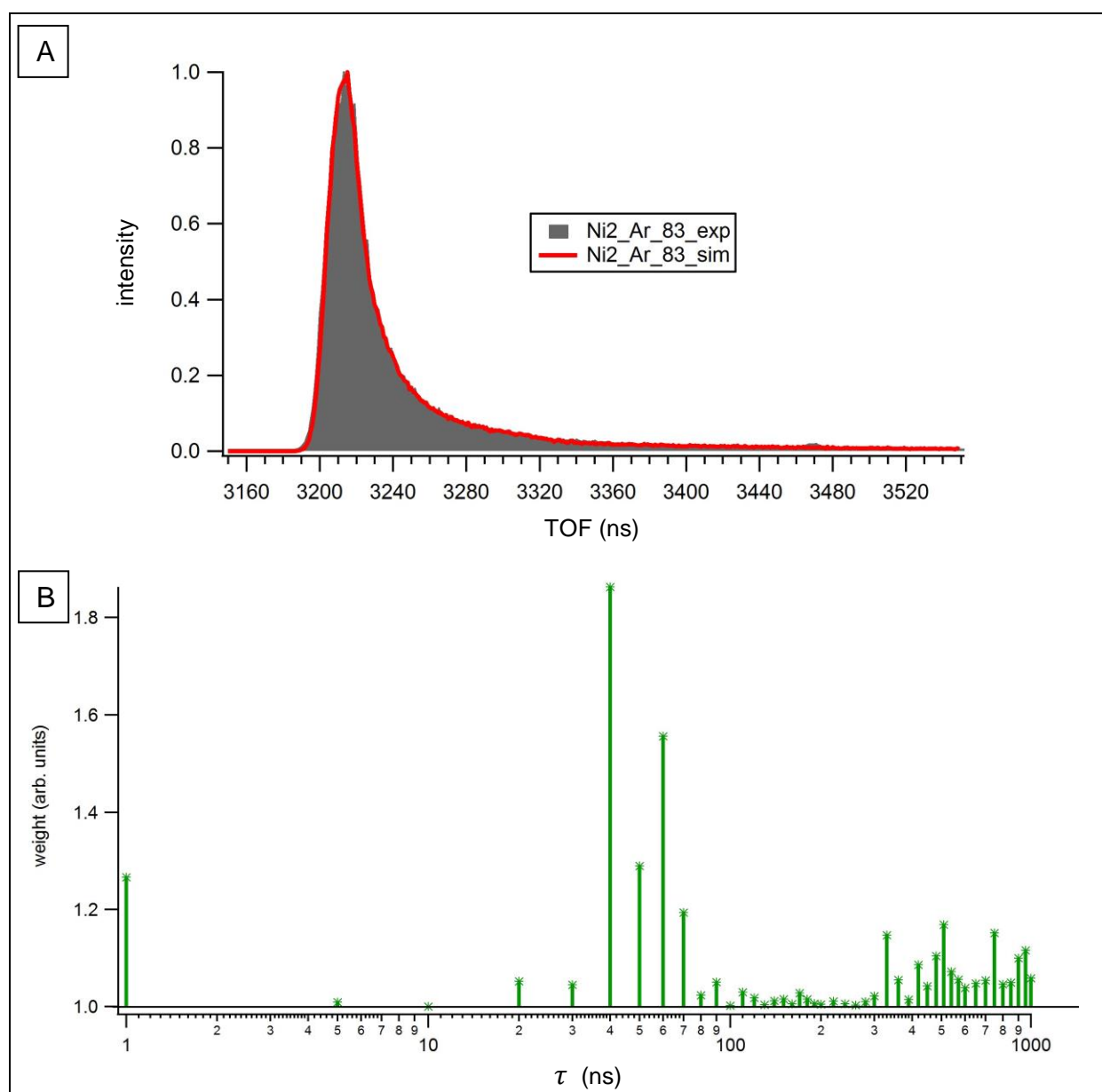


Figure 3.15. **A)** comparison between experimental data (in grey) and lineshape obtained by simulations and fitting procedure (in red). **B)** Weighting factors used to combine simulated lineshapes of each τ value and obtain the total simulated lineshape reported in red in the panel A.

The limit of the present experimental technique is that, detecting kinetic energy unresolved photoelectrons (see experimental section 2.2.3.2), the exact amount of internal energy deposited in the system is unknown, however a range of parent ion internal energies can be identified (Figure 3.16.B). The lower limit of E_{int} able to produce fragment 83^+ is determined by the appearance energy of this fragment ($AE(83^+) = 10.6$ eV), and is indicated as blue lines in Figure 3.16.A and B. The upper limit is in principle related to the photon energy, $h\nu$. However, according to the branching ratio plot shown in Figure 3.3 only internal energies up to 12.2 eV, green lines in Figure 3.16.A and B, can produce fragment 83^+ . Therefore, we can

restrict the range of experimentally accessible internal energies to 1.25 – 2.85 eV, and this is expected to be photon energy independent at $h\nu > 12.2$ eV.

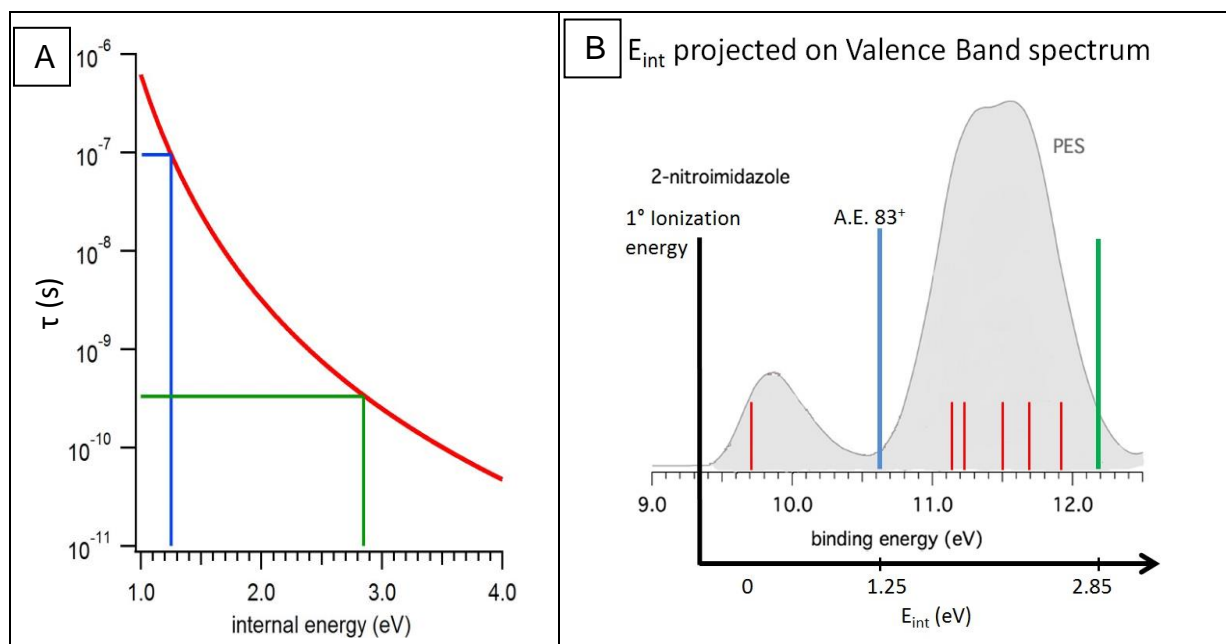


Figure 3.16. A) Theoretical calculation of τ , inverse of the fragmentation rate obtained by equation 3.4. The lowest (blue lines) and highest (green line) values of possibly available internal energy in the experiment and respective values of τ are indicated. **B)** Projection of internal energy axis on valence band spectrum. 1st ionization energy (black line), AE(83⁺) (blue line), highest value of E_{int} to produce ion 83⁺ (green line) and energy position of molecular orbital (Table 3.3) (red lines) are reported.

Within this range of E_{int} , the theoretically predicted values of τ are 0.5-100 ns; considering that it is a lower limit, the theoretical results are consistent with the experimental determination in Figure 3.15. Considering both theoretical and experimental information we can recognize two different types of fragmentation processes:

i) The ‘fast’ processes ($\tau < \text{few ns}$) occur when larger amount of internal energy are available and are therefore related to more excited electronic states. As already mentioned, the fitting procedure and the setup itself are unable to discriminate the details of fast processes. Therefore, the component at 1 ns has to be considered as a range representative of prompt fragmentation.

ii) The ‘slow’ processes ($\tau \approx 10^2\text{-}10^3$ ns) are related to electronic states with less amounts of internal energy. In the range of tens to a few hundreds of ns there is agreement between theory and experiments, consistently indicating the existence of metastable processes in this time domain. Extending in the range of a several hundreds of ns, the experimental observation is not fully able to discriminate among different τ values, because lineshapes are very similar among themselves and extend over a long range in the region of low counts of the experimental data. Therefore, the results from the fitting procedure indicate that also some ‘very slow’ fragmentation processes (τ several 10^2 to 10^3 ns) are present, even though it is not possible to be more specific.

The not homogeneous distribution of τ in the experimental analysis appears to be not consistent with the smoothly varying distribution of the theoretical calculations (Figure

3.15). This could be attributed to several reasons. A possible explanation is the inability to precisely determine, by the present simulations, the τ values in the 'fast' and very 'slow ranges', which could have led to a non-unique solution of the fitting. Another possible explanation, more interesting from the physical chemical point of view, is related to the possible different fragmentation decay rates of the different electronic states under the same photoelectron band that originates fragment 83^+ ; these different electronic states are not considered in the theory and fragmentation is always assumed from the parent ion in the ground state.

The observation that the lineshape of fragment m/z 83^+ does not depend on the photon energy (spectra measured with He, Ne and Ar) is consistent with this description and with the PEPICO spectra showing how fragment 83^+ is extremely state-selective and can only be generated by specific molecular orbitals in the internal energy range which is almost completely accessible already at the photon energy of the Ar gas in the discharge lamp.

After a detailed description of the NO-loss and formation of ion 83^+ , an overall analysis of all main fragments and their relation with metastable fragmentations by the analysis of peak lineshape can be proposed. The spectra of 2-NI (Figure 3.13) and 4(5)-NI (Figure 3.17) obtained at the different photon energies of the rare gas discharge lamp show that the different peaks display specific behaviour with photon energy: i) symmetric peaks due to prompt fragmentations, with an intensity that decreases with photon energy, ii) asymmetric peaks due to metastable fragmentation, with an evolution of intensity and/or lineshape while iii) other peaks with no variation with photon energy.

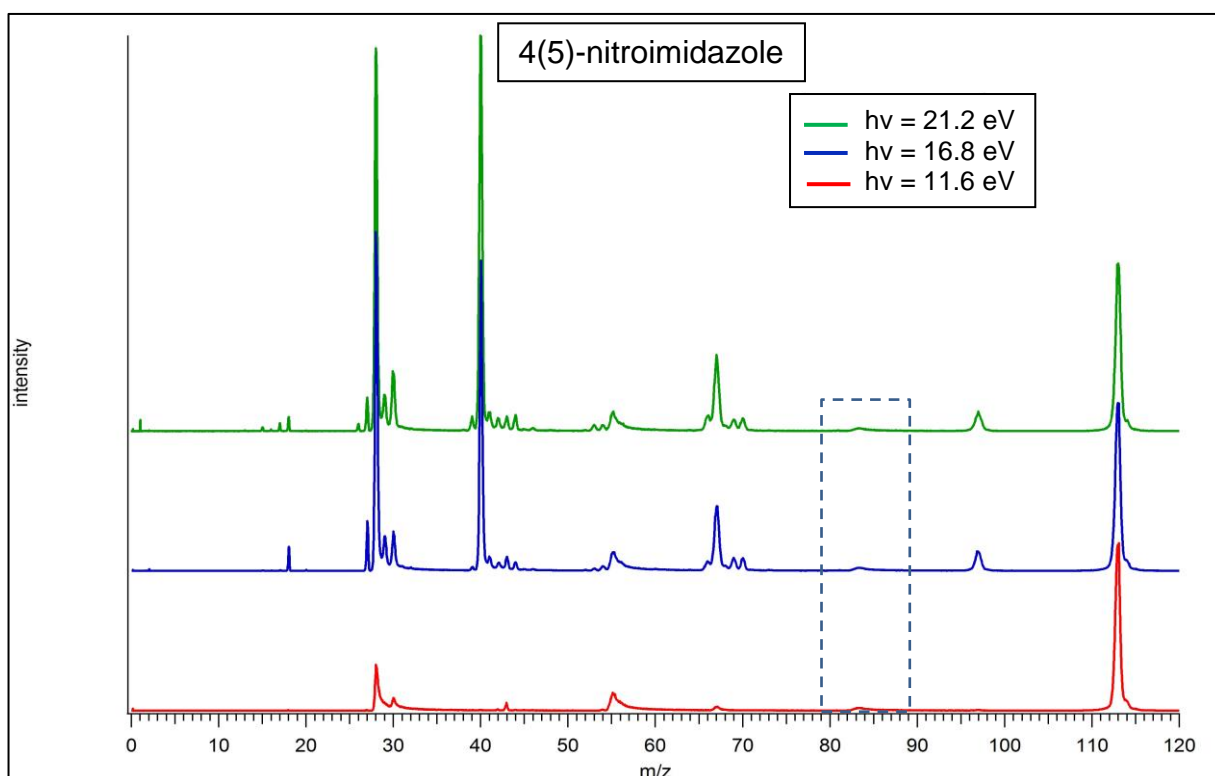


Figure 3.17. Mass spectra of 4(5)-NI measured with the TOF mass spectrometer installed at the CNR-ISM in Rome equipped with a rare gas discharged lamp operated at 21.2 eV (He gas), 16.8 eV (Ne gas) and 11.6 eV (Ar gas) photon energy. Peaks attributed to NO-loss (m/z 83^+) are highlighted in a box.

These trends can be better appreciated in Figure 3.18 and Figure 3.19 where a zoom of some 2-NI and 4(5)-NI fragments, respectively, is shown (in some cases the intensity is adjusted to

highlight the lineshape). Despite differences in intensity, peaks at the same m/z have a similar behaviour in all NI isomers:

i) peaks of ions 97^+ , 67^+ and 40^+ have a symmetric lineshape, or at least the symmetric component is always the dominant one. The intensity decreases or remains constant from 21.2 eV (He lamp) to 16.8 eV (Ne lamp) but drops to zero in the spectrum measured with the Ar lamp, because the 11.6 eV photon energy emitted by the Ar lamp is below the AE of all of these fragments. This is consistent with the observation that the formation of these ions is not correlated with ion 83^+ .

ii) peaks of ions 30^+ , 28^+ and 56^+ (56^+ only in 2-NI) are the combination of symmetric (prompt) and asymmetric (metastable) components. As it can be seen in panels B and D of Figure 3.18 and Figure 3.19, only the prompt component decreases with photon energy while the metastable one remains almost constant. As demonstrated by PEPICO measurements, these fragments can be produced in a wide range of the binding energy (Figure 3.3) and by different mechanisms, including (but not exclusively) the formation and decomposition of fragment 83^+ (specific of the second band in the PES spectrum). We therefore propose that the metastable component in the lineshape of all of these fragments is related to the formation and decomposition of 83^+ and its complementary fragment 30^+ .

iii) ions 83^+ and 55^+ (55^+ only in 4(5)-NI) have the same shape and relative intensity at all the investigated photon energies; according to the branching ratio spectra (Figure 3.3) their production is state-selective, correlating to the ionization of the second band in the PES spectrum. Indeed, according to Figure 3.4, ion 55^+ in 4(5)-NI is the second step in the fragmentation of ion 83^+ and for this reason it follows the same dynamics.

All peaks with an asymmetric lineshape are attributed to fragments that are correlated to the formation and decomposition of ion 83^+ by photoionization of the second band in the PES spectrum (11-12 eV in BE). It is reasonable to assume that all fragments generated as second fragmentation step of ion 83^+ , inherit the asymmetric lineshape from the first step.

Therefore, an overall model of metastable fragmentation in NI isomers can be proposed.

In the mass spectrum taken with the Ar gas in the discharge lamp all fragments directly (83^+ , 30^+) or indirectly (28^+ , 55^+ , 56^+) related to the NO-loss have a dominant metastable component because the photon energy (11.6 eV) is close to the energy barrier characteristic of this process (11-12 eV). The photon energy with Ne and He gases in the discharge lamp is well above all energy barriers by several eV and prompt processes dominate the spectra. The change of the ratio between fast and slow fragmentations is possible only for ions that can be formed over a wide region of valence band like ions 28^+ , 30^+ and 56^+ (Figure 3.3). Viceversa, fragmentation processes occurring only in a narrow range of the valence band, leading to formation of ion 55^+ and 83^+ , cannot be produced by the parent ion with high internal energy not even if higher photon energy is used. This scenario is supported by the agreement between the fragmentation rates calculated by theory and the simulation. Metastable fragmentations could be attributed to specific characteristics of the NO-loss process, like the molecular rearrangement of the nitro group that involves heavy atoms. Indeed the same theoretical calculation performed for the NO_2 -loss fragmentation path giving the ion 67^+ produces the maximum value for the estimated τ of the order of few ns. This is consistent with the symmetric lineshape observed for this fragment.

2-nitroimidazole

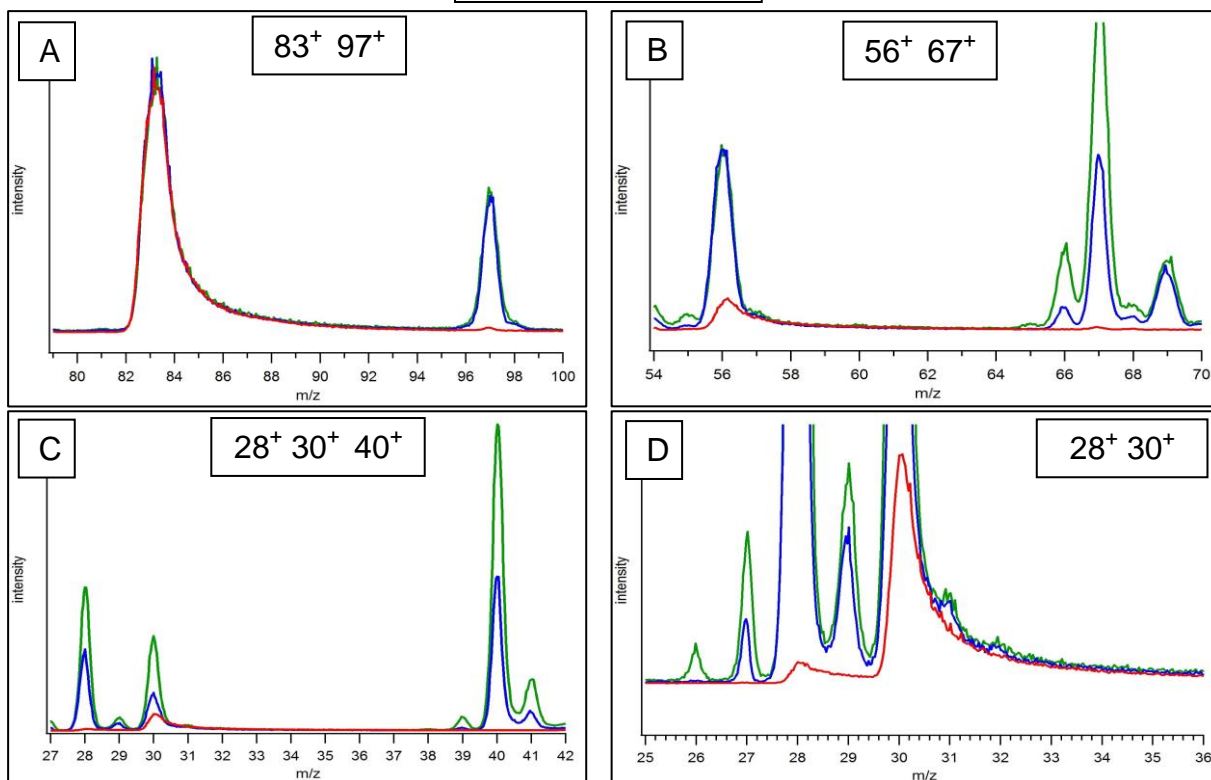


Figure 3.18. Zoom of different regions of the mass spectra of 2-NI obtained with the TOF mass spectrometer installed at the CNR-ISM in Rome with the rare gas discharged lamp operated at 21.2 eV (He gas, green), 16.8 eV (Ne gas, blue) and 11.6 eV (Ar gas, red) photon energy. A) ions 83^+ and 97^+ (the spectra are renormalized to highlight that the lineshape of ion 83^+ is independent of photon energy), B) ions 56^+ and 67^+ , C) ions 28^+ , 30^+ and 40^+ , D) ions 28^+ and 30^+ .

4(5)-nitroimidazole

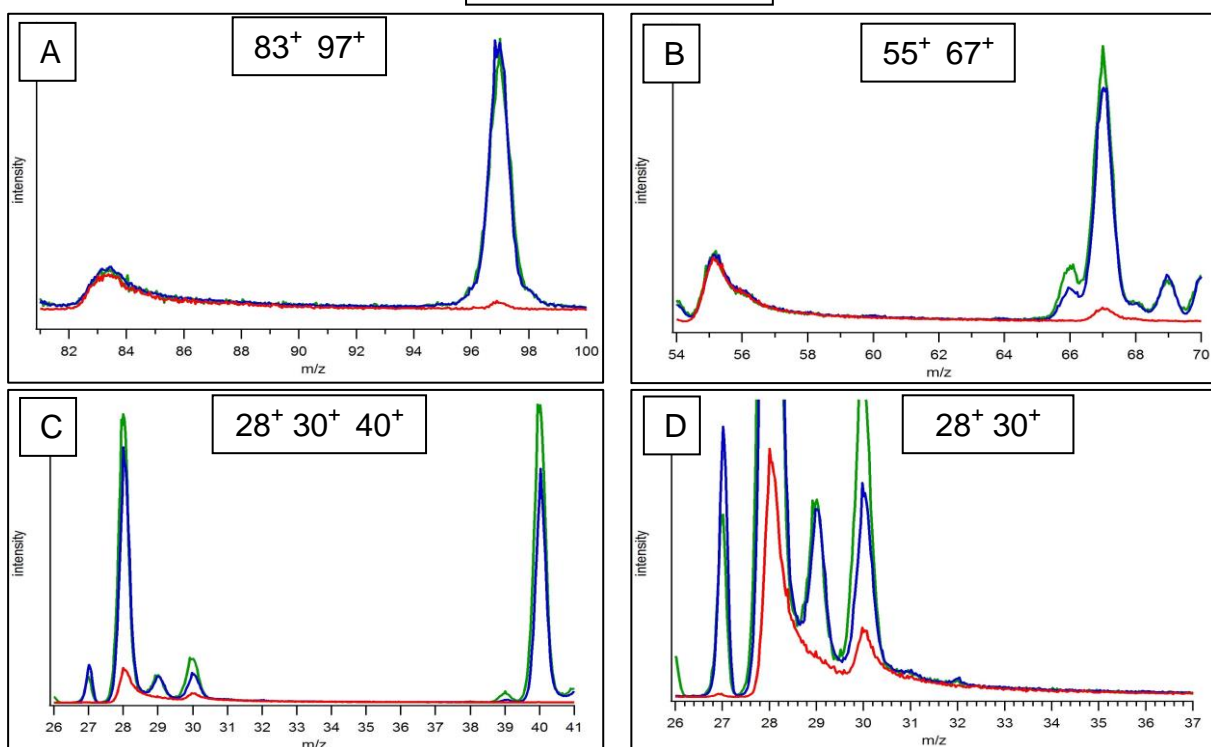


Figure 3.19. Zoom of different regions of the mass spectra of 4(5)-NI obtained with the TOF mass spectrometer installed at the CNR-ISM in Rome with the rare gas discharged lamp operated at 21.2 eV (He gas, green), 16.8 eV (Ne gas, blue) and 11.6 eV (Ar gas, red) photon energy. A) ions 83^+ and 97^+ , B) ions 55^+ and 67^+ , C) ions 28^+ , 30^+ and 40^+ , D) ions 28^+ and 30^+ .

3.2 From model systems to real drugs : misonidazole and metronidazole

In section 3.1 the identified differences in the photofragmentation mechanisms of 2-NI and 4(5)-NI have been considered to be relevant to justify the different efficacy of the radiosensitisers built on these isomers. In this section we would like to test the idea that the results from the model systems (that can be handled easily both from the experimental and theoretical point of view) can be extended to understand the properties of the more complex (and difficult to treat) molecules used as radiosensitisers in medical trials, metronidazole (METRO) and misonidazole (MISO), see Table 3.7 [26,30,130]. Metronidazole (IUPAC name: 2-(2-methyl-5-nitro-1H-imidazol-1-yl) ethanol) is built on 5-NI structure, with a $\text{CH}_2\text{CH}_2\text{OH}$ chain (T1) bound to N1 and a methyl group to C2. Misonidazole (IUPAC name: (RS)-1-methoxy-3-(2-nitroimidazol-1-yl)propan-2-ol) is built on 2-NI structure, with the longer chain $\text{CH}_2\text{CHOHCH}_2\text{OCH}_3$ (T2) bound to N1.

To study metronidazole and misonidazole we have used the same experimental (TOF-MS, PEPICO and AE) and theoretical (AE_{th}) approaches adopted for imidazole and nitroimidazole isomers. The samples, which are in the form of powder at ambient temperature and pressure conditions, have been purchased from Sigma-Aldrich (METRO) and Vinci-Biochem srl (MISO), with a purity of 95% and desorbed in the gas phase by thermal evaporation ($T \approx 150^\circ\text{C}$ is required for both molecules)

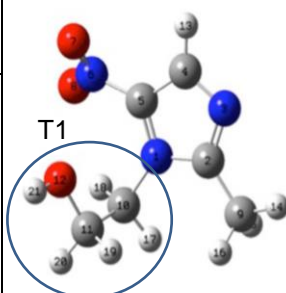
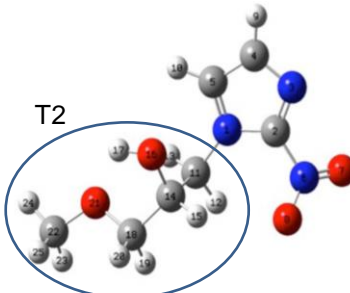
Name of compound	Chemical formula	Mass (Da)	Molecular structure
misonidazole	$\text{C}_7\text{H}_{11}\text{N}_3\text{O}_4$	201	<div style="display: flex; justify-content: space-around;"> <div style="text-align: center;"> <p>Metronidazole</p>  </div> <div style="text-align: center;"> <p>Misonidazole</p>  </div> </div>
metronidazole	$\text{C}_6\text{H}_9\text{N}_3\text{O}_3$	171	

Table 3.7. Chemical formula, mass and molecular structure for misonidazole and metronidazole. In the molecular structure the labelling of each atom and tails T1 and T2 are indicated.

3.2.1 The TOF mass spectra

The TOF mass spectra obtained at the GasPhase beamline of Elettra synchrotron with photon energy of 60 eV are reported in Figure 3.20. The increased complexity and fragility of the samples are immediately reflected in the formation of a large amount of fragments. The assignment of the main fragments is reported in Table 3.8. The parent ion is observed in both molecules, but with more intensity in METRO than in MISO, suggesting a higher fragility of the latter. However, while the spectrum of MISO is dominated by only two fragments (m/z 155⁺ and 45⁺), in METRO there is a large variety of fragments of similar intensity, indicating that many more fragmentation channels are active. Considering Figure 3.20 and Table 3.8, we see that MISO fragmentation is dominated by the loss of neutral NO_2 (m/z

155⁺) and part of the charged T2 chain (m/z 45⁺), and in both cases the imidazole ring is preserved (as confirmed by theory in section 3.2.4). It is likely that the long T2 chain in MISO provides an efficient channel to dissipate the excess energy due to the photoionisation, giving a higher stability to the ring in MISO with respect to METRO. At variance with the nitroimidazoles case, the NO-loss channels (expected at m/z 30⁺ or 141⁺ for METRO and 30⁺ or 171⁺ for MISO) are almost completely absent in the mass spectra and considered unlikely channels also from the theoretical point of view (see section 3.2.4).

In both the MISO and METRO spectra, the fragments attributed to the NO₂-loss, HONO-loss and production of m/z 45⁺ are among the main fragments; in METRO also fragments at m/z 81⁺ and 54⁺ are very intense. We therefore concentrated the theoretical investigation on the formation of these fragments.

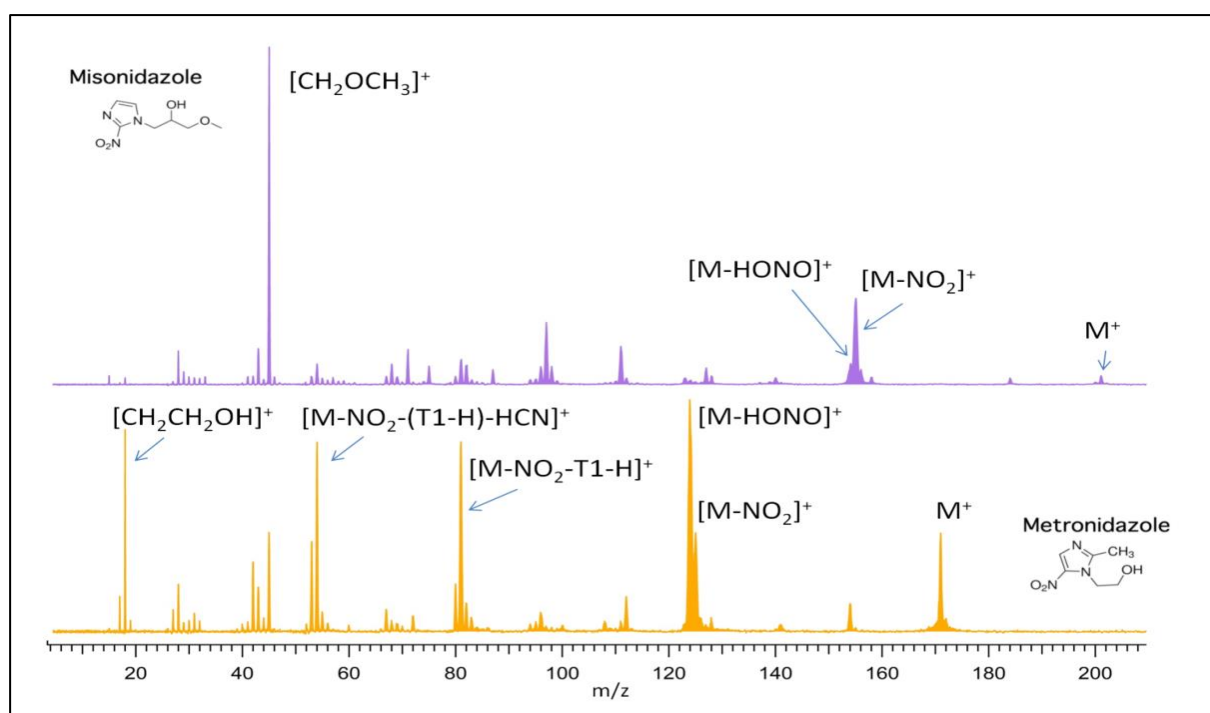


Figure 3.20 Mass spectra of MISO (violet) and METRO (orange) measured at 60 eV photon energy. The most relevant fragments for the present discussion are indicated by their respective assignments while “M” indicates in each case the relative intact molecule.

MISO		METRO	
m/z	fragment	m/z	fragment
201	M ⁺	171	M ⁺
184*	[M-OH] ⁺	154 *	[M-OH] ⁺
156*	[M-H ₃ COCH ₂] ⁺	126 *	[M-T1] ⁺
155	[M-NO ₂] ⁺	125	[M-NO ₂] ⁺
154	[M-HONO] ⁺	124	[M-HONO] ⁺
111*	[M-T2-H] ⁺	112*	[M-T1-CH ₃] ⁺
97*	[M-T2-O+H] ⁺	81	[M-NO ₂ -(T1-H)] ⁺
45	H ₃ COCH ₂ ⁺	54	[M-NO ₂ -(T1-H)-HCN] ⁺
		45	CH ₂ CH ₂ OH ⁺ (T1)

Table 3.8. Assignment of the main peaks observed in the TOF mass spectra of MISO and METRO reported in Figure 3.18 in agreement with literature ([131,149] for MISO and [131,150] for METRO). Assignments indicated by * are proposed in this thesis with the qualitative criteria of minimizing the number of atomic bonds breakings to produce the fragment.

3.2.2 The branching ratio from the PEPICO measurements

In Figure 3.21 the PEPICO branching ratios of the main fragments and the PES spectra of MISO and METRO are reported.

In MISO the onset of most of the fragments is in correspondence of the two lower bands of the PES. The PEPICO branching ratios of the different fragments define three regions in the PES spectrum. The majority of fragments are produced exclusively by ionization of valence states in the energy 9 - 12 eV (first region). Several fragments, as for example m/z 155⁺ and 154⁺, can already be produced close to the ionization threshold, i.e. in the HOMO state. This explains the low intensity of the parent ion observed in the mass spectrum. In the BE range 12 – 18 eV (second region) two competing channels, leading to m/z 45⁺ and 97⁺ are observed, while the states at BE > 18 eV (third region) mainly see the formation of ion 45⁺.

In METRO the PEPICO branching ratios of fragments vs binding energy are generally broader than in MISO and the fragmentation channels producing smaller fragments are gradually opened for increasing binding energy. Only the parent ion is formed at the HOMO band of PES and all fragmentation paths open at least 1 eV above the ionization threshold. Other fragments (154⁺, 124⁺ and 112⁺) are preferentially produced by ionization of the second band of the PES spectrum and smaller fragments, e.g. ions 45⁺, 54⁺ and 81⁺, have the onset at BE > 13 eV.

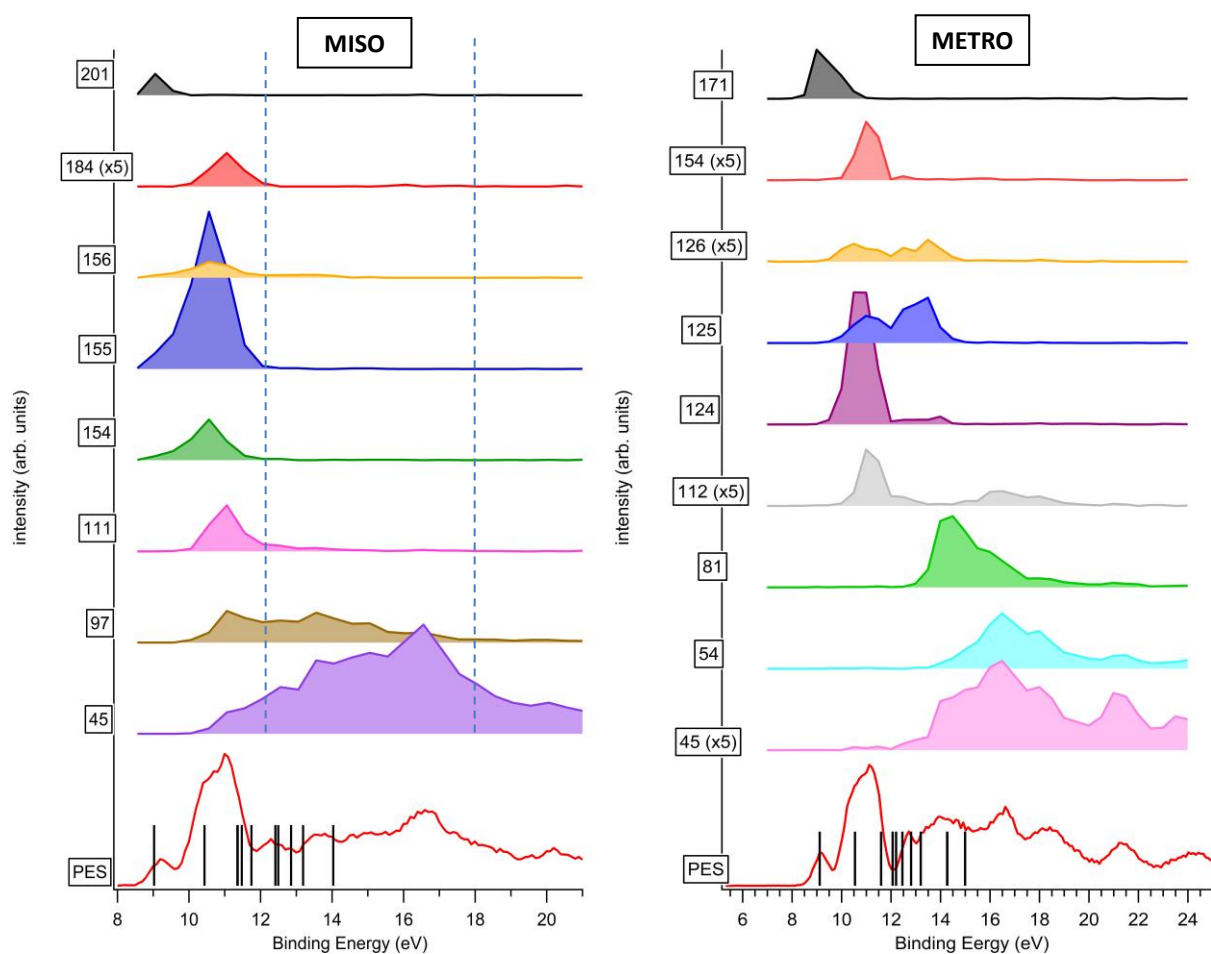


Figure 3.21 PES and PEPICO spectra for the main fragments of MISO (left) and METRO (right); spectra related to less intense fragments have been multiply by a factor 5 as indicated in the label. In the PES spectra also the theoretical position of the lower molecular orbitals obtained from literature [151] are reported as black sticks. In MISO spectra the three regions described in the text are indicated by dashed lines.

3.2.3 Appearance energy measurements

The experimental values and the theoretical predictions of AE for the main fragments produced by the photoionisation of the METRO and MISO molecules are reported in Table 3.9. A good agreement between theory and experiment is obtained, although the theoretical values are in general higher than the experimental ones, but for fragment 45⁺ in METRO. The AE extrapolated from the PEPICO branching ratio curves, although characterised by a lower precision (0.5-1 eV uncertainty), are in agreement with the AE and reinforce the reliability of results.

As already observed from the mass spectra, also the AE values suggest that MISO is more fragile than METRO, with several fragmentation channels opened already at few hundreds of meV above the IE. On the contrary, in METRO the fragments have AE values at least 0.5 eV higher than the IE and smaller fragments (81⁺, 54⁺ and 45⁺) have AE values between 12 and 13 eV.

MISO				METRO			
m/z	AE _{th} (eV)	AE _{exp} (eV)	AE PEPICO (eV)	m/z	AE _{th} (eV)	AE _{exp} (eV)	AE PEPICO (eV)
201	8.77	8.55 ± 0.03	8.5 - 9	171	8.6	8.57 ± 0.05	8 - 9
184			9.5 - 10.5	154			9.5-10.5
156	9.74		9- 10	126			9- 10
155	9.1	8.9 ± 0.04	8.5 - 9.5	125	9.59	9.33 ± 0.07	9 - 10
154		8.91 ± 0.04	8.5 - 9.5	124		9.14 ± 0.1	9 - 10
111			10-10.5	112			9.5-10.5
97			10-11	81		12.22 ± 0.1	12.5- 13.5
45	10.4	10.2 ± 0.1	10 - 11	54	13.55	13.42 ± 0.1	13.0 - 14
				45	11.34	12.09 ± 0.1	11 - 12.5

Table 3.9. Theoretical and experimental AE's for the main fragmentation channels of MISO and METRO; for the parent ions, AE_{th} is the IE. The AE values extrapolated from PEPICO spectra as first onset of the respective ion signal are also reported.

3.2.4 Discussion of experimental and theoretical data

The discussion and interpretation of the mass spectrometry results is guided by the study of the theoretical potential energy profiles. A preliminary consideration for the theoretical investigation concerns the molecular structure of these molecules. Differently from NI, where only a relatively simple group (NO₂) is attached to the imidazole ring, in METRO and MISO the longer T1 and T2 chains have many rotational degrees of freedom leading to a large number of stable conformers, very close in energy. Several of these conformers can already be populated at room temperature. The initial conformation of the molecule can influence the fragmentation path, the calculated transition states and the energy barriers that determine a dissociation path. Thus, a preliminary step in the theoretical modelling has been the identification of the most stable conformer. This is the only one included in the calculation of the potential energy surfaces.

In the following, the fragmentation paths due to NO₂-loss and leading to ion 45⁺ are considered for both METRO and MISO molecules, while fragmentation paths leading to ions 81⁺ and 54⁺ are discussed only for METRO.

In Figure 3.22 - Figure 3.24, to simplify the representation of paths on the potential energy surfaces, only the main transition states and the initial and final optimized geometries have been reported together with the relevant energies referred to the calculated IE.

The NO₂-loss fragmentation channel

Figure 3.22 reports the NO₂-loss fragmentation path for formation of ion 155⁺ for MISO (left panel) and 125⁺ for METRO (right panel)

In MISO the NO₂ group bound to C2 is removed and, by two different transition states, replaced by a H atom from C11 with a total energy barrier of 0.33 eV.

In METRO, instead, an energy barrier of about 1 eV without any transition state has to be overcome to release NO₂, causing the rearrangement of the residual ion in a bi-cyclic structure by the formation of a bond between C5 (previously bonded with NO₂) and O12 on the T1 chain.

In both samples, the theoretical and experimental AE values are in agreement (Table 3.9) indicating a more energetically expensive rearrangement of the T1 chain in METRO leading to the NO₂ loss. In both cases, the theoretical calculations do not observe any path leading to the isomerisation of the NO₂ group and the following NO loss, the main process observed in the 2-NI and 4(5)-NI. This is consistent with the experimental observation, and represents one of the major differences with respect to the model system. However, also the release of NO₂, an important source of radical species [24], could be related to radiosensitising mechanisms.

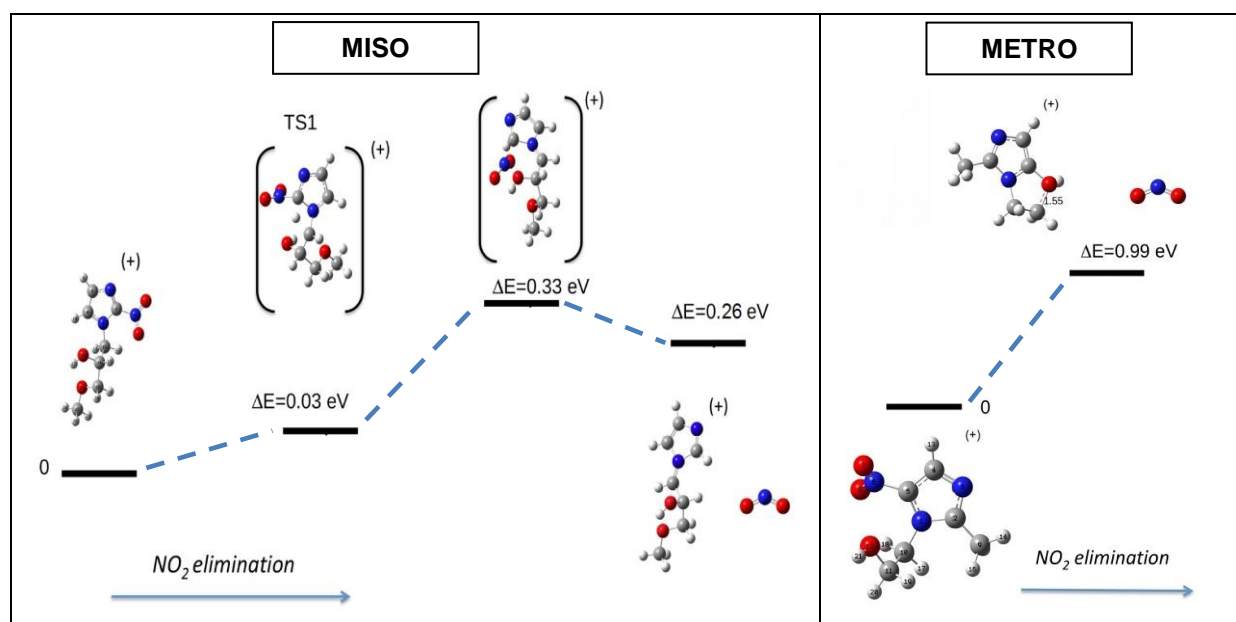


Figure 3.22 Potential energy paths for NO₂ elimination and production of ion 155⁺ in MISO (left panel) and 125⁺ in METRO (right panel). The ion's structures before fragmentation, after fragmentation and at transition state are also reported. Energies of each considered state with respect to the energy of the parent ion are indicated.

The 'tail-loss' fragmentation channel and formation of fragment m/z 45⁺

The fragmentation mechanism involving the release of the entire or of a fraction of the tail, either T1 in METRO or T2 in MISO, is considered as the main source for fragment m/z 45⁺ (Figure 3.23).

In METRO (Figure 3.23, right panel), this fragment is attributed to the entire charged chain T1 (CH₂CH₂OH). Dissociation occurs by breakage of the C10-N1 bond, overcoming an energy

barrier of 2.74 eV. The complementary fragment to 45^+ ($T1^+$) is 126^+ ($[M-T1]^+$), corresponding to a similar bond breaking, but with residual charge remaining on the ring moiety. This complementary channel has not been investigated theoretically. However, from the PEPICO branching ratios (Figure 3.21 and Table 3.9) it appears to have a smaller AE value, even though its intensity is significantly lower than the one of the $T1^+$ channel, probably due to the difficulty for such a large fragment to survive as an intact unit.

In MISO (Figure 3.23, left panel), two different paths leading to the formation of fragments 45^+ (part of T2, assigned to CH_3OCH_2) or 156^+ ($C_5H_6N_3O_3$) are described. Similarly to the previous case (45^+ and 126^+ in METRO) these are two complementary fragments, corresponding to a similar bond breakage, but differing by the charged/neutral moiety and their corresponding structures. The path with the lower barrier (1 eV) leaves the charge on the ring moiety, m/z 156^+ , while the formation of m/z 45^+ requires the overtaking of an energy barrier of about 1.63 eV. These barriers produce AEs of 10.4 eV for ion 45^+ and 9.74 eV for ion 156^+ , in agreement with the experimental determinations of AE. It is interesting to note that, in MISO as well as in METRO, the fragmentation path involving the tail-loss mechanism is characterised by higher energy, but larger probability when the charge is on the tail part.

Comparing Figure 3.22 and Figure 3.23, it can be noticed how, among the loss of the NO_2 and a group with mass 45, the former is energetically favoured in both molecules.

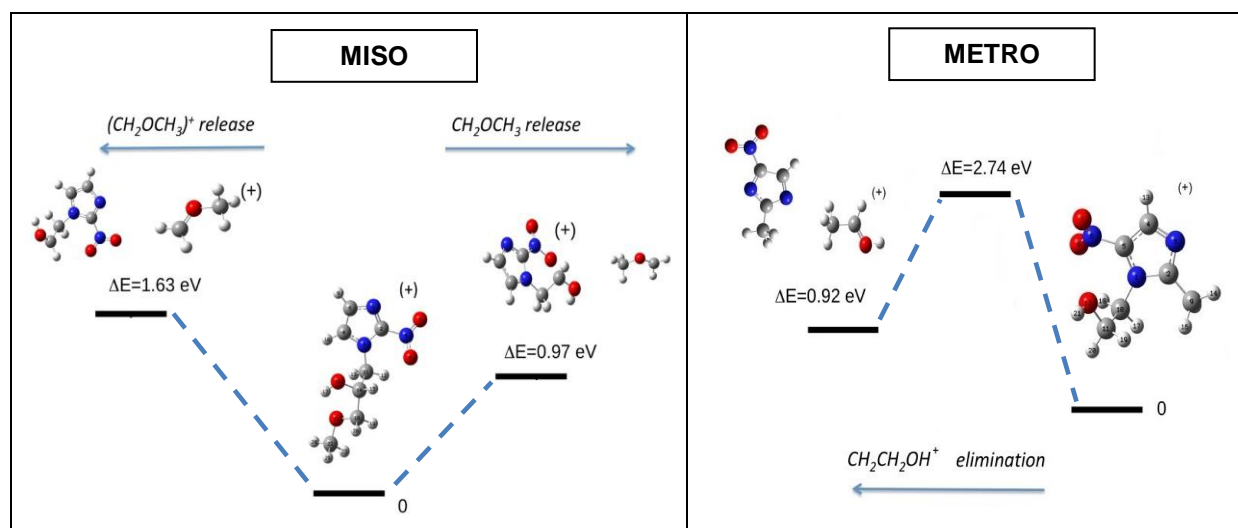


Figure 3.23 Potential energy paths for CH_2OCH_3 elimination as charged specie for METRO (right panel) and both neutral or charged specie for MISO (left panel). The ion's structures before and after fragmentation and the energy of each considered state with respect to the energy of the parent ion are also reported.

Breaking of imidazole ring in METRO: formation of ions 81^+ and 54^+

For the case of METRO, also the fragments m/z 81^+ and 54^+ , very intense in the mass spectra, have been analysed. Ion 81^+ is due to the successive losses of NO_2 (leading to ion 125^+ , already discussed in the previous section) and of CH_2CHOH (Figure 3.24). Its formation has required a molecular rearrangement with breakage of the double ring and H migration toward the aromatic ring, to either C5 or N1 (see initial structures in Figure 3.24.A and B, respectively). In our calculated paths of formation of 54^+ , these 81^+ structures are considered the starting points, as both these configurations can further evolve, by breaking C2 - N1 bond, producing fragment ion 54^+ and neutral HCN. This is a complex path, requiring several molecular rearrangements and the complete fragmentation is achieved by

overcoming quite high energy barriers (> 4 eV), consistently with the high experimental AE value of 13.42 eV.

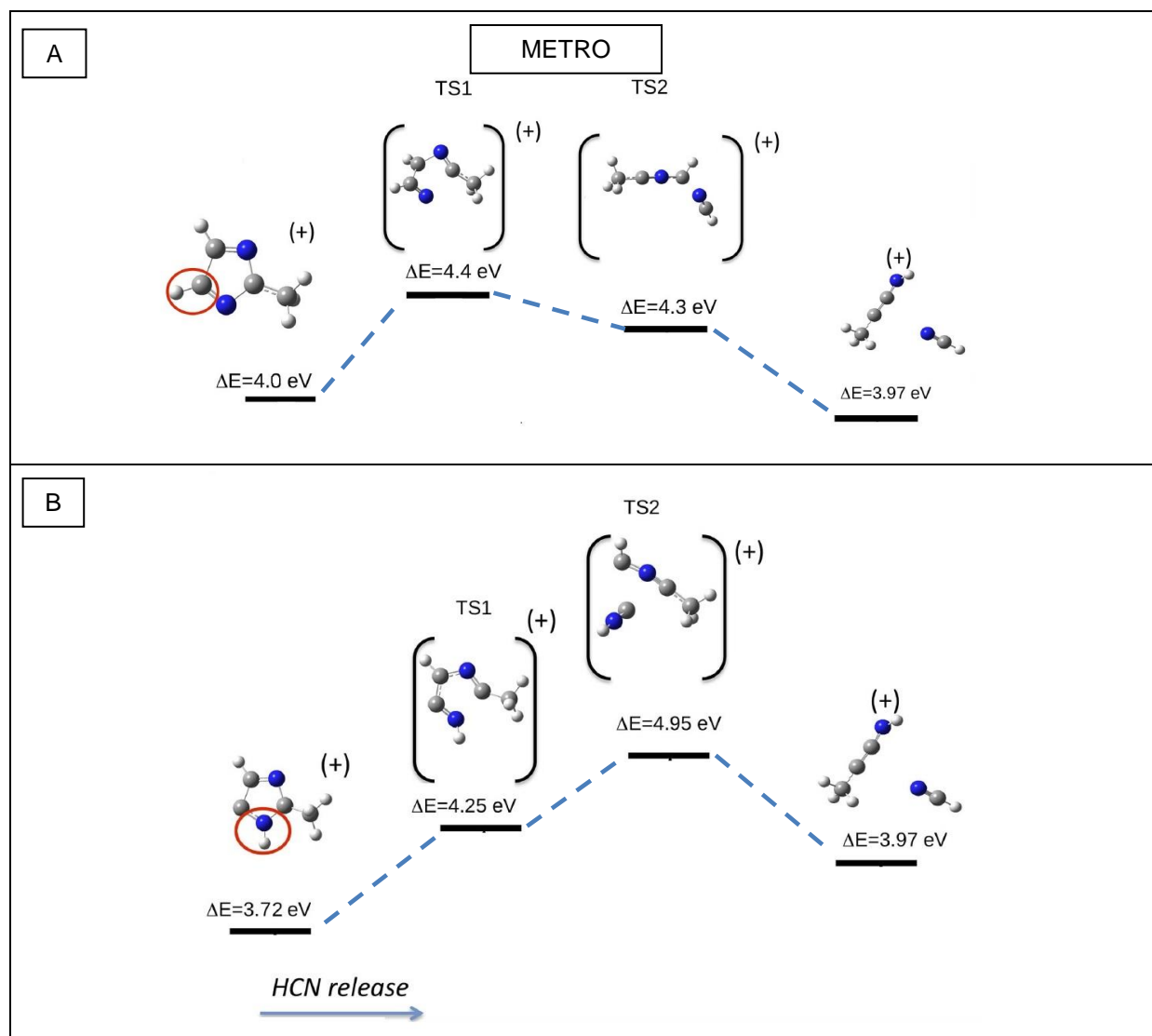


Figure 3.24 Potential energy paths for HCN and ion 54^+ release by fragmentation of ion 81^+ in the case of METRO molecule; ion 81^+ is considered in two different structures that differ by the position of the H atom migrated during the molecular rearrangement described in the text. Along the fragmentation paths, also the structures of ions before fragmentation, after fragmentation and at transition states are reported. Energies of each considered state with respect to the energy parent ion are indicated.

3.3 Conclusions

To summarize, in this chapter we have investigated the photofragmentation of both model systems, nitroimidazole isomers, and real drugs, METRO and MISO built on 5-NI and 2-NI, respectively, used as 'oxygen mimetic' radiosensitisers. Even though slightly bigger than the nitroimidazole model systems and being still relatively small molecules, in METRO and MISO the addition of less than 10 atoms in the two molecular chains resulted in a relevant increase of the number of fragmentation pathways in the mass spectra (Figure 3.1 and Figure 3.20) and in a dramatic increase in the complexity of the theoretical calculations required for a detailed investigation of photofragmentation. Despite this, the proposed joint experimental and theoretical approach is still able to describe all fragmentation paths by realistic model, reproducing the path for the most intense fragments observed in the mass spectra. The reliability of the proposed mechanisms is supported by an overall good agreement between theoretical AE values, extrapolated by potential energy surfaces, and experimental AE and PEPICO measurements.

Understanding the photofragmentation mechanisms of a class of radiosensitising molecules spanning from model systems (nitroimidazoles) to real drugs (metronidazole and misonidazole) has the main goals i) to identify the possible mechanisms of functioning, in relation to the specific molecular structure and ii) to verify whether the model systems, easier to handle, represent a reliable test case for the real systems.

In this work the production of molecular species with relevant biological functions and possible involvement in radiotherapy enhancement, like NO, NO₂, CO and HCN, has been identified. Abundance of NO and NO₂ may have a positive effect during radiotherapy because the first is a well-known reactive radical with vasodilation effect, while the second can be a source of radical species. On the contrary, molecules like CO and HCN may reduce the concentration of molecular oxygen, therefore increasing the probability to repair DNA damages produced on cancer cells by direct or indirect processes related to radiotherapy.

Similarly in the model systems and real drugs, the 2-NI based misonidazole molecule show more propensity to preserve the intact structure of the imidazole ring, which is instead heavily damaged in 4(5)-NI based molecules. At variance, the proposed mechanisms related to NO-release in the model systems is not confirmed in the study of metronidazole and misonidazole, suggesting that new photofragmentation mechanisms may be active in these more complex molecules. In particular, the leading role of the NO₂ - loss mechanism that can be inferred in both misonidazole and metronidazole, plays a more important role in misonidazole, while a larger variety of fragments characterise the fragmentation of METRO, some of them having a toxic effect.

To conclude, in both model and real systems, it seems that molecules based on 4-NI and 5-NI produce, by photofragmentation, a balanced amount of molecular species useful and harmful to increase the radiotherapy efficacy, while molecules based on 2-NI release preferentially species that increase the radiotherapy efficacy.

4 Enzymes deposition by ESI for biosensor application

This chapter is devoted to the description of the ESI deposition technique at ambient pressure and the obtained biosensors. The chapter is organized as follows. Section 4.1 is devoted to laccase, the enzyme used as biological active component in the biosensor we have prepared, its structure, the oxidation reactions it catalyses and the methods to characterise its activity. In section 4.2 the optimal conditions for the depositions and the measurements of the residual activity of the enzyme after the deposition are discussed. Section 4.3 is devoted to the results on the procedures to control the diameter of the deposit and the amount of deposited enzyme, while section 4.4 to the chemical physical characterization of deposited enzyme by X ray photoemission spectroscopy (XPS). Finally in section 4.5 results about electrochemical characterization of laccase biosensors is presented.

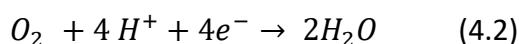
4.1 The laccase enzyme and its activity

To explore the possibility to use ESI as deposition technique for manufacturing biosensors, the first experiments have been performed with the laccase enzyme [152,153,154,155], which is a known enzyme used in biosensors applications [39,47,156].

Laccases are a group of enzymes that belong to the family of multicopper oxidases and can be isolated from several fungi although they are also present in plants, bacteria, and insects [153,155, 157]. The biological functions of laccases depend on the organism and can be associated to lignin formation, lignin degradation or wound healing in plants [153,155,158]. In this study commercial laccase from *Trametes Versicolor* fungi has been used (Sigma Aldrich, CAS number 80498-15-3).

The *Trametes Versicolor* laccase is composed of 499 amino acid residues [159].

All laccases are proteins with a folded globular structure, approximate dimension of 5-10 nm in diameter (Figure 4.1.A)[160,161,162] and a mass in the range 50.000 – 80.000 Da [153,155,157]. These enzymes can oxidise a wide range of molecules like phenols, polyphenols, amines etc. [153,154,155]. All different laccases have a similar structure, with four copper sites that catalyse the oxidation (Figure 4.1.B) and can be distinguished in T1, T2 and T3 according to different absorption spectra and redox properties [152,160,163]. The T1 copper site is located on one side of the enzyme adjacent to a hydrophobic cavity where the molecule to oxidase (analyte) is hosted during reaction (equation 4.1); the electrons removed from the analyte are transferred to the other three copper atoms, one in T2 site and two in T3 sites, located about 12 Å at the other side of the laccase molecule. Here oxygen is reduced to water consuming electrons (equation 4.2). All these reactions do happen in solutions [152,160,163].



In this study two different analytes have been used to test the activity of laccase in different conditions, i.e. in solution and after deposition.

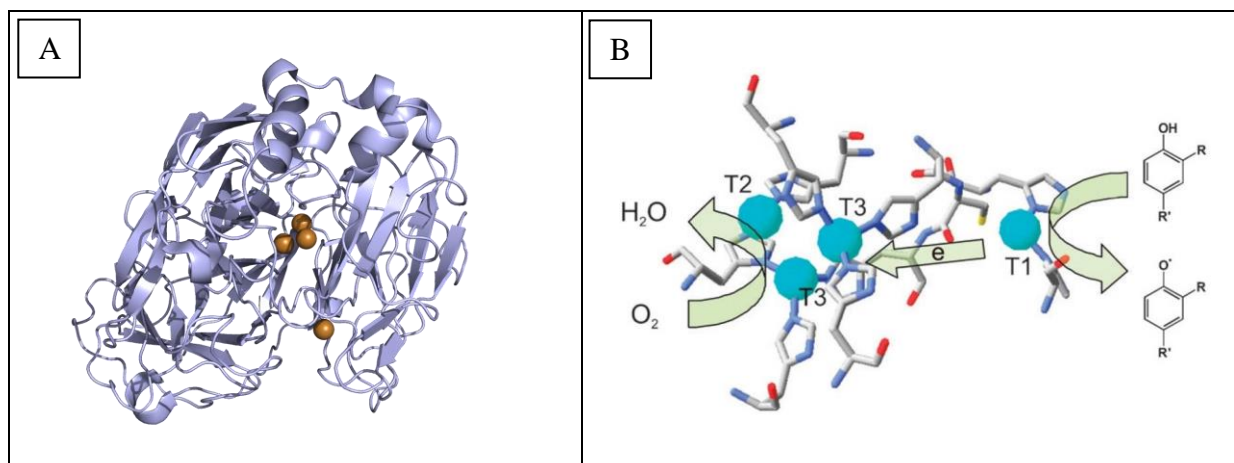


Figure 4.1. A) The globular folded structure of laccase. Ribbon representation shows the secondary structures. Copper atoms are indicated as orange spheres [164]. **B)** Copper sites of laccase and a schematic representation of the catalytic reaction[165]. The specific case of oxidation of a generic phenol to respective radical is reported.

The enzymatic activity is a measure of the catalytic ability of the enzyme; to measure the laccase activity in solution, the syringaldazine assay is used [166,167]. In a proper water solution syringaldazine is oxidised by laccase to the corresponding quinone (Figure 4.2.A) producing water from oxygen molecules in solution; quinone production is monitored by light adsorption measurements at 530 nm [47,167,168]. The absorbance A_{bs} is directly proportional to concentration (c) of the absorbing specie and the length of the optical path in the sample (l) by the Lambert-Beer equation [168]:

$$A_{bs} = \varepsilon cl \quad (4.3)$$

where ε is the molar extinction coefficient.

The activity A_{ct} of the enzyme is proportional to the variation of concentration, c , of the species produced by the catalysed reaction and can be quantified by measuring the variation of the absorption in a temporal range, Δt , where absorption is linear with respect to time (equation 4.4) [167]. Other parameters as ε and l , which are constants, and concentration of the syringaldazine, which is supposed to be in excess with respect to the enzyme concentration, can be neglected

$$A_{ct} \propto \frac{\Delta A_{bs}}{\Delta t} \quad (4.4)$$

To measure the activity of laccase deposited on the working electrode of a biosensor, catechol is used as analyte. In this case laccase oxidases the catechol to benzoquinone producing water, and the benzoquinone is reduced to catechol on the working electrode extracting two electrons (Figure 4.2.B)[169,170]. When stable conditions are reached, constant electric current on the working electrode is measured; this is an indirect measure of laccase activity.

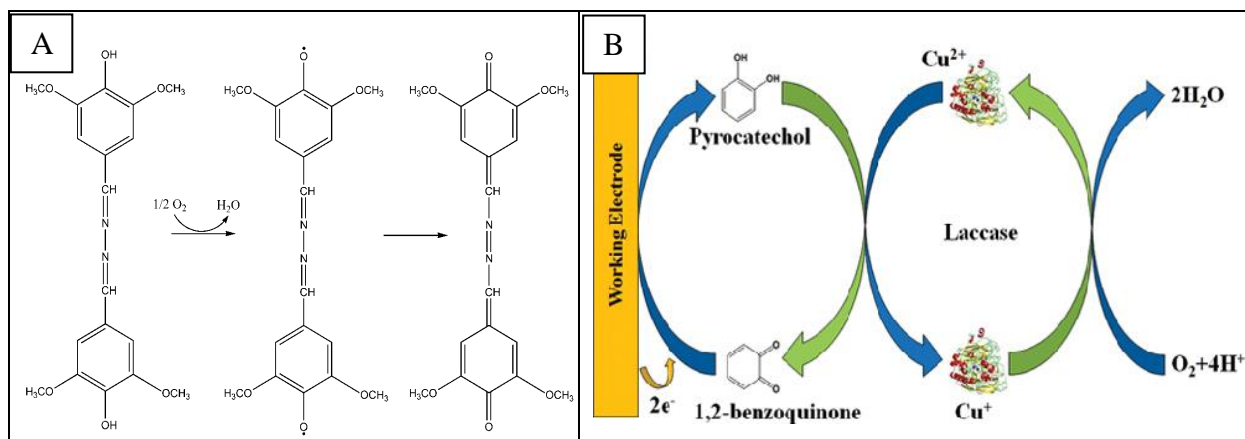


Figure 4.2. A) The laccase reaction with syringaldazine as analyte, where the intermediate product is a free radical and the quinone, deep purple in colour, is formed by a disproportionation between the radical and the quinone of the syringaldazine [153]. **B)** Schematic representation of laccase catalysed oxidation of catechol to benzoquinone [169].

4.2 Deposition of laccase by ESI, experimental procedure and activity measurement

Laccase deposition by ESI requires the optimisation of several parameters, like the composition of the solution, the enzyme solubility and concentration, the flow rate of the syringe pump, the distance between spraying nozzle and the target used for the deposition, the high voltage applied to the nozzle and the size of the deposit suitable for a specific application. Most of these parameters are correlated so that an extensive preparation and optimisation work is needed to obtain an effective immobilisation for a working biosensor.

To favour spray formation organic solvents like ethanol (EtOH) or methanol (MeOH) are generally mixed with water to form the solution. Small concentrations of chemicals like acetic acid or formic acid are often added to the solution in order to increase analyte protonation (see section 2.1.2.1). The first challenge in ESI deposition for biosensor applications is represented by the preparation of a suitable solution of laccase that can be efficiently sprayed and, at the same time, does not affect significantly the activity of the enzyme. Biocompatibility of the solution with laccase has been measured by the syringaldazine assay, while the stability of the spray has been monitored by a camera, zoomed and focalised on the Taylor cone at the exit of the nozzle.

Concerning the preparation of the solution, laccase, which is in the form of powder, is typically dissolved in few ml of pure water with a concentration of 5 mg/ml (stock solution) to be kept at -18 °C and partitioned in smaller amounts, conserved in a freezer, for daily use. This procedure avoids temperature degradation of the sample and all tests use a fresh solution of equal concentration. Then the laccase from stock solution is diluted and mixed to solvent in different relative concentrations to be tested.

Preliminary tests indicated that an amount of methanol (MeOH) or ethanol (EtOH) up to about 20% is a good compromise, which allows a good electrospray process while preserving the laccase enzyme activity with minor losses. For this reason, solutions with 20% concentrations of methanol or ethanol, with or without the addition of 0,01% of Formic Acid (AcForm) as a protonating agent, have been investigated to select, among the different combinations, the solution leading to the best performances. Five solutions have been prepared and tested to investigate influence on the laccase activity (Table 4.1).

Solution	Solvents	preparation
A	80% H ₂ O / 20% MetOH	100 µl H ₂ O / 50 µl MetOH / 100 µl laccase stock solution
B	80% H ₂ O / 20% EtOH	100 µl H ₂ O / 50 µl EtOH / 100 µl laccase stock solution
C	80% H ₂ O / 20% MetOH / 0,01% AcForm	100 µl H ₂ O / 50 µl MetOH / 100 µl laccase stock solution / 1 µl AcForm 2,5%
D	80% H ₂ O / 20% EtOH / 0,01% AcForm	100 µl H ₂ O / 50 µl EtOH / 100 µl laccase stock solution /1 µl AcForm 2,5%
Blank	100% H ₂ O	150 µl H ₂ O / 100 µl laccase stock solution

Table 4.1. The four solutions prepared to test the best ESI condition preventing enzyme denaturation. The 'Blank' solution has been prepared for the absorbance test.

A flow rate of 1 µl/min has been found as the optimal value to obtain a stable electrospray for all solutions. All solutions in Table 4.1 have a laccase concentration of 2 µg/µl (≈ 0.033 mM) and preliminary tests indicate that the target quantity of enzyme to deposit to obtain a well detectable response in screen printed electrodes is of about few tens of µg; therefore, a deposition time of 30 minutes has been used.

Syringaldazine assay (Figure 4.3) has been performed using a UV-vis spectrophotometer 30 minutes after solution preparation in order to mimic realistic conditions and to monitor the activity of laccase after the typical time required for deposition. All activity measurements are performed on a mixture of 30 µl of laccase solution A, B, C, D and Blank in Table 4.1, using 1320 µl of buffer (0.1M at pH 4.5 citric acid/sodium citrate solution) and 150 µl of syringaldazine ($7.78 \cdot 10^{-2}$ mg/ml or 0.216 mM), where the initial molar concentration of laccase is much lower than the molar concentration of syringaldazine.

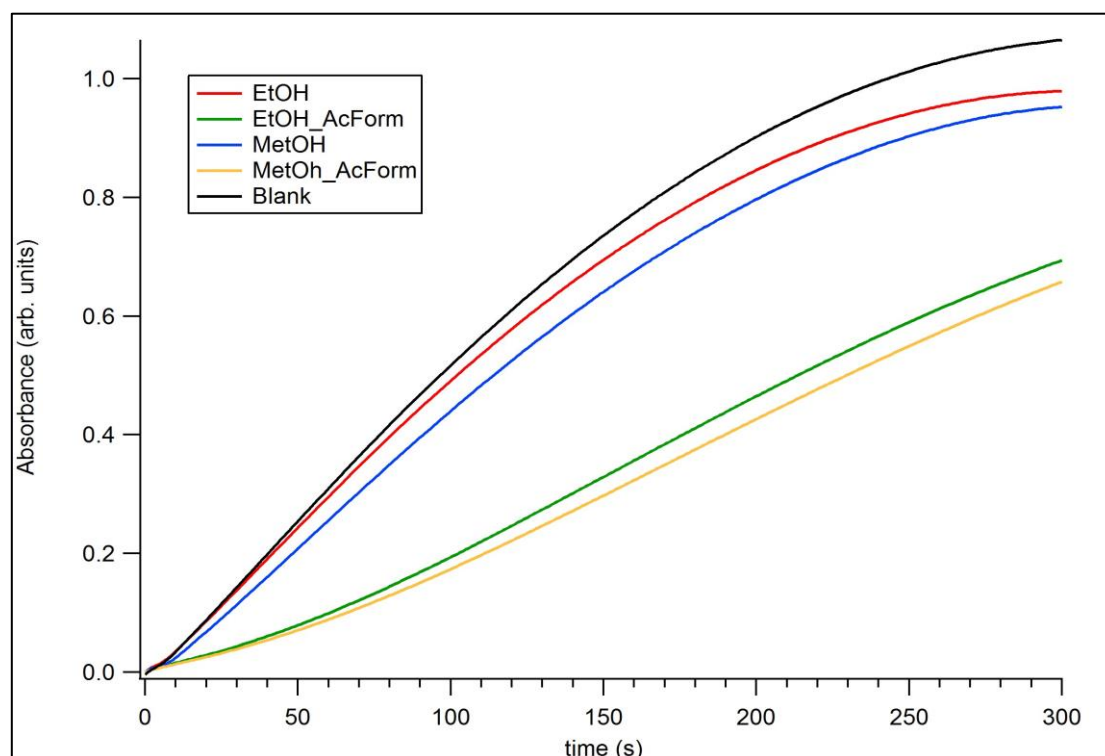


Figure 4.3. Comparison of absorbance curves at 530 nm of solution A (blue curve), B (red curve), C (yellow curve), D (green curve) and Blank (black curve) according to the procedure indicated in the text.

The results obtained in the spectrophotometric assay suggest that the use of formic acid as a protonating agent is not recommended as it significantly reduces the activity of the enzyme

already in solution. A 20% solution of methanol or ethanol instead has a negligible influence on the activity. Knowing from literature the greater stability of the electrospray process with methanol solutions, it has been decided to use spraying solutions with methanol at concentrations as in A of Table 4.1.

Having optimised the solution to preserve the enzyme activity in the solutions, the same information has been acquired and confirmed also for the laccase subjected to the electrospray depositions.

All deposition parameters optimized for solution A are summarized in Table 4.2.

Solution composition	Flow rate	Needle HV	Needle distance	Deposit diameter
A (see Table 4.1)	1 $\mu\text{l}/\text{min}$	4.92 kV	14 mm	15-16 mm

Table 4.2. Optimized deposition parameters for the assessment of residual laccase activity after electrospray deposition.

The preserved activity of laccase after deposition on a support of alluminium has been investigated by syringaldazine assay performed on 30 μl of solution A and on laccase deposited by ESI using 30 μl of solution A and then dissolved again using 1350 μl of buffer solution. In both tests performed directly on the solution A and on the deposited laccase, which has been dissolved again after the deposition, the total amount of solution is 1500 μl (Table 4.3).

	Buffer solution	Laccase solution A	Syringaldazine solution	Total volume	Amount of laccase
Before deposition	1320 μl	30 μl	150 μl	1500 μl	60 μg
After deposition	1350 μl	0 μl	150 μl	1500 μl	60* μg

Table 4.3. Composition of solution for the measurements of absorbance before and after ESI deposition. *) 60 μg has to be considered as the 'nominal' value, assuming that the entire amount of deposited laccase has been dissolved again.

Absorbance spectra, comparing the variation in the linear range (480-620 seconds), show a preserved activity of 75 % (Figure 4.4), a very competitive value compared with other deposition techniques that do not exceed the 66 % [171,172].

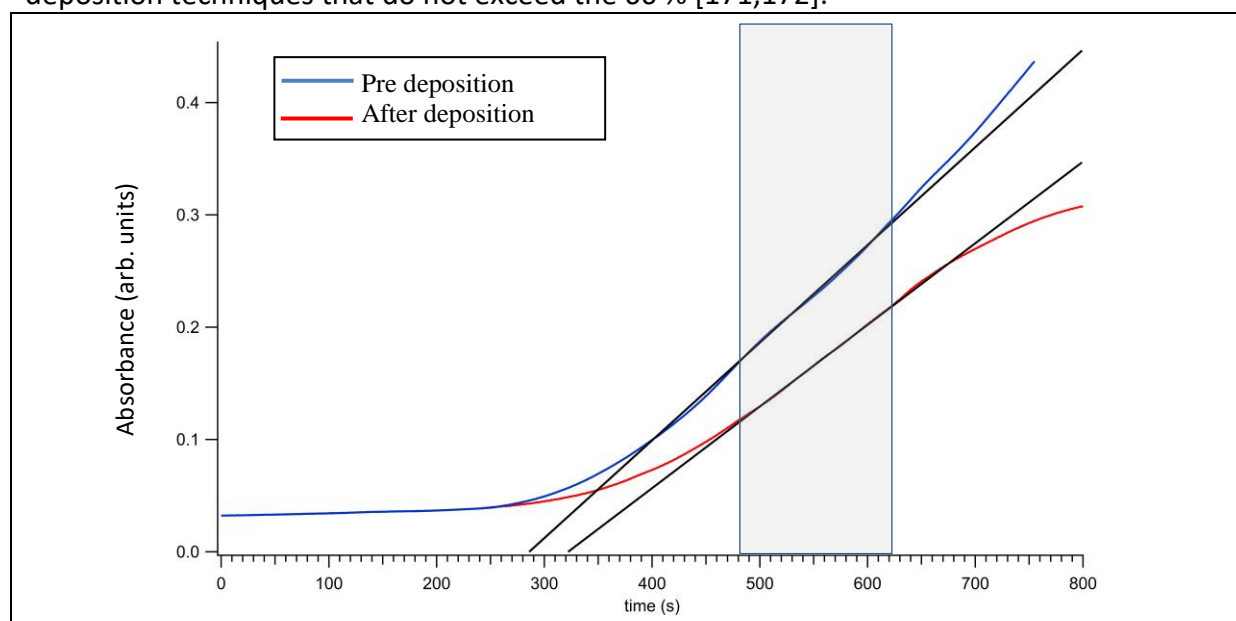


Figure 4.4. Comparison of the Absorbance at 530 nm between the solution A (blue curve) and resolubilized laccase deposited by ESI (red curve). The linear fits (black lines) in the linear range (grey box) are also shown.

4.3 Characterization of the electrospray deposition technique

In order to characterize the deposition technique two aspects have been investigated: the possibility to control the deposition area focusing the spray by mean of an additional electrode and the assessment of the amount of enzyme deposited by mean of a quartz crystal microbalance (QCM).

4.3.1 Deposition area

The possibility to use the spray and to reduce the deposition area is crucial as in most applications a limited and well defined area has to be covered (see sections 4.3.2 and 4.4). Moreover the use of a mask to reduce the diameter of the deposit results in a waste of material and an increase of deposition time.

After preliminary tests that have identified the conical rather than flat shape as the most effective for the focusing electrode, five conical electrodes of different heights and widths have been tested, measuring the diameter of the deposited material in each geometry, Table 4.4.

The new electrode has been mounted on a translator and placed 3 mm away from the target; the distance between the spraying needle and the target has been kept at 14 mm (Table 4.4). The introduction of this additional electrode required a new optimisation of the high voltage potential on the spraying nozzle (in the range 4.5 – 5 kV) and to adjust the potential of the new electrode (2 – 2.5 kV) to obtain a stable spray. These tests have demonstrated how using conical electrodes it is possible to easily reduce the deposition area down to 3 mm (Table 4.4). Other diameters were beyond the scope of the present work, and were not investigated.

Electrode label	h (mm)	ϕ_1 (mm)	ϕ_2 (mm)	ϕ_{deposit} (mm)
C1	6	12	6.5	6
C2	6	13	6.5	5
C3	8	12	6	4
C4	6	9	6	3.5
C5	6	12	5	3

Table 4.4. Geometry of cones and diameter of the deposit for each tested focusing electrode.

4.3.2 Deposition rate

The conical electrode is a powerful tool to control the deposition area minimising wasted material. However, a potential drawback is that being the cone of a comparable size with respect to the spray itself, it introduces the risk to intercept the spray, losing a fraction of the sprayed material.

To investigate this process and, in case, to quantify the fraction of intercepted material, the amount of deposited enzyme has been evaluated by mean of quartz crystal microbalance (QCM) used as target of the deposition. The QCM (Figure 4.5.A) is composed by two gold

electrodes with a diameter of 6 mm obtained by vapour deposition on a quartz crystal disk of 14 mm diameter.

The crystal used in the present work and the related electronics have been manufactured and at the Istituto di Inquinamento Atmosferico (IIA) of the CNR, Area di Ricerca di Roma 1 in Montelibretti (Dr. A. Bearzotti and E. Zampetti). It has a resonance frequency $f_0 = 10$ MHz. Within certain limits, the variation of the resonance frequency is proportional to the amount of deposited mass [173]; however, it is also much influenced by the properties of the deposited material as well as its adhesion properties on the gold material and among different layers. As such, the response $\Delta(\text{frequency})$ versus $\Delta(\text{mass})$ had to be calibrated specifically for laccase.

The QCM calibration procedure was based on the reading of the frequency variation for known amount of deposited laccase, controlled by drop casting at known mass concentration and volume. By this procedure the formula to calculate the deposited mass of laccase from resonant frequency variation has been derived:

$$m (\mu\text{g}) = -6.67 \cdot 10^{-4} \left(\frac{\mu\text{g}}{\text{Hz}} \right) \Delta f (\text{Hz}) \quad (4.5)$$

Equation (4.5) can be used in the range of linearity 1-30 μg , with an uncertainty of 15% estimated by different repetitions of the dropcast. The use of micropipettes for the dropcast may have largely contributed to the estimated uncertainty.

Having calibrated the response of the QCM to laccase by dropcast, the QCM has been used to measure the amount of the ESI deposited laccase for each focusing electrode, repeating three depositions for each cone. The same characterisation has been repeated for different deposition times, in order to test linearity in the ESI deposition rate. The corresponding mean values are reported in Figure 4.5.

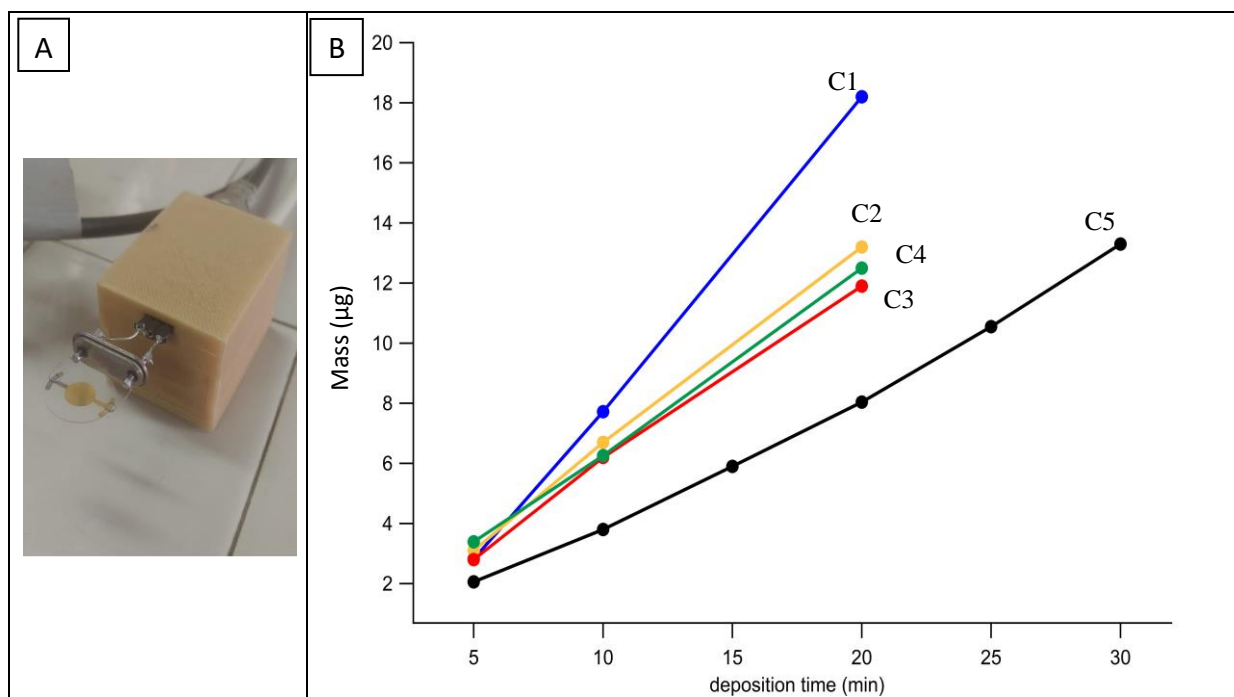


Figure 4.5. A) The QCM microbalance, manufactured at the CNR-IIA, connected to the electronics for frequency measurement. B) Mass of deposited laccase on the QCM electrode using conical electrodes tabulated in Table 4.4 to focalise the electrospray. The spray solution and parameters, have been set according to A in Table 4.1 and Table 4.2.

Considering that the concentration of the sprayed solution is 2 µg/µl and the spraying rate is 1 µl/min, the expected 'nominal' amount of deposited material can be easily calculated and compared to the measured one, Figure 4.5 . Using this procedure to evaluate the fraction of deposited material, an average between 45 to 21 % depending on the focusing electrode has been determined.

However, considering the area of deposit and with the assumption of a spatially uniform deposition, the amount of deposited enzyme is still higher with respect to the one that could be achieved by using a mask to reduce the deposition area, as estimated by equation 4.6

$$mass = Vol \cdot c \cdot \left(\frac{\phi_i}{\phi_0}\right)^2 \quad (4.6)$$

where Vol is the total volume of solution sprayed by ESI, c is enzyme's concentration in the solution, ϕ_i and ϕ_0 are the diameters of the deposits obtained respectively with and without the focusing electrode, with $\phi_0 = 15$ mm. In Table 4.5 the amount of enzyme deposited in 20 min by the use of conical electrodes (Figure 4.5.B) or in the hypothesis to use a mask to achieve the same size of the deposit (equation 4.6) are reported. The comparison clearly shows a gain in the amount of deposited material of about a factor 3-5 thanks to the focusing electrode.

Quantity of enzyme deposited in 20 min (µg)					
	Cone C1	Cone C2	Cone C3	Cone C4	Cone C5
Focussing electrodes	18.2 (45 %)	13.2 (33 %)	11.8 (30 %)	12.5 (31 %)	8.4 (21 %)
hypothetical mask	6.4 (16 %)	4.4 (11 %)	2.9 (7 %)	2.2 (6 %)	1.6 (4 %)

Table 4.5. Amount of deposited enzyme after 20 min by the use of conical electrodes or in the hypothesis to use a mask (equation 4.6) The percentage of deposited enzyme with respect to the nominal amount (40 µg) is reported in bracket.

4.4 Characterization of the deposited enzyme: chemical-physical investigation by XPS

To obtain information on the chemical physical characteristics of deposited laccase, X-ray photoemission spectroscopy (XPS) measurements have been performed. This technique is a powerful tool to obtain quantitative information on the chemical composition of the sample [174].

In XPS the sample is illuminated by a photon beam in the soft X ray energy range ($h\nu \approx 1 - 5$ keV) and the photoemitted electrons are selected according their kinetic energy (E_k) that is correlated to the binding energy of electrons in the sample (BE) by the energy conservation:

$$E_k = h\nu - BE - \phi \quad (4.7)$$

Where ϕ is the work function of the analyser.

Due to the used photon energy, electrons are preferentially emitted by core levels, which have a strong atomic character. The measured BE assumes values specific for each atom and its chemical environment. This on one hand provides information on the atoms present in the sample and on the other the “chemical” shift between atoms of the same species allows to discriminate them depending on the bonds they are involved.

The intensity of the detected photocurrent depends on the photon current density, on the atom areal density in the sample and photoionization cross section, on the spectrometer angle and energy acceptance and on the detector efficiency. In the hypothesis of stable experimental conditions, the intensity is proportional to the atomic areal density and the spectra of the same core shell for different samples can be directly compared in intensity.

This technique is surface sensitive because only photoemitted electrons, coming from the first atomic layers (≈ 10 nm) [175] and elastically scattered in the sample, contribute to the measured XPS core level spectra.

The XPS measurements have been performed at the LASEC laboratory of Roma Tre University [176]. The measurement chamber of the experimental apparatus (Figure 4.6) consists of a vacuum chamber with a background pressure of $1 \cdot 10^{-9}$ mbar hosting a monochromatised X-ray photon source OMICRON Al K α ($h\nu = 1486.7$ eV), a hemispherical analyser operated at 40 eV pass energy and a corresponding energy resolution of 0.5 eV at full width half maximum (FWHM). The chamber is equipped also with an electron gun where the electron beam, generated by thermoionic effect, is focused onto the sample by a five cylinder lens system, reaching a spot dimension of 1 mm diameter; the electron beam can be directed to different regions of the sample by vertical and horizontal deflectors.

The XPS spectra of laccase deposited either by ESI technique or by drop casting on Fluorine doped Tin Oxide (FTO) conductive glass have been measured.

In the samples prepared by drop casting, an amount of solution containing an equal amount of laccase as estimated for ESI deposition have been transferred onto the support and let to dry for more than 12 hours to allow a slow evaporation of the solvent. This is a soft technique, however the obtained deposits are not uniform as the shape of the drop drives the deposition towards an outer ring (Figure 4.7) [177] and there is a less degree of control and reproducibility over the quantity of deposited material. Five different samples prepared by both drop casting (DC) and ESI deposition (Table 4.6) using different solutions and amount of deposited laccase (i.e. deposition time) have been analysed by XPS. The diameter

of the deposits has been chosen to be 5-6 mm to avoid contribute of the signal coming from the surface not covered by laccase.

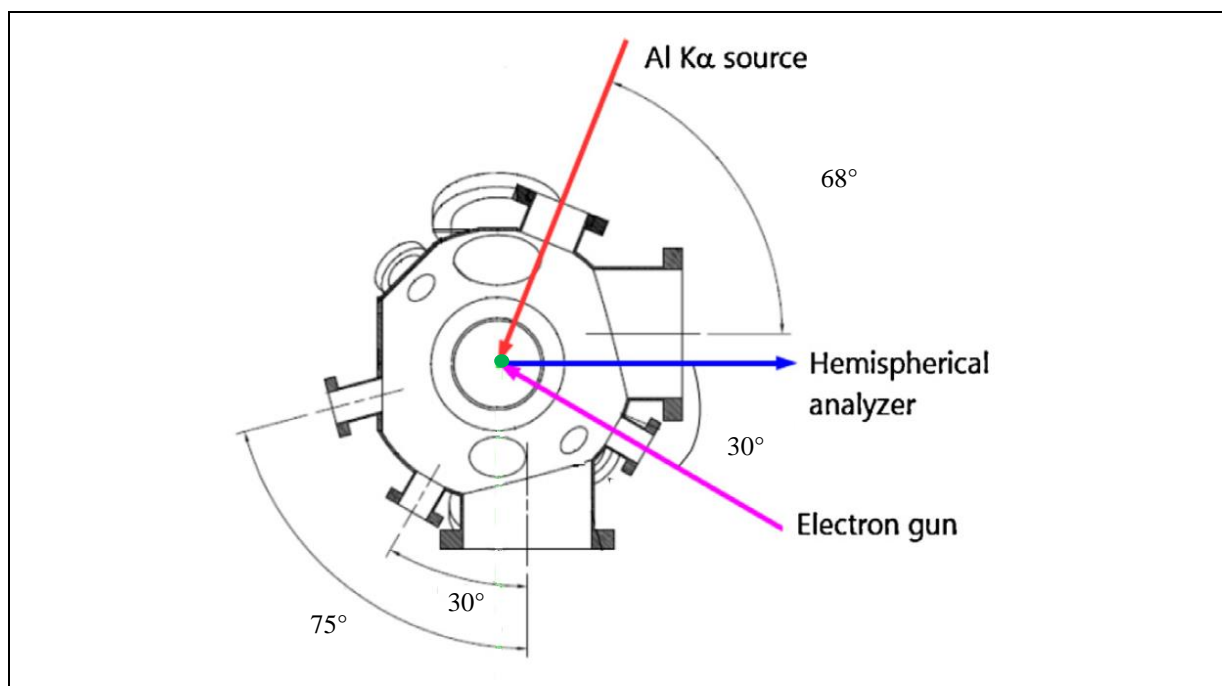


Figure 4.6. In-scale reproduction of the scattering plane in the LASEC experimental chamber Roma 3 University, with the arrangement of the two ionising sources and electron analyser. The position of the sample is indicated by a green dot [176].

Sample label	Deposition technique	Solution composition	Laccase concentration ($\mu\text{g}/\mu\text{l}$)	Deposition time (min)	Deposited amount of solution (μl)	Deposit diameter (mm)
Water DC	DC	100 % H ₂ O	2		15	5
MetOH DC	DC	80% H ₂ O 20% MetOH	2		30	6
ESI 5'	ESI	80% H ₂ O 20% MetOH	2	5	5	6
ESI 20'	ESI	80% H ₂ O 20% MetOH	2	20	20	6
ESI 30'	ESI	80% H ₂ O 20% MetOH	2	30	30	6

Table 4.6. Description of deposition parameters used to produce the samples for the XPS studies.

The selection of the samples has been driven by the idea to investigate the differences between samples dissolved in pure water or in a mixture of water and methanol, samples deposited by ESI and DC or samples containing different amount of laccase.

The deposited layer of laccase is not conductive and becomes electrically charged by the electron depletion due to photoemission. This charging effect reduces the kinetic energy of the photoelectrons and produces a shift towards higher binding energy in the measured XPS spectra; the reduction of kinetic energy results to be proportional to the amount of deposited material, which is in turn proportional with the time of deposition (Figure 4.8) [178,179]. The electron gun operated at 50 eV of electron energy has been used to

compensate for the electric charge and neutralize the energy shift. For each sample an electron beam of 50 nA intensity has been found to shift the XPS peak to a stable position, while a further increase of the current does not produce any variation in BE. This has been assumed as the 'real' (compensated) energy position of the peaks and in all samples the same BE (red spectra in Figure 4.8) for equivalent atoms has been observed.

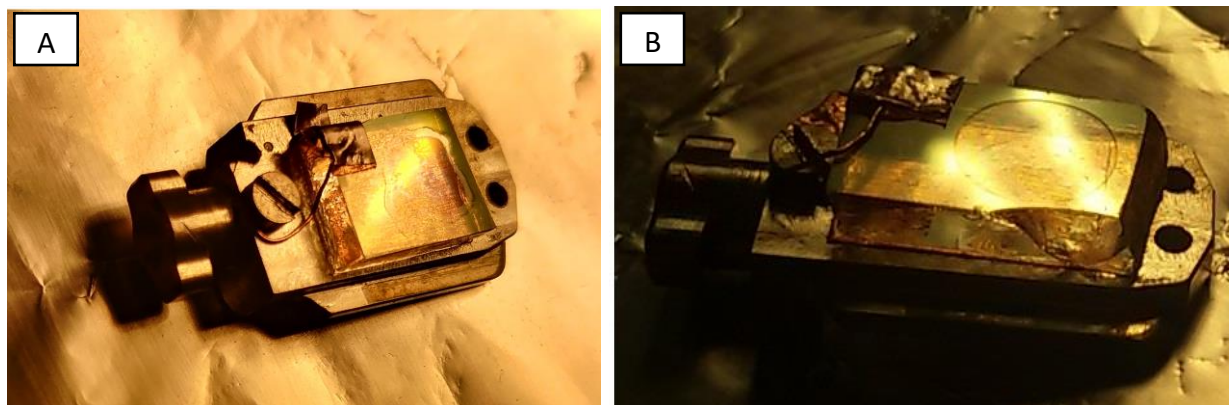


Figure 4.7. Pictures of FTO glass mounted on the sample holder used to move the sample inside the XPS vacuum chamber. Deposit obtained by DC (A) and ESI (B) are visible on the glass. The ESI deposit is clearly more regular in shape and, at least by eyes, very uniform differently from DC where a difference between the edge and centre of the deposit can be observed.

Moving the electron beam along the sample has been observed that the maximum shift is obtained when the edge of the sample is invested by electrons; this also reduces the modification of the sample due to electron interaction.

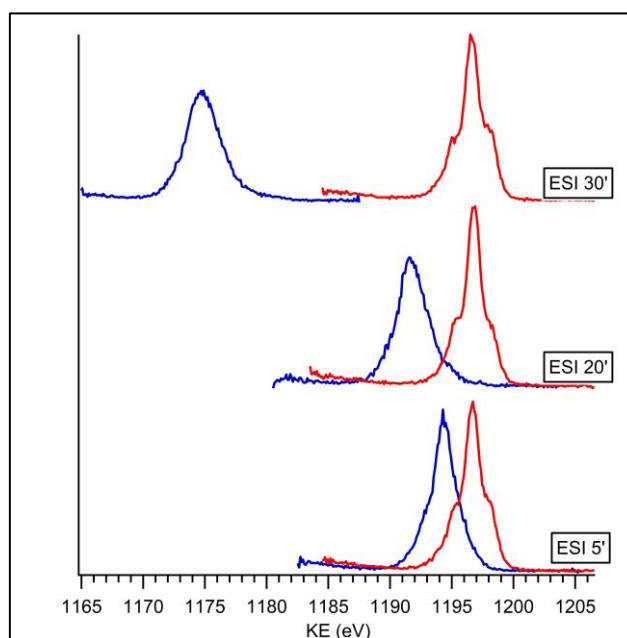


Figure 4.8. C1s spectra of samples obtained by ESI deposition with (red spectra) and without (blue spectra) electron beam compensation; the decrease of photoelectron kinetic energy is qualitatively related to the thickness of the sample, even though a quantitative analysis is not possible due to the empirical and unpredictable characteristics of the charging effects.

As mentioned in section 4.1, the *Trametes versicolor* laccase is composed of 499 amino acid residues [159]. The most abundant atoms are carbon (2420 atoms), oxygen (707 atoms) and nitrogen (653 atoms), while copper (4 atoms) and sulphur (7 atoms) represent a minor

contribution. For this reason the C1s, N1s and O1s core levels have been investigated while the other atoms like copper atoms, even though interesting being the catalytic sites, have a too low concentration to produce a detectable signal. All XPS spectra are calibrated in binding energy using C1s of HOPG graphite (284.4 eV in BE) [180] and normalized in intensity to the acquisition time.

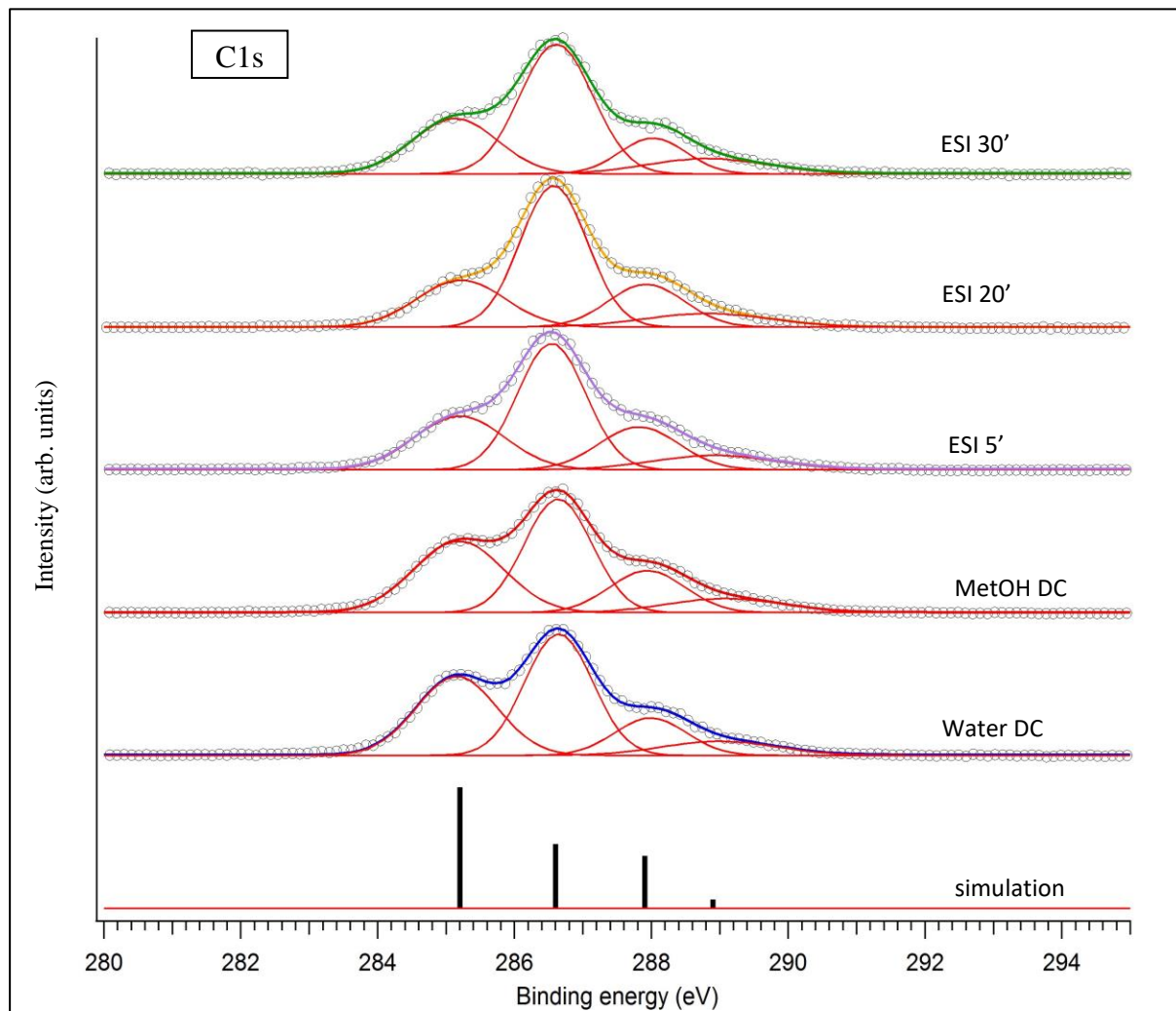


Figure 4.9. C1s spectra of all the samples obtained by ESI and DC depositions on FTO conductive glass. The experimental data are reported as open circles; the coloured full lines are the results of the fitting procedure with four Gaussian functions while the red lines are the four components of the fitting. The black sticks in the bottom panel represent the results of the 'simulation' of the C1s XPS spectrum obtained by taking into account the sum of the contribution of each amino acid in the laccase sequence (see text).

Component label	Binding energy (eV)	FWHM (eV)	Attribution
C1	285.17 ± 0.05	1.48 ± 0.08	C-C , C-H , C-S , C-COO , C=C-N
C2	286.58 ± 0.05	1.20 ± 0.05	C-N , C-O , C-N-O , N=C-NH
C3	287.92 ± 0.1	1.26 ± 0.12	O=C-N , COO
C4	288.9 ± 0.15	2.10 ± 0.10	HC-(NH ₂) ₃ , COOH

Table 4.7. Binding energy and FWHM of each component; mean values and uncertainty are obtained considering values for the different samples obtained by fitting procedure. In the last column several possible attributions for each components are reported, the considered carbon atom is highlight in red [181].

In Figure 4.9 the C1s spectra of all samples presented in Table 4.6 are reported. These spectra clearly show the presence of four partially resolved components (Table 4.7). They can be attributed to the different local environments and chemical bonds that typically involve C atoms in amino acids. Unfortunately, unique attribution is not possible because each one of these components result from the superposition of the contributions of carbon atoms with similar chemical environment, but located in different amino acids. The results of the deconvolution procedure (Table 4.7 and Table 4.8) together with the proposed attributions as obtained from XPS spectra on amino acids in condensed phase are reported in Table 4.7 [181]. The BE position were found to be quite unaffected by the specific sample, at least within the accuracy of the present experimental procedure that, requiring the compensation of the charging of the sample, is estimated to be around 150 meV. Therefore, only the average position among the five samples is reported in Table 4.7, even though minor effects on the BE positions among the different sample cannot be excluded.

C1s XPS: comparison with simulated spectrum and literature data. Based on the stoichiometric composition of the laccase enzyme it is possible to roughly simulate its XPS spectrum (Figure 4.9) according to the following procedure: i) by the crystalline structure [159] the abundance of each amino acidic residue is known; ii) the XPS of each amino acid can be estimated by taking into account the chemical environment of each C atom (see relevant functional groups in Table 4.7); iii) the estimated XPS spectrum of each amino acid is multiplied by the abundance of that amino acid in laccase and finally all these contributions are added up. This simple procedure does not take into account neither the chemical shift of the same type of C atom in different amino acids nor the peptide bond between adjacent amino acids or the globular structure of the enzyme, but just abundance of amino acids and C1s BEs for each amino acid in the crystal structure (i.e. in zwitterion form). Therefore, possible shifts between simulated and measured spectra can be due to the many hydrogen bond interactions that determine the enzyme conformation and to the peptide bond between adjacent amino acids, not included in the crystal, are not taken into account. Both these aspects may affect the binding energy (in particular of the C3 feature of the carboxylic group involved in peptide bond formation) as well as the intensity distribution of the simulated spectrum [181].

Nevertheless, this simple model provides a very good description of the measured C1s XPS spectrum as far as the number and position of the main features is concerned and a close representation of the distribution of intensity, apart for the reversed intensity distribution between C1 and C2, with the first being more intense in the simulation while the second more intense in the experimental spectrum.

Samples	C1	C2	C3	C4
ESI 30'	0.25 ± 0.01	0.52 ± 0.01	0.13 ± 0.05	0.10 ± 0.05
ESI 20'	0.22 ± 0.01	0.51 ± 0.01	0.18 ± 0.05	0.09 ± 0.05
ESI 5'	0.26 ± 0.01	0.46 ± 0.01	0.18 ± 0.05	0.10 ± 0.05
MetOH DC	0.34 ± 0.01	0.40 ± 0.01	0.17 ± 0.05	0.09 ± 0.05
Water DC	0.34 ± 0.01	0.43 ± 0.01	0.14 ± 0.05	0.09 ± 0.05
simulation	0.49	0.26	0.21	0.04

Table 4.8. Relative intensity of each component observed in C1s spectra (Figure 4.9) in each sample.

This four-component structure of the C1s spectrum was also observed in previous works, with a relative intensity [161,165,182] different with respect to our experiments, but closer

to the simulated one. This discrepancy between the present C1s XPS and the literature one may be due to a different type of laccase or to instrumental artefacts because, differently from our case, in all other literature studies the support for laccase deposition were always materials rich in carbon atoms, introducing uncertainty in the deconvolution of the spectra. Alternative explanations can be a modified conformation of the enzyme due to its permanence in a solution containing methanol alcohol, the deposition process and the interaction with the support and among laccase molecules or a structural damage/fragmentation of the enzyme due to the electron beam bombardment to compensate for charging effects.

Considering that previous spectrophotometric tests in solution performed before and after ESI deposition (section 4.2) warranty a preserved laccase activity > 70% after ESI spray, the observed discrepancy could be consistent with this estimate. Being unknown the cause of the lost efficiency, it is at the moment not possible to provide a more specific explanation of the observations and more experiments will be performed in the future.

The role of the solvent. The C1s spectra of the two samples deposited by DC from a laccase solution in pure water or in a mix of water and a 20% of MetOH are very similar in the relative intensity of the different components (see Table 4.8). This observation is fully consistent with the conclusions of the spectrophotometric study reported Figure 4.3 that the addition of 20% MetOH to the laccase solution does not affect the enzyme activity and, presumably, its structure and conformation.

The time of deposition. The C1s spectra in all ESI and DC deposited samples have very similar total intensity regardless of the amount of laccase that has been deposited, suggesting that already after 5 minutes of ESI deposition a thickness higher than the sensitivity of XPS is reached.

For organic matter the mean free path of photoemitted electrons is 3 – 5 nm [161], therefore the lower limit of enzyme layer thickness to reach signal saturation is about 15 – 20 nm.

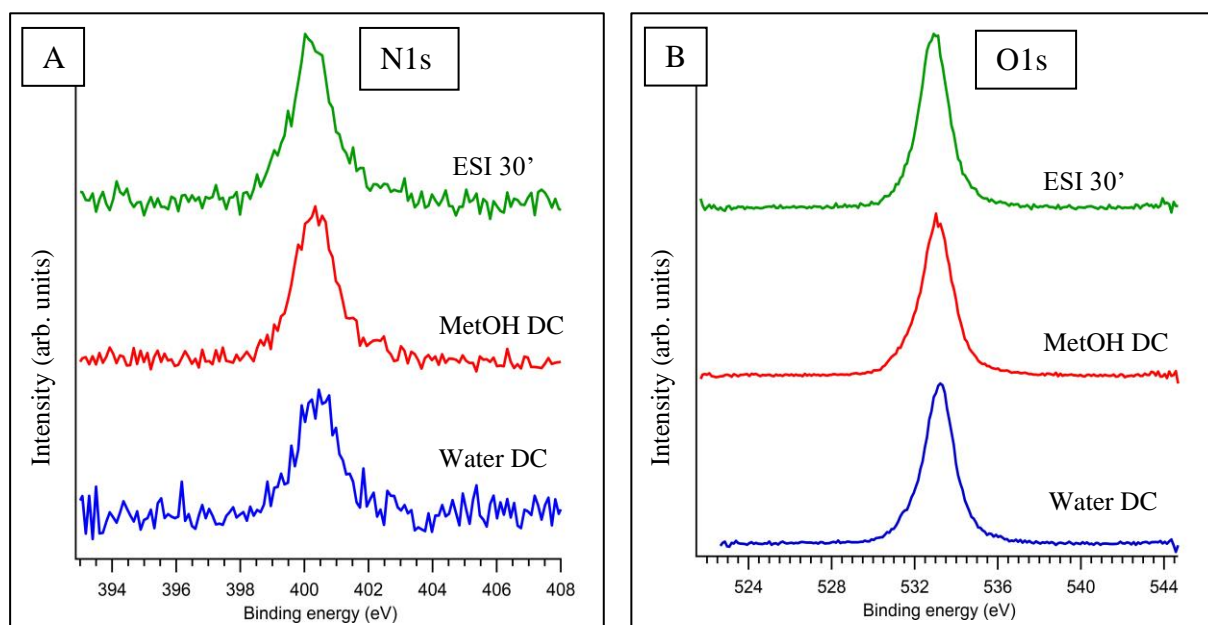


Figure 4.10. O1s e N1s of samples obtained by DC in water solution (blue spectrum) water and MetOH solution (red spectrum) and 30' ESI deposition (green spectra).

ESI and DC. As discussed above, the C1s spectra of the two DC samples are very similar to each other, and the same observation stands for the three ESI samples. However, differences in the relative intensity of the C1 (BE = 285.2 eV) and C2 (BE = 286.6 eV) components are observed between the DC and ESI deposits, with the first being more intense in DC samples while the second in ESI samples. Having used the same experimental procedure and conditions for the XPS measurements, this difference has to be ascribed to peculiar features in the ESI technique. This could be attributed to a degradation/fragmentation or variation in the enzyme conformation due to the electrospray process (high voltage, nebulisation) or the 'hard' landing onto the support, smashing and denaturing the complex and fragile enzyme.

This observation may be the evidence of a loss enzymatic activity estimated to be in the order of < 30% in Figure 4.5 of section 4.2.

The N1s and O1sXPS spectra. The N1s and O1s XPS spectra of samples obtained by drop casting, and the sample obtained by 30' ESI deposition are reported in Figure 4.10. In both cases the observed BE are consistent with literature [161,165,182]. The N1s peaks intensity (Figure 4.10.A) is very low and, as a consequence, it displays a poor signal to noise ratio compared with the C and O1s spectra; this is probably due to the lower cross section of N1s core shell at 1486.7 eV photon energy with respect to O1s [183] and lower abundance of atoms with respect to carbon. For this reason the N1s spectra are difficult to analyse and deconvolve in different components. In the O1s spectra a peak with asymmetric lineshape and a FWHM of about 2 eV is observed, suggesting the presence of different components from the sample itself. An unquantified contribution from the tin oxide, at 530-532 eV BE [184,185], cannot be excluded.

4.5 The laccase biosensor on screen printed electrodes

Having acquired a good confidence that the electro spray process and the related experimental procedures in the deposition do not significantly affect the enzymatic activity, optimised the deposition parameters and characterised the corresponding deposition rate, laccase has been finally deposited by ESI, using the solution A (Table 4.3) and the conical electrode C5 (Table 4.4), on the working electrode of a commercial graphite screen printed electrodes (Dropsense DRP-110) to produce an electrochemical biosensor (collaboration with dr.ssa Viviana Scognamiglio, CNR-IC, and M.C. Castrovilli, CNR-ISM). The working electrode is only 3-4 mm in diameter and to avoid interference during electrochemical measurements the enzyme has to be deposited only on the working electrode. For this reason the use of the cone C5 has been mandatory. With a deposition time of 30 minutes, 13-15 μg of laccase have been deposited. Electrochemical measurements are performed by a commercial potentiostat (PalmSense 4).

Among all interesting properties and characteristic of a biosensor the very first that needs to be investigated is the range of linearity of the response of the sensor with respect to the analyte concentration, as this determines if the device can be used in real applications

To investigate this aspect, the ESI deposition has been repeated with the same conditions onto a large number of SPE that have been tested for decreasing amounts of analyte to be detected. It is implicit that, in order to perform this test a stable and reproducible deposition is needed.

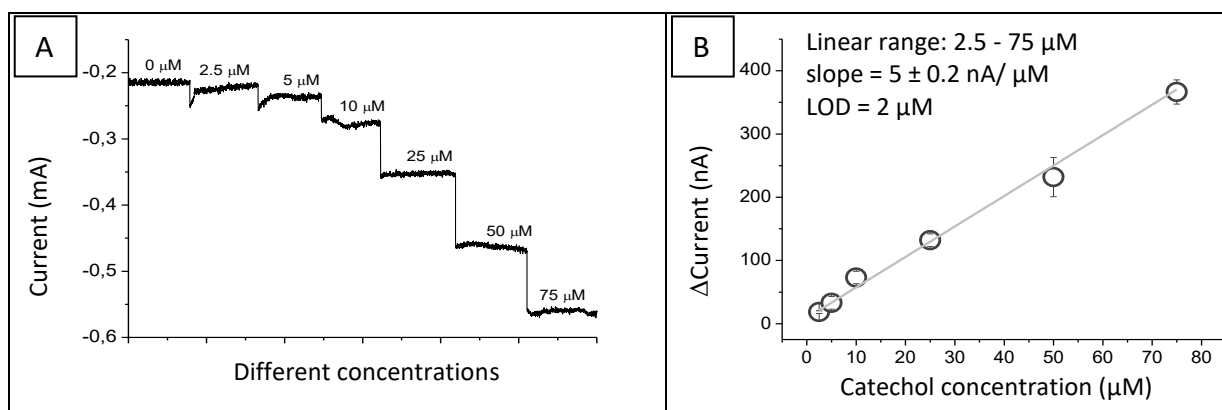


Figure 4.11. A) Electric current on the working electrode increasing the catechol concentration in solution. The graph reports only the current measured in stable condition after exposition of different electrodes to catechol solution of concentration indicated in figure. **B)** Variation of electric current on the working electrode vs catechol concentration; a linear response is observed. In all measurements of the electrical current the potential of working electrode with respect to the reference electrode is -0.160 V.

Each ESI deposited SPE has been exposed to a solution ($100 \mu\text{l}$) of specific catechol concentrations in the range $2.5 - 75 \mu\text{M}$ (Figure 4.11.A) and the produced current has been measured. Tests at each catechol concentration has been repeated at least three times, in different days and from different stock solutions, showing a good inter-electrode reproducibility and providing the error bars in Figure 4.13.B. Linearity of the response, i.e. the variation of the electric current with respect to the background signal, has been observed in the entire range (Figure 4.11.B). No higher concentrations of the analyte have been investigated. Extrapolation from Figure 4.13 allows to extract the lower limit of detection (LOD) calculated by equation 4.8 [47]:

$$LOD = 3 \frac{STD}{slope} \quad (4.8)$$

where STD is the standard deviation of current signal in stable condition of electrode (Figure 4.11.A) and the slope is calculated from current variations (Δ Current) vs concentration plot (Figure 4.11.B). A LOD of $2 \pm 0.1 \mu\text{M}$, is obtained.

This measured detection range and LOD are comparable with other biosensors based on laccase [39,47,156], and are very promising for a new technique, already used for sensors fabrication [32], but for the first time applied to the deposition of the bioactive component of a biosensor.

4.6 Conclusions

In this chapter the possibility to use ESI to perform deposition of enzymes for biosensor application has been investigated. Feasibility has been proved up to the realisation of a working biosensor on commercial screen printed electrodes, with linear response and detection limit comparable to similar biosensors achieved by standard techniques [156]. Many other tests still have to be performed to fully evaluate the performances of the ESI deposited laccase biosensor. However, the technique results to be very promising because high percentage, at least 75 %, of enzymatic activity is preserved after deposition, an excellent result in comparison with other hard deposition techniques like PLD. The ESI depositions performed at atmospheric pressure requires a relatively simple, compact and economic instrumentation, and quite short deposition times as compared to standard techniques like drop cast that requires some longer time to desorb the solutions. Furthermore, the ESI technique results to be very versatile, offering the opportunity to control the size of the deposit, produced with (probably) good spatial homogeneity. The deposition area can be modified by the focusing electrode reducing deposition time, allowing the deposition on several kind of targets, different in size, for different purposes and avoiding enzyme waste. However the focusing electrode can be improved because with the actual setup more than the 50% of the enzyme is lost.

The technique can be improved on several aspects, a detailed investigation of the morphology has not yet been performed, but eventually the homogeneity of deposit layer could be optimised by a more sophisticated focusing system. One of the main limit observed during the investigation is the long response time, the working electrode current requires 10-20 min to stabilise; this aspect requires a deeper investigation.

Moreover other characteristics of the biosensor have to be tested to really understand the applicability of the technique.

To conclude, these preliminary results on the use of ESI as a technique to deposit enzymes for biosensors applications at ambient pressure show a relevant and promising potential.

5 Construction and characterization of in vacuum ESI apparatus

In this chapter, the simulation of the first stage of the in vacuum ESI apparatus (see section 2.1.4) is described. This study, based on the comparison between simulations and real measurements, is essential for understanding the role of each optical element and of the unknown variables in the initial conditions of the ESI beam, providing a reference to understand the behaviour of the other stages of the apparatus.

In section 5.1 the overall strategy adopted to perform simulations is reported. In section 5.2 a comparison between experimental measurements and simulations is presented to support the methodology used to choose the initial conditions of the simulations described in section 5.3.

In section 5.4 a set of simulations to investigate the ion kinetic energy in several regions of the apparatus is presented while section 5.5 is devoted to tests performed using different molecules. In section 5.6 a summary of the results is reported, while in section 5.7 conclusions and possible future perspectives are presented.

5.1 Strategy of the simulation to study the apparatus

In section 2.1.4.4 the SIMION software used to perform the simulation of the ion trajectories driven by the electric field has been presented. The definition of the electric field in the different sections of the apparatus is only the first step to perform realistic simulations. The second step is to find proper initial conditions (kinetic energy, velocity spread, position etc.) for the ions injected in the setup. In an ESI apparatus this is not an easy task, because a quantitative and detailed description of the ESI nebulization at ambient pressure is a theoretically and computationally demanding job [58,186-191], often leading to a not fully reliable descriptions. Therefore, in the present study, literature results have been used [48,49,192,193].

The ESI ion beam is transported in vacuum via a heated capillary (125 mm long and of 0.3 mm inner diameter) together with air as buffer gas pulled by the pressure difference between the ambient and first chamber. Along the path in the capillary, a large number of collisions between the ions and the buffer gas molecules as well as with the inner wall of the capillary occur, and eventually lead to the thermalisation of the ions [49]. This is a reasonable assumption according to the kinetic theory of gases, where the mean free path at room temperature ($T = 300$ K) and ambient pressure ($P = 1013$ mbar) for molecules of mass in the range between $10 - 10.000$ Da is less than $1 \mu\text{m}$. Then, ions with a final kinetic energy distribution centered around $K_B T \sim 26$ meV at 300 K, where K_B is the Boltzman constant, are expected near the exit of the capillary.

A feature that is not possible to reproduce in the present simulations is the presence of a high background pressure in the region between capillary and skimmer, because the frequent collisions between the ion beam and the fast moving gas modify, in a not easily predictable way, the 'ideal' ion trajectories calculated by the SIMION simulation. The most critical part of the setup is the region between the capillary and the skimmer, where the measured pressure is 10^{-1} mbar, i.e. too high to use the approximation of molecular flow. Moreover, the pressure gradient of six orders of magnitude between the entrance of the capillary (10^3 mbar) and the region after the skimmer (10^{-3} mbar) is such that fluid dynamic behaviour of neutral molecules in the buffer gas strongly influence the ion beam trajectories.

Numerical approaches [49] based on the solution of the Navier-Stokes equations and direct simulation Monte Carlo (DSMC) methods [194,195], predict that the flow velocity quickly increases downstream the capillary, mostly near the core of the beam, due to the aerodynamic drag and ‘pump’ effect of the vacuum from the skimmer chamber. In this scenario, the buffer gas turns into a supersonic flow [49], and due to the high gas density of this region, the ion properties can be assumed to be equal to those of the gas.

While the presence of a static background gas can be included in the basic package for SIMION simulations, fast expansion and turbulence effects require dedicated software or programming packages. Nevertheless, they significantly affect and perhaps even dominate the beam parameters with respect to electrostatic constraints in this first part of the apparatus and, as a consequence, the entire simulation.

In order to circumvent this limited knowledge of the initial parameters due to all the physical effects that is not possible to take into account without specific software and techniques, a semi-empirical approach has been adopted. This consists in testing several combinations of ‘fictitious’ initial ion kinetic energies and background pressures in the region between capillary and skimmer, including values different from real/realistic ones (KE \sim 30 meV and P \sim 10^{-1} mbar). For each (KE, P) pair the trend of the ion current on the skimmer and at the exit of the octupole as well as the kinetic energy distribution of the ions after the L12 lens versus the voltages applied at several electrodes (capillary, tube lens, octupole reference and lens L11) have been simulated. The comparison with the experimentally measured currents provides the essential feedback between the ‘real’ world of the experiments and the ‘virtual’ one of the simulations. The (KE, P) pair that consistently provides a good representation of the experimental results:

- current read on skimmer, I_{sk} ;

- current read on channeltron, I_{ch} ;

is assumed as ‘good’ initial condition. With this approach, it has been assumed that, despite the fact that the used initial conditions may be not the real ones, kinematic effects on the ion transmission lead to realistic properties. As it will be discussed in the next section, the ion beam kinetic energy turned out to be a more sensitive parameter, and its characterisation has required a more careful evaluation of the simulated results.

5.2 Apparatus transmission vs scanning voltages, a qualitative overview

In this section, the results obtained with the simulations and their comparison with the experimental data obtained from the setup in equivalent conditions (geometry and voltages) are reported and discussed. Tests have been performed with a solution of rhodamine 6G ($m = 480$ Da) at a concentration of $1.5 \cdot 10^{-5}$ mol in water and ethanol (1:1) and 0.5 % of acetic acid.

As already introduced in section 2.1.4.2, the transmission of the setup has been assessed by monitoring the electron current produced by the ion beam impinging on an optical element along the ion beam path and a channeltron detector at the end of the line.

Reading small currents, in the pA scale, on a polarized electrode is not easy, due to the background noise of the power supply that introduces excessive disturbs. From previous tests it has been observed that the skimmer voltage needed to operate correctly the spectrometer is in the range 0 – 10 V. Then, it is possible to set it to 0 V and to connect it directly to the picoammeter for current reading, without dramatic effects on the setup behaviour. Therefore, the skimmer is the most natural check-point to monitor

experimentally the stability of the ion beam (I_{sk}) at a very early stage in the setup. The I_{ch} instead provides information about the overall transmission of the setup. It is important to keep in mind that, besides being located at different stages along the line, I_{sk} represents the fraction of ions that, hitting the skimmer, is not transmitted and will not be counted in I_{ch} . Therefore, I_{sk} and I_{ch} carry complementary information. While I_{sk} is a very well suited information to monitor the stability, for the optimisation of the transmission the most relevant parameter is I_{ch} , and its trend vs a scanning voltage is expected to be very different from I_{sk} , as will be shown in sections 5.2 and 5.4.

The determination of the currents on skimmer, I_{sk} , and channeltron, I_{ch} , vs a scanning voltage has been used to identify the best experimental conditions for maximum transmission. Peculiar features and trends can be observed in Figure 5.1 -Figure 5.4 (top panels). The goal is i) to identify 'good' ion beam initial parameters (pressure, kinetic energy, source region, direction of emission, etc.) to reproduce these experimental trends of currents vs applied voltages and ii) to provide a clear picture of the physical processes behind the observed trends.

To qualitatively describe the properties of the ion beam, images obtained from simulations (Figure 5.1 - Figure 5.4 bottom panels) will be used, while the details of the results of the simulations will be discussed later in section 5.4.

In Table 5.1 the typical voltages used are reported; except for the 'scanning voltage', all the other values are fixed during experimental and 'virtual' (i.e. simulated) scans. In this description, scan with respect to the skimmer and lens L12 are not considered because:

- skimmer is held to ground to measure current and is used as reference for all other voltages. The potential role of $V_{sk} \neq 0$ will be discussed in the conclusions.
- lens L12 is heavily influenced by the high voltage applied to the cone of the channeltron; furthermore, its role in 'guiding' the ion beam towards the next stage of the apparatus, in the polarisable gate valve, will be completely different in the final configuration of the apparatus. Therefore, the study of the role and optimisation of L12 is postponed to the next stage of the project, when the whole apparatus will be assembled.

It is worth mentioning here that the present work is based on the optimisation of the ion transmission, but it does not take into account the composition of the ion beam, in terms of preservation/fragmentation of the parent molecular ion, clustering or desorption of the solvent.

Electrode	Voltage (V)	note
capillary, V_{cap}	15	
tube lens, V_{tl}	40	
skimmer, V_{sk}	0	
octupole reference, V_{oct}	-2 / -25	See right figure for octupole RF parameters
octupole amplitude	55	
lens 11, V_{L11}	-40	
lens 12, V_{L12}	-40	
channeltron, ch	-1700	

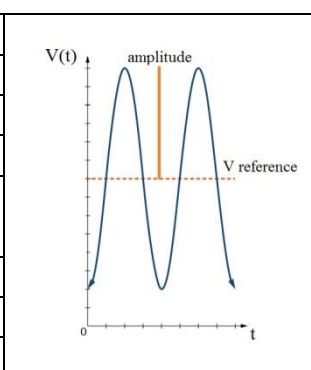


Table 5.1. Typical parameters for operating the apparatus. This setting is the result of a preliminary survey of the apparatus behaviour. RF parameters for the octupole are described in the right panel.

In the following, the role of the most relevant optical elements in this region are analysed one by one. The combination of capillary, tube lens and skimmer can be considered as a non-conventional three element lens.

5.2.1 Capillary voltage scan

The ion beam can be drastically influenced by the voltage on the capillary (V_{cap}), as shown in Figure 5.1. If the applied voltage is too negative, the (positive) ion beam is attracted back towards the capillary itself (Figure 5.1.A) and both I_{sk} and I_{ch} are negligible. Increasing the applied voltage around zero or slightly positive values, ions are pushed away from the capillary and are able to reach the skimmer: some will hit the skimmer (resulting in an increasing I_{sk}), while others will be able to move beyond it (producing a rising I_{ch}), and both currents increase. At $V_{cap} = 10 - 20$ V, the ion beam is efficiently guided through the skimmer aperture and I_{ch} reaches its maximum intensity (Figure 5.1.B). At larger V_{cap} values, ions are accelerated too much, their trajectories are not deflected and only a fraction of the ions crosses the skimmer (Figure 5.1.C), while others hit not only the outer, but also the inner part of the skimmer. In this range I_{sk} keeps increasing while I_{ch} decreases, also because of the large divergence of the beam entering the octupole. Eventually, both currents reach the plateau, which is a maximum for I_{sk} and a minimum for I_{ch} .

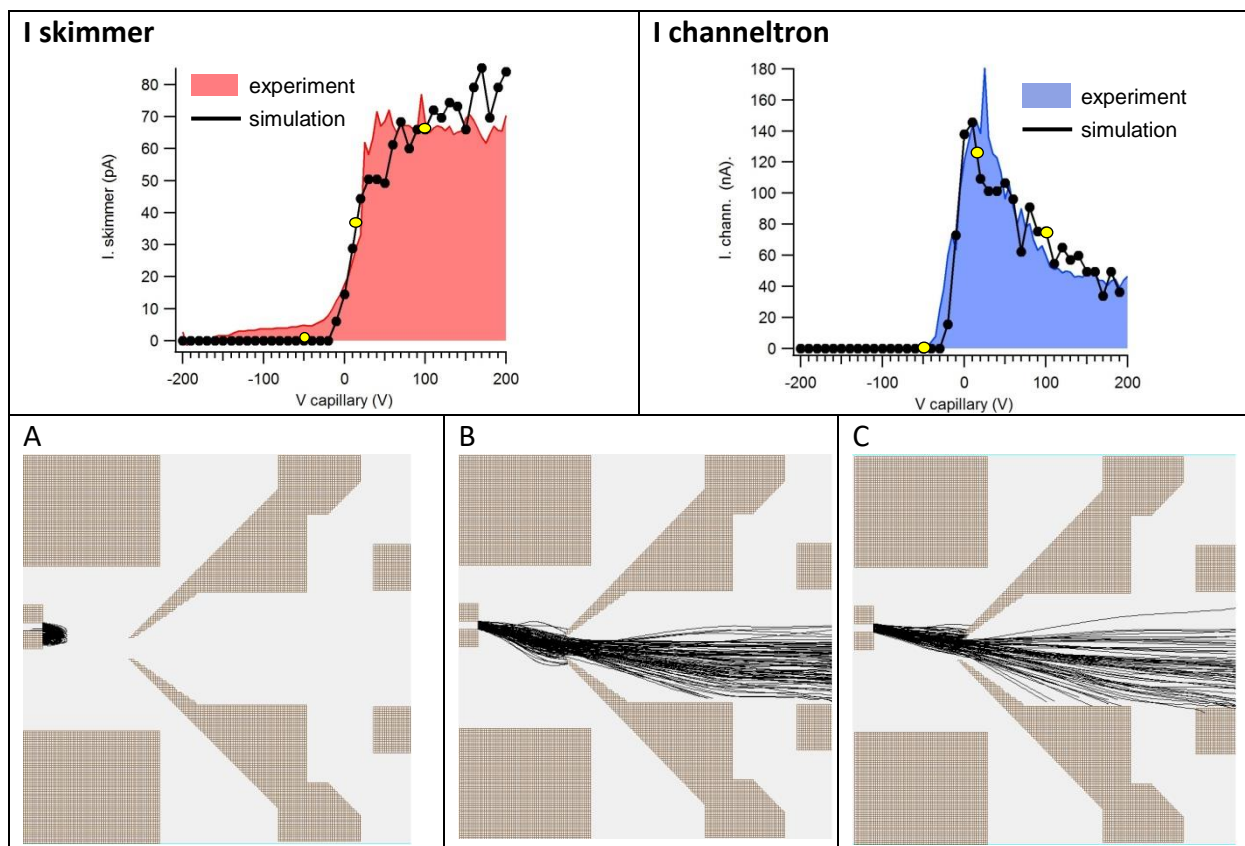


Figure 5.1. Top) Experimental and simulated I_{sk} (left panel) and I_{ch} (right panel) obtained by varying the voltage applied to the capillary (V_{cap}). **Bottom)** Snapshots of simulations in the capillary – skimmer region of the apparatus: each figure shows trajectories of 100 ions when $V_{cap} = -50$ V (A), 15 V (B) and 100 V (C) marked by the yellow dots in the top panels. It is to be noted that the skimmer is intentionally placed off-axis with respect to the capillary for reducing the gas load in the octupole chamber.

5.2.2 Tube lens voltage scan

The tube lens is the optical element surrounding the capillary-skimmer region. Its role is to focus the ion beam towards the skimmer hole, facilitating maximum transmission of the

beam through this region. As for the previous case, with the aid of simulations it is easy to rationalise the observed behaviour of the measured I_{sk} and I_{ch} : if the tube lens voltage (V_{tl}) is too negative, ions are attracted to the tube lens itself, the beam is completely defocussed and both I_{sk} and I_{ch} are negligible (Figure 5.2.A). When V_{tl} becomes positive, it begins to function as focussing element and both I_{sk} and I_{ch} increase (Figure 5.2.B) as the beam waist reduces and the ions pass through the skimmer hole. In particular, when the beam is better collimated I_{ch} reaches its maximum value (Figure 5.2.C). Further increases of the V_{tl} focussing field act as a barrier at the skimmer interface, a fraction of the ions (depending on angular spread and kinetic energy) is deviated back towards the capillary and both currents decrease (Figure 5.2.D), up to the point where no ion is transmitted towards the octupole with proper conditions to reach the end of the transport line.

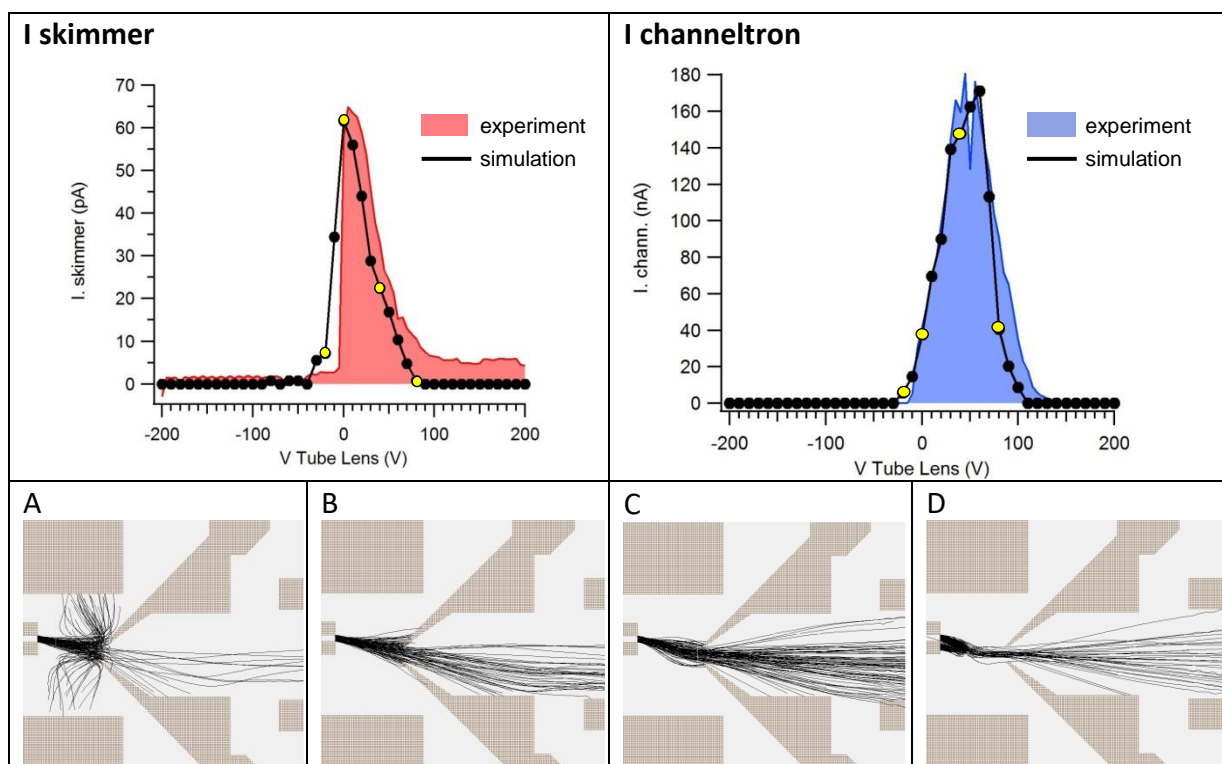


Figure 5.2. Top) Experimental and simulated I_{sk} (left panel) and I_{ch} (right panel) obtained by varying the voltage applied to the tube lens (V_{tl}). **Bottom)** Snapshots of simulations in the capillary – skimmer region of the apparatus: each figure shows trajectories of 100 ions when $V_{tl} = -20$ V (A), 0 V (B), 40 V (C) and 80 V (D) marked by yellow dots in top panel.

5.2.3 Octupole reference voltage scan

The octupole reference (V_{oct}) is the reference DC voltage for the octupole radio frequency, and its value is quite critical and relatively sharp for the transmission of the ions after the skimmer. Its functioning is strictly connected to the setting of its neighbouring optical elements, i.e. the exit lenses L11 and L12.

As it is clearly visualised in the simulations, if V_{oct} is too negative with respect to V_{L11} and V_{L12} , the octupole operates as a trap where the ions are either i) lost by hitting the octupole rods or escaping the field (Figure 5.3.A) or ii) continue to oscillate in the octupole region (Figure 5.3.B and C). This ‘trapping mode’ of operation is clearly demonstrated in Figure 5.3.B, where only one ion trajectory is reported. This figure shows how the ion reverses its flight direction along the octupole axis several times. According to the simulations, when the

time of flight of a single trajectory becomes too long (more than 2 ms) with respect to 'normal' one (< 0.1 ms), then that particular ion trajectory is aborted.

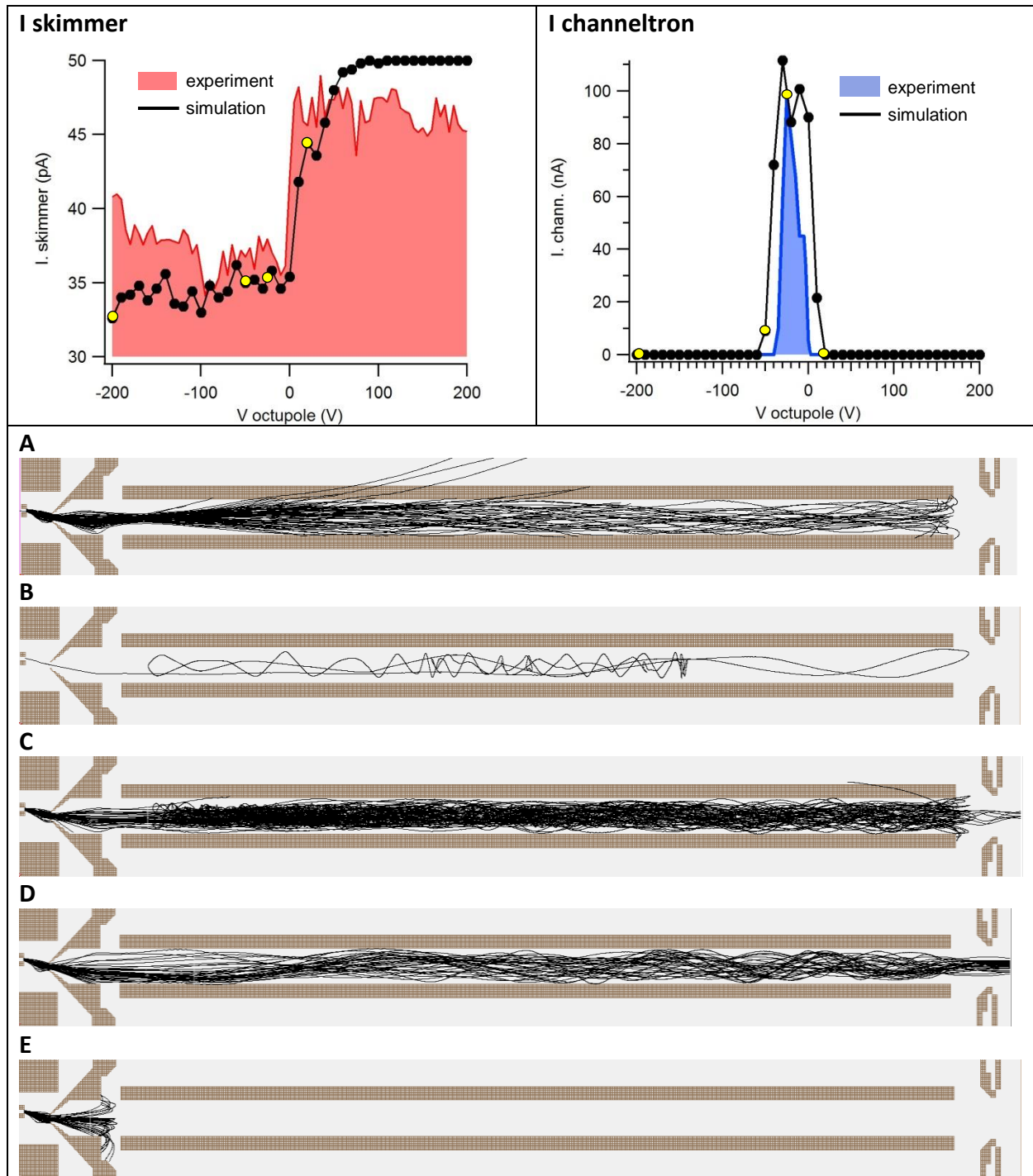


Figure 5.3. Top Experimental and simulated I_{sk} (left panel) and I_{ch} (right panel) obtained by varying V_{oct} . **Bottom** Snapshots of the simulations of the entire first stage of the apparatus: each figure shows trajectories of 100 ions, except for figure B where only one ion is used in the simulation in order to better show the 'ion trap' mode of operation of the octupole. Applied voltages are $V_{oct} = -200$ V (A), -50 V (B,C), -25 V (D) and 20 V (E), marked by yellow dots in the top panel.

This 'ion loss mechanism' is very common in the simulation of this mode of operation, where the octupole works as an ion trap. This mode of operation suggests that ions can be trapped for really long times in the octupole and a careful optimisation of the operating conditions can be used to achieve the bunching of the ion beam, i.e an operation of the octupole in

pulsed mode rather than ion guide (D). On the top panel of Figure 5.3 the I_{ch} trend versus V_{oct} shows how the octupole works as ion guide for a well defined region of V_{oct} (-40 V - 0 V). If V_{oct} is too positive with respect to the skimmer voltage (at ground potential in our case), the ions cannot enter at all in the octupole: they are rejected by the too high potential barrier that they cannot overtake, and hit back on the skimmer (Figure 5.3.E), resulting in an increased I_{sk} .

5.2.4 Lens L11 voltage scan

Lens L11 is the first element of the exit lens from the octupole and it has a slight conical shape ending in a 6 mm aperture. It has a dual purpose, acting as i) 'mechanical' differential pumping element between the octupole and its next stage, and ii) optical element to focus/collimate the ion beam emerging from the octupole. The skimmer is too far from the L11 to be affected by the changes in V_{L11} . Thus I_{sk} in these measurements can be used to check for the stability of the beam.

The I_{ch} shows a slow increase for V_{L11} approaching zero from negative values, followed by a sharp step, where the current drops to zero. If V_{L11} is too negative, ions are too tightly focused, gaining a large divergence immediately after and only a fraction reaches the CEM (Figure 5.4.A); in this situation I_{ch} is high but does not reach the maximum. On the opposite, if V_{L11} is too positive, ions are repelled towards the octupole (Figure 5.4.C) and I_{ch} is zero. In intermediate conditions, there is a range of optimal values of V_{L11} that maximize I_{ch} (Figure 5.4.B).

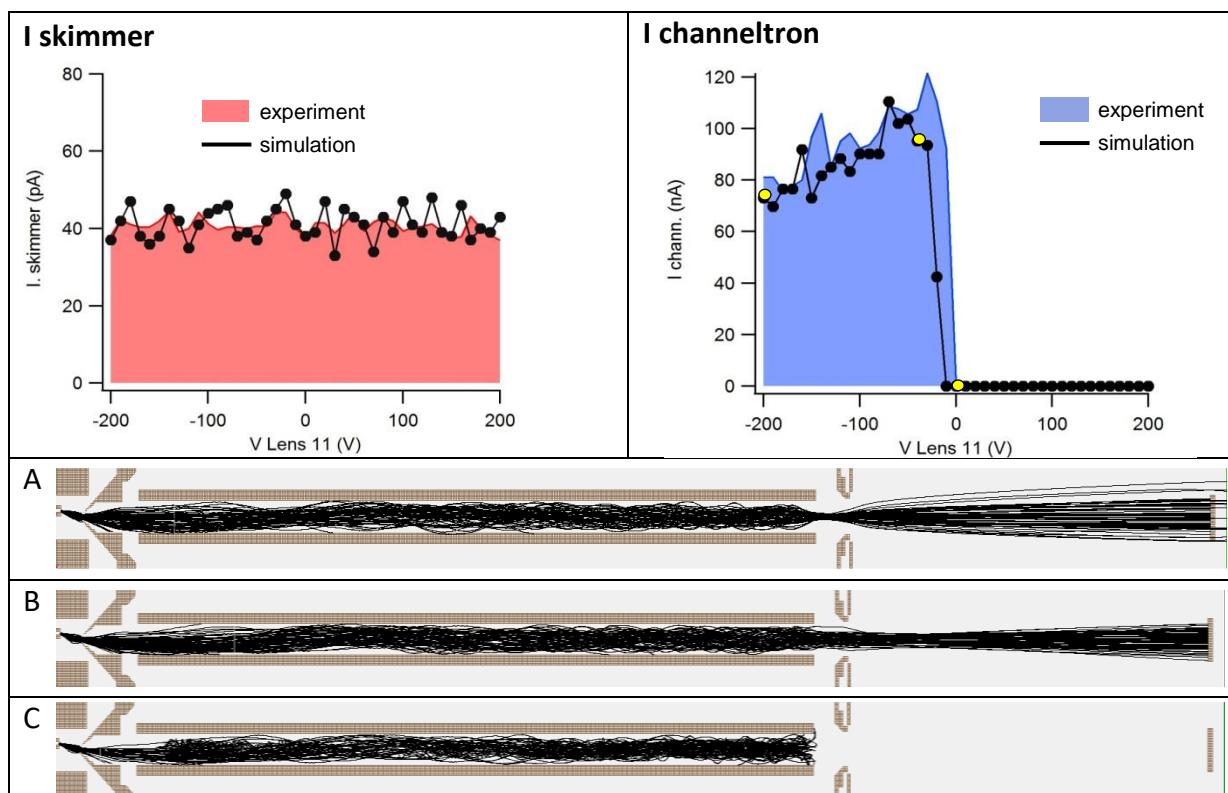


Figure 5.4. Top) Experimental and simulated I_{sk} (left panel) and I_{ch} (right panel) obtained by varying V_{L11} . **Bottom)** Section of the whole first stage of the apparatus. Each figure shows trajectories of 100 ions obtained using $V_{L11} = -200$ V (A), -40 V (B) and 0 V (C), marked by yellow dots in the top panel.

This first qualitative description of the results of these four independent voltage scans has the great merit to disclose the physical picture behind the experimental observations and

trends, providing intuitive arguments to explain the role of each optical element in the transport of the beam.

In the following, the simulations will be discussed in more details, showing that they are a powerful tool also to obtain a quantitative description.

5.3 Choice of initial conditions for the simulations

In the simulations, the I_{sk} and I_{ch} currents are calculated by counting the number of ions impinging on skimmer and channeltron, respectively, as a function of a scanning voltage. In each of the graphs that will be shown in the following, these ‘simulated ion currents’ are then directly compared to the experimentally measured trends, using an arbitrary scaling factor.

During the voltage scans, a typical range of ± 200 V in steps of 10 V has been considered, launching 100 ions, which sample several initial conditions for each voltage setting. This amounts to 4100 ion trajectories simulated to obtain an entire scan, requiring a simulation time in the order of 10 - 20 minutes with a standard PC (processor i7-4790, CPU 3.60 GHz, Ram 16 GB).

The needed initial ion beam parameters for the simulations are:

MASS: ESI nebulises the solution of the analyte in very small droplets that, travelling through the heated capillary, should eventually be (almost) completely solvent-free: therefore, only ions with a mass of 480 Da (Rodhamine 6G) are considered in the simulations;

POSITION: the source region for the ions is the exit aperture of the capillary, 0.3 mm inner diameter, so x is fixed and y and z are chosen with a uniform probability distribution over the capillary bore and zero outside (see Figure 5.5 for the definition of x,y,z reference axis);

DIRECTION: to mimic the air flow in the capillary chamber, initial direction is fixed towards the skimmer orifice, values are chosen from a Gaussian distribution with a central value and a standard deviation of $0^\circ \pm 5^\circ$ and $13^\circ \pm 5^\circ$ for azimuth and elevation, respectively, see Figure 5.5;

PRESSURE and KINETIC ENERGY: as already mentioned in section 5.1, a procedure to select the ‘optimal’ values of pressure (P) and initial kinetic energy (KE) by performing simulations at different (P , KE) combinations has been adopted, comparing the simulated and experimental trends of I_{sk} and I_{ch} obtained by scanning V_{cap} in the range ± 200 V, as reported in Figure 5.6. Similar results, obtained by scanning the V_{ti} are reported in Figure 5.7. Plots in Figure 5.6 and Figure 5.7 refer to the (P , KE) combinations of Table 5.2.

Pressure, P (mbar)	Kinetic Energy, KE (eV)
b: 6×10^{-1}	1: 100
c: 6×10^{-2}	2: 10
d: 1×10^{-2}	3: 1
	4: 0.1

Table 5.2. Pressure and kinetic energy values for the simulations reported in Figure 5.6 and Figure 5.7.

In the experiment, the expected kinetic energy of the ions at the exit of the capillary would be in the range of 0 - 1 eV as based on arguments of thermalisation by collisions with the buffer gas in the heated capillary [49]. However, they are also expected to gain speed [48,49] by the dragging effect of the buffer gas expanding into the first vacuum chamber. Accordingly, in the simulations, we also considered two higher kinetic energy values.

In order to choose the best (P, KE) combination for the simulations to represent the experimental data, both experimental and simulated I_{ch} and I_{sk} vs V_{cap} and V_{tl} are reported, because these electrodes should be the most sensitive to the initial condition. The physical reasons for these P and KE chosen values are explained later in this section.

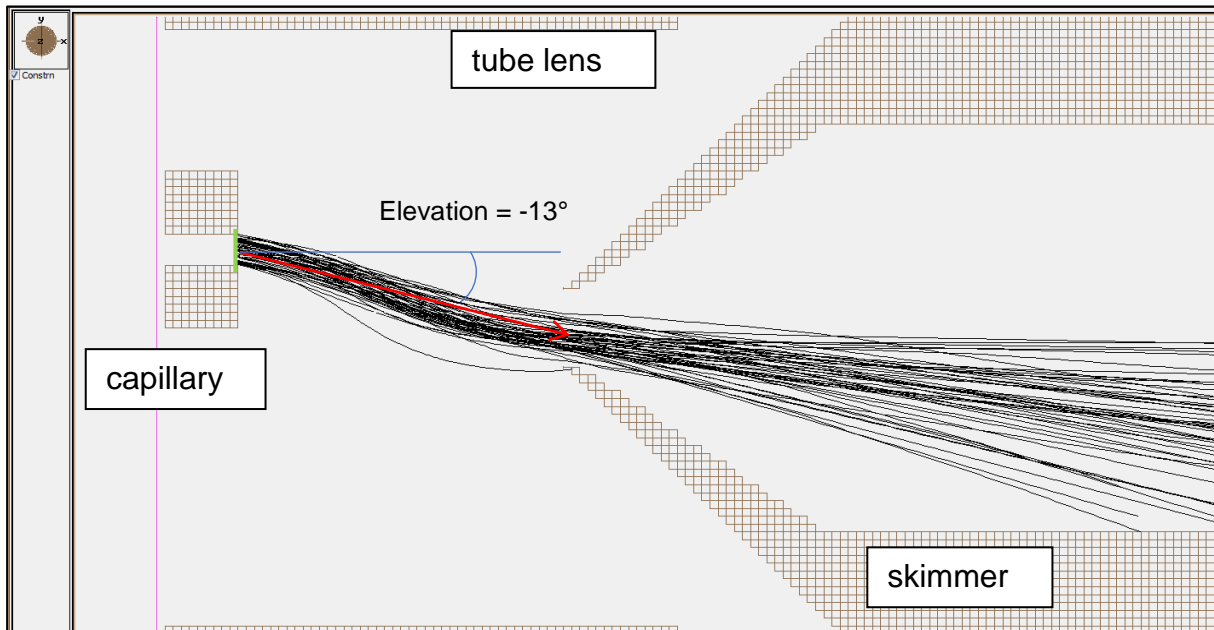


Figure 5.5. Snapshot of ions trajectories simulated with the SIMION program from the capillary to the skimmer according to the initial parameters defined above in the text. The green dots and the red arrow at the capillary exit indicate, respectively, the initial position and direction of emission of the ions.

Experimental pressure in the capillary chamber is 6×10^{-1} mbar, but from the analysis of Figure 5.6 and Figure 5.7 it is clear that using this pressure (red plots) simulations cannot reproduce the experimental data. This is particularly clear analysing I_{ch} , that is close to zero for each setting of applied voltages of V_{cap} and V_{tl} . Another interesting feature is the lack of sensitivity in the ion transmission with respect to the initial kinetic energy of the ions; this is due the high number of collisions with the buffer gas that thermalize the ions. Comparison with the experiments is even worse when using pressure values higher than 6×10^{-1} mbar in the simulations (data not shown).

Simulations performed at pressure values in the range of 10^{-2} mbar in the capillary chamber (green and blue plots in Figure 5.6 and Figure 5.7) show a relevant dependence from the initial KE. They are quite similar among themselves but, in particular from the analysis of Figure 5.7, it is clear that the 'optimal' combination of pressure and kinetic energy values to be used in the simulations to reproduce the experimental I_{sk} and I_{ch} trends are $P = 6 \times 10^{-2}$ mbar and $KE \approx 10 - 100$ eV. These values correspond to the simulations indicated by the green colour in Figure 5.6 and Figure 5.7.

While the selected pressure is lower than the real one (experimentally measured value is 6×10^{-1} mbar), the KE is much larger than the thermal kinetic energy.

This can be justified by considering a simple physical picture where:

- in the SIMION simulation the background pressure fills the capillary chamber like a static gas cell (molecules have random paths at the chosen pressure and temperature conditions) that is crossed by the ion beam pulled by just the electric field generated by the electrodes;
- in the real experiment, the ions travel together with the air flow pulled by the large pressure gradient from atmospheric pressure to the $10^{-1} - 10^{-3}$ mbar vacuum in the capillary and octupole chambers, respectively.

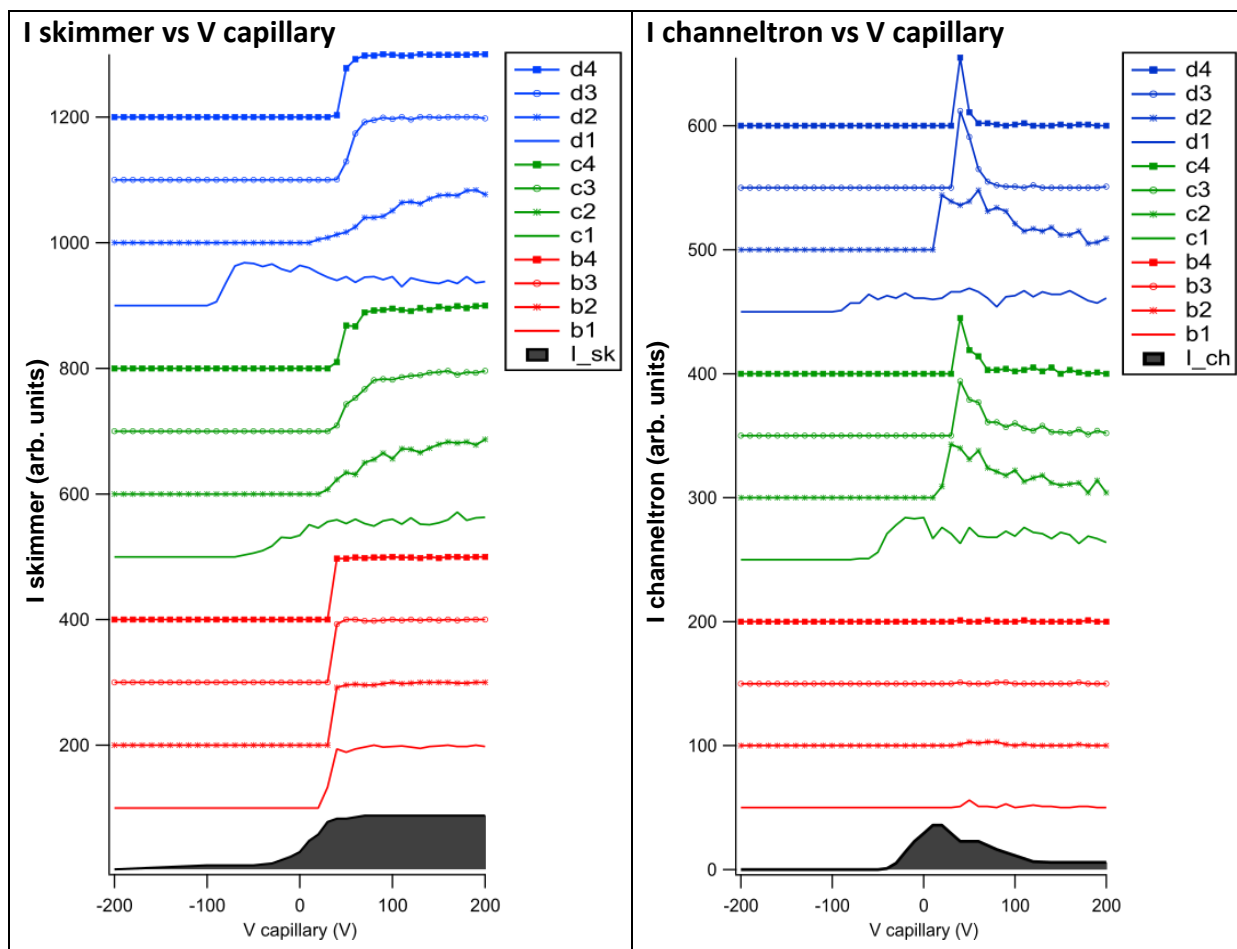


Figure 5.6. Simulated I_{sk} (left panel) and I_{ch} (right panel), versus the capillary voltage, V_{cap} , at several combinations of (P , KE) values in the capillary chamber (see Table 5.2 for correspondence between labels and values). For comparison, the experimental data from Figure 5.1 are also reported as black filled areas at the bottom of each panel.

As a consequence, it is reasonable to expect that the ions are pushed preferentially towards the skimmer orifice by the expanding buffer gas that drags them forward. This situation can be mimicked in a standard SIMION simulation by attributing a larger nominal KE to the ion beam and less number collisions (lower pressure). Having identified an ‘optimal’ P value and KE range, we have refined our search investigating in more detail the range 10 – 100 eV of KE, with a smaller step size. Figure 5.8 and Figure 5.9 report the simulated I_{sk} and I_{ch} obtained scanning the voltage applied to capillary and tube lens, respectively, at $P = 6 \times 10^{-2}$ mbar and several KE values of the ions between 10 and 90 eV.

In Figure 5.8, a clear shift of the onset of both the I_{sk} and I_{ch} ion currents towards more negative V_{cap} values can be observed for higher KE values. The shift is almost linear with initial KE. This can be qualitatively attributed to the fact that the higher is the initial KE, the lower is the voltage needed on the capillary to push the ions towards the skimmer. Beside the shift, there is another characteristic of I_{ch} that depends on KE: the absolute value of I_{ch} after the onset became less sensitive to V_{cap} for increasing KE and the ‘peak shape’ is broadened.

This may be due to the fact that faster ions are less sensitive to the applied capillary voltage and preserve their initial direction toward the skimmer aperture.

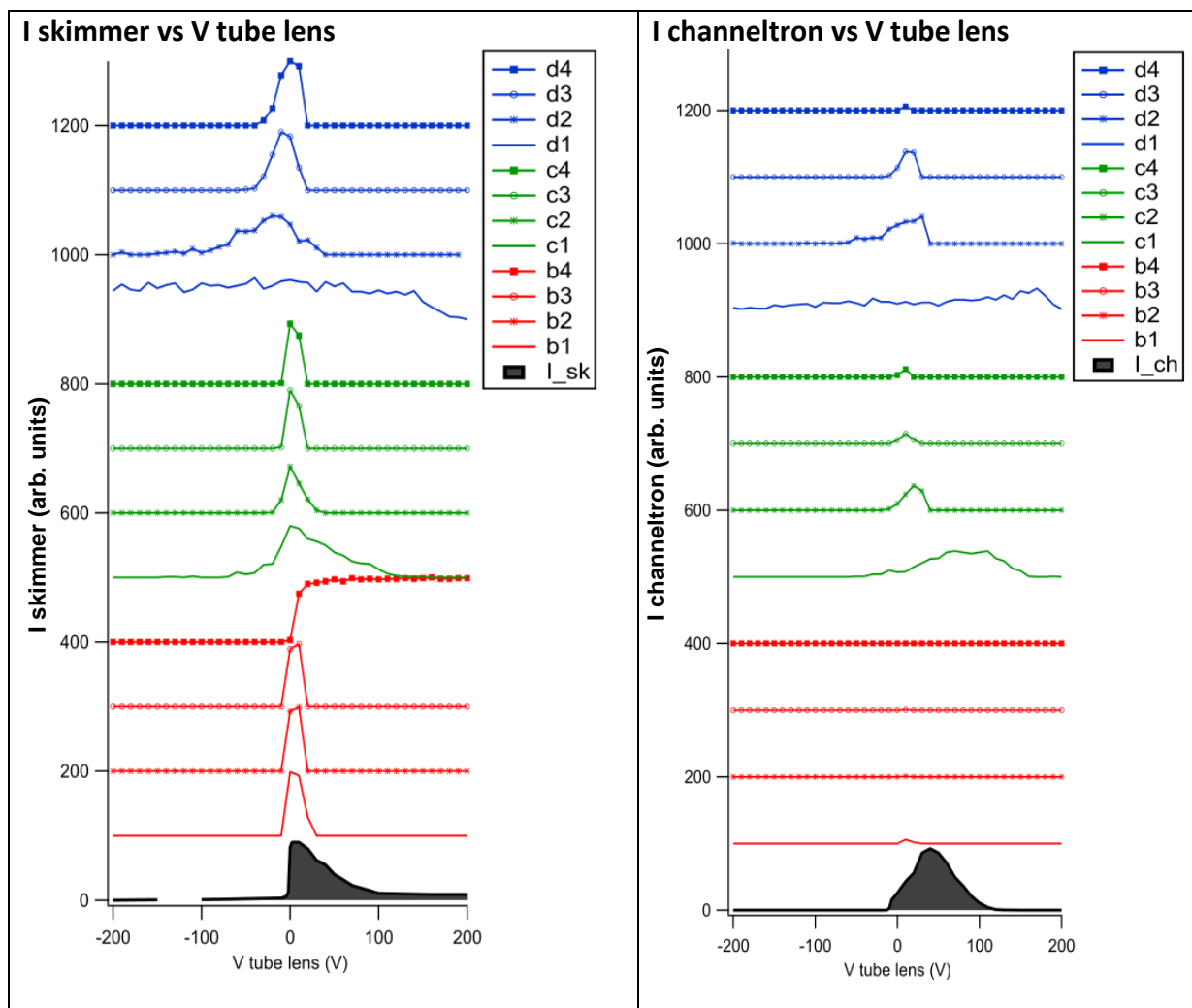


Figure 5.7. Simulated I_{sk} (left panel) and I_{ch} (right panel) versus V_{tl} at several combinations of (P, KE) values in the capillary chamber (see Table 2 for correspondence between labels and values). For comparison, the experimental data from Figure 10 are also reported as black filled plots at the bottom of each panel.

In Figure 5.9, where the role of V_{tl} at different KE is investigated, the most relevant effect of increasing the ion KE is to produce broader distributions vs the tube lens voltage, indicating (as for I_{ch} in Figure 5.8) a lower sensitivity to V_{tl} in the case of the faster ions. For example, I_{sk} in Figure 5.9 decreases more slowly to reach a negligible value at higher voltage for faster ions because they require a higher potential energy barrier to be blocked. In the same way, I_{ch} is broader with respect to V_{tl} because faster ions are less sensitive to the applied voltage and preserve their initial direction towards skimmer aperture.

In all cases discussed in Figure 5.8 and Figure 5.9, the closest correspondence between experimental data and simulations, in terms of position and width of the main features, is obtained with initial kinetic energy $KE = 50$ eV, so the (P, KE) pair of $(6 \times 10^{-2}$ mbar, 50 eV) is chosen in the simulations.

In conclusion, the selected initial conditions to be used in the simulations are summarized in Table 5.3. Simulations based on these initial parameters and the real geometry/voltage setting through the entire apparatus reproduce fairly well the experimental data in terms of ion transmission vs selected scanned voltages. However, the conditions reported in Table 5.3 might be not unique, in particular as far as the (P, KE) combination is concerned, because it has been 'fictitiously' selected among the explored combinations as the most suited one to reproduce the experimental ion transmission.

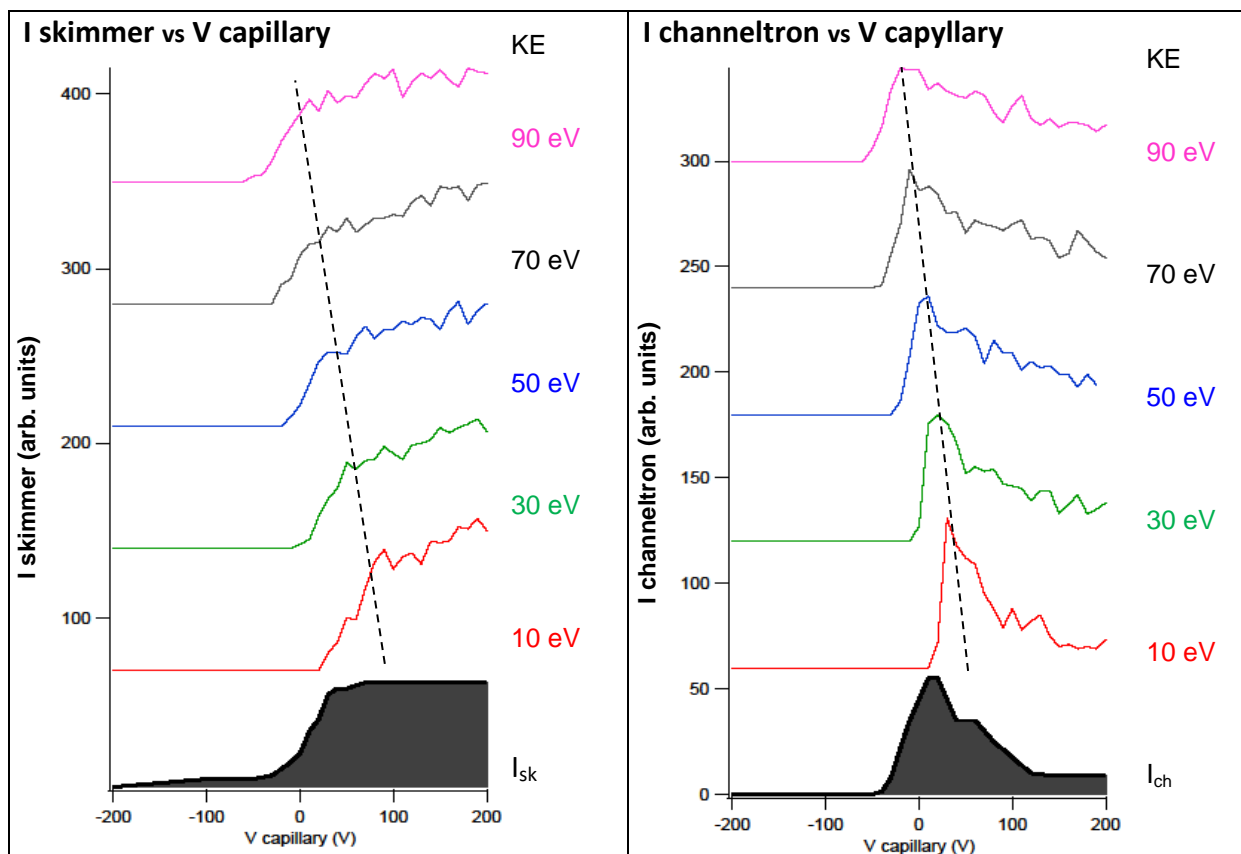


Figure 5.8. Simulated I_{sk} (left panel) and I_{ch} (right panel) by varying V_{cap} at $P = 6 \times 10^{-2}$ mbar and several initial kinetic energy values. For comparison, the experimental data are also reported at the bottom; the dotted lines indicate the shift.

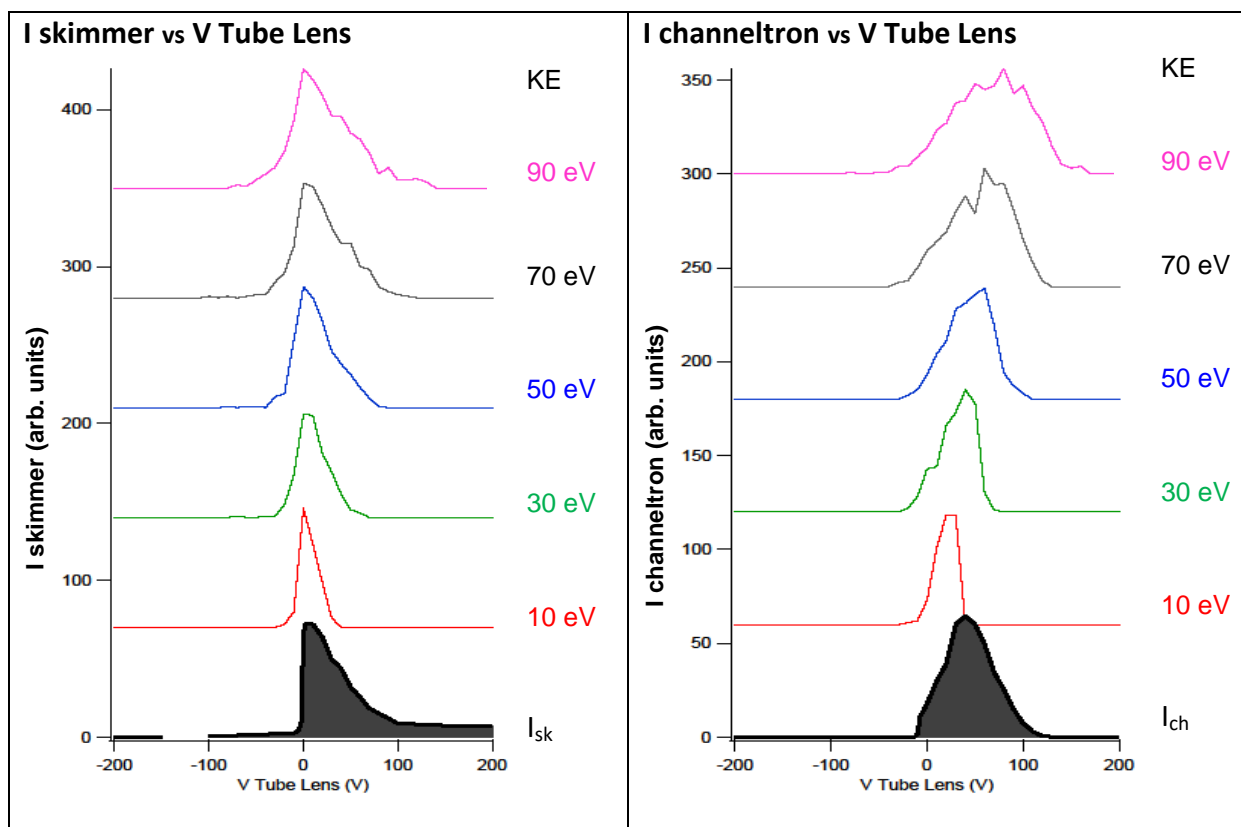


Figure 5.9. Simulated I_{sk} (left panel) and I_{ch} (right panel) by varying V_{tl} for several initial kinetic energy values. For comparison, the experimental data are also reported (black plots at the bottom).

Pressure in the capillary chamber	mass (Da)	azimuth angle (°)	elevation angle (°)	Kinetic energy(eV)	x	y (mm)	z (mm)
6.0×10^{-2} mbar	480	0 ± 5	-13 ± 5	50 eV	capillary tip	0.8/ 1.2	-0.2/ 0.2

Table 5.3. Initial conditions for the SIMION simulations of rhodamine 6G ion beam transmission.

5.4 Estimate of the ion beam kinetic energy

In Figure 5.8 and Figure 5.9, the simulations obtained with 50 eV initial kinetic energy are the most consistent with the experimental data in terms of the distributions of the ion beam intensity (I_{sk} and I_{ch}) vs scanning voltages. However, all simulations show a similar behaviour despite the large difference in the initial KE values; in this section the simulation will be pushed towards a more quantitative approach, investigating in detail the differences and similarities between simulated and experimental results in order to obtain information about the kinetic energy of the ion beam along the entire setup. To the purpose, another feature from the SIMION program will be exploited, visualising the potential landscape produced by the optical elements and experienced by the flying ions; considering only ions with a single positive charge, we refer indistinctly to the potential (measured in V) or potential energy (measured in eV).

5.4.1 The role of fluid dynamics

As discussed in the previous section, the main unknown in the simulations is the modelling of the background gas. To describe the fluid dynamics of the fast moving buffer gas and its drag effect on the electrosprayed ion beam, the possible theoretical approaches are related to two completely different regimes (see section 2.1.1), the continuum or viscous flow and the molecular flow.

A quantitative manner to discriminate by continuum, molecular and intermediate regimes is given by the value of the Knudsen number, K_n . The estimate K_n number (see section 2.1.1) for each region of our apparatus is reported in Table 5.4:

Region	Pressure (mbar)	n (molecules/ m ³)	λ (m)	L (m)	K_n
capillary	10^3	10^{25}	10^{-7}	10^{-3}	10^{-4}
tube lens	1	10^{22}	10^{-4}	10^{-2}	10^{-2}
skimmer	10^{-1}	10^{21}	10^{-3}	10^{-3}	1
octupole	10^{-3}	10^{19}	10^{-1}	10^{-1}	1
channeltron	10^{-5}	10^{17}	10^2	10^{-2}	10^4

Table 5.4. Knudsen number in the different regions of the experimental apparatus.

Table 5.4 clearly demonstrates how all flow regimes, from viscous (in the capillary) to molecular (in the detector chamber) are experienced by the ions and buffer gas travelling through our apparatus. This also explains how the SIMION simulations, that work well in the molecular flow regime, can be expected to become more and more realistic, with no need of 'fictitious' and semi-empirically adjusted parameters, as the ion beam progresses towards region of high vacuum conditions.

As it will be illustrated and discussed by several examples in this section, the lack of a realistic environment and simulating conditions for the early stage of the apparatus, i.e. considering static instead of flowing gas, has relevant consequences for the description of the kinetic energy of the ions. Some of the underlying physical mechanisms triggered by the flowing buffer gas are briefly introduced.

- A consideration relevant in the following descriptions concerns the velocity of the involved species: the macroscopic fluid velocity of the continuum flow is related to the velocity/kinetic energy of individual molecules, but it is not the same physical quantity.

- Another relevant observation, that concerns both experiments and simulations, is about the potential energy. To reach the skimmer from the capillary, the ions have to overcome a non-negligible energy barrier when standard voltages are applied. In the typical operating conditions ($V_{tl} = 40$ V and $V_{sk} = 0$ V, see Table 5.1), this barrier is about 17 eV when $V_{cap} = 15$ V and 39 eV when $V_{cap} = -20$ V (see Figure 5.10), respectively, corresponding to the conditions of maximum transmission and first onset in I_{ch} during the V_{cap} scan described in Figure 5.1.

Consistently with the results of the simulations in Figure 5.9, it is not possible to expect that thermal ions travelling from inside the capillary would be able to overcome these barriers. In the simulations, ion trajectories are launched with a ‘guessed’ initial kinetic energy high enough to make the ions to complete their travel considering also that a fraction of their initial kinetic energy is dissipated in collisions with the steady background gas, included in the simulation. In the experiment, instead, the background gas is not static (as in the simulations), but in motion. This is a really complex process, governed mainly by pressure gradients and apparatus geometry and does influence the ion flow in a decisive manner. Indeed, the flowing gas, whose density is several orders of magnitude larger than the ion’s one, undergoes a fast expansion in the region between the capillary and the skimmer gaining large velocities [49,192], continuously colliding with the ions and pushing them forward. This provides the necessary ‘drive’ to overcome the electrostatic energy barriers otherwise insuperable with the only force generated by the electric field of the electrodes.

Once again, it is useful to highlight that, in the region before the octupole, ions trajectories are influenced by the electric field, but they cannot be described in a realistic manner without considering the flowing background gas. Even though this ‘dragging effect’ is not included in the simulations, its existence has been somehow mimicked and taken into account in the previous section by the use of ‘fictitious’ initial (P , KE) parameters leading to a good description of the ion beam transmission vs scanning voltages.

- While in the approach described above a good qualitative description can be achieved, quantitative analysis of the kinetic energy is a far more stringent test and requires more attention. On the one hand, when ions enter the octupole chamber the gas flow is less relevant because pressure is lower (10^{-3} mbar) and the absence of small orifices does not produce fast gas streams. Then in the octupole region a standard description of collisions with a resting background gas is applicable. Ions finally reach equilibrium with background gas and kinetic energy is mainly governed by the electric field. On the other hand, the parameters of the ions entering the octupole chamber are ‘inherited’ by the simulation in the capillary - tube lens – skimmer region. Even though these did not seem to affect so much the simulated transmission vs scanning voltages, it will be shown that they can significantly affect the KE properties and behaviour.

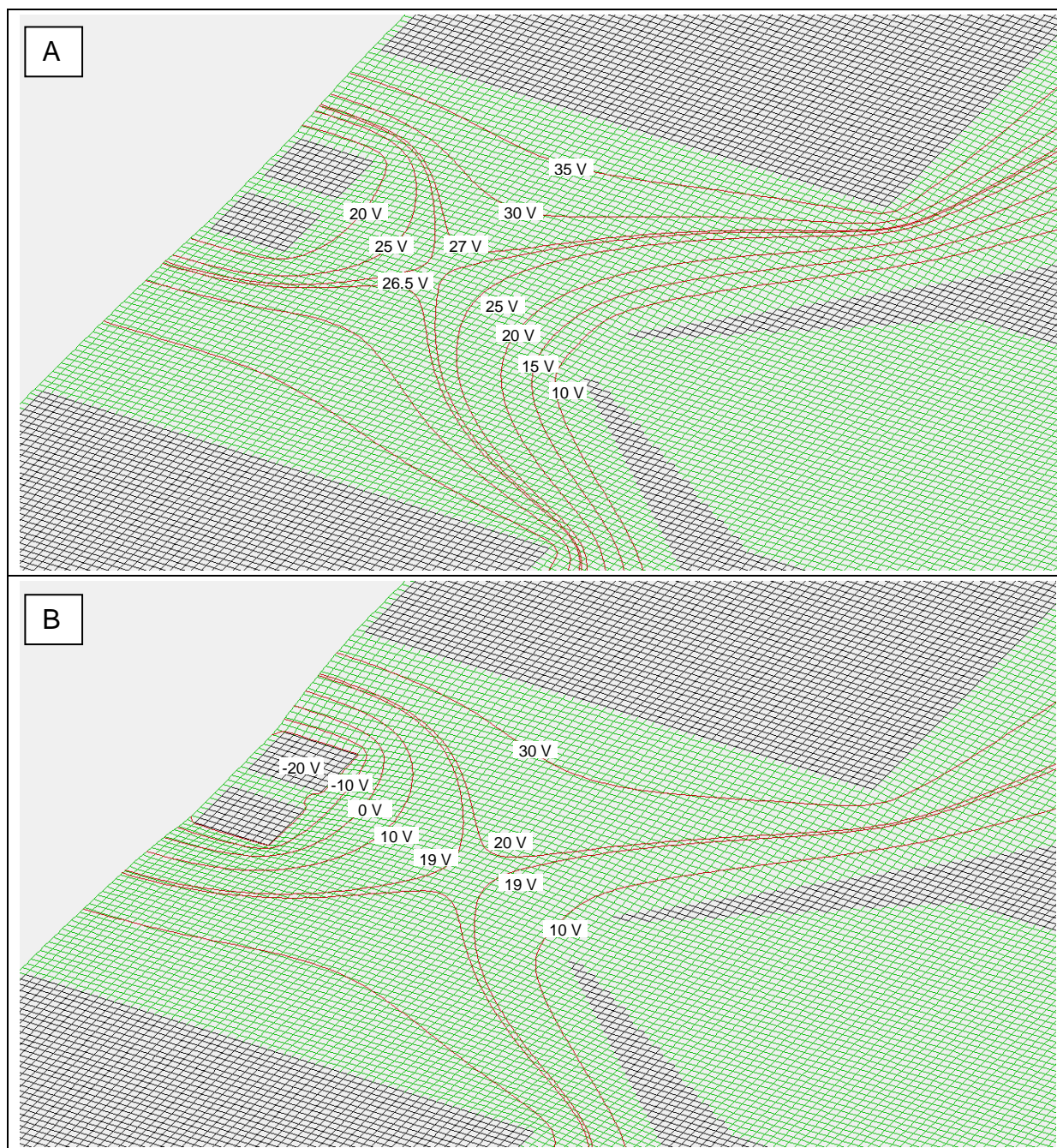


Figure 5.10. Potential surface on a plane across the axis of the instrument; the black grids represent capillary, tube lens and skimmer. Two different voltages setting are considered: **A)** $V_{cap} = 15 \text{ V}$, $V_{tl} = 40 \text{ V}$, $V_{sk} = 0 \text{ V}$ (maximum transmission) and **B)** $V_{cap} = -20 \text{ V}$, $V_{tl} = 40 \text{ V}$, $V_{sk} = 0 \text{ V}$ (first onset of I_{ch} in V_{cap} scan). Some equipotential lines are indicated in red with relative potential values indicated to better define the saddle shape of potential surface. The focussing effect generated by this 'three-elements' lens as well as the rising of the energy barrier that the ions have to overtake to pass beyond the skimmer are clearly visible.

5.4.2 Differences and analogies between experiments and simulations

The kinetic energy and energy spread of the ions at the end of the octupole should be less affected by background gas dynamic, and this can be properly taken into account by the electron optics simulations. To obtain quantitative information about the kinetic energy distribution, several measurements and simulations of I_{ch} versus the V_{L11} voltage for three different values of the octupole reference, $V_{oct} = -10, -30$ and -60 V, respectively (Figure 5.11) have been performed to produce a variable potential energy barrier at the octupole exit. In general a broad 'step-function' is observed, even though in some cases, most evidently in Figure 5.11.A, but likely also in Figure 5.11.B and Figure 5.11.C, the experimental trend is more complex than in simulations. After a detailed investigation, this modulation is believed to be a purely instrumental artifact, and can be explained by considering the channeltron efficiency (see appendix at the end of this chapter), without anyway modifying the major information on the kinetic energy of the ion beam, embedded in the I_{ch} vs V_{L11} trend.

The fundamental idea is that for larger and positive values, the lens L11 raises a high potential energy barrier that rejects ions towards the octupole, the transmission (I_{ch}) decreases and eventually drops to zero. Therefore, the step in I_{ch} and the slope contain respectively information about the mean KE value and the dispersion of the distribution of the kinetic energy of the ions.

In Figure 5.11 it is evident that I_{ch} begins to decrease for values of V_{L11} close to and less negative than V_{oct} ; moreover, it is also interesting to note that the simulated I_{ch} slope is less sharp than in the experiment, and this difference increases for more negative V_{oct} values with respect to the grounded skimmer. Also, the simulated I_{ch} vanishes at values of V_{L11} less negative than in the experiments. This indicates a higher kinetic energy in simulation than in experiments, and that the kinetic energy spread in simulations increases with more negative V_{oct} .

In order to understand the source of these differences, the potential energy profile along the instrument axis for several voltage settings has been analysed (Figure 5.12). The potential energy is close to zero in the skimmer ($x = 5$ mm), then drops rapidly due to the negative octupole reference and at the end of the octupole, in the region of lenses L11 and L12 ($x = 150 - 160$ mm) it is modulated by the voltage V_{L11} (indicated in the legends of Figure 5.12). This produces an energy barrier with respect to the octupole reference. The higher the barrier, the lower is the number of ions that can reach the detector, because only ions with sufficiently large kinetic energy can overcome the electrostatic barrier.

Then in Figure 5.13 the evolution of the kinetic energy of the ion beam along the instrument has been analysed performing simulations for $V_{oct} = -10, -30$ and -60 V. In each plot, the central line is the mean kinetic energy mediated over 100 - 150 different ion trajectories, while the band width describes the standard deviation.

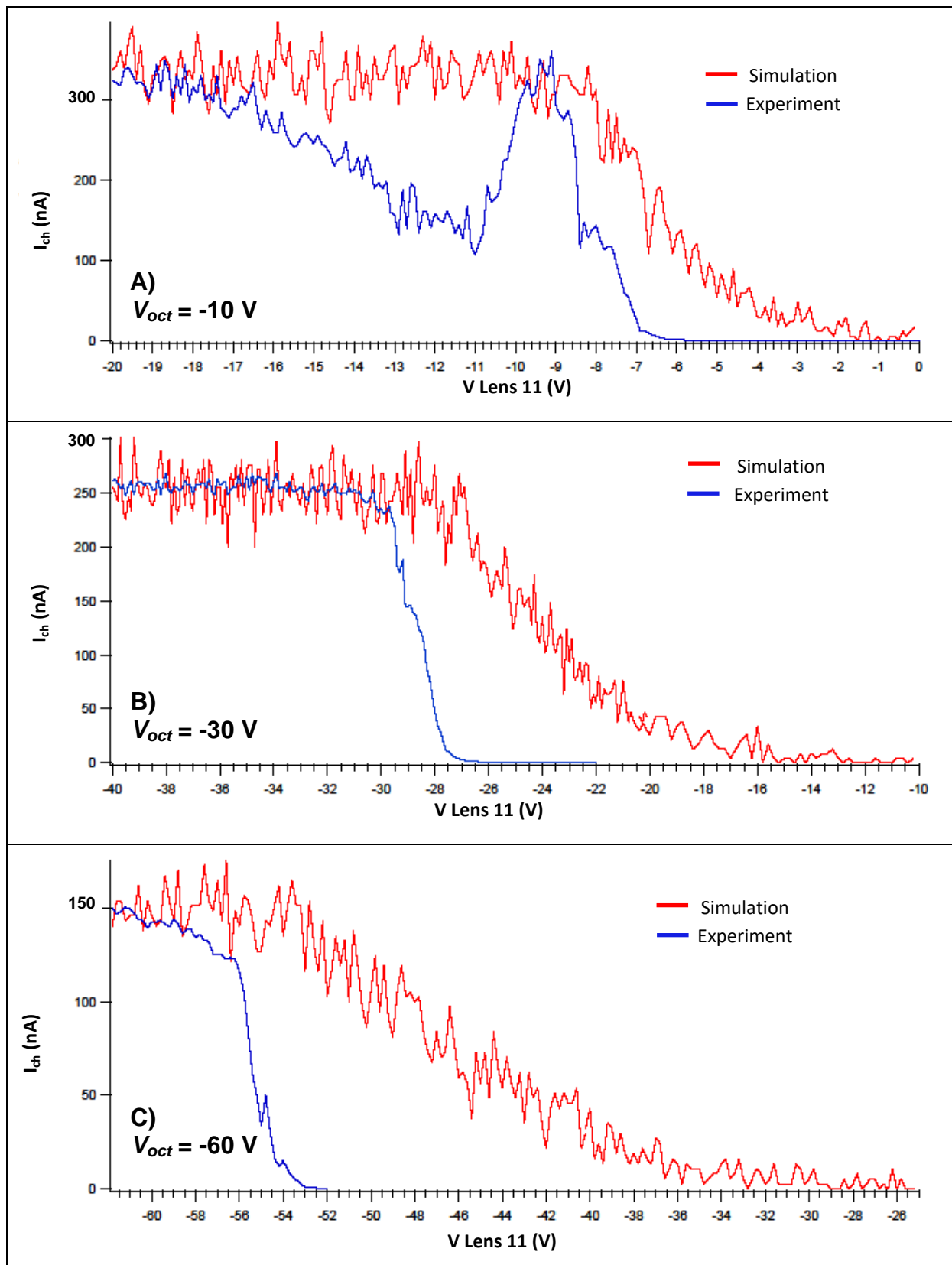


Figure 5.11. Simulated and experimental I_{ch} obtained scanning V_{L11} for three different values of V_{oct} : -10 V (A), -30 V (B) and -60 V (C). The simulated I_{ch} is normalised to the experimental one at maximum. All other voltages are the same as reported in Table 1 except for V_{L12} that has been chosen in order to avoid another energy barrier besides the one produced by lens L11; V_{L12} is -40 V, -60 V and -200 V for (A), (B) and (C), respectively.

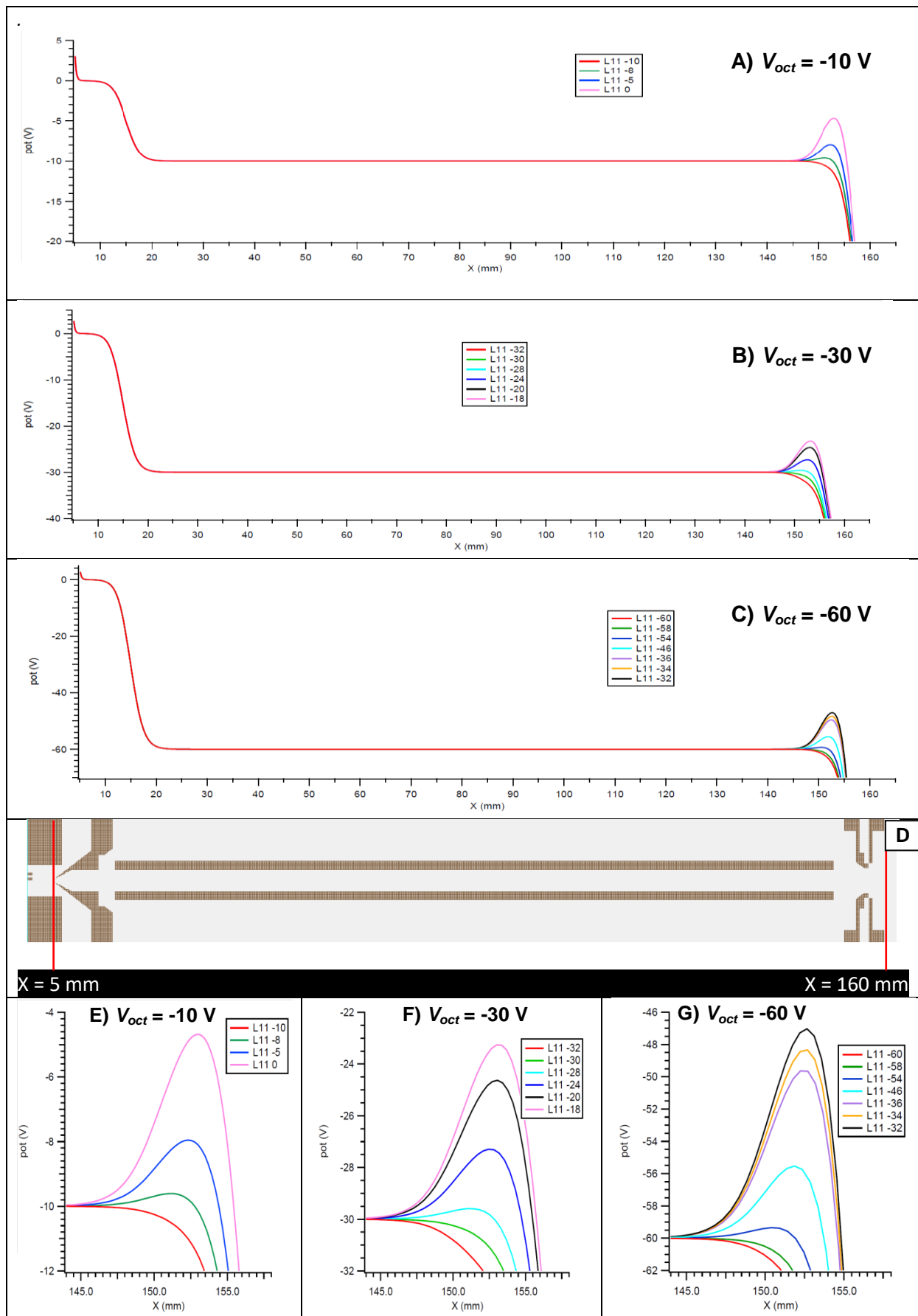


Figure 5.12. Profile of the potential on the apparatus axis for several V_{L11} for each V_{oct} considered in Figure 5.11 (A-C) and a scheme of the apparatus (D) to visualise the corresponding X position. Panels E-G report a zoom of the area with the potential barrier produced by lens L11. Values of V_{L11} are reported in the legends.

5.4.3 Experimental vs simulated: explanation

In the simulations, the ions arrive at the skimmer with 10 - 15 eV KE, and this is substantially independent from the specific value of V_{oct} . The KE values reported in Figure 5.13, moving from the skimmer towards the octupole, show that the ions are accelerated by the negative V_{oct} voltage to a kinetic energy equal to the voltage difference between skimmer and octupole reference, i.e equal to V_{oct} . Then they lose part of the kinetic energy by collisions with the residual gas along the path in the octupole guide. With the current simulation parameters, the number of collisions between ions and residual gas is not large enough to dissipate all their KE and at the exit of the octupole the ions still preserve some residual kinetic energy with an energy spread proportional to their kinetic energy at the entrance of the octupole (Table 5.5).

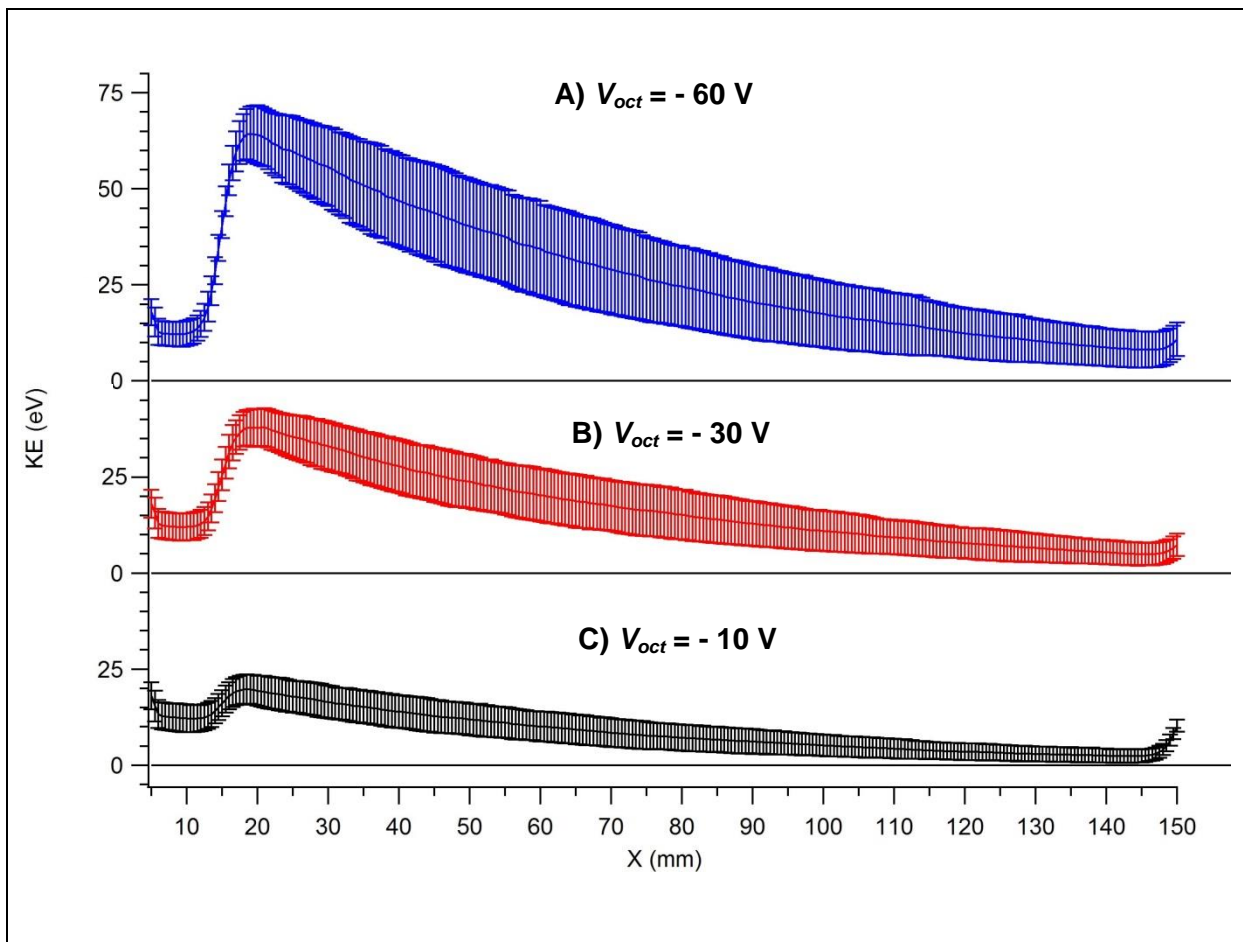


Figure 5.13. Simulated mean value of kinetic energy (central line) including relative standard deviation obtained considering 100-150 ions for three different values of V_{oct} . The vertical bars on each data point identify the standard deviation of the kinetic energy. This figure shows that, according to the simulations, the increase of V_{oct} results in higher KE of the ions at the end of octupole.

The mean values of the residual KE, including relative standard deviation, at $x = 140 - 150$ mm are consistent with the value of the energy barrier at the V_{L11} value (Figure 5.12) where the simulated I_{ch} (Figure 5.11) approaches zero (see Table 5.5). This further confirms that the width of the step and the slope of the I_{ch} vs V_{L11} contain quantitative information on the kinetic energy of the ions.

V_{oct} (V)	Mean residual KE (eV)	KE standard deviation (eV)	Mean KE + standard deviation (eV)	V_{L11} (V)	Potential barrier (V)
-10	2.4	1.8	4.2	-2	4.0
-30	5	3	8	-16	8.2
-60	8.1	4.7	12.8	-32	13

Table 5.5. Comparison between simulated energy barrier on axis (Figure 5.12) and ions ‘residual’ kinetic energy (Figure 5.13) at different V_{oct} voltages.

5.4.4 The energy barrier controlled by lens L11

The previous sections have shown how simulations have the potential to provide relevant information, but still need to be ‘interpreted’ and understood before their results can be directly compared with the experiments.

An aspect to consider, before finally obtaining a quantitative determination of the real KE of the ions, is that the filtering of slow ions is ruled by the height of the barrier in the L11 region. This is not uniform over the finite size of the ion beam and can be also influenced by the other optical elements in this region. Therefore, it is mandatory to take into account the shape of the potential energy barrier not only on the axis of the instrument, as reported in Figure 5.12, but also off axis, and we need to correlate V_{L11} to the effective height of the barrier. By removing the amplitude of the octupole radio frequency and considering only the octupole reference voltage, the potential energy at five different distances, d , from the axis ($d = 0, 0.6, 1.2, 1.8, 2.4$ mm) has been obtained for three values of V_{L11} for each of the V_{oct} values of Figure 5.12.

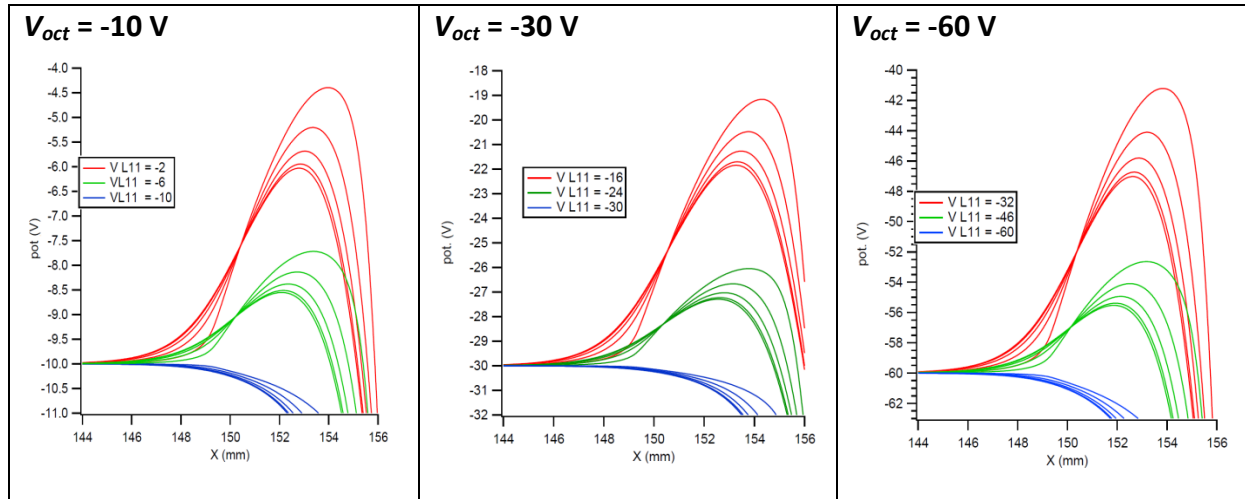


Figure 5.14. The electrostatic potential along lines parallel to the axis of symmetry of the octupole at distances, $d = 0, 0.6, 1.2, 1.8, 2.4$ mm from the axis itself (same colour group). Values of V_{L11} are reported in legends.

The results are shown in Figure 5.14. In order to link the V_{L11} values to the potential energy produced by this electrode, the mean value of the potential energy barrier (read at its maximum value, i.e. at variable x positions as it can be seen in Figure 5.14) has been calculated and its spread considering only values at the largest distance ($d = 2.4$ mm) for several V_{L11} and V_{oct} settings; then, by a quadratic fit, the relationship between the voltage applied to lens L11 and the effective potential energy barrier has been characterised (Figure 5.15). The values of the parameters of these fitting are reported in Table 5.6.

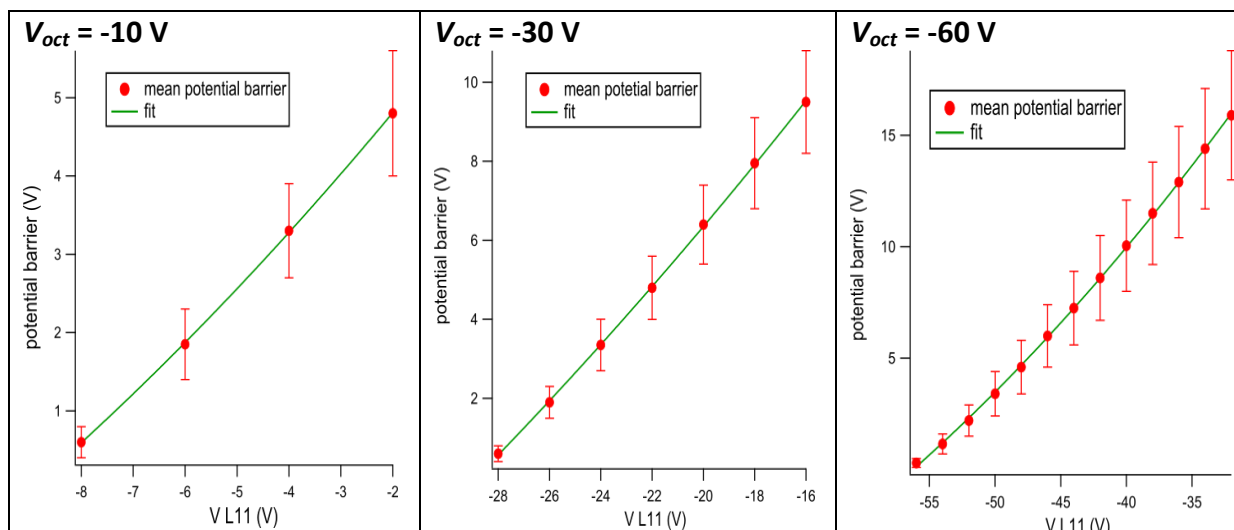


Figure 5.15. Relationship between V_{L11} and potential energy barrier for the three different values of V_{oct} used in in Figure 5.14, i.e. $V_{oct} = -10$, -30 , and -60 V. Mean values (red dots) and spread are obtained by considering barrier on axis (lowest value) and at $d = 2.4$ mm from axis. The green lines are the best fits obtained considering a quadratic function whose fitting parameters are reported in Figure 5.6.

V_{oct} (V)	a (std. dev.)	b (std. dev.)	c (std. dev.)
-10	6.46 (± 0.09) 2.3	0.86 (± 0.04) 0.25	0.016 (± 0.004)
-30	24.2 (± 0.6) 7.3	1.02 (± 0.05) 0.25	0.006 (± 0.001)
-60	47.3 (± 0.9) 14.9	1.16 (± 0.05) 0.26	0.005 (± 0.0005)

Table 5.6. Parameters of the representation of the potential energy vs V_{L11} measured with respect to V_{oct} : a second degree polynomial for positive potential energies read at the maximum of the barrier (potential barrier = $a + b V_{L11} + c V_{L11}^2$, Figure 5.15); a linear function for negative potential energies measured at $x = 150$ mm (a, b parameters reported in red).

For V_{L11} values that generate negative potential energy with respect to V_{oct} a similar strategy has been adopted, but the potential has been measured at fixed position $X = 150$ mm, i.e. at the octupole exit, and the potential energy vs V_{L11} has been represented with a linear function (see Table 5.6). The reason for this choice will be discussed later in this section.

To summarise, at this stage, the achievements are:

- a clear explanation and interpretation of the discrepancies/analogs between simulated and experimental trends of I_{ch} vs V_{L11} ;
- a quantitative relationship that correlates the potential landscape to the experimental parameter V_{L11} and allows to estimate the experimental ion kinetic energy distribution.

5.4.5 Determination of the ions kinetic energy distribution

The experimental behaviour of I_{ch} vs V_{L11} is well represented by a sigmoid function, as shown in Figure 5.16 left panel, which is the result of the combination of the potential energy distribution generated by electrode L11 at the different distance d from the axis and the spatial/energy distribution of the ion beam. The derivative of the sigmoid (Figure 5.16, left panel) produces a bell function that, in a first approximation, can be related to the distribution of the kinetic energy of the ion beam (Figure 5.16, right panel). In Figure 5.15 and Table 5.6 a relationship between V_{L11} and the height of the potential barrier to be overcome by the ion has been established. Thus, in the 'I' boxes of the right panels of Figure 5.16 the derivative of the sigmoid function is reported versus the height of the potential barrier obtained by the conversion function of Figure 5.15, with the (a,b,c) parameters collected in Table 5.6.

Looking at Figure 5.14 and Figure 5.16 one notes that in the experiments I_{ch} begins to decrease at V_{L11} values less negative or equal to V_{oct} , i.e. values which are not yet able to build a potential energy barrier. See for example the case $V_{oct} = -30$ V and $V_{L11} = -30$ V where, according to Figure 5.14 the potential landscape at the octupole exit ($x=150$ mm) assumes values smaller than V_{oct} , while in Figure 5.16, a tiny but unmistakable reduction of I_{ch} is already observed. The difference between V_{L11} and V_{oct} at $x=150$ mm has been fitted by a linear regression (parameters a, b reported in red in Table 5.6). The results of this conversion corresponds to the negative values on the axis of the potential energy in the 'II' boxes

To explain these results, the potential felt by the ions travelling along the apparatus has been analysed by simulating the travel of 5000 ions. Figure 5.17 reports in blue the mean potential (basically $V_{oct} - V_{sk}$, equal to V_{oct} in our case where $V_{sk} = 0$) and as red bars the standard deviation. Operating condition of the instrument in the simulation were: $V_{cap} = 15$ V, $V_{tl} = 40$ V, $V_{sk} = 0$ V, $V_{oct} = -30$ V, $V_{L11} = -30$ V, $V_{L12} = -60$ V and a radio frequency with 55 V amplitude.

Keeping in mind again Figure 5.11, where $V_{L11} = -30$ V corresponds to the first decrease of I_{ch} for $V_{oct} = -30$ V, it can be observed in Figure 5.17 (that refer to the same setting) that while the standard deviation of ions kinetic energy is large (5 - 10 V) inside the octupole, due to the presence of radio frequency with 55 V amplitude, this becomes smaller (0 - 1 V) outside the octupole. At $x = 150$ mm the radio frequency is attenuated, but not yet negligible. Therefore, a residual contribution of the radio frequency might raise the potential landscape by 0.5 - 2 V, i.e. an amount that, being comparable or larger than the difference between V_{L11} and V_{oct} , can create a temporary energy barrier that rejects some low kinetic energy ions, producing the first onset of I_{ch} decrease

Considering the several approximations adopted in the above procedure, the extracted distributions of the kinetic energy as represented in Figure 5.16 have to be considered as rough estimates. Nevertheless, Figure 5.16 shows that these distributions are all very similar in the range 0 - 2 eV, regardless of the specific V_{oct} value.

In summary, it has been shown how by this analysis it is possible to estimate that the distribution of the kinetic energy of the ion beam at the end of the octupole extends over a range 0 - 2 eV regardless of the specific V_{oct} value. An important practical consequence is that each element of the ion optics after the octupole with a potential more positive than V_{oct} will partially (or completely) cut the transmission of the ion beam.

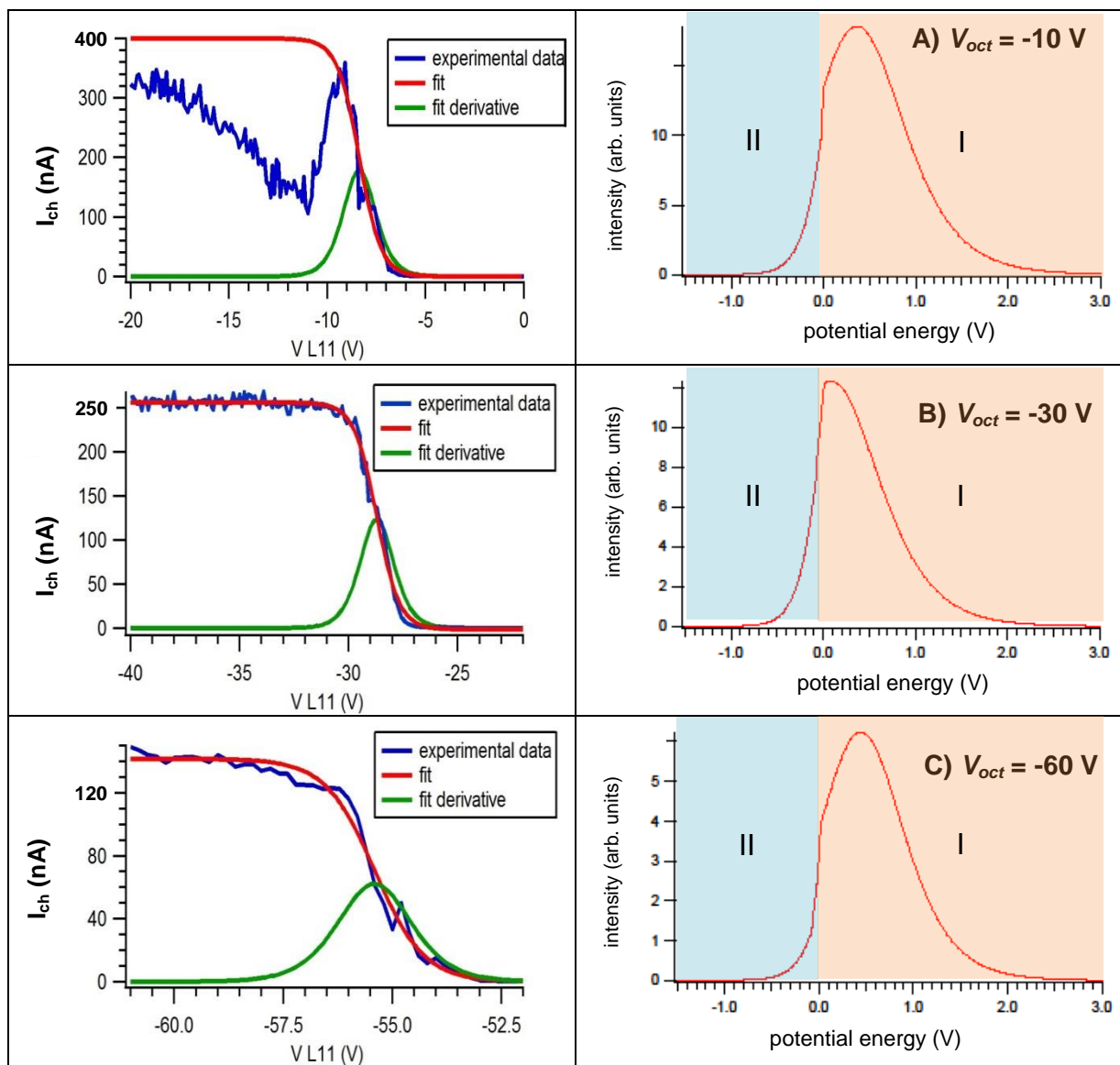


Figure 5.16. Left) Experimental I_{ch} vs V_{L11} and relative sigmoidal fit at the three V_{oct} values of Figures 5.12 and 5.14, $V_{oct} = -10, -30$ and -60 V. The derivative of the sigmoidal fit is also represented. **Right)** Kinetic energy distribution vs potential energy generated by V_{L11} calculated with respect to V_{oct} . Regions in the orange (I) and light blue (II) boxes correspond to potential energy $> V_{oct}$, i.e. energy barriers, (positive values) and a potential energy $\leq V_{oct}$ (negative values), respectively, and have been generated by using different conversion functions $Potential\ Energy = f(V_{L11})$, with the parameters reported in Table 5.6. For the positive region, 'potential energy' can be interpreted as 'kinetic energy'.

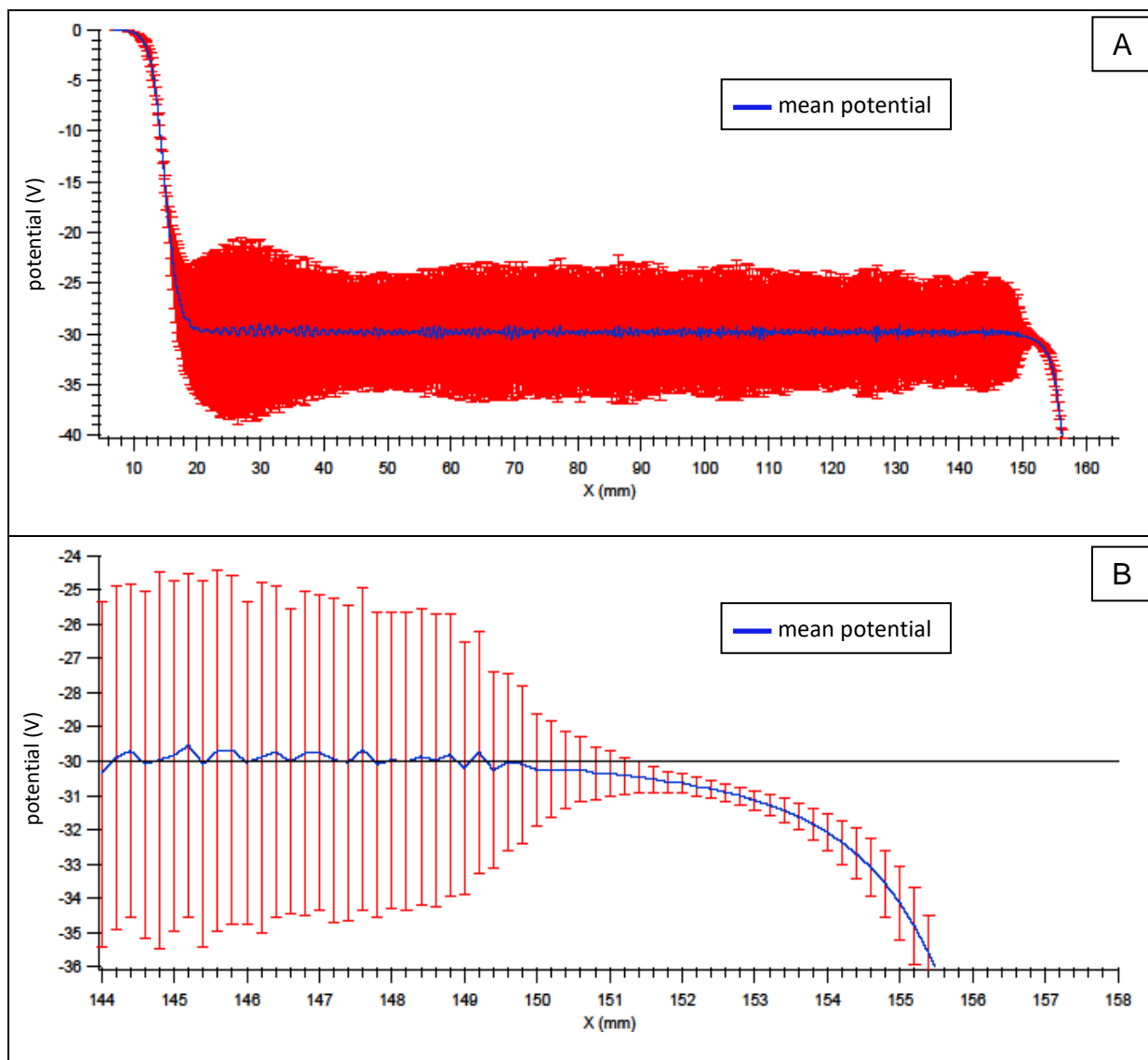


Figure 5.17. Mean potential (blue line) and standard deviation (red bars) obtained considering 5000 ions. Voltage settings are $V_{cap}=15V$, $V_{ti}=40V$, $V_{sk}=0V$, $V_{oct}=-30V$, $V_{L11}=-30$, $V_{L12}=-60V$. A) and B) refer to the same set of simulations, but while in A) we consider the whole instrument, B) is a zoom in the border region between octupole, lens L11 and L12.

5.4.6 Can the ion's kinetic energy be controlled?

In order to shed light on the role that the other optical elements (capillary and tube lens in particular) may have on the kinetic energy of the ion beam, additional tests and simulations have been performed. The tests consist in the investigation of the relation between V_{cap} and KE inside the skimmer and at the end of the octupole, holding all other voltages and initial parameters fixed according to Table 5.1. The simulation included 500 ions departing from the capillary (see Table 5.2) for each V_{cap} value; the 'estimated' kinetic energies at $x = 5$ mm (skimmer entrance) of the ions passing through the skimmer and reaching the octupole chamber (50-90%) are reported in Table 5.7. These simulations show that, an increase of V_{cap} , results in a higher kinetic energy of the ion even though, due to collisions, the increase in KE is not simply the product of the ion charge by the applied voltage, $\Delta V = V_{cap} - V_{sk} = V_{cap}$ (considering that $V_{sk} = 0$ in the present configuration), but only a fraction of it. The results of

the simulations (Table 5.7) suggest that V_{cap} is the ‘handle’ to control the KE of the ions passing through the skimmer.

Initial kinetic energy (eV)	V capillary (V)	Kinetic energy at skimmer (eV)
50	15	18.5 ± 4.2
50	50	26.1 ± 6.1
50	100	37.6 ± 9.9
50	150	48.2 ± 13.2
50	200	61.1 ± 20

Table 5.7. Kinetic energy of ions inside the skimmer estimated by simulating the ions transmission for several V_{cap} values (see Table 5.3 and Table 5.5). The reported kinetic energy is the mean value and standard deviation obtained considering 250 - 450 ions for each initial kinetic energy.

Then the transmission of this group of ions vs V_{oct} or V_{L11} has been simulated, see Figure 5.18. In all cases, the main structure in the experimental I_{ch} is fairly well represented. However there are differences between experiment and simulations. In the simulations, the increase of KE results in a broadening of the transmission versus V_{oct} .

This can be qualitatively explained considering that V_{oct} provides the first energy barrier for the ions emerging from the skimmer and entering in the octupole, and it contributes (together with V_{L11}) to determine the second barrier that ions have to overtake to leave the octupole towards the detector. In other words, more negative values of V_{oct} are related to the transmission towards the exit of the octupole, while the more positive values are related to the entrance.

Then on one hand, I_{ch} begins to increase at more negative V_{oct} values for ions of larger KE, which are therefore able to overcome a higher energy barrier between V_{oct} and V_{L11} (broadening on the left handside). On the other hand, ions with higher kinetic energy are also able to enter the octupole at $V_{oct} > V_{sk}$ (broadening on the right handside). This is consistent with the observations in Figure 25 where higher ions kinetic energies result in a shift toward less negative V_{L11} and in a broader decrease.

However, the (I_{ch} vs V_{oct}) variations predicted by the simulations at different V_{cap} are not confirmed by the experiments. In Figure 5.19, the experimental measurements of I_{ch} performed at several V_{cap} values do not show any relevant difference, neither in the position nor in the shape. Once again, it is reasonable to assume that this may be explained considering the fluid dynamic regime of the background gas because: i) the higher the V_{cap} the higher the acceleration that the electric field imposes to the ions in the entrance stage of the apparatus, but, ii) in the experiment the ion collisions with the flowing gas in the continuum regime (not included in simulations) dominate over the electric field, and almost cancel out the effect of the larger kinetic energy imposed by the electric field. In the simulations, collisions with the static gas are definitely less efficient to thermalize the ions. This would imply a longer time to reach the equilibrium with the background gas and therefore produce the differences observed in Figure 5.18.

It is very clear at this stage that basically all differences between experiments and simulations are caused by the ‘inadequate’ description of the fluid dynamics of the carrier gas in the first stage of the apparatus, the capillary – skimmer chamber. The simulated results become trustworthy in the octupole region where, as already mentioned, pressure gradient and fluid dynamics of the background gas play a minor role.

Even though the experimental kinetic energy is not sensitive to V_{cap} , we observe that I_{ch} vs V_{tl} is indeed affected by the specific V_{cap} value (Figure 5.20). This can be easily explained considering that a change of V_{cap} modifies the entire potential landscape in the capillary - tube lens – skimmer region. The simulations show that as V_{cap} increases also higher V_{tl} values are required to correctly guide the ion beam to the skimmer orifice. This is because the ions are more energetic, as well as because a higher V_{tl} with respect to V_{cap} is required to build the focussing saddle potential (see Figure 5.10).

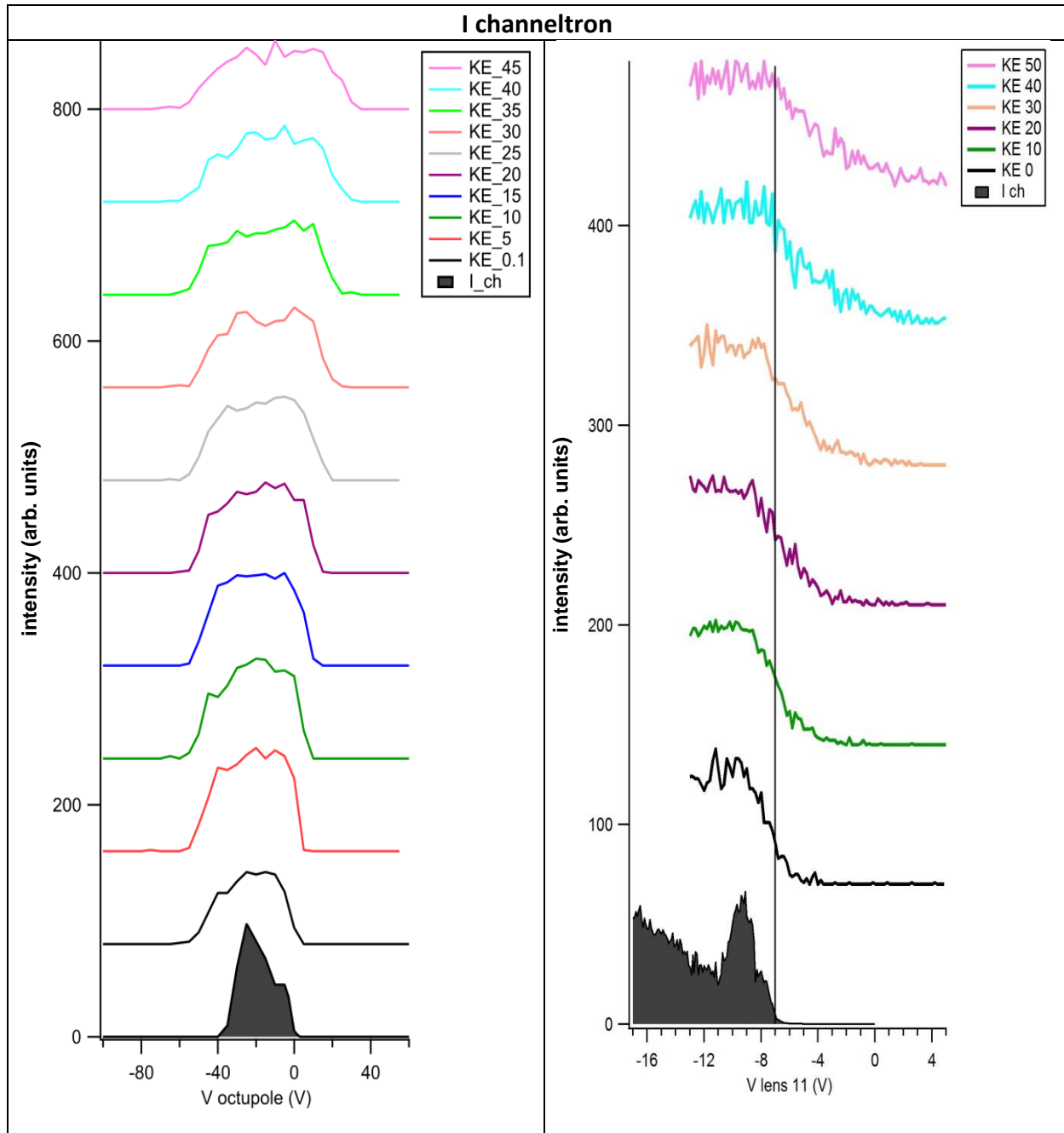


Figure 5.18. Simulated I_{ch} by varying the V_{oct} (left panel, $V_{L11} = -40$ V) and V_{L11} voltage (right panel, $V_{oct} = -10$ V) for several initial ion kinetic energies at skimmer. For comparison, the experimental data at $V_{cap} = 15$ V are also reported (black plots at the bottom).

Being aware of the difficulties introduced by the several ‘unquantifiable’ physical effects that do influence or even dominate the region between capillary and skimmer, it can be concluded that the simulations in the first region of the set-up are not completely faithful

and cannot be generalised. Moreover, the kinetic energy in the skimmer is not sensitive to V_{cap} contrary to simulation results reported in Figure 5.7.

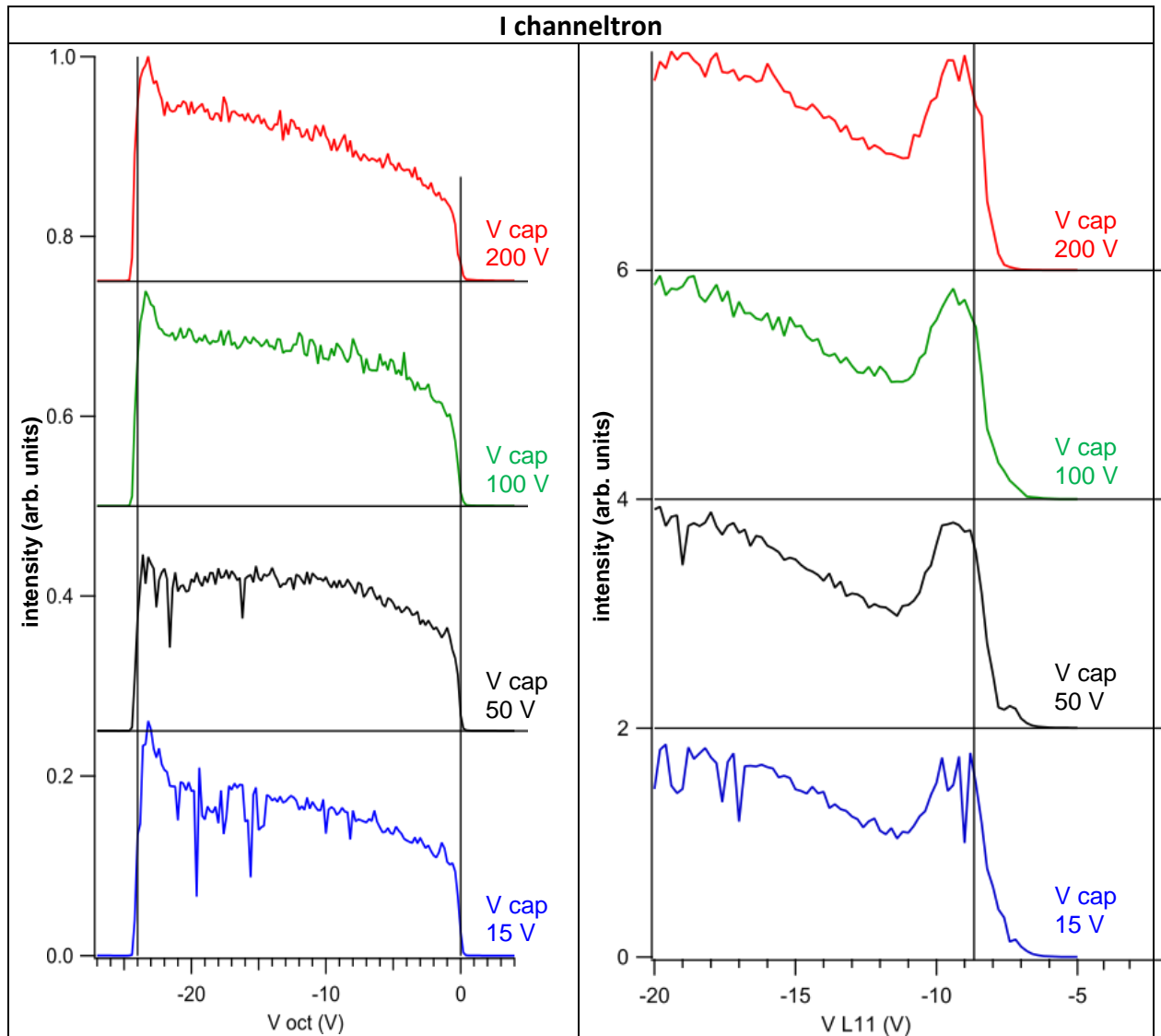


Figure 5.19. Experimental I_{ch} vs V_{oct} (left panel, $V_{L11} = -40$ V) and I_{ch} vs V_{L11} voltages (right panel, $V_{oct} = -10$ V) for several values of V_{cap} . The vertical black lines allow to visualise the alignment of the different plots.

To summarise the results of this section, the presented analysis has shown that:

- i) it is possible to use a combination of experimental measurements of the ion beam transmission I_{ch} vs V_{L11} and SIMION simulations to estimate the distribution of the kinetic energy of the ion beam at the exit of the octupole;
- ii) the distribution of the kinetic energy of the ion beam has been found to be in the range (0 - 2 eV) at the end of the octupole;
- iii) this result is independent of the specific V_{oct} value;
- iv) contrary to the simulations, experimental parameters like V_{cap} or V_{tl} do not affect this result and therefore cannot be used to 'tune' the final ion beam kinetic energy or shift their mean kinetic energy. This is because the ion collisions with the background gas dominate the transmission of the ion beam in the capillary-skimmer chamber of the apparatus.
- v) the octupole exit lens V_{L11} can be used as a high pass filter toward low kinetic energy ions.

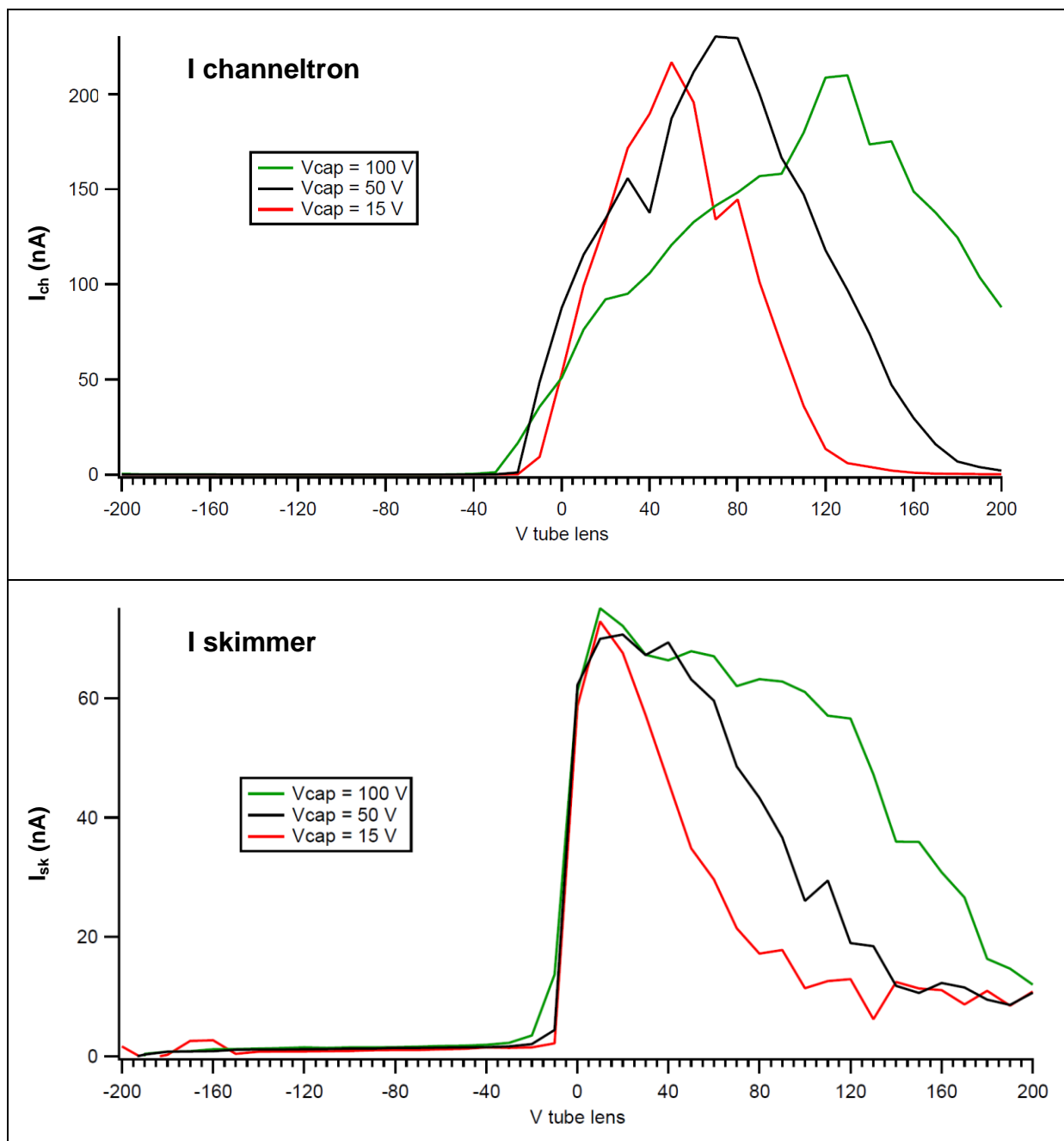


Figure 5.20. Experimental I_{ch} and I_{sk} obtained scanning V_{tl} for several values of V_{cap} . All voltages used for other electrodes are the ones listed in Table 5.1. The change in the local potential due to the different I_{cap} requires adjustment in V_{tl} to optimise ion transmission.

5.5 Tests with different molecules (adenine and laccase)

Until now, all tests have been performed using Rhodamine 6G and assuming that only the singly charged species, i.e. the unbroken, singly protonated and well desorbed molecular ion is present in the experiment. In this section the effect of different ion mass and/or mass over charge ratios (m/z) is briefly investigated.

Measurements with other two molecules, a lighter (adenine, $m = 146$ Da) and a heavier (laccase, $m \approx 60.000$ Da) one than Rhodamine 6G have been performed. This last molecule is particularly relevant for the achievement of in-vacuum deposition. The data of the used ESI solutions are reported in Table 5.8.

Molecule of interest	concentration	solvents	Needle HV
adenine	10^{-4} mol	H ₂ O, MeOH 1:1 + 5 % acetic acid	3.2 kV
Rhodamine 6G	$1.5 \cdot 10^{-5}$ mol	H ₂ O, EtOH 1:1 + 1 % acetic acid	3.2 kV
laccasi	2 mg/ml	H ₂ O, EtOH 4:1	3.75 kV

Table 5.8. Samples preparation.

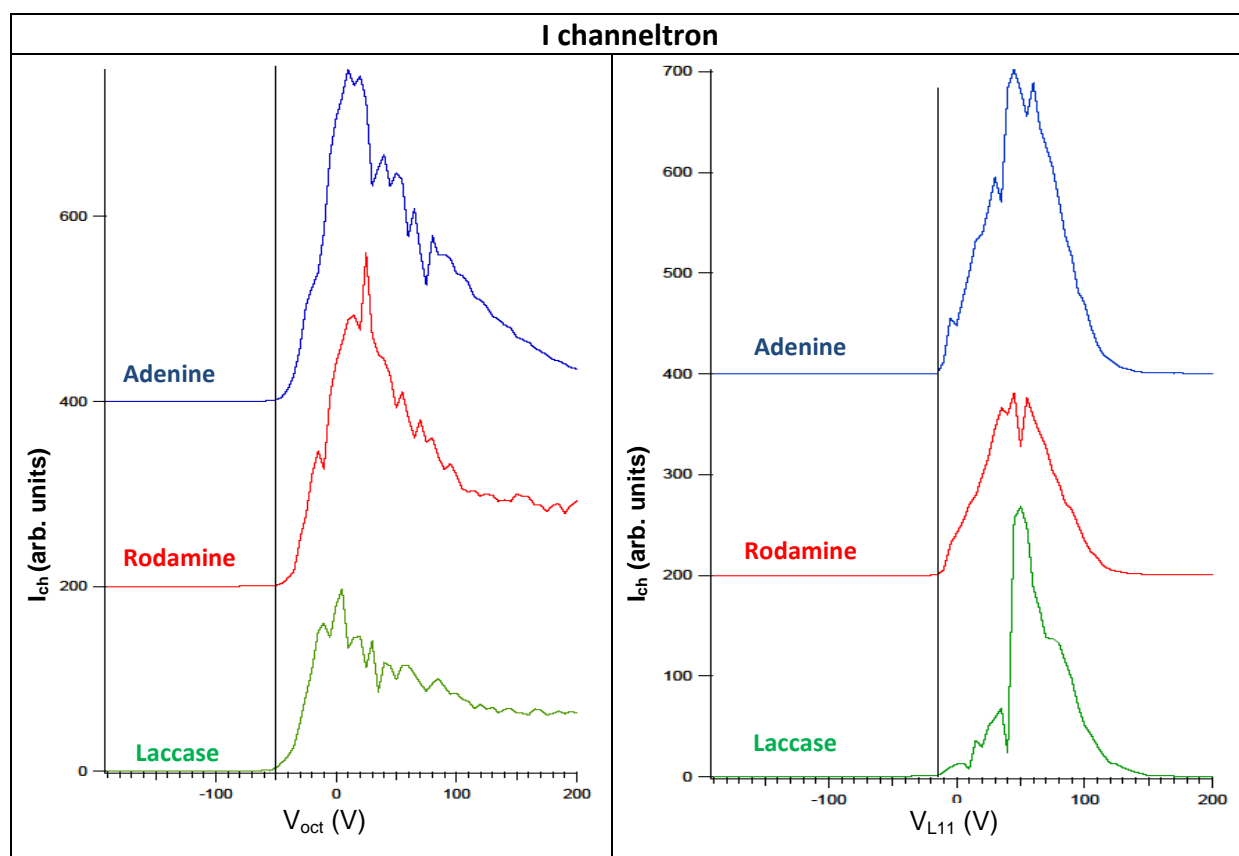


Figure 5.21. Experimental I_{ch} obtained by varying the V_{cap} (left panel) and V_{ij} (right panel) for the three samples reported in Table 5.8. All voltages used for other electrodes are the ones listed in Table 5.1. Vertical black lines are added to facilitate the comparison of the three spectra.

Molecules like Rhodamine and adenine in the ESI process most likely produce singly protonated ions, while large proteins as laccase are certainly multiply protonated and will produce an entire distribution of protonated species in the same solution. This would make the comparison with simulations very questionable, as the entire distribution of the m/z species should be included. Therefore, simulation for these samples has not been performed, but only the experimental trends are here reported.

The first observation is that, except for the high voltage, HV needed to produce the spray, all other settings are very similar for all solutions. The different HV depends from the higher concentration of water in the solution and not to the specific characteristics of the samples. Figure 5.21 reports the experimental I_{ch} vs V_{cap} and V_{tl} scans for the three samples.

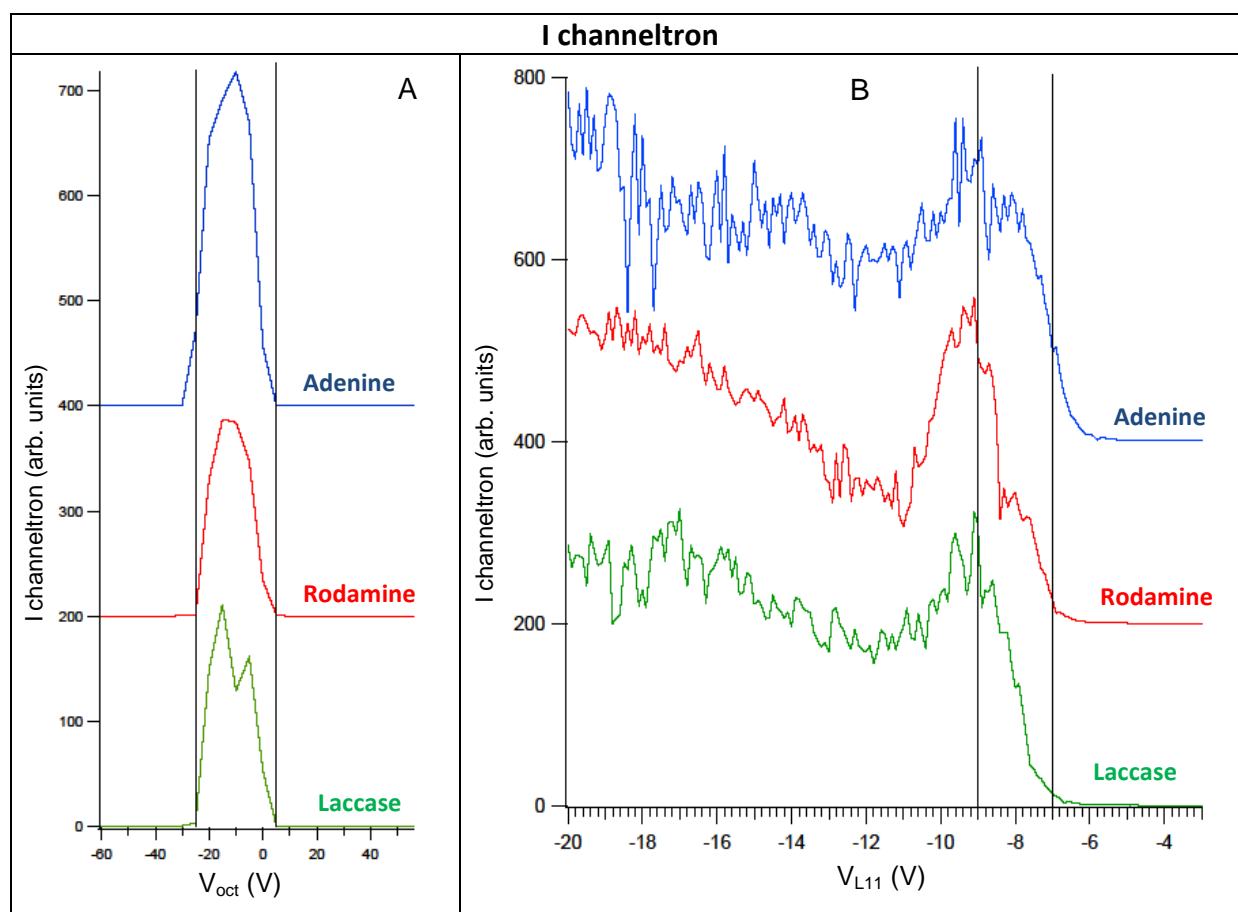


Figure 5.22. Experimental I_{ch} obtained by varying the voltage applied to V_{oct} (left panel) and V_{L11} (right panel) for the three molecules of Table 5.8. All voltages used for other electrodes are the ones listed in Table 5.1 ($V_{L11} = V_{L12} = -40$ V, $V_{oct} = -10$ V). Vertical black lines are added to better compare the different plots.

All voltages used for other electrodes are the ones listed in Table 5.1. Trends of I_{ch} are very similar and also the magnitude of the I_{ch} is comparable, with a maximum of 200 nA for laccase, 300 nA for rhodamine and 350 nA for adenine (similar values are obtained scanning other electrodes). Figure 5.22 reports I_{ch} vs V_{oct} and V_{L11} scans. Also in this case trends are very similar except for two details that show how adenine ions seem to preserve higher kinetic energy at the end of the octupole. Indeed, in Figure 5.22.A, the transmission of adenine ions begins at more negative V_{oct} than in rhodamine and laccase. This is more evident in Figure 5.22.B, where I_{ch} for adenine drops to zero at a less negative value of V_{L11} . All in all, based on the descriptions and extensive discussion of section 5.4, it can be safely stated that the kinetic energies at the exit of the octupole are in the range 0 - 3 eV regardless of the sample.

It is indeed really impressive to observe such similar results, in particular as for the very similar value of kinetic energy at the end of octupole, for ion species which are so different. This furtherly confirms that the ion dynamics in this first stage of the ESI apparatus is governed by the flow of the background gas and is mainly independent of ion mass or m/z ratio.

5.6 Summary

Several examples reported in sections 5.2 – 5.4 have shown how the interaction of the ion beam with the buffer gas in the very first stages of the ESI apparatus, from the capillary to the skimmer, plays a crucial role in the ion dynamics. This feature, not being included in the simulations, may lead to significant differences between experimental and simulated results, that require a thoughtful and sometimes not straightforward analysis but still allow to extract quantitative information on the ion beam transmission and KE distribution, according to the following picture:

a/ Experimentally, the ions are dragged through capillary and skimmer by the fast-moving neutral gas and are focussed through the skimmer by the ‘capillary-tube lens-skimmer’ electric field until they reach the octupole chamber, almost thermalized. In the capillary chamber, the effects of fluid dynamics dominate over electrostatic forces.

SIMION simulations, even with the introduction of a static background gas but without the fast moving gas, make a poor description of this first stage of the apparatus.

In the comparison, while a qualitative agreement on ion beam transmission versus setup voltages can be achieved by the use of ‘fictitious’ (pressure, kinetic energy) initial parameters, the effects on the treatment of the kinetic energy are more severe.

b/ Entering the octupole chamber, the (about) thermal ions are re-accelerated by the $V_{sk} - V_{oct}$ attracting field, but then they thermalize again while travelling in the relatively long octupole because of collisions with the background gas. In this region, simulations are a faithful representation of the experiment because pressure gradient of the background gas is less significant and this guarantees good reliability of the simulated ion trajectories in the ‘molecular flow’ approximation. Nevertheless, the input parameters of the ion beam from the simulations in the skimmer chamber lead to erroneous initialization of the parameters of the ion beam after the skimmer. Mainly, the kinetic energy of the ions at skimmer is overestimated by the simulations.

c/ At the exit of the octupole, the ions eventually have a kinetic energy of about 0 - 2 eV in a region where there is a mean potential of V_{oct} , regardless of the specific V_{oct} value.

The important consequence of this result is that, being the ion of low kinetic energy in the field of the octupole, from that stage on any optical element at a more positive potential will be seen as a barrier, with the unavoidable consequence to reject the ions. From this respect, a relatively low and negative voltage for V_{oct} would be advisable for practical reasons.

Parameters like V_{cap} , V_{tl} , V_{oct} have no effect over the kinetic energy distribution of the ions at the exit of the octupole. It is however possible that other experimental conditions like pressure/pumping speed in the skimmer and octupole chambers can indirectly affect the kinetic energy.

d/ In the present work V_{sk} was set to ground and conveniently used as a check point for ion current, in order to optimise ion transmission and to monitor its stability. It is however possible to polarise this electrode, even though some quick tests did not show major improvements in transmissions. If in anycase it should turned out to be useful in specific applications to apply a voltage to $V_{sk} \neq 0$, all the present voltage setting should be just ‘shifted’ by the value of V_{sk} . This could find application, for example, in the possibility to have a grounded target for deposition or current measurements.

e/ The exit lens of the octupole, L11 in particular, has the main purpose to focus the beam at the exit of the octupole. Depending on its specific value with respect to V_{oct} , it also has the more subtle effect to raise a potential energy barrier that can reject low energy ions. For this reason, it is advised to be set at a more negative value with respect to V_{oct} .

f/ The observation that with a proper combination of V_{oct} and V_{L11} , the octupole can be operated either as ion guide or ion trap is strictly correlated with point (e). In the guiding mode ($V_{\text{L11}} < V_{\text{oct}}$) the ions are transmitted towards the next stage of the apparatus while the neutral buffer molecules are pumped away, the solvent is desorbed and the ion kinetic energy is thermalized. Viceversa in the trapping mode ($V_{\text{L11}} > V_{\text{oct}}$), the ions rejected by the V_{L11} barrier, being thermalized by collisions with the residual gas, travel back towards the skimmer but cannot overtake anymore the barrier $V_{\text{sk}} > V_{\text{oct}}$. Therefore, they remain trapped, travelling back and forth in the octupole while new ions are injected. With a careful characterisation, this configuration can be used to build enough ion density for a pulsed mode of operation of the spectrometer. The detailed investigation of this mode of operation is beyond the scope of the present analysis, but it is still worth keeping in mind the potential of this technique for future applications.

g/ In the light of the above summary, advised operating conditions for the apparatus are:

$$V_{\text{TL}} > V_{\text{cap}} > V_{\text{sk}} > V_{\text{oct}} > V_{\text{L11}} \approx V_{\text{L12}}$$

h/ According to the experimental results, the above considerations appear to be independent of the mass of the ion and/or m/z ratio.

i/ The present work refers to positive ion.

5.7 Conclusions and future work

In an approach where experiments and simulations are combined the major features of the ion beam transmission through the first stage of the ESI source installed at CNR-ISM have been reproduced and explained and the role played by each optical element has been characterized. The simulations have provided access to information otherwise not achievable experimentally and have allowed to visualise the mode of operation of the spectrometer for different settings. However, a critical evaluation of the results of the simulations has to be taken for the first stage of the apparatus, as some incorrect results have been identified and explained.

It is believed that this work provides not only many information on the apparatus and its operation (sections 5.4 - 5.6) but, because of the identified limits, it suggests a methodology and a guide for users that are willing to use SIMION to simulate an ESI system where SIMION reliability may be poor and its use discouraged. On the other hand, ion optics simulations are relatively simple and widespread to conveniently characterise electrostatic apparatuses, while alternative treatments based on fluid dynamics are either very complex, or do not allow StartToEnd simulations.

It has been demonstrated that the use of SIMION over the entire first part of the set-up lead to many correct results and that the ones not consistent with the experiments can be "interpreted". This work suggests a methodological approach and provides a guide to the use of SIMION for the entire ESI apparatus.

It is relevant to mention that some experimental parameters like temperature of the capillary, V_{cap} and V_{oct} could in fact have more physical-chemical effect related to the integrity/fragmentation of the molecular ions transported in this first chamber. However, without having included the quadrupole mass spectrometer, presently this aspect cannot be evaluated.

Appendix of chapter 5

A.5.1 I_{ch} modulation due to channeltron detector efficiency

In this section, a qualitative explanation of the peculiar behaviour observed in I_{ch} vs V_{L11} , Figure 5.11.A is provided, suggesting that the channeltron detection efficiency is modulated by the ion beam focussing, which is in turn governed by the V_{L11} voltage.

Channel electron multipliers (CEM), like the one used to measure the I_{ch} current after the octupole, see section 2.1.4.2, respond to charged particles, X-rays, and ultraviolet radiation. A CEM has a high surface resistance. When a potential is applied between the input and output end of the CEM, the resistive surface forms a continuous dynode, with the property of emitting secondary electrons when primary particles impinge upon it (Figure A1).

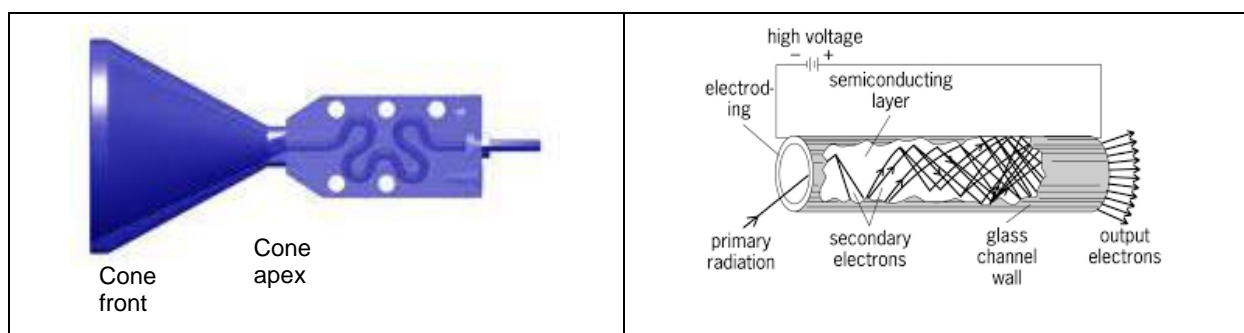


Figure A1. Left) Cut view of a CEM Dr. Sjuts (<http://www.sjuts.com/>) as the one used in our apparatus. A supporting body of ceramic material contains a specially formulated silicate glass path inside the supporting body. **Right)** The path is such to produce electron multiplication. A voltage gradient exists all along the path, due to the resistive material.

This process is called secondary electron emission. Through this process, a CEM is capable of detecting a particle or photon that has entered its funnel-shaped input aperture. These primary particles generate secondary electrons that are accelerated down the channel by a positive bias. Upon striking the interior surface of the CEM walls, these electrons then generate further secondary electrons. The resulting avalanche process produces an easily detectable output pulse/current that can be counted/measured.

The channeltron electron multiplier efficiency is determined by many factors related to its operation mode but also to the parameters of the impinging beam. The high voltage, HV, applied between (cone) and back of the channeltron is the most relevant parameter, but also the kinetic energy, size and angle of incidence of the impinging ion beam may affect the efficiency. For example, ions that exit the octupole at very large angles and do not hit the inner surface of the cone are lost and not counted; but also if the beam waist is very small and well collimated, it may directly enter the inner path of the CEM, avoiding to hit the cone. In this case, the multiplier efficiency may be reduced because the electron multiplication process will be initiated few millimetres later with respect to particles that hit the entrance of the cone, therefore resulting in a smaller output current.

In Figure 5.11.A, drawn also in Figure A2 for reference, the experimental data show two major differences with respect to the simulated results: i) a sharper signal cut at $V_{L11} > -9$ V and ii) a dip in the range V_{L11} between -16 and -10 V. While the first observation has been largely discussed in section 5.4, the second will be discussed now. Simulations performed at $V_{L11} = -20$ -12 and -9 V in the bottom panel of Figure 2A show that different V_{L11} lens settings, besides influencing the transmission, also affect the beam focalization. It's interesting to

note how the beam size at the position of the CEM is smaller at voltages corresponding to a minimum in transmission (condition B). This is consistent with the general concept introduced at the beginning of this section, where it was proposed that a well collimated beam not hitting the cone but entering straight in the inner path would correspond to a less efficient electron amplification. A quantitative description of the correlation between beam size and channeltron efficiency is beyond the purposes of this work and requires a more detailed channeltron modelling, while in the present simulations the channeltron is schematized as a uniform charged disk rather than a cone).

Despite the simplicity of our channeltron description, it is reasonable that focussing effects of the final optical elements may change the ion beam waist (proved by simulations) or scatter some ions away from the channeltron (not shown by simulations but possible) and therefore explain peculiar modulations in I_{ch} .

Therefore, it is suggested that the dip in the range V_{L11} between -16 and -10V is indeed an instrumental artefact, that cannot be reproduced by SIMION simulations.

The use of an MCP detector in replacement of the CEM would remove this effect and confirm our hypothesis.

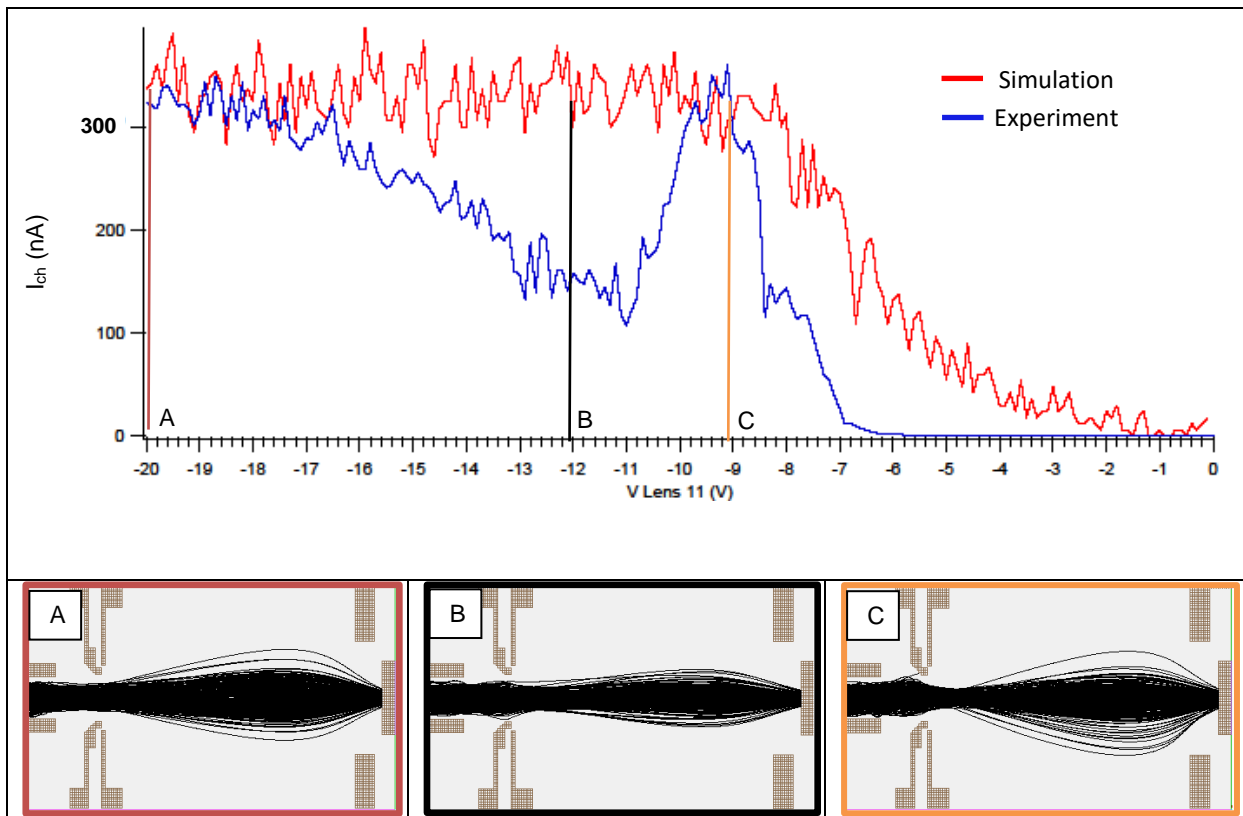


Figure A2. Top) Experimental and simulated I_{ch} vs V_{L11} (same as 5.11.A) with indicated by colored vertical lines the settings corresponding to images A - C. **Bottom)** Beam shape in the final part of the apparatus, i.e. near the CEM, obtained by simulation of 500 ion trajectories for three different values of V_{L11} : -20 V (A), -12 V (B), -9 V (C).

A.5.2 The retarding field analyser

Section 2.1.4.2 mentions the possibility to mount three grids in front of the CEM in order to realise a retarding field analyser (RFA) [105]. A RFA is a relatively simple, compact, and affordable device that can be used to measure kinetic energy distribution of the ions by means of a stack of three electrically insulated grids and an ion collecting electrode.

In a conventional mode of operation of our setup, the first and last grids, G1 and G3, should be at the same electric potential generated by the octupole exit lens so that the ions feel no discontinuity in the field; while it is the second grid, G2, where a retarding potential (V_R) is applied, to act as a KE filter: only ions that have an initial kinetic energy at the entrance of the RFA that is larger than qV_R , with q the ion's charge, will overcome this field and reach the collector. It therefore acts as a high pass filter for the ion energy, and the kinetic energy dispersion is calculated by measuring and differentiating the collector current while V_R is swept.

The use of both a RFA and a bare channeltron as tools to measure the ion beam kinetic energy at the exit of the octupole has been tested and compared.

The RFA system offers the advantage to provide, in principle, a direct measure of the kinetic energy of the ions by tuning the G2 voltage V_R , without interfering with the apparatus operation (exit lens of the octupole). In practice, large discrepancies between experiments and RFA simulations have been observed. So clearly, there are features in the experiment that are not included in the simulations. In fact, in the ideal world of the SIMION, a grid is a 'surface' with 100% transparency (in terms of transmission) and a perfect reference for the electric field, that holds the field at the exact voltage set in the parameters of the simulations. In a real experiment, none of these assumptions is true.

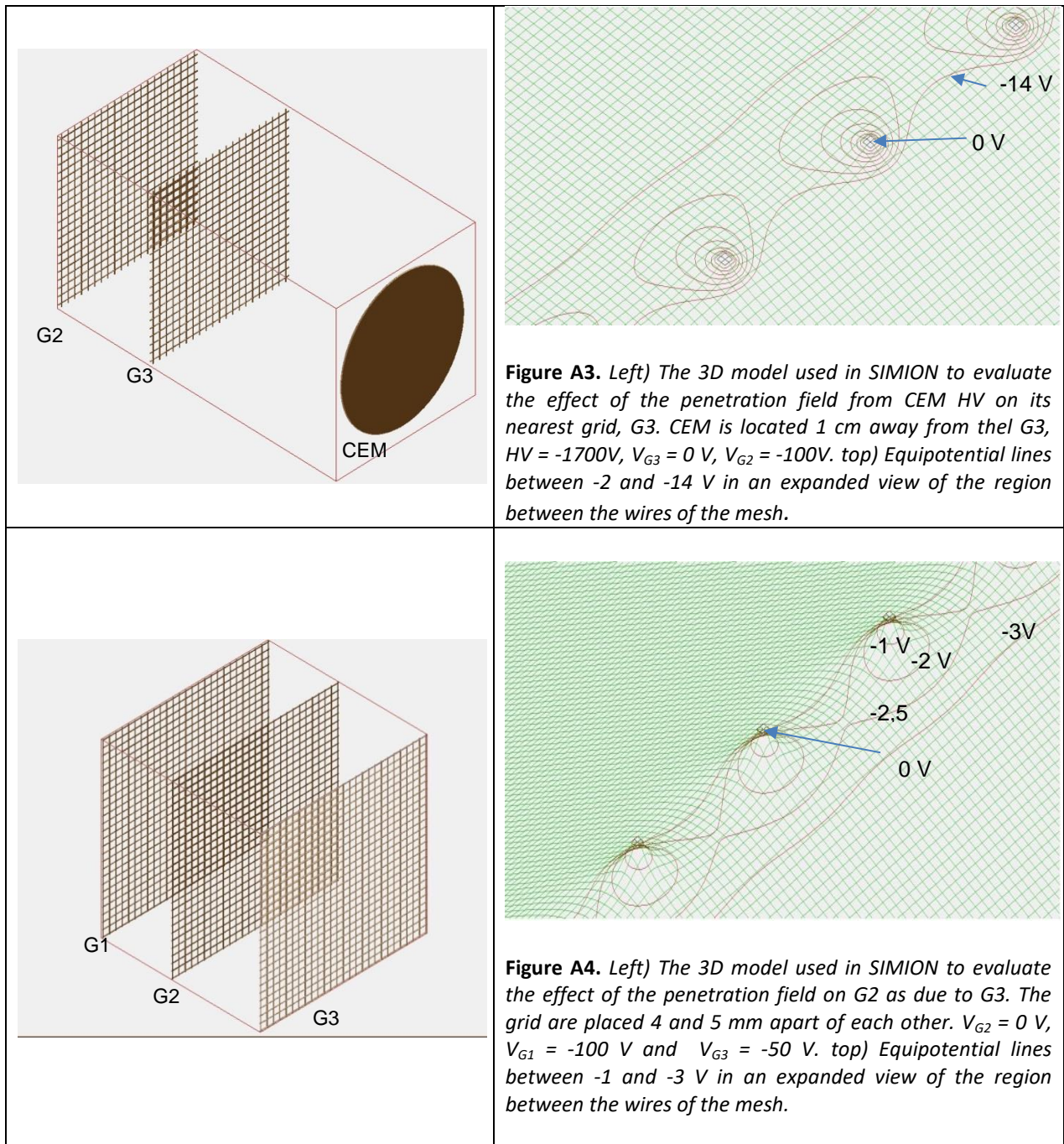
Experimental tests with the RFA use an a gold mesh of 2.8 lines/mm, corresponding to a 90% transparency. However, the grid also rejects and scatters ions in the beam that hit the wires. Even more critical in the present work, are the differences in terms of the electric field, that is far from the ideal one assumed by SIMION. Indeed, a real grid is not a perfect equipotential surface as drawn by SIMION: only the wires are at the exact set potential, while the areas between wires suffer the penetration field from nearby elements, introducing electrostatic lens effects between the wires. These effects will manifest in the change of energy barriers and saddles that focus/defocus of the ion beam [105] affecting both its transmission and kinetic energy. None of the two effects is included in the basic SIMION simulations. As a consequence, the V_R voltage scan cannot be interpreted, as the V_R axis cannot be converted into KE scale.

In order to prove the above description and to shed light on the role of the grids on the evaluation procedure of the ions kinetic energy, few SIMION simulations of the RFA drawing the grids in their real geometry have been performed, considering an area of 8 mm X 8mm, wire section = 20 μm , distance between wires 360 μm , SIMION resolution 1 GU = 10 μm .

In the RFA tested in our experimental apparatus to measure kinetic energy the ions have to cross three grids, and each one of them suffers the effects described above, affecting the beam transmission and the kinetic energy of the ions. The penetration field suffered by G3 due to the CEM HV (Figure A3) and the penetration field suffered by G2 as due to G3 have been evaluated.

As shown in Figures A3 and A4, the strongest effect is clearly due to the CEM HV on G3, but also the grids interfere among themselves, creating saddle potentials for the ions. Clearly, the smaller the applied voltages V_{G1} , V_{G2} , V_{G3} and HV, the smaller the distortions, up to the

limit of being negligible if just few eV could be applied, or if the grids could be displaced more further apart.



On the base of these results, the following considerations can be summarised:

- in the present tests, a CEM to amplify the current reading, I_{ch} , has been used and this necessarily introduces a high voltage HV to the front of the CEM cone, strongly affecting G3 (Figure A3);
- operating the apparatus at $V_{sk} = 0$ V for current monitoring on the skimmer, and testing scanning voltages V_{oct} and V_{L11} over a large range, there is a relatively high field at the octupole exit, significantly affecting G1.

This explains, also in a roughly quantitative way (order of magnitude) the differences observed between simulations and experiments in the use of the RFA for KE evaluation,

where the 'measured' KE appeared to be about 10 V higher with respect to the one obtained from simulations (results not shown).

It is likely that in future applications, the operation of the setup with polarised skimmer will allow to use low voltages on the RFA for direct reading of the current on the simple metallic plate as collector, with no need of CEM amplification.

6 Conclusions

In this thesis a bottom-up approach has been used to study the chemical-physics properties of biomolecules and molecules of biological interest of increasing complexity and to develop an instrument with the potential to be used in the manufacturing of biosensors.

In chapter 3 it has been shown that a specific process, the molecular photofragmentation, can be fully characterized from model systems, the nitroimidazole molecules, to the real drugs used in the therapy, misonidazole e metronidazole using highly selective and detailed experimental techniques and theoretical methods. This has allowed to propose that in these "oxygen mimetic" radiosensitizers, the efficacy of the therapy strongly depends from the release of NO or NO₂, which may produce permanent damage on DNA (NO) or increase the formation of radical species (NO₂), with respect to other molecules, like CO and HCN which may produce an opposite effect. Indeed drugs based on 4- and 5-nitroimidazoles, which show an abundant production of CO and HCN, have been observed to be less effective during clinical trials with respect to drugs built on 2-nitroimidazole.

In chapter 4 it has been proved that the ESI source developed to produce charged beams of intact macromolecules, is a suitable immobilisation technique to deposit these molecules in a controlled way on proper substrates and can be used to manufacture a biosensor. The test case has been the immobilisation of the laccase enzyme with at least 75% of enzyme activity preserved after deposition. To the purpose a compact setup has been built. The results of electrochemical tests showed that the biosensor produced in this way is competitive in terms of range of applicability and "lowest detection limit" with respect to others reported in literature.

The scale-up of the ESI source in a setup where the beam of macromolecules is transported in vacuum in order to allow both a chemical-physics investigation of their properties via spectrometric and spectroscopic techniques and a more selective deposition in terms of the cleanliness and of the m/z ratio which determines the conformation and the possible functions of the biomolecule, has been the object of chapter 5. The first section of this setup, which transports the beam from ambient conditions to the high vacuum region, has been built, the beam transport simulated and the simulations validated by a series of experiments.

In conclusion, the results of this work show that spectrometric and spectroscopic techniques applied to molecules of biological interest can provide valuable information on their molecular structure and on the correlation between the structure and the functions that these molecules perform. At present the strong limitation of this approach, both from the experimental and theoretical point of view, is the size of the molecules that can be investigated. This may be mitigated by using proper soft techniques to produce in vacuum beams of complex biomolecules (masses up to a few thousands of Dalton). The thesis has shown that an ESI source can be a viable approach to this, although it is still an open question if the density of the beams produced in this way is large enough to apply the same spectroscopic techniques used in the case of isolated molecules. Once the setup presented in chapter 5 will be completed, it will be possible to give an answer to this question. The present work has already allowed to propose possible improvements of the present source, especially in a different coupling between air and vacuum as well as in the first stages of the transport line under vacuum.

Another relevant result is represented by the proof that the ESI source can be efficiently used, even in air, to produce biosensors competitive with the ones already present on the market. This application can be furtherly exploited with the setup operating at ambient conditions to produce cheap and more environmental friendly biosensors, for example using a paper substrate for applications in life science and in the agrifood sectors. Another example that is being considered, is the deposition of suitable aptamers for the detection of troponin, the protein related to the functioning of the myocardium, whose excessing production is indication of cardiac stress.

On the other hand, the complete setup operating in vacuum conditions can be used to deposit biomolecules in a clean environment and in specific conformations, in order to investigate the peculiar response of biomolecules in each selected structure and whether this can be exploited for even more selective and performing biosensors. It is worth mentioning that the application of the electrospray ionisation to the immobilisation of biomolecules investigated in this thesis is only one of the many possibilities opened up by this machine, that can equally well produce beams of biomolecules as well as nanotubes or size selected nanoparticles for nanoengineering applications.

Bibliography:

- [1] dictionary.cambridge.org/it/dizionario/inglese/biomolecole
- [2] T. Jiang, S.G. Kumbar, L.S. Nair and C.T. Laurencin: Biologically Active Chitosan Systems for Tissue Engineering and Regenerative Medicine, *Current Topics in Medicinal Chemistry*, **8**, 354-364, 2008
- [3] B.D. Ratner and S.J. Bryant, *Biomaterials: Where We Have Been and Where We Are Going*, *Ann. Rev. Biomed. Eng.*, **6**, 41-75, 2004
- [4] C.R. Reyes, T.A. Petrie, K.L. Burns, Z. Schwartz and A.J. Garcia: Biomolecular surface coating to enhance orthopaedic tissue healing and integration, *Biomaterials*, **28**, 3228-3235, 2007
- [5] W.F. Oliveira, I.R.S. Arruda, G.M.M. Silva, G. Machado, L.C.B.B. Coelho and M.T.S. Correia: Functionalization of titanium dioxide nanotubes with biomolecules for biomedical applications, *Materials Science and Engineering*, **C 81**, 597- 606, 2017
- [6] S.K. Ravi and S.C. Tan: Progress and perspectives in exploiting photosynthetic biomolecules for solar energy harnessing, *Energy Environ. Sci.*, **8**, 2551—2573, 2015
- [7] P. Ensslen, S. Gartner, K. Glaser, A. Colsmann and A.H. Wagenknecht: A DNA–Fullerene Conjugate as a Template for Supramolecular Chromophore Assemblies: Towards DNA-Based Solar Cells, *Angew. Chem. Int. Ed.*, **55**, 1904 –1908, 2016
- [8] F. Toschi, D. Catone, P. O’Keeffe, A. Paladini, S. Turchini, J. Dagar and T.M. Brown: Enhanced Charge Separation Efficiency in DNA Templated Polymer Solar Cells
- [9] A.T. Blanchard and K. Salaita: Emerging uses of DNA mechanical devices, *Science* **365**, 6458, 1080-1081, 2019
- [10] L. Trotochaud, A.R. Head, O. Karshoglu, L. Kyhl and H. Bluhm: Ambient Pressure Photoelectron Spectroscopy: Practical Considerations and Experimental Frontiers, *J. Phys.: Condens. Matter*, **29**, 053002, 2017
- [11] D.I. Patel, S. Bahr, P. Dietrich, M. Meyer, A. Thiben and M.R. Linford: Ambient air, by near ambient pressure XPS, *Surface Science Spectra*, Vol. 26, 2019
- [12] J.W. Riley, B. Wang, M.A. Parkes and H.H. Fielding: Design and characterization of a recirculating liquid-microjet photoelectron spectrometer for multiphoton ultraviolet photoelectron spectroscopy, *Rev. Sci. Instrum.* **90**, 083104, 2019
- [13] R. Seidel, S. Thurmer and B. Winter: Photoelectron Spectroscopy Meets Aqueous Solution: Studies from a Vacuum Liquid Microjet, *J. Phys. Chem. Lett.*, **2**, 633–641, 2011
- [14] R. Wen, M. Hong and H.R. Byon: In Situ AFM Imaging of Li–O₂ Electrochemical Reaction on Highly Oriented Pyrolytic Graphite with Ether-Based Electrolyte, *J. Am. Chem. Soc.*, **135**, 10870–10876, 2013
- [15] S. Boutet et al.: High-Resolution Protein Structure Determination by Serial Femtosecond Crystallography, *Science*, **337**, 6092, 362 – 364, 2012

- [16] C.M. Oikonomou, Y.W. Chang and C.J. Jensen: A new view into prokaryotic cell biology from electron cryotomography, *Nature Reviews Microbiology*, 14, 205-2210, 2016
- [17] R. Baskar, K.A. Lee, R. Yeo and K.W. Yeoh: Cancer and Radiation Therapy: Current Advances and Future Directions, *Int. J. Med. Sci.* 9, 3, 193-199, 2012
- [18] G. Kraft: *Progress in Particle and Nuclear Physics*, 45,S2, S473-S544, 2000
- [19] <https://www.drebit-ibt.com/applications-of-ion-beams-html>
- [20] B. Boudaiffa, P. Cloutier, D. Hunting, M.A. Huels and L. Sanche: Resonant Formation of DNA Strand Breaks by Low-Energy (3 to 20 eV) Electrons , *Science*, 287, 1658-1660, 2000
- [21] H. Wang, H. jiang, M. Van DeGucht and M. De Ridder: Hypoxic Radioresistance: Can ROS Be the Key to Overcome It?, *Cancer*, 11 , 112, 2019
- [22] M.Dizdaroglu, P. Jaruga, M. Birincioglu and H. Rodriguez: Free radical-induced damage to DNA: mechanisms and measurement, *Free Radical Biology & Medicine*, 32, 11, 1102-1115, 2002
- [23] M. Dizdaroglu and P. Jaruga: Mechanisms of free radical-induced damage to DNA, *Free Radical Research*, 46, 4, 382-419, 2012
- [24] A.P. Breen and J.A. Murphy: Reactions of oxyl radicals with DNA, *Free Radical Biology and Medicine*, 18, 6, 1033-1077, 1995
- [25] R.Baskar, K.A. Lee, R. Yeo and K.W. Yeoh: Cancer and radiation therapy: current advances and future directions *Int. J. Med. Sci.*, 9, 193-199, 2012
- [26] P. Wardman: Chemical Radiosensitizers for Use in Radiotherapy, *Clinical Oncology*, 19, 397-417, 2007
- [27] B.J. Hong, J. Kim, H. Jeong, S. Bok, Y.E. Kim and G.O. Ahn: Tumor hypoxia and reoxygenation: the yin and yang for radiotherapy, *Radiat. Oncol. J.*, 34, 4, 239-249, 2016
- [28] M. Bonnet, C.R. Hong, Y. Gu, R.F. Anderson, W.R. Wilson, F.B. Pruijn, J. Wang, K.O.Hicks and M.O. Hay: Novel nitroimidazole alkylsulfonamides as hypoxic cell radiosensitisers, *Bioorganic and Medicinal Chemistry*, 22, 2123-2132, 2014
- [29] M.A. Stevenson, S.K. Calderwood and N. Coleman: Effects of nitroimidazoles on neuronal cells in vitro,*Int. J. Radiation Oncology Biol. Phys*,16, 1225-1230, 1989
- [30] M.M. Poggi, C.N. Coleman and J.B. Mitchell: Sensitizers and protectors of radiation and chemotherapy, *Curr. Probl. Cancer*, 25,334-411, 2011
- [31] G.S. Higgins, S.M. O’Cathail, R.J. Muschel and W.G. McKenna: Drug radiotherapy combinations: review of previous failures and reasons for future optimism, *Cancer Treat. Rev.* 41, 105-113, 2015
- [32] R. Ahmad, O.S. Wolfbeis, Y.B. Hahn, H.N. Alshareef, L. Torsi and K.N. Salama: Deposition of nanomaterials: A crucial step in biosensor fabrication , *Materials Today Communications*, 17, 289-321, 2018

- [33] R. Monosik, M. Stredansky and E. Sturdik: Biosensors - classification, characterization and new trends, *Acta Chimica Slovaca*, 5,1,109-120, 2012
- [34] P. Mehrotra: Biosensors and their applications – A Review, *Journal of Oral Biology and Craniofacial Research*, 6, 153 – 159, 2016
- [35] F. Jia, B. Narasimhan and S. Mallapragada: Materials-based strategies for multi-enzyme immobilization and co-localization: A review , *Biotechnology and Bioengineering*, 111, 2, 209-222, 2014
- [36] A.D. Dias, D.M. Kingsley and D.T. Corr: Recent Advances in Bioprinting and Applications for Biosensing, *Biosensors*, 4, 111-136, 2014
- [37] E.H. Yoo and S.Y. Lee: Glucose Biosensors: An Overview of Use in Clinical Practice, *Sensors*, 10, 5, 4558-4576, 2010
- [38] M. Pohanka and P. skladal: Electrochemical biosensors- principles and applications. *J. Appl. Biomed.* 6, 57-64, 2008
- [39] M. Portaccio, D. Di Tuoro, F. Arduini, D. Moscone, M. Cammarota, D.G. Mita and M. Lepore: Laccase biosensor based on screen-printed electrode modified with thionine–carbon black nanocomposite, for Bisphenol A detection, *Electrochimica Acta*, 109, 340-347, 2013
- [40] www.dropsens.com/en/sreen_printed_electrodes_pag.html
- [41] C.M. Silveira, T. Monteiro and M.G. Almeida: Biosensing with Paper-Based Miniaturized Printed Electrodes–A Modern Trend, *Biosensors*, 6, 51, 2016
- [42] P.R. Solanki, A. Kaushik, V.V. Agrawal and B.D. Malhotra: Nanostructured metal oxide-based biosensors, *NPG Asia Materials* , 3, 1, 17-24, 2011
- [43] G. Preda, O.S. Bizerea and B. Vlad-Oros: Sol-gel technology in enzymatic electrochemical biosensors for clinical analysis, *Environment and Biosecurity*, DOI: 10.5772/19622, 2011
- [44] I. Mazurenko et al. : How the Intricate Interactions between Carbon Nanotubes and Two Bilirubin Oxidases Control Direct and Mediated O₂ Reduction, *ACS Appl. Mater. Interfaces*, 8, 23074–23085, 2016
- [45] D. Saini, S. Saini and S. Sharma: Nanotechnology: The Future Medicine, *Nanotechnol. Rev*, 5, 4, 393-416, 2016
- [46] A. Merkoci: Electrochemical biosensing with nanoparticles, *FEBS Journal* 274, 310–316, 2007
- [47] M. Verrastro, N. Cicco, F. Crispo, A. Morone, M. Dinescu, M. Dumitru, F. Favati and D. Centonze: Amperometric biosensor based on Laccase immobilized onto a screen-printed electrode by Matrix Assisted Pulsed Laser Evaporation, *Talanta*, 154, 438-445, 2016
- [48] X. Zhou and Z. Ouyang: Following the Ions through a Mass Spectrometer with Atmospheric Pressure Interface: Simulation of Complete Ion Trajectories from Ion Source to Mass Analyzer, *Anal. Chem.* 2016, 88, 7033-7040

- [49] N. Gimelshein, S. Gimelshein, T. Lilly and E. Moskovets: Numerical Modeling of Ion Transport in an ESI-MS System, *J. Am. Soc. Mass Spectrom.* 2014, 25, 820-831
- [50] K. Huang: *Statistical mechanics*, Wiley editor, 2008
- [51] B. Sunden and J. Fu: *Heat Transfer in Aerospace Applications*, chap 4.9, Academic Press, 2017
- [52] J. Tabet, S. Edan, S. Feil, H. Abdul Carime, B. Farizon, M. Farizon, S. Ouaskit and T.D. Mark: Absolute molecular flux and angular distribution measurements to characterize DNA/RNA vapor jets, *Nuclear instruments and Methods in Physics research B* , 2458-2466, 2010
- [53] L. Bernier, H. Pinfold, M. Pauly, S. Rauschenbach and J. Reiss: Gas Flow and Ion Transfer in Heated ESI Capillary Interfaces, *J. Am Soc. Mass. Spectrom.*, 29, 761-773, 2018
- [54] www.pfeiffer-vacuum.com/en/know_how/introduction-to-vacuum-technology/fundamentals/types-of-flow/
- [55] G.E. Johnson, D. Gunaratne and J. Laskin: Soft- and reactive landing of ions onto surfaces: Concepts and applications, *Mass. Spectrometry review*, 00, 1-41, 2015
- [56] L. Adler-Abramovich, D. Aronov, P. Beker, M. Yevnin, S. Stempler, L. Buzhansky, G. Rosenman and E. Gazit: Self-assembled arrays of peptide nanotubes by vapour deposition, *Nature Nanotechnology*, 4, 849-854, 2009
- [57] M. Barber, R.S. Bordoli, R.D. Sedgwick and A.N. Tyler: Fast atom bombardment of solids (F.A.B.): a new ion source for mass spectrometry, *Journal of the Chemical Society, Chemical Communication*, 7, 325, 1981
- [58] P. Kebarle and U.H. Verkerk: Electrospray: from ions in solution to ions in the gas phase, what we know now, *Mass Spectrometry Review*, 28, 6, 2009
- [59] K. Tanaka: *Lecture for the Nobel Prize in Chemistry*, 2002
- [60] K.J. Ross and B. Sonntag: High temperature metal atom beam sources, *Rev.Sci Instrum* 66, 4409, 1995
- [61] www.thermocoax.com
- [62] H. Levola, K. Kooser, E. Rachlew, E. Nommiste and E. Kukk: Fragmentation of thymidine induced by ultraviolet photoionization and thermal degradation, *International Journal of Mass Spectroscopy* 353, 7-11, 2013
- [63] D.S. Peterson: Matrix-free methods for laser desorption/ionization mass spectrometry, *Mass Spectrometry Reviews*, 26, 19-34, 2007
- [64] V.V. Golovlev, S.L. Allman, W.R. Garrett, N.I. Taranenko and C.H. Chen: Laser-induced acoustic desorption, *International Journal of Mass Spectrometry and Ion Processes* 169/170, 69-78, 1997
- [65] S.H. Kim, A. Lee, J.Y. Song and S.Y. Han: Laser-induced thermal desorption facilitates postsource decay of peptide ions, *J. Am Soc. Mass. Spectrum.*, 23, 935-941, 2012

- [66] K. Dreisewerd: The desorption process in MALDI, *Chem. Rev.*, 103, 395-425, 2003
- [67] J.D. Cuiffi, D.J. Hayes, S.J. Fonash, K.N. Brown and A.D. Jones: Desorption-Ionization Mass Spectrometry Using Deposited Nanostructured Silicon Films, *Anal. Chem.*, 73, 1292-1295, 2001
- [68] D.J. Rousell, S.M. Dutta, M.W. Little and K.K. Murray: Matrix-free infrared soft laser desorption/ionization, *J. Mass Spectrom.*, 39, 10, 1182-1189, 2004
- [69] V. Horneffer, K. Dreisewerd, H.C. Ludemann, F. Hillenkamp, M. Lage and K. Strupat: Is the incorporation of analytes into matrix crystals a prerequisite for matrix-assisted laser desorption/ionization mass spectrometry? A study of five positional isomers of dihydroxybenzoic acid, *Int. J. Mass Spectrom.*, 185-187, 859-870, 1999
- [70] B.H. Wang, K. Dreisewerd, U. Bahr, M. Karas and F. Hillenkamp: Gas-Phase cationization and protonation of neutrals generated by matrix-assisted laser desorption, *J. Am. Soc. Mass Spectrom.*, 4, 5, 393-398, 1993
- [71] A. El-Aneed, A. Cohen and J. Banoub: Mass Spectrometry Review of the Basics: Electrospray, MALDI and Commonly Used Mass Analyzers, *Applied Spectroscopy Reviews*, 44, 210-230, 2009
- [72] K. Dreisewerd, S. Berkenkamp, A. Leisner, A. Rohlfing and C. Menzel: Fundamentals of matrix-assisted laser desorption/ionization mass spectrometry with pulsed infrared lasers, *Int. J. Mass Spectrometry* 226, 189-209, 2003
- [73] R.C. Beavis, B.T. Chait and K.G. Standing: Matrix-assisted laser-desorption mass spectrometry using 355 nm radiation, *Rapid Commun. Mass Spectrom.*, 3, 12, 233, 1989
- [74] A. Vertes, L. Balazs and R. Gijbels: Matrix-assisted laser desorption of peptides in transmission geometry, *Rapid Commun. Mass Spectrom.*, 4, 7, 228, 1990
- [75] R.B. Hall: Pulsed-laser-induced desorption studies of the kinetics of surface reactions, *J. Phys Chem*, 91, 5, 1007-1015, 1987
- [76] J.B. Fenn, M. Mann, C.K. Meng, S.F. Wong and C.M. Whitehouse: Electrospray ionization for mass spectrometry of large biomolecules, *Science*, 246, 4926, 64-71, 1989
- [77] J.B. Fenn: Lecture for the Nobel Prize in Chemistry, 2002
- [78] S. Banerjee and S. Mazumdar: Electrospray Ionization Mass Spectrometry: A Technique to Access the Information beyond the Molecular Weight of the Analyte, *International Journal of Analytical Chemistry*, 282574, 2012
- [79] I.A. Kaltashov and A. Mohimen: Estimates of Protein Surface Areas in Solution by Electrospray Ionization Mass Spectrometry, *Anal Chem*, 77, 5370-5379, 2005
- [80] J. B. Fenn: Ion Formation from Charged Droplets: Roles of Geometry, Energy and Time, *J. Am. Soc. Mass Spectrom.*, 4, 524-535, 1993
- [81] T. Meyer, V. Gabelica, H. Grubmuller and M. Orozco: Proteins in gas phase, *WIREs Comput. Mol. Sci.*, 3, 408-425, 2013

- [82] E. Ahadi and L. Konermann: Modeling the Behavior of Coarse-Grained Polymer Chains in Charged Water Droplets: Implications for the Mechanism of Electrospray Ionization, *J. Phys. Chem. B*, 116, 1, 104-112, 2012
- [83] J.F. de la Mora: Electrospray ionization of large multiply charged species proceeds via Dole's charged residue mechanism, *Anal. Chim Acta*, 406, 1, 93-104, 2000
- [84] J.M. Wells and S.A. McLuckey: Collision-induced dissociation (CID) of peptides and proteins, *Methods in Enzymology*, 402, 148-185, 2005
- [85] J.H.D. Eland: Photoelectron Spectroscopy: An introduction to Ultraviolet Photoelectron Spectroscopy in the Gas Phase, Butterworths-heinemann, 1984
- [86] A. Cartoni, P. Bolognesi, E. Fainelli and L. Avaldi: Photofragmentation spectra of halogenated methanes in the VUV photon energy range, *The Journal of Chemical Physics*, 140, 184307, 2014
- [87] S. Mobilio, F. Boscherini and C. Meneghini: Synchrotron Radiation, 3 DOI: 10.1007/978-3-642-55315-8_1, Springer-Verlag Berlin Heidelberg, 2015
- [88] Z.Huang: Brightness and coherence of synchrotron radiation and FELs, SLAC-PUB-15449 2013
- [89] <https://en.wikipedia.org/wiki/SOLEIL>
- [90] K. Zhukovsky: Undulators for Short Pulse X-Ray self Amplified spontaneous emission Free Electron Lasers, High energy and short Pulse Laser, DOI:10.5772/64439, edited by Richard Viskup, 2016
- [91] R. R. Blyth, R. Delaunay, M. Zitnik, J. Krempasky, R. Krempaska, J. Slezak, K.C. Prince, R. Richter et al.: The high resolution Gas Phase Photoemission beamline, *Elettra, J. Electron Spectrosc. Relat. Phenom.*, 101-103, 959-964, 1999
- [92] A. Derossi, F. Lama, M. Piacentini, T. Prospero and N. Zema: High flux and high resolution beamline for elliptically polarized radiation in the vacuum ultraviolet and soft x-ray regions, *Rev. Sci. Inst.* 66,1718,1995
- [93] E. de Hoffmann and V. Stroobant: Mass Spectrometry. Principles and Applications, Wiley, 2007
- [94] J.H. Gross: Mass Spectrometry: A Textbook, Springer, 2011
- [95] M. Guilhaus: Principles and instrumentation in time-of-flight mass spectrometry. Physical and instrumental concepts, *Journal of Mass Spectrometry*, 30, 11, 1519, 1995
- [96] M. Yildirim, O. Sise, M. Dogan and H.S. Kilic: Designing multi-field linear time-of-flight mass spectrometers with higher-order space focusing, *International Journal of Mass Spectrometry* 291, 1-12, 2010
- [97] W.C. Wiley and I.H. McLaren: Time-of-Flight Mass Spectrometer with Improved Resolution, *Rev. Sci. Inst.* 26, 1150, 12,1955

- [98] P. Bolognesi, A.R. Casavola, A. Cartoni, R. Richter, P. Markus, S. Borocci, J. Chiarinelli, S. Tomic, H. Sa'adeh, M. Masic, B.P. Marinkovic, K.C. Prince and L. Avaldi: Communication: "Position" does matter: The photofragmentation of the nitroimidazole isomers, *J. Chem. Phys.*, 145, 191102, 2016
- [99] J. Chiarinelli, P. Bolognesi, A. Domaracka, P. Rousseau, M.C. Castrovilli, R. Richter, S. Chatterjee, F. Wang and L. Avaldi: Insights into the dissociative ionization of glycine by PEPICO experiments, *Phys. Chem. Chem. Phys.*, 20, 22841-22848, 2018
- [100] O. Plekan, M. Coreno, V. Feyer, A. Moise, R. Richter, M. de Simone, R. Sankari and K.C. Prince: Electronic state resolved PEPICO spectroscopy of pyrimidine, *Phys. Scr.*, 78, 5, 058105, 2008
- [101] M. Satta, P. Bolognesi, A. Cartoni, A.R. Casavola, D. Catone, P. Markus and L. Avaldi: A joint theoretical and experimental study on diiodomethane: Ions and neutrals in the gas phase, *J. Chem. Phys.*, 143, 244312, 2015
- [102] M.C. Castrovilli, P. Bolognesi, A. Cartoni, D. Catone, P. O'Keeffe, A.R. Casavola, S. Turchini, N. Zema and L. Avaldi: Photofragmentation of Halogenated Pyrimidine Molecules in the VUV Range, *J. Am. Soc. Mass. Spectrom.* 25, 351, 2014
- [103] A. Cartoni, A.R. Casavola, P. Bolognesi, M.C. Castrovilli, D. Catone, J. Chiarinelli, R. Richter and L. Avaldi: Insights into 2- and 4(5)-Nitroimidazole Decomposition into Relevant Ions and Molecules Induced by VUV Ionization, *J. Phys. Chem A*, 122, 16, 4031-4041, 2018
- [104] D. A. Dahl: SIMION for the personal computer in reflection, *Int. J. Mass Spectrom.* 3, 200, 2000
- [105] T. H. M. van de Ven, C.A. de Meijere, R.M. van der Horst, M. van Kampen, V.Y. Banine and J. Beckers: Analysis of retarding field energy analyser transmission by simulation of ion trajectories, *Rev. Sci. Instrum.* 89, 043501, 2018
- [106] D. Gerlich: Inhomogeneous RF Fields: a versatile tool for the study of processes with slow ions, *Advanced in Chemical Physics Series*, Vol. LXXXII, 1992
- [107] D.J. Douglas and J.B. French: Collisional Focusing Effects in Radio Frequency Quadrupoles, *American Society for Mass Spectrometry*, 3, 398-408, 1992
- [108] P. Tosi, G. Fontana, S. Longano and D. Bassi: Transport of an ion beam through an octopole guide operating in the r.f.-only mode, *Int. J. Mass Spectrom.* 93, 95-105, 1989
- [109] B.E. Wilcox C.L. Hendrickson and A.G. Marshall: Improved ion extraction from a linear octopole ion trap: SIMION analysis and experimental demonstration, *J. Am. Soc Mass Spectrom.*, 13, 1304-1312, 2002
- [110] P.H. Dawson: Quadrupole mass analyzers: Performance, design and some recent applications, *Mass Spectrometry Reviews*, 5, 1, 1-37, 1986
- [111] M.L. Gross and R. Caprioli: *The Encyclopedia of Mass Spectrometry. Volume I: Theory and Ion Chemistry*, 182-195, Elsevier, 2003

- [112] L.D. Landau and E.M. Lifschitz: *Elettrodynamics of Continuous Media. Theoretical Physics*, vol. 1, pag. 93, Pergamon press, 1960
- [113] H. D. Zeman: Deflection of an ion beam in the two-dimensional electrostatic quadrupole field, *Rev. Sci. Instrum.* 48 , 1079, 1977
- [114] C. Hägg and I. Szabo: New ion-optical devices utilizing oscillatory electric fields. IV. Computer simulations of the transport of an ion beam through an ideal quadrupole, hexapole, and octopole operating in the rf-only mode, *Internation Journal of Mass Spectrometry and Ion Processes*, 73, 295-312, 1986
- [115] D.J. Douglas: Linear quadrupoles in mass spectrometry, *Mass Spectrometry Reviews*, 28, 937-960, 2009
- [116] D. Manura and D. Dahl: SIMION[®] 8.0 User Manual, Scientific Instrument Services, Inc Ringoes, 2008
- [117] A.D. Appelhans and D.A. Dahl: Measurement of external ion injection and trapping efficiency in the ion trap mass spectrometer and comparison with a predictive model, *International Journal of Mass Spectrometry* 216, 269-284, 2002
- [118] L. Ding, M. Sudakov and S. Kumashiro: A simulation study of the digital ion trap mass spectrometer, *International Journal of Mass Spectrometry* 221, 117-138, 2002
- [119] M. J. Frisch, et al.: gaussian 09, Revision A.02, Gaussian, Inc., Wallingford,CT, 2009
- [120] B.H. Bransden and C.J. Joachain: *Physics of atoms and molecules*, Longman Scientific & Technical 1990
- [121] www.lct.jussieu.fr/pagesperso/toulouse/enseignement/introduction_dft.pdf
- [122] P. Hohenberg and W. Kohn: Inhomogeneous Electron Gas, *Phys. Rev.* 136, B864, 1964
- [123] K. Raghavachary, G.W.Trucks, J. A. Pople, and M. A. Head-Gordon: A fifth-order perturbation comparison of electron correlation theories, *Chem.Phys. Lett.* 157, 479–483, 1989
- [124] C. Møller and M. S. Plesset: Note on an Approximation Treatment for Many-Electron Systems, *Phys. Rev.* 46, 618, 1934
- [125] M. Head-Gordon, J.A. Pople and M.J. Frisch: MP2 energy evaluation by direct methods, *Chemical Physics Letters*, 153, 6, 503–506, 1988
- [126] M. W. Wong: Vibrational frequency prediction using density functional theory, *Chem. Phys. Lett.* 256, 391–399, 1996
- [127] H.B. Schlegel: Exploring potential energy surfaces for chemical reactions: An overview of some practical methods, *J. Comput. Chem.*, 24, 1514 –1527, 2003
- [128] K.J. Laidler: A glossary of terms used in chemical kinetics, including reaction dynamics, *Pure and Applied Chemistry*, 68 ,1 ,149.192 ,1996

- [129] kida.obs.u-bordeaux1.fr/reaction/5119/CH+_NH3.html
- [130] G. S. Higgins, S.M. O’Cathail, R.J. Muschel and W.G. McKenna: Drug radiotherapy combinations: review of previous failures and reasons for future optimism, *Cancer Treat. Rev.* 41, 105-113, 2015
- [131] J. Chiarinelli, A.R. Casavola, M.C. Castrovilli, P. Bolognesi, A. Cartoni, F. Wang, R. Richter, D. Catone, S. Tomic, B.P. Marinkovic and L. Avaldi: Radiation Damage Mechanisms of Chemotherapeutically Active Nitroimidazole Derived Compounds, *Front. Chem.* ,7 , 329, 2019
- [132] L. Feketeova, O. Plekan, M. Goonewardane, M. Ahmed, A.L. Albright, J. White, R.A.J. O’Hair, M.R. Horsman, F. Wang and K.C. Prince: Photoelectron Spectra and Electronic Structures of the Radiosensitizer Nimorazole and Related Compounds, *J. Phys. Chem. A*, 119, 9986-9995, 2015
- [133] See www.nist.gov for data from NIST Standard Reference Database 69:NIST Chemistry WebBook; NIST MS number 353138
- [134] W. Arbelo-Gonzalez, R. Crespo-Otero and M. Barbatti: Steady and Time-Resolved Photoelectron Spectra Based on Nuclear Ensembles, *J. Chem. Theory Comput.* 12, 5037-5049, 2016
- [135] L. Klasinc, B. Ruscic, F. Kajfez and V. Sunjic: Photoelectron spectroscopy of the heterocycles imidazole and methylimidazoles , *International Journal of Quantum Chemistry*,5 367-371, 1978
- [136] P. Bolognesi, J.A. Kettunen, A. Cartoni, R. Richter, S. Tomic, S. Maclot, P. Rousseau, R. Delaunay and L. Avaldi: Site- and state-selected photofragmentation of 2Br-pyrimidine, *Phys. Chem. Chem. Phys.*, 17, 24063-24069, 2015
- [137] K. Kimura et al.: *Handbook of HeI photoelectron Spectra of Fundamental Organic Molecules*, Japan Scientific Societies press, Halsted press, 1981
- [138] M. Schwell, H.W. Jochims, H. Baumgartel and S. Leach: VUV photophysics and dissociative photoionization of pyrimidine, purine, imidazole and benzimidazole in the 7–18 eV photon energy range , *Chem. Phys.* 353, 145.162, 2008
- [139] K.J. Klebe, J.J. Van Houte and J. Van Thuijl: Loss of HCN and H• from the molecular ion of imidazole , *Org. Mass Spectrom*, 6, 1363-1368, 1972
- [140] J.M. Berg, J.L.Tymoczko and L. Stryer: *Biochemistry*, 7th ed., W.H. Freeman and Company, ISBN 9781429229364, 2012
- [141] S. Yoshikawa and W.S. Caughey: Infrared evidence of cyanide binding to iron and copper sites in bovine heart cytochrome c oxidase. Implications regarding oxygen reduction, *J. Biol. Chem.*, 265, 7945-7958, 1990
- [142] J. Laskin and C. Lifshitz: Kinetic energy release distributions in mass spectrometry, *J. Mass Spectrom.*, 36, 459-478, 2001

- [143] T. Bear, B. Sztaray, J.P. Kercher, A.F. Lago, A. Bodi, C. Skull and D. Palathinkal: Threshold photoelectron photoion coincidence studies of parallel and sequential dissociation reactions, *Phys. Chem. Chem. Phys.*, 7, 1507-1513, 2005
- [144] B. Sztaray and A. Bodi: Modeling unimolecular reactions in photoelectron photoion coincidence experiments, *J. Mass Spectrom*, 45, 1233-1245, 2010
- [145] W.H. Press, S.A. Teukolsky, W.T. Vetterling and B.P. Flannery: *Numerical Recipes in C*, Cambridge University Press, 2002
- [146] L.M. Barone, E. Marinari, G. Organtini and F. Ricci-Tersenghi: *Scientific Programming*, World Scientific, 2013
- [147] L. Feketeova, J. Postler, A. Zavras, P. Scheier, S. Denifl and R.A.J. O'Hair: Decomposition of nitroimidazole ions: experiment and theory, *Phys. Chem. Chem. Phys.*, 17, 12598, 2015
- [148] T. Strutz: *Data Fitting and Uncertainty (A practical introduction to weighted least squares and beyond)*. 2nd edition, Springer Vieweg, 2016
- [149] L. Feketeova, A.L. Albright, B.S. Sorensen, M.R. Horsman, J. White, R.A.J. O'Hair and N. Bassler: Formation of radical anions of radiosensitizers and related model compounds via electrospray ionization, *Int. J. Mass Spectr.* 56, 365-366, 2014
- [150] H. Guo, L. Zhang, L. Jia and F. Qi: Photon induced side-chain elimination of metronidazole: Photoionization mass spectrometric and theoretical studies *Journal of Spectroscopy and Dynamics*, 2, 2, 2012
- [151] W. Von Niessen, J. Schirmer and L.S. Cederbaum: Computational methods for the one-particle green's function, *Comput. Phys Rep*, 1, 57-125, 1984
- [152] T. Bertrand, C. Jolival, P. Briozzo, E. Caminade, N. Joly, C. Madzak and C. Mougin: Crystal structure of a four-copper laccase complexed with an arylamine: insights into substrate recognition and correlation with kinetics, *Biochemistry*, 41, 23, 7325-7333, 2002
- [153] C.F. Thurston, The structure and function of fungal laccases, *Microbiology*, 140, 19-26, 1994
- [154] B. Dedeyan, A. Klonowska, S. Tagger, T. Tron, G. Iacazio, G. Gil and J. Le Petit: Biochemical and molecular characterization of a laccase from *Marasmius quercophilus* *Appl. Environ. Microbiol.*, 66, 3, 925-929, 2000
- [155] V. Madhavi and S.S. Iele: Laccase: Properties and Applications, *BioResources*, 4, 4, 1694-1717, 2009
- [156] M.C. Castrovilli, P. Bolognesi, J. Chiarinelli, L. Avaldi, P. Calandra, A. Antonacci and V. Scognamiglio: The convergence of forefront technologies in the design of laccase-based biosensors - An update, *Trends in Analytical Chemistry*, 119, 115615, 2019
- [157] S.V. Shleev, O.V. Morozova, O.V. Nikitina, E.S. Gorshina, T.V. Rusinova, V.A. Serezhenkov, D.S. Burbaev, I.G. Gazaryan and A.I. Yaropolov: Comparison of physico-chemical characteristics of four laccases from different basidiomycetes, *Biochimie*, 86, 693-703, 2004

- [158] A. Christenson, N. Dimcheva, E. E. Ferapontova, L. Gorton, T. Ruzgas, L. Stoica, S. Shleev et al.: Direct Electron Transfer Between Ligninolytic Redox Enzymes and Electrodes, *Electroanalysis*, 16, 13, 1074- 1092, 2004
- [159] See laccase *Trametes versicolor* at www.rcsb.org/
- [160] K. Piontek, M. Antorini and T. Choinowski: Crystal Structure of a Laccase from the Fungus *Trametes versicolor* at 1.90-Å Resolution Containing a Full Complement of Coppers, *Journal of Biological Chemistry*, 277,40, 37663-37669, 2002
- [161] A. Blout, F. Billon, C. Calers, C. Methivier, A. Pailleret, H. Perrot and C. Jolival: Orientation of a *Trametes versicolor* laccase on amorphous carbon nitride coated graphite electrodes for improved electroreduction of dioxygen to water, *Electrochimica Acta*, 277, 255-267, 2018
- [162] M. Mazur, P. Kryszynski, A. Kaminska, and J. Bukowska: Immobilization of laccase on gold, silver and indium tin oxide by zirconium-phosphonate-carboxylate (ZPC) coordination chemistry, *Bioelectrochemistry*, 71,1 , 15-22, 2007
- [163] S.M. Jones and E. L. Solomon: Electron Transfer and Reaction Mechanism of Laccases, *Cell. Mol. Life Sci.*, 72, 5, 869- 883, 2015
- [164] C.F. Blanford: Laccase. The Armstrong Research Group Inorganic Chemistry Laboratory. 2007. <http://armstrong.chem.ox.ac.uk/laccase.html>
- [165] M.Sosna, J.M. Chrétien, J. D. Kilburn and P. N. Bartlett: Monolayer anthracene and anthraquinone modified electrodes as platform for *Trametes hirsute* laccase immobilization, *Phys. Chem. Chem. Phys.*, 12, 10018-10026, 2010
- [166] <https://www.sigmaaldrich.com/technical-documents/protocols/biology/enzymatic-assay-of-laccase.html>
- [167] A. Leonowicz and K. Grzywnowicz, Quantitative estimation of laccase forms in some white-rot fungi using syringaldazine as a substrate, *Enzyme and Microbial Technology*, 3, 55-58, 1981
- [168] A. Manole, D. Herea, H. Chiriac and V. Melnig: Laccase Activity Determination, *Scientific Annals of Alexandru Ioan Cuza din Iasi University, Tomul I, Biomaterials in Biophysics, Medical Physics and Ecology* 2008
- [169] J. Qu, Y. Wang, J. Gou, T. Lou and Y. Dong: Determination of Catechol by a Laccase Biosensor Based on Silica-Modified Zirconia Nanoparticles, *Analytical Letters*, 47, 2537-2547, 2014
- [170] R.S. Freire, N. Duran and L.T. Kubota: Effect of fungal laccase immobilization procedures for the development of a biosensor for phenol compounds, *Talanta* 54, 681- 686, 2001
- [171] V.N. Morozov and T.Y. Morozova: Electrospray Deposition as a Method To Fabricate Functionally Active Protein Films, *Anal. Chem.* , 71, 1415-1420, 1999

- [172] S. Malinowski P. Anthony, F. Herbert, J. Rogalski and J.J. Wolinska: Laccase Enzyme Polymerization by Soft Plasma Jet for Durable Bioactive Coatings, *Polymers*, 10, 5, 532, 2018
- [173] T. Wasilewski, B. Szulczynski, W. Kamysz, J. Gebicki and J. Namiesnik: Evaluation of Three Peptide Immobilization Techniques on a QCM Surface Related to Acetaldehyde Responses in the Gas Phase, *Sensors*, 18, 3942, 2018
- [174] F. Reinert and S. Hufner: Photoemission spectroscopy - from early days to recent applications, *New Journal of Physics*, 7, 97, 2005
- [175] C.C. Chusuei and D.W. Goodman: *Encyclopedia of Physical and Technology*, Third Edition, volume 17, Academic press, 2002
- [176] G.M. Pierantozzi, M. Sboscia and A. Ruocco: Templating effect of the substrate on the structure of Cu-phthalocyanine thin film, *Surface Science*, 669, 176-182, 2018
- [177] Y. Li, Q. Yang, M. Li and Y. Song: Rate-dependent interface capture beyond the coffee-ring effect, *Scientific Reports*, 6, 24628, 2016
- [178] B.J. Tielsch and J.E. Fulghum: Differential Charging in XPS. Part I: Demonstration of Lateral Charging in a Bulk Insulator Using Imaging XPS, *Surface and Interface Analysis*, 24, 28-33, 1996
- [179] F. Leisenberger, R. Duschek, R. Czaputa, F.P. Netzer, G. Beamson and J.A.D. Matthew: A high resolution XPS study of a complex insulator: the case of porous silicon, *Applied Surface Science*, 108, 273-281, 1997
- [180] F. Sette, G.K. Wertheim, Y. Ma, G. Meigs, S. Modesti and C.T. Chen: Lifetime and screening of the C 1s photoemission in graphite, *Physical Review B*, 41, 9766, 1990
- [181] J.S. Stevens, A.C. de Luca, M. Pelendritis, G. Terenghi, S. Downes and S.L.M. Schroeder: Quantitative analysis of complex amino acids and RGD peptides by X-ray photoelectron spectroscopy (XPS), *Surf. Interface Anal.*, 45, 1238-1246, 2013
- [182] <https://vuo.elettra.eu/services/elements/WebElements.html>
- [183] S. Wu, S.Yuan, L. Shi, Y. Zhao and J. Fang: Preparation, characterization and electrical properties of fluorine-doped tin dioxide nanocrystals, *Journal of Colloid and Interface Science*, 346, 12-16, 2010
- [184] M. Kwoka, L. Ottaviano, M. Passacantando, S. Santucci, G. Czempik and J. Szuber: XPS study of the surface chemistry of L-CVD SnO₂ thin films after oxidation, *Thin Solid Films*, 490, 36-42, 2005
- [185] A. Ayoub Arbab, R.A. Arain, R.F. Qureshi, I.A. Sahito, K. C. Sun and S.H. Jeong: Nonwoven Polyethylene Terephthalate Paper Loaded with Enzyme Coupled Multiwall Carbon Nanotubes for Superior Photocatalytic Activity for Water Remediation, *Fibers and Polymers*, 20, 4, 770-778, 2019

- [186] J.B. Fenn: Electrospray wings for molecular elephants, *Angew. Chem., Int. Ed.* , 42, 3871, 2003
- [187] P. Liuni, D.J. Wilson: Understanding and optimizing electrospray ionization techniques for proteomic analysis, *Exp. Rev. Proteomics*, 8, 197, 2011
- [188] G.J. Van Berkel, V. Kertesz: Using the Electrochemistry of the Electrospray Ion Source, *Anal. Chem.* , 79, 5511, 2007
- [189] N. B. Cech, C.G. Enke: Practical implications of some recent studies in electrospray ionization fundamentals, *Mass Spectrom. Rev.* , 20, 362, 2001
- [190] J.B. Fenn, M. Mann, C.K. Meng, S.F. Wong, C.N. Whitehouse: Electrospray ionization—principles and practice *Mass Spectrometry Reviews* 9, 37-70, 1990
- [191] L. Konermann, E. Ahadi, A. D. Rodriguez S. Vahidi: Unraveling the Mechanism of Electrospray Ionization, *Anal. Chem.*, 85, 2–9, 2013
- [192] W. Wang et al.: Numerical Simulation of Ion Transport in a Nano-Electrospray Ion Source at Atmospheric Pressure, *J. Am. Soc. Mass Spectrom.* 29, 600-612, 2018
- [193] X. Zhou and Z. Ouyang: Ion transfer between ion source and mass spectrometer inlet: electro-hydrodynamic simulation and experimental validation, *Rapid Commu. Mass Spectrom.* ,30 (Suppl. 1), 29-33, 2016
- [194] G. A. Bird: *Molecular gas dynamics and the direct simulation of gas flows*, Oxford University Press, Oxford, 1994
- [195] C.M. Benson, J. Zhong, S.F. Gimelshein, D.A. Levin, A .Montaser: Simulation of droplet heating and desolvation in inductively coupled plasma, Part II: coalescence in the plasma, *Spectrochim. Acta B At. Spectrosc.* 58(8), 1453–1471, 2003

List of publications

Publications related to the thesis work

M.C. Castrovilli, P. Bolognesi, **J. Chiarinelli**, L. Avaldi, P. Calandra, A. Antonacci and V. Scognamiglio: The convergence of forefront technologies in the design of laccase based biosensors - An update, *Trends in Analytical Chemistry*, 119, 115615, 2019

J. Chiarinelli, A.R. Casavola, M.C. Castrovilli, P. Bolognesi, A. Cartoni, F. Wang, R. Richter, D. Catone, S. Tasic, B.P. Marinkovic and L. Avaldi: Radiation Damage Mechanisms of Chemotherapeutically Active Nitroimidazole Derived Compounds, *Frontiers in Chemistry*, 7, 329, 2019

P. Bolognesi, V. Carravetta, L. Sementa, G. Barcaro, S. Monti, P.M. Mishra, A. Cartoni, M.C. Castrovilli, **J. Chiarinelli**, S. Tasic, B.P. Marinkovic, R. Richter and L. Avaldi: Core Shell Investigation of 2-nitroimidazole, *Frontiers in Chemistry*, 7, 151, 2019

A. Cartoni, A.R. Casavola, P. Bolognesi, M.C. Castrovilli, D. Catone, **J. Chiarinelli**, R. Richter and L. Avaldi: Insights into 2- and 4(5)-Nitroimidazole Decomposition into Relevant Ions and Molecules Induced by VUV Ionization, *Journal of Physical Chemistry A*, 122, 16, 4031-4041, 2018

P. Bolognesi, A.R. Casavola, A. Cartoni, R. Richter, P. Markus, S. Borocci, **J. Chiarinelli**, S. Tasic, H. Sa'adeh, M. Masic, B.P. Marinkovic, K.C. Prince and L. Avaldi: Communication: "Position" does matter: The photofragmentation of the nitroimidazole isomers, *Journal of Chemical Physics*, 145, 191102, 2016

Other publications

J. Chiarinelli, P. Markus, P. Bolognesi, L. Avaldi, V. Turco Liveri and P. Calandra: Photofragmentation of alkyl phosphates in the gas-phase, *Journal of Photochemistry & Photobiology A: Chemistry*, 365, 13-22, 2018

J. Chiarinelli, P. Bolognesi, A. Domaracka, P. Rousseau, M.C. Castrovilli, R. Richter, S. Chatterjee, F. Wang and L. Avaldi: Insights into the dissociative ionization of glycine by PEPICO experiments, *Physical Chemistry Chemical Physics*, 20, 22841-22848, 2018

ACKNOWLEDGEMENTS (Ringraziamenti)

Al termine di questi tre anni desidero ringraziare il dott. Lorenzo Avaldi, la dott. ssa Paola Bolognesi e il prof. Alesandro Ruocco per avermi dato la possibilità di lavorare a questo questo progetto, per avermi aiutato e guidato durante tutto il mio dottorato. Ringrazio i miei amici e colleghi tutti, in particolare Annarita, Mauro e Antonella per il supporto teorico e Robert per l'aiuto durante i turni di misura sulla beamline GasPhase.

Ringrazio Pietro per l'aiuto nei primi esperimenti sulla tecnica ESI.

Ringrazio anche Viviana per avermi aiutato con la sua grande esperienza in biosensoristica, Andrea ed Emiliano con la loro esperienza in microbilance al quarzo, Gianluca per l'aiuto durante le misure di caratterizzazione nel laboratorio LASEC ed Emanuela per l'aiuto nel realizzare e caratterizzare i depositi ESI.

Un ringraziamento va ai colleghi e collaboratori di GANIL Patrick, Alicja e Jean Marc ed ai tecnici Andrea e Antonello per il grande aiuto nella realizzazione della nuova camera sperimentale ESI.

Ringrazio anche tutta la mia famiglia per avermi aiutato, sostenuto e in particolare sopportato in questo ultimo periodo.

E infine un grazie affettuosissimo ad Alessandra, Patrick, Annarita, Andrea, Antonello, Laura, Adriana, Patrizia, Veronica e tutti gli amici della segreteria ISM-CNR Roberto, Pina, Alessandra, Loredana e Fosca per l'aiuto, per le chiacchierate, le piacevoli e numerose 'pause' caffè, le varie scorpacciate tutti i momenti passati insieme. Un ringraziamento particolare va a Mattea per l'aiuto quotidiano, nel lavoro e non solo, e per le tante risate fatte insieme.